# The Accelerator Neutrino-Neutron Interaction Experiment

By

TEAL JOEL PERSHING
DISSERTATION

Submitted in partial satisfaction of the requirements for the degree of

DOCTOR OF PHILOSOPHY

in

Physics

in the

OFFICE OF GRADUATE STUDIES

of the

UNIVERSITY OF CALIFORNIA

DAVIS

Approved:

Robert Svoboda, Chair

Emilija Pantic

Mani Tripathi

Committee in Charge

2020

*To my family and friends. Thank you for your support.*

# CONTENTS

# LIST OF FIGURES

# List of Tables

# ABSTRACT

## The Accelerator Neutrino-Neutron Interaction Experiment

The current era of high-precision neutrino physics demands the characterization and modeling of physical processes once found negligible. The number of neutrons ejected from nuclei in neutrino-nucleus interactions, known as the neutron multiplicity, is one such process. More experimental data is needed to properly model the neutron multiplicity of neutrino interactions, and will reduce systematic uncertainties in measurements of proton decay, neutrino cross-sections, and neutrino oscillation parameters.

The Accelerator Neutrino-Neutron Interaction Experiment (ANNIE) is a gadolinium-doped water Cherenkov detector that will measure the neutron multiplicity of charged-current neutrino interactions on oxygen. Following an overview of the current status of neutrino physics and neutrino-neutron multiplicity measurements, this thesis describes the ANNIE detector along with the calibration, monitoring, and analysis tools developed for the ANNIE collaboration. First measurements of ANNIE's neutron detection efficiency using an AmBe source are presented; the neutron capture detection efficiency at the center of the ANNIE tank was measured to be $0.64^{+0.03(stat)\,+0.01(sys)}_{-0.02(stat)\,-0.00(sys)}$. The first neutrino beam data measured by ANNIE is also presented, and demonstrates that the ANNIE detector is operational and taking high quality data.

# Acknowledgments

First and foremost, I want to thank my advisor, Robert Svoboda, for advising and funding all of my research efforts. It takes time and money to support graduate students, and I appreciate Bob's constant assistance in all the projects I pursued and tackled.

Thank you to all of the support I received from my family in the pursuit of math and science. Thanks to my parents, Teresa and Joel, for a great envionment to grow up and learn in. And thank you to my sister, Haley, for supporting my research and studies even when her own were pressing. I would not have come anywhere near where I am now without their love and encouragement.

I also want to thank my wife, Annabel Li-Pershing, for her patience and support throughout my studies. You always took my long weeks, travel away from home, and stressful episodes in unfailing stride. As you pursue your future research and career goals, I only hope that I can give back a fraction of the support you gave me.

# Chapter 1

# Introduction to neutrinos and neutrino detection

Since the first speculations of its existence, the neutrino has continued to challenge, puzzle, and surprise experimental and theoretical particle physicists alike with each new observation. Neutral, weakly interacting, incredibly light in mass, and oscillating between different flavors during propagation; the neutrino is just observable enough to be studied, yet bizarre enough to produce a plethora of interesting questions.

The study of neutrino physics is still a relatively young field with many unanswered questions. However, an impressive amount of knowledge has accumulated in a short amount of time in the drive to understand neutrinos and their properties. A review of the neutrino as it is understood now, and was investigated in the past, is warranted.

## 1.1 The discovery of the neutrino

The neutrino was first postulated in 1930 by Wolfgang Pauli following the first precision measurements of beta decay's energy emission spectrum [1]. It was initially predicted that beta decay of particles was a two-body decay of the form

$$A_{N,Z} \rightarrow A_{N,Z+1} + e^{-} \ . \tag{1.1}$$

Similar to the two-body alpha decay, the beta decay process in equation 1.1 would emit a monoenergetic electron. However, measurements made by James Chadwick in 1914 verified that the beta emission spectrum was continuous, violating energy conservation under a two-body decay hypothesis [2]. After puzzling researchers for years, Pauli sent his theory of the "neutron" in 1930 (renamed to the neutrino by Fermi in 1931) via letter to a physics conference in Tubingen, as he was attending a ball in Zurich. The beta decay process would thus be modified to have the form

$$A_{N,Z} \to A_{N,Z+1} + e^- + \nu \; , \tag{1.2}$$

wherein the three-body decay permits a continuous energy spectrum for the observed electron and the unobserved neutrino. With today's knowledge, Pauli's postulated $\nu$ is actually the electron antineutrino $\bar{\nu}_e$. The development of Enrico Fermi's weak theory in 1934 and the experimental observation of antineutrinos in the Reines-Cowan experiment in 1956 solidified the neutrino's existence and the birth of the neutrino physics field [3, 4].

## 1.2 Properties of the neutrino

The neutrino is one of the fundamental particles that form all matter in the universe. It comes in three flavors (electron ($e$), muon ($\mu$), and tau ($\tau$)) that, when paired with the three flavors of charged leptons, help form the three known lepton families. All neutrino flavors are neutral fermions of spin $\frac{1}{2}$ which are treated as massless in the Standard Model; however, the observation of neutrinos oscillating between different flavors gives evidence that the neutrino does in fact have mass. Given neutrinos are neutral leptons, they do not participate in either the electromagnetic or strong interactions. In other words, neutrinos do not undergo interactions mediated with the photon or gluon; the neutrino only interacts via the weak force, mediated by the $W$ and $Z$ bosons. The current Standard Model of fundamental particles and the neutrino's place in this model are shown in figure 1.1.

### 1.2.1 Weakly interacting

In the Standard Model, electroweak interactions are described via the charged weak currents [6, 7, 8]

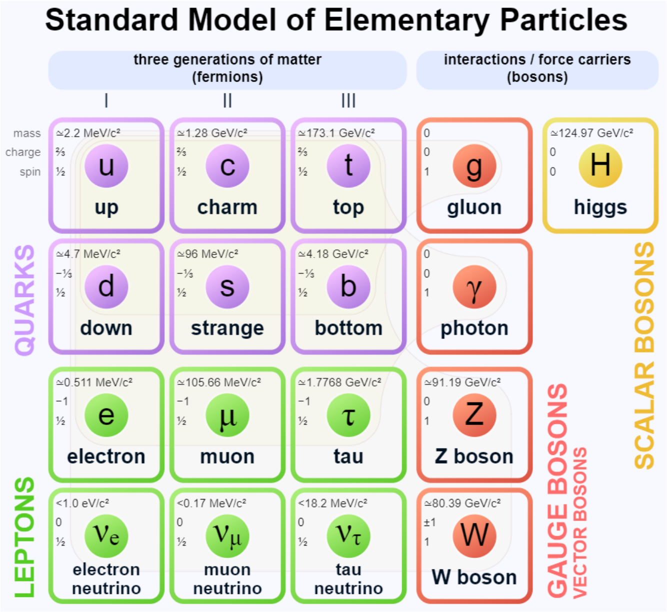

Figure 1.1. The Standard Model of fundamental particles. The quarks and leptons form the fundamental fermions of spin $\pm\frac{1}{2}$ while the bosons of integer spin are the mediators of interactions. Figure from [5].

$$\mathcal{L} = \frac{g}{\sqrt{2}}\left(J_\mu W^{\mu+} + J_\mu^\dagger W^{\mu-}\right) + \frac{g}{\cos\theta_W}\left(J_\mu^3 - \sin^2\theta_W J_\mu^{em}\right) Z^\mu + g\sin\theta_W J_\mu^{em} A^\mu \ , \qquad (1.3)$$

where the first term describes weak charged current interactions, the second describes weak neutral current interactions, and the third describes electromagnetic neutral current interactions. $\theta_W$ is the Weinberg angle and is related to the constants $g$ and $g'$ by $g/g' = \tan\theta_W$. The electron charge is also related to $g$ by $e = g\sin\theta_w$. The neutral current $J$ terms have the form

$$\begin{aligned} J_\mu^{em} &= \textstyle\sum_f q_f \bar{f}\gamma_\mu f \ , \\ J_\mu^3 &= \textstyle\sum_f I_f^3 \bar{f}\gamma_\mu \frac{1-\gamma_5}{2} f \ , \end{aligned} \qquad (1.4)$$

where $f$ is any of the leptons or quarks, $q_f$ is the fermion's charge, and $I_f^3$ is the third component of isospin for the fermion, while the charged-current $J$ terms have leptonic and quark terms of the form

$$\begin{aligned} J_W^\mu &= J_{W,L}^\mu + J_{\mu,Q}^\mu \ , \\ J_{W,L}^\mu &= \bar{l}\gamma^\mu(1-\gamma_5)\nu_l \ , \\ J_{W,Q}^\mu &= V_{ij}^{CKM}\bar{q}_i\gamma^\mu(1-\gamma_5)q_j \ , \end{aligned} \qquad (1.5)$$

where $l$ is one of the three leptonic generations $(e, \mu, \tau)$ and $V_{ij}^{CKM}$ are elements of the Cabbibo-Kobayashi-Masakawa quark mixing matrix. These couplings form the fundamental interaction terms used to describe scattering amplitudes and calculate cross sections of electroweak interactions. For a more thorough description of electroweak theory in the Standard Model and how these currents are used to derive measurable cross sections, see appendix B.2.

Prominent examples of neutral-current and charged-current interactions are neutrino-electron scattering and the Inverse Beta Decay (IBD). In the electron scattering interaction for a muon neutrino, written as

$$\nu_\mu + e^- \rightarrow \nu_\mu + e^- \ , \tag{1.6}$$

notice that no conversion between lepton and neutrino flavor is observed. At tree level, only neutral current terms associated with $Z_\mu$ couplings will contribute to calculating the scattering amplitude. On the other hand, the IBD interaction for an electron antineutrino on a proton is given by

$$\bar{\nu}_e + p \rightarrow n + e^+ \ . \tag{1.7}$$

The conversion of the electron antineutrino to a positron proceeds via the $W$-boson coupling and its cross section depends only on terms associated with $W_\mu^\pm$ at tree level.

Given it only interacts via the weak force, the neutrino is a challenging particle to observe and detect (as demonstrated by the neutrino's first significant observation following over 25 years after its prediction!). For scale, consider the average distance that an antineutrino of $\approx\ 5\,MeV$ (common energy for reactor antineutrinos) must travel through water before undergoing an IBD interaction on hydrogen 50% of the time. The probability of interaction for a neutrino as a function of penetration depth is modeled as follows:

$$P(E_\nu, x) = e^{-\sigma(E_\nu)\rho x} \ , \tag{1.8}$$

where $\sigma$ is the total neutrino cross section at neutrino energy $E_\nu$, $\rho$ is the number density of targets (for water, $\rho_H \ \approx\ 10^{26}\frac{H\,atoms}{m^3}$), and $x$ is the penetration depth. Using that the inverse beta decay cross section on hydrogen is $O(10^{-42}\,cm^2)$ at reactor antineutrino energies [9], the penetration depth for a 50% probability of interaction is

$$P(5\,MeV, x_d) \;=\; 0.5 \;\approx\; e^{-10^{-42}\,cm^2 \times 10^{26} cm^{-3} x_d}\;, \tag{1.9}$$

$$x_d \;\approx\; 10^{18}\,cm\;. \tag{1.10}$$

Essentially, a neutrino would have to travel over 10 light-years through water to interact 50% of the time. This is why, despite the massive presence of neutrinos and antineutrinos throughout the universe, kiloton-scale water Cherenkov detectors only see a few neutrino interactions per day.

### 1.2.2 Neutrino handedness

The handedness of a particle refers to whether or not its intrinsic spin is parallel or antiparallel to its direction of travel. A particle's handedness is associated with the sign of its helicity, defined as

$$h \;=\; \frac{\vec{S}\cdot\vec{p}}{|\vec{S}||\vec{p}|}\;, \tag{1.11}$$

where $\vec{S}$ is the spin of the particle and $\vec{p}$ is the momentum. Helicity has a value of -1 or +1, where the particle would be referred to as "left-handed" or "right-handed", respectively. An example of the two handedness definitions can be seen in figure 1.2.

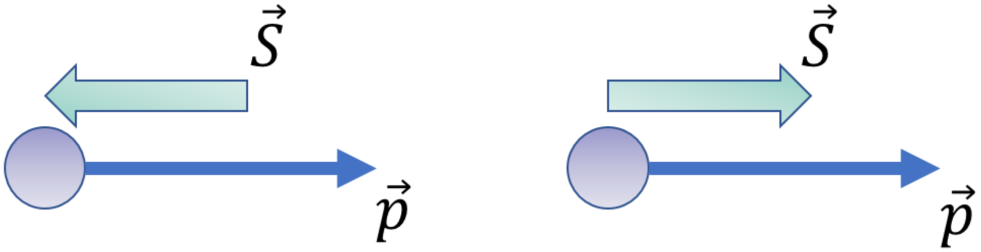

Figure 1.2. Orientation of intrinsic spin and momentum for left-handed (left) and right-handed (right) particles.

For most massive particles, the handedness is not a meaningful property; a Lorentz boost could be made to change the particle's momentum in the new reference frame and reverse the sign of the helicity value. However, in the case where a particle is massless and moves at the speed of light, a Lorentz boost cannot be made which flips the sign of the particle's helicity. In this case, handedness becomes a fundamental property of the particle.

#### 1.2.2.1 The neutrino's fixed handedness and parity violation

To date, neutrinos have always been experimentally observed as left-handed, and antineutrinos as right-handed. The first experimental indications of this property surfaced in results of the C.S. Wu experiment, which searched for parity violation in weak interactions.

Up to 1957, it was assumed but not experimentally confirmed that weak interactions conserved parity. To test this, $^{60}Co$ was placed in a magnetic field, polarizing the nucleus' intrinsic spin with the field's direction. When the $^{60}Co$ undergoes beta decay, given by

$$^{60}Co \rightarrow {}^{60}Ni + e^- + \bar{\nu}_e \ , \tag{1.12}$$

no preference in the direction of electron emission would be observed if parity were conserved. As shown in figure 1.3, a clear preference for electrons to emit in the opposite direction of the $^{60}Co$ spin was observed, providing evidence that weak interactions violate parity conservation. Following the C.S. Wu experiment, the Goldhaber experiment directly measured the helicity of the neutrino as always -1, further solidifying that weak interactions violate parity conservation seemingly as a product of the neutrino's handedness [11].

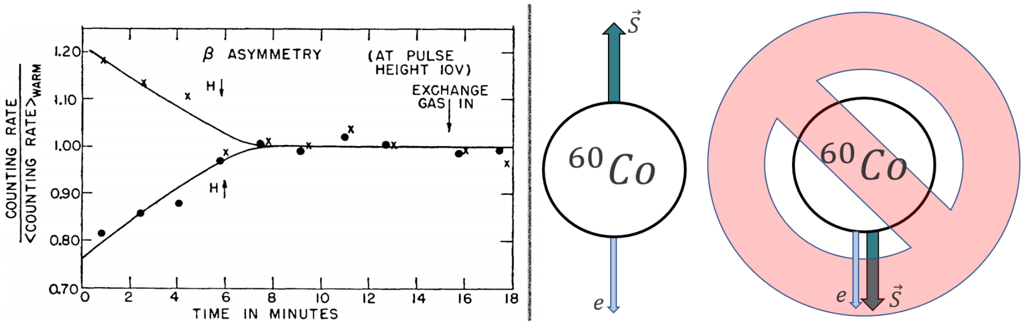

Figure 1.3. Left: Experimental results from the C.S. Wu experiment. Electron counts were detected above the source with an anthracene scintillation crystal. Given the count rate increased for a downward polarization direction (and vice versa), a preference for $^{60}Co$ betas to emit opposite the polarization direction was observed (figure taken from [10]). Right: Implications of allowed and forbidden electron directions if parity violation is maximal.

Paired with the conclusions that fixed handedness holds for massless particles, observations made in the Wu and Goldhaber experiments provided convincing evidence that the neutrino is massless. This was assumed to be the case for decades to come, until the confirmation of neutrino oscillations, discussed in section 1.2.4, shattered this theory and deepened the mystery behind the neutrino's mass nature.

### 1.2.3 Neutrino flavors

The neutrino comes in three different active neutrino flavors: the electron, the muon, and the tau. Much like the spin of a particle, the flavor of a neutrino is not known definitely until the neutrino wavestate collapses to one of the flavor wavestates. This wavestate collapse usually occurs in the form of an interaction with matter and, in the case of charged-current interactions, can be tagged through the production of an electron, muon, or tau lepton.

While equivalent, two useful working definitions of neutrino flavor are:

1. The neutrino flavors are different linear superpositions of the neutrino mass states.
2. The neutrino flavors are the neutrino wavestates that result in the production of different leptons (electron, muons, or taus) following charged-current weak interactions.

Definition one is more relatable to the neutrino oscillation theory context (see section 1.2.4), while definition two is more relatable to the observation of neutrino electroweak interactions in detectors.

The discovery of each neutrino flavor proceeded by detecting charged-current interactions of the form:

$$\bar{\nu}_l + u \to d + l^+ \ , \tag{1.13}$$

$$\nu_l + d \to u + l^- \ . \tag{1.14}$$

For these discovery measurements, an identification of a $(l^+)$ $l^-$ in detector data indicated the interaction originated from an (anti)neutrino of flavor $l$. The Reines-Cowan experiment made the first significant detection of the electron antineutrino (and the neutrino in general!) in 1956 by observing the positron-neutron coincidence signal following inverse-beta decay interactions. Shortly after, the muon neutrino was discovered at Brookhaven National Lab in 1962 by observing muons produced following muon neutrino interactions originating from a neutrino beam

[12]. Finally, the DONUT experiment directly observed the tau neutrino by searching for $\nu_\tau$ interactions following the decay of $\tau$ particles produced with Fermilab's 800 GeV Tevatron [13]. Examples of tracks observed in BNL's spark chamber and DONUT's emulsion cloud chamber are shown in figure 1.4.

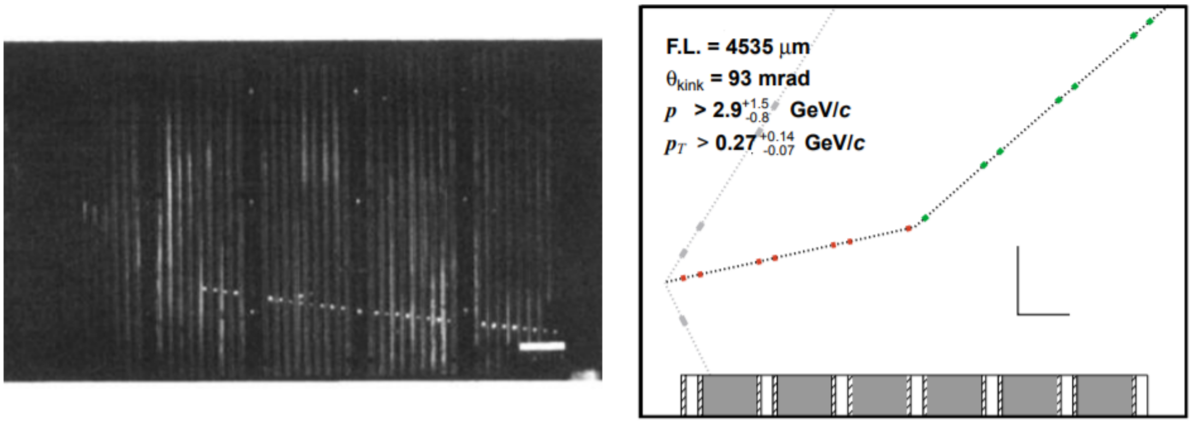

Figure 1.4. Left: Candidate muon neutrino event in the aluminum spark chamber placed in BNL's neutrino beam. The visible track is characteristic of a muon produced following a neutrino charged-current interaction. Right: Candidate tau neutrino event in the DONUT detector. DONUT's target material layers are shown at the bottom, representing steel (shaded), emulsion (cross-hatched), and plastic (no shading). Figures from [12, 13].

#### 1.2.3.1 Evidence for the existence of only three active neutrino flavors

Measurements of the Z-boson decay width via electron-positron collisions has provided the most accurate constraint on the total active neutrino flavor count to-date. The number of active light neutrinos $N_\nu$ is extracted from a measurement of the cross section $\sigma_{e^-e^+\rightarrow Z\rightarrow f\bar{f}}(s) \equiv \sigma_f(s)$, described in the Standard Model by [14]

$$\sigma_f(s) = \frac{12(hc)^2}{M_Z^2}\frac{s\Gamma_e\Gamma_f}{(s-M_Z^2)^2+s^2\frac{\Gamma_Z^2}{M_Z^2}} \ , \tag{1.15}$$

where

$$\Gamma_Z \ = \ 3\Gamma_l + \Gamma_{had} + N_\nu\Gamma_\nu \ . \tag{1.16}$$

Note that each partial decay width is directly calculable in the Standard Model. Calculations yield $\Gamma_l \approx 3\%$ for each flavor, all the same due to lepton universality, $\Gamma_{had} \approx 70\%$, and $\Gamma_\nu \approx 7\%$ per active flavor with $m_\nu < \frac{m_Z}{2}$ assuming lepton universality [15].

Given its importance in determining the number of active neutrino flavors, a brief digression on decay widths is warranted. Consider the collision of electrons and positrons at total energies of $s = (p_1 + p_2)^2 \approx M_Z^2$, where $M_Z$ is the mass of the Z-boson and $p_1, p_2$ are the 4-momenta of the electron and positron. The collisions can lead to the production of the Z-boson, which then decays through one of several processes (primary channels are lepton, neutrino, or hadron production as shown in equation 1.16). Each decay process has a characteristic lifetime that contributes to the total lifetime of the Z-boson. If the total Z-boson lifetime is short enough (leading to a small uncertainty $\Delta t$ on the lifetime), the decay products will have a fundamental decay energy uncertainty governed by the Heisenberg Uncertainty principle $\Delta E \Delta t \geq \frac{\hbar}{2}$. This energy uncertainty is related to the decay width $\Gamma = \frac{\Delta E}{2}$, manifesting as an observable spread in distributions that are a function of decay energy. One such distribution is the Z-boson's cross section for decaying to hadrons, $\sigma_{had}(s)$.

By measuring $\sigma_{had}(s)$, letting $f \rightarrow had$ in equation 1.15, substituting in equation 1.16's $\Gamma_{had}$ into equation 1.15, and varying $N_\nu$ in equation 1.15 to fit the data, the number of active light neutrino flavors can be determined. The results of this analysis as performed by LEP experiments at CERN are shown in figure 1.5. The combined fit from the four experiments shown gave $N_\nu = 2.9841 \pm 0.0083$ [14].

Although the LEP experiments wouldn't have seen any neutrino generations with a mass greater than $\frac{m_Z}{2}$, cosmological data has limited the upper bound for the sum of active neutrino masses to be well below an eV [16]. The pairing of the two measurements overwhelmingly indicate that only three active neutrino flavors exist. However, many searches for *sterile neutrino* flavors (i.e. flavors of neutrino that do not participate in the weak force) are still ongoing; sterile neutrino searches are discussed further in section 2.5.

### 1.2.4 Neutrino oscillations and neutrino mass

In 1957, Pontecorvo first proposed the concept of neutrino oscillations. Following up on the possibility of $K^0 - \bar{K^0}$ oscillations proposed by Gell-Mann and Pais, a published letter by Pontecorvo discusses other possible mixed-particle systems such as mesonium ($\mu^+ e^-$) and antimesonium ($\mu^- e^+$) [17]. Almost in passing at the end, he also comments on the possibility of neutrino-antineutrino oscillations; although it has been observed that neutrinos oscillate between

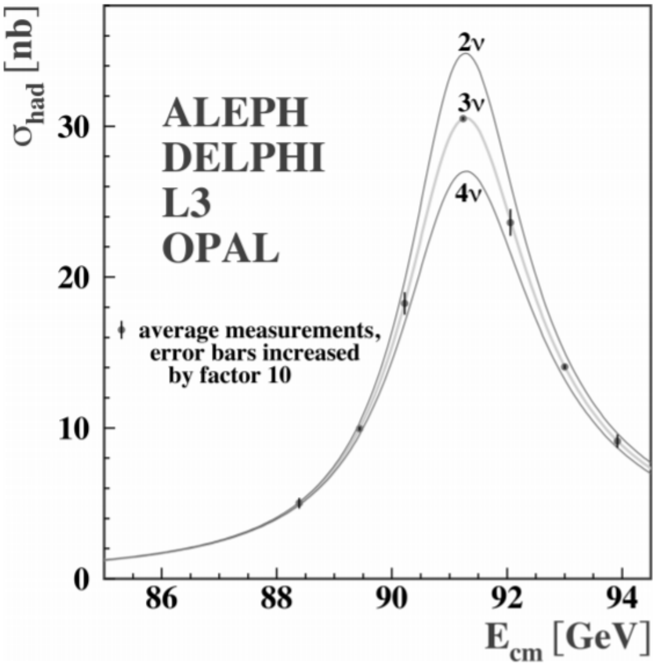

Figure 1.5. Hadronic cross section data as measured near $E_{cm} = M_Z$ for $e^+e^-$ collisions by LEP experiments. Error bars on the data are increased by a factor of 10 to show the precision of the measurement. The combined fit for the number of active neutrino generations is in considerable agreement with 3. Figure from [14].

different flavors rather than particle-antiparticle states, the idea was nevertheless mentioned and gradually expanded upon. Following the discovery of the muon neutrino in 1962, the application of neutrino mixing within neutrino flavors was also taken into consideration in a paper published in 1968. [18].

Neutrino oscillation theory became prominent after being presented as a possible solution to the solar neutrino problem. First observed in the Homestake experiment , the solar neutrino problem stemmed from a $\approx 60\%$ smaller observed solar neutrino flux than that predicted by solar models [19]. While some thought that the Homestake Experiment may have simply made an error, neutrino oscillation theory could explain the deficit if a portion of solar electron neutrinos oscillated to a different flavor; this is because Homestake's neutrino detection relied on counting argon atoms produced in the reaction $\nu_e +^{37} Cl \rightarrow e^- +^{37} Ar$, which is only sensitive to the electron neutrino flavor.

Oscillation theory needed more experimental evidence before gaining serious traction though. Neutrino-antineutrino oscillations would require the presence of a right-handed neutrino and left-handed antineutrino, but fixed handedness observations discussed in section 1.2.2 provided no evidence for this. $\bar{\nu_R} \rightarrow \nu_R$ and $\nu_L \rightarrow \bar{\nu_L}$ oscillations could still proceed if $\nu_R$ and $\bar{\nu_L}$ were sterile neutrinos, but this would be difficult to experimentally verify. On another hand, flavor oscillations would require the neutrino to have different mass eigenstates (and be massive in general), but measurements of the beta decay energy spectrum gave no indication of a neutrino mass. If the neutrino had a visible mass, any beta decay energy spectrum endpoint should see a cutoff from the neutrino's mass energy (see section 2.4).

The needed experimental evidence for neutrino flavor oscillations was provided when the SNO and Super-Kamiokande (also referred to as SuperK) experiments measured flavor change in solar neutrinos and the KamLAND experiment confirmed oscillations in reactor antineutrinos. Neutrino flavor oscillations have since been verified many times over by other neutrino detectors as well with multiple neutrino sources of different neutrino flavor. Results also indicated this oscillation phenomenon occurs in both vacuum and matter, although the effect is modified in matter (see appendix A for the vacuum and matter oscillation derivations).

#### 1.2.4.1 First confirmation of neutrino flavor change

Neutrinos changing flavor during propagation was first confirmed with discovery significance by the SNO and Super-Kamiokande experiments. Prior to measurements made by SNO, Super-Kamiokande precisely measured the total solar neutrino flux through neutrino-electron elastic scattering and also found indications of an oscillation pattern in atmospheric neutrinos [20, 21]. However, the SNO detector's usage of heavy water and chlorine salting provided a sensitivity to both the total neutrino flux (neutral current interactions) and the electron neutrino flux (charged-current interactions) [22]. As shown in figure 1.6, the comparison of the total solar neutrino flux to the electron neutrino flux confirmed a non-electron neutrino component in the solar flux at a $3.3\sigma$ significance. This combined result provided evidence that electron neutrinos produced in the Sun change to other neutrino flavors, and the two collaborations shared the Nobel prize in 2015 for the discovery.

#### 1.2.4.2 Description of neutrino oscillations

The mechanism for neutrino oscillations follows the framework of $K^0 - \bar{K^0}$ oscillations, wherein the neutrino flavor eigenstates are not the same as the mass eigenstates. For the three neutrino

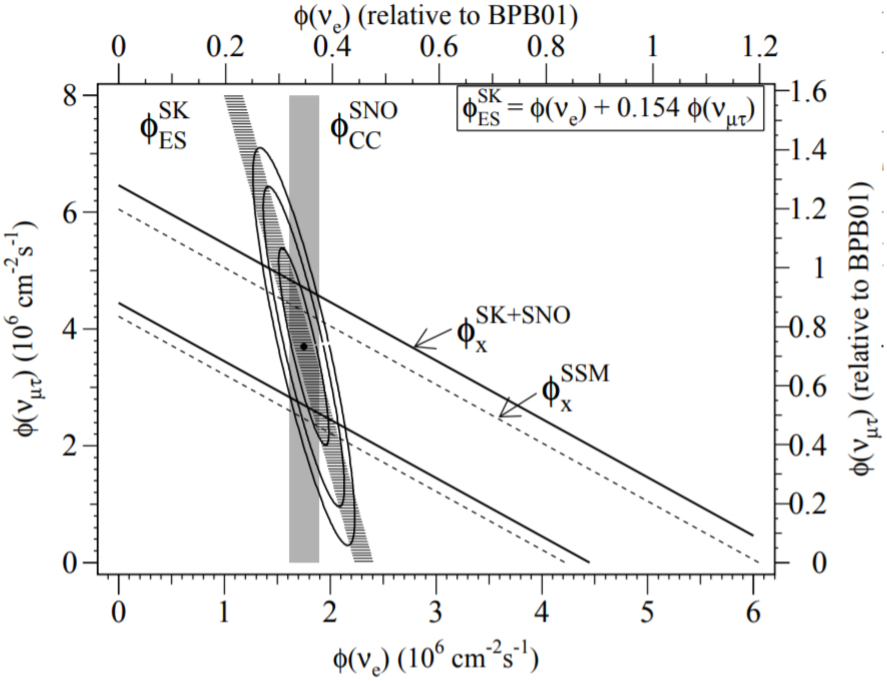

Figure 1.6. The first combined fit of the total solar neutrino flux using the results of SuperK and SNO. The shaded bands show the SNO fit to the electron neutrino flux with charged-current interactions ($\phi_{CC}$) and the SuperK electron neutrino flux fit with elastic scattering events ($\phi^{SK}_{ES}$). The diagonal hollow bands give the $1\sigma$ uncertainty on the total solar neutrino flux as measured by SK+SNO neutral current interactions and predicted by the BPB01 solar model. Figure from [22].

flavor case, and assuming that only three neutrino mass eigenstates exist (and form a complete eigenbasis), the flavor eigenstates can be written as a linear superposition of the mass eigenstates. For example, the electron neutrino wave function in the plane-wave approximation can be written in bra-ket notation as

$$|\nu_e\rangle = U_{e1}\,|\nu_1\rangle + U_{e2}\,|\nu_2\rangle + U_{e3}\,|\nu_3\rangle \ , \tag{1.17}$$

where the $U$ coefficients are terms from the unitary matrix that transform neutrino states from the mass basis to the flavor basis. In general, any linear superposition of the flavor eigenstates can be rotated to the mass basis using a unitary transformation, given by

$$\begin{pmatrix} \nu_e \\ \nu_\mu \\ \nu_\tau \end{pmatrix} = \begin{pmatrix} U_{e1} & U_{e2} & U_{e3} \\ U_{\mu 1} & U_{\mu 2} & U_{\mu 3} \\ U_{\tau 1} & U_{\tau 2} & U_{\tau 3} \end{pmatrix} \begin{pmatrix} \nu_1 \\ \nu_2 \\ \nu_3 \end{pmatrix} . \tag{1.18}$$

$U$ is also referred to as the ”neutrino mass mixing matrix”, and is the fundamental building block for describing neutrino oscillations. Using this relation, the probability for a neutrino of flavor $\alpha$ to oscillate to flavor $\beta$ after traveling a distance $L$ can be shown to be (see appendix A for derivation)

$$P(\nu_\alpha \to \nu_\beta, L) = \sum_{k=1}^{3} \sum_{j=1}^{3} U_{\beta k} U^*_{\alpha k} U^*_{\beta j} U_{\alpha j} e^{-i\frac{\Delta m^2_{jk} L}{2E}} , \tag{1.19}$$

which is often broken into its real and imaginary parts and represented as

$$P(\nu_\alpha \to \nu_\beta, L) = \delta_{\alpha\beta} - \sum_{k>j}^{3} Re(U_{\beta k} U^*_{\alpha k} U^*_{\beta j} U_{\alpha j}) \sin^2 \Delta_{kj} \pm \sum_{k>j}^{3} Im(U_{\beta k} U^*_{\alpha k} U^*_{\beta j} U_{\alpha j}) \sin 2\Delta_{kj} . \tag{1.20}$$

The $\pm$ sign is $+$ for neutrinos and $-$ for antineutrinos, and

$$\Delta_{kj} = \frac{1.27 \Delta^2_{kj} L[km]}{E_\nu [GeV]} . \tag{1.21}$$

Several features of equation 1.20 are worth highlighting. First, the frequency of oscillation as a function of neutrino energy is characterized by $\Delta m^2_{jk} = m^2_j - m^2_k$ and the baseline distance from the neutrino source. In short, if any neutrino flavor oscillations demonstrate an energy dependence, there must be some difference in the masses of the neutrino mass states. Second, the amplitude of each term in the oscillation probability is entirely governed by the elements of the $U$ matrix.

One could attempt to measure each $U_{ij}$ individually with enough oscillation measurements, but this would be an unnecessarily difficult task; it is more convenient to parameterize $U$ and determine these parameters through experimental measurements. Assuming in the model that $U$ is unitary, an $N \times N$ unitary matrix can be parameterized by $N^2$ parameters; for three generations of neutrinos ($N = 3$), $U$ can be represented completely by three mixing angles and six phase angles. However, by re-phasing the neutrino fields themselves without loss of generality, all but one of the phase angles can be removed [6]. As such, the mass mixing matrix $U$ can be parameterized completely with four free parameters to form the Pontecorvo-Maki-Nakagawa-Sakata (PMNS) matrix [23]. The PMNS matrix is

$$U_{PMNS} = \begin{pmatrix} c_{12}c_{13} & s_{12}c_{13} & s_{13}e^{-i\delta_{CP}} \\ -s_{12}c_{23} - c_{12}s_{23}s_{13}e^{i\delta_{CP}} & c_{12}c_{23} - s_{12}s_{13}s_{23}e^{i\delta_{CP}} & s_{23}c_{13} \\ s_{12}s_{23} - c_{12}c_{23}s_{13}e^{i\delta_{CP}} & -c_{12}s_{23} - s_{12}c_{23}s_{13}e^{i\delta_{CP}} & c_{23}c_{13} \end{pmatrix} , \quad (1.22)$$

where $s_{mn} \equiv \sin\theta_{mn}$ and $c_{mn} \equiv \cos\theta_{mn}$. The mass mixing matrix $U$ does not technically have to be unitary, and searches for deviations from the unitary model are possible as the uncertainty of each $U_{ij}$ term improves with upcoming experiments. Note that if the neutrino contained Majorana mass terms in the standard model Lagrangian, the $U_{PMNS}$ would be modified by additional *Majorana phases*, but would ultimately not impact the probability of neutrino oscillations (see section 2.3.2).

The three $\theta_{mn}$ angles are referred to as the neutrino mixing angles, while $\delta_{CP}$ is referred to as the CP-phase angle. A non-zero $\delta_{CP}$ would mean that neutrino/antineutrino oscillations demonstrate the following property:

$$P_{\nu_\alpha \to \nu_\beta} \neq P_{\bar{\nu}_\alpha \to \bar{\nu}_\beta} , \quad (1.23)$$

where $\alpha$ and $\beta$ are neutrino flavors. For more discussion on current best fits to these parameters and the ongoing efforts to measure $\delta_{CP}$, see section 2.1.

The KamLAND measurement of reactor antineutrinos provides a great example of how neutrino oscillation parameters can be extracted from detector data. Assuming the three-flavor oscillation model and the $\theta_{13}$ regimes set by CHOOZ ($\cos^4\theta_{13} \geq 0.92$) [24], the $\bar{\nu}_e \to \bar{\nu}_e$ survival probability at KamLAND was approximated by [25]

$$P(\bar{\nu}_e \to \bar{\nu}_e) \approx \cos^4\theta_{13}\left[1 - \sin^2\theta_{12}\sin^2\frac{\Delta m^2_{12}L}{4E_\nu}\right] . \quad (1.24)$$

The observed antineutrino event spectrum at KamLAND was then fit with a full model of the expected reactor antineutrino rate (see section 1.3.2) after subtracting geoneutrino backgrounds and incorporating oscillation effects. The $P(\nu_e \to \nu_e : E_\nu, L)$ extracted by comparing detector data to the no-oscillation hypothesis is shown in figure 1.7.

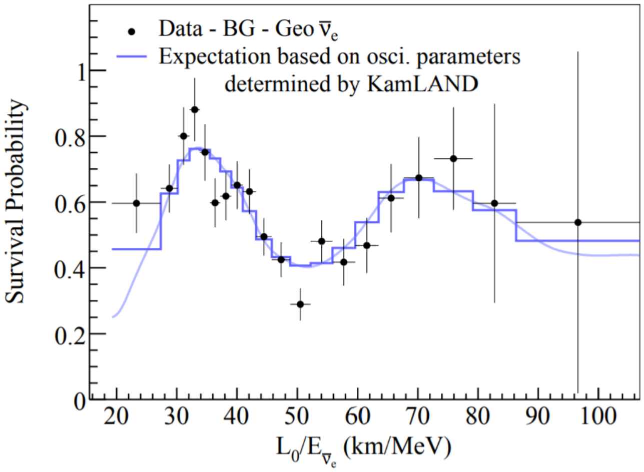

Figure 1.7. Survival probability of reactor electron antineutrinos observed by the KamLAND experiment. Data points are the ratio of observed antineutrinos to the rate predicted in the no-oscillation case. The frequency of the oscillation pattern shown yields the mass-squared difference $\Delta m^2_{12}$. Figure from [26].

The effects of neutrino oscillation are emphasized when plotted as a function of $L/E_\nu$, with the frequency and mean amplitude providing the means to measure $\Delta m^2_{12}$ and $\theta_{12}$, respectively. The parameters derived from the fit to KamLAND's spectrum were $\Delta m^2_{12} = 7.58^{+0.14}_{-0.13}(stat)$ $^{+0.15}_{-0.15}(syst) \times 10^{-5} eV^2$ and $\tan^2\theta_{12} = 0.56^{+0.10}_{-0.07}(stat)^{+0.10}_{-0.06}(syst)$ [26].

#### 1.2.4.3 Significance of neutrino oscillations to neutrino mass

The confirmation of neutrino oscillations sparked a surge of neutrino oscillation experiments designed to measure the PMNS oscillation parameters and mass-squared differences. Of significance to the neutrino mass, long-baseline reactor measurements and solar neutrino experiments measured non-zero values of $\Delta m^2_{12} = m_1^2 - m_2^2$ while accelerator experiments and cosmic neutrino measurements yielded a non-zero value for $\Delta m^2_{23}$ (see section 2.1). The major revelation from non-zero mass-squared differences is this: if the three neutrino masses are all different values, then at least two of them are non-zero and must have mass.

Perhaps the biggest implication of non-zero neutrino masses is that the Standard Model must be modified. Although only the interaction terms for the electroweak model were shown in equation 1.3, the complete Lagrangian can be realized through the *Higgs mechanism*, wherein another scalar field doublet is introduced to the theory [27]. When introduced into the theory, the Higgs scalar fields couple to both the bosonic and fermionic fields, effectively giving both their mass terms. In the Standard Model though, the neutrino has no mass term, because no right-handed neutrino exists within the theory. If the Higgs cannot couple to the neutrino, how does it get its mass?

The question of *how* the neutrino acquires mass in the Standard Model is just one of the neutrino mass-related questions that should be addressed. Although oscillation measurements yield the mass splittings, the absolute scale of the neutrino mass must be determined. The ordering of the neutrino masses from lightest to heaviest must also be determined. A detailed discussion of these issues and how experiments are attempting to answer them follows in chapter 2.

## 1.3 Neutrino sources

Despite how weakly they interact, neutrinos and antineutrinos are produced in numerous processes within the universe. These neutrinos leave their signature in different ways. Lower energy big bang relic neutrinos have considerable impact on the Cosmic Microwave Background's power spectrum, higher energy galactic neutrinos interact with matter and produce dramatic showers of high-energy particles, and a zoo of processes exist in between. Thanks to all of these, a broad range of neutrino fluxes and energy ranges are available to perform a plethora of neutrino oscillation and interaction measurements. A summary of the most prominent neutrino sources and their energy scales are shown in figure 1.8.

Given the broad scope of a neutrino source discussion, emphasis will be placed upon neutrino sources commonly observed with water Cherenkov detectors. An overview of all neutrino interactions, how they are modeled, and how they are measured can be found in [28].

### 1.3.1 Geoneutrinos

The Earth's crust and mantle produce an abundance of antineutrinos known as the geoneutrino flux. The Earth contains a large portion of long-lived radioactive elements, most prominently $^{238}U$, $^{232}Th$, $^{40}K$, and their daughter isotopes, that are constantly decaying over time. The primary decay modes observed are alpha and beta decay, where all beta decays are the source of antineutrinos.

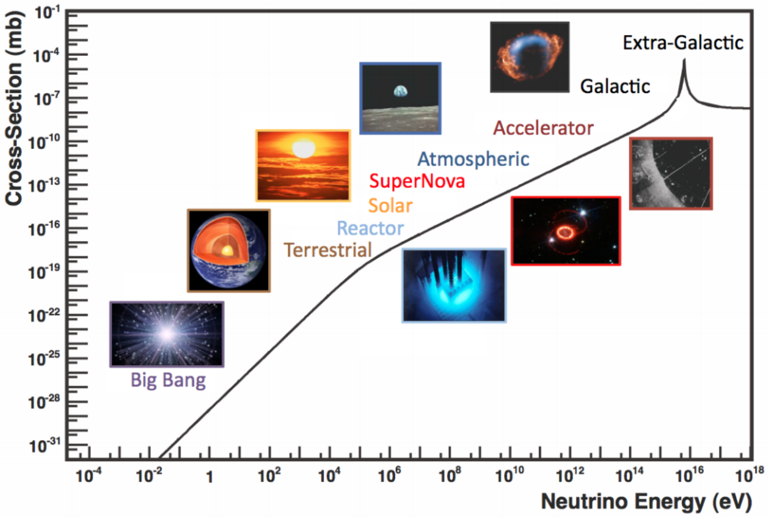

Figure 1.8. Overview of the prominent neutrino and antineutrino sources known within the universe to-date. The $\bar{\nu}_e e^- \rightarrow \bar{\nu}_e e^-$ cross section is also shown as a function of neutrino energy. Figure taken from [28].

Simulations of the geoneutrino flux utilize inputs including soil sampling from across the globe, ultrasonic measurements of deep-crustal rock types, and gravitational anomalies due to core composition [29]. A prediction of the geoneutrino flux through a combination of these inputs at across the Earth is shown in figure 1.9.

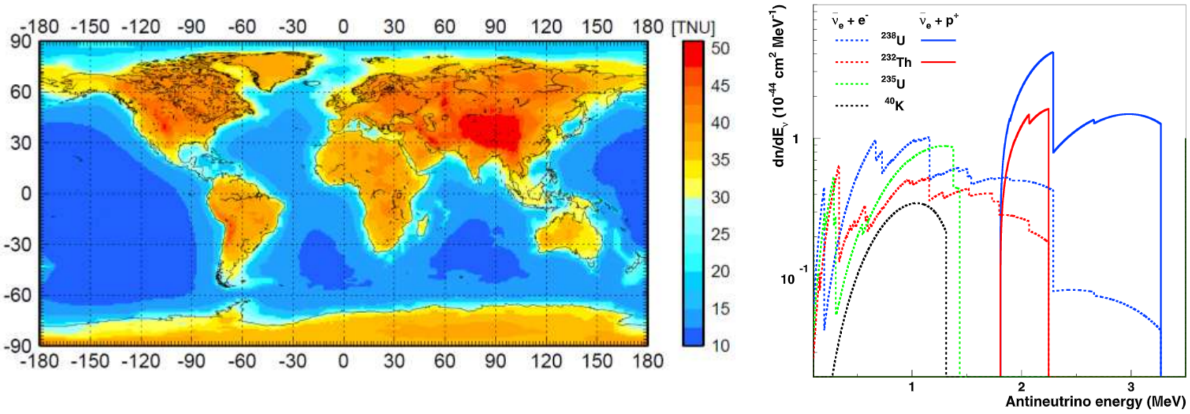

Figure 1.9. Left: Prediction of the geoneutrino flux at different locations above the Earth's surface. The flux is given in Terrestrial Neutrino Units (TNU), the number of inverse beta decay events that a 100% efficient detector with $10^{32}$ proton targets would see in a single year of observation. Right: Product of the geoneutrino flux and with the electron scattering (dotted lines) and inverse beta decay (solid lines) cross sections. Figures from [29, 30].

As shown in figure 1.9, most geoneutrino detectors will observe the largest signal detecting Inverse Beta Decay (IBD) events of the form $\bar{\nu}_e + p \rightarrow n + e^+$. The IBD cross section for electron antineutrinos is several orders of magnitude higher than the electron scattering cross section, meaning IBD-focused detectors will have higher neutrino interaction rates and reduced statistical uncertainties. Furthermore, IBD events can be selected with little backgrounds by searching for its characteristic double coincidence signal. The prompt signal is produced by the positron, generally detected via scintillation or Cherenkov light. Then, after thermalization, the neutron captures in the detection medium and gives a delayed signal. Using water as an example, the neutron's characteristic thermal capture time on hydrogen in water is $\approx 200\,\mu s$, and the de-excitation of the produced deuteron can yield a $2.2\,MeV$ gamma signal.

Even when selecting IBD events, geoneutrino measurements are challenging due to their relatively low energy ($E_{\bar{\nu}_e,geo} < 3\,MeV$), low rates (10s events/year for a detector with $10^{32}$ proton targets), and reactor backgrounds. If a detector is deployed near nuclear reactors, the IBD signal from reactor antineutrinos produce an irreducible background that overlays much of the geoneutrino spectrum. For reference, KamLAND had to operate for almost 10 years to observe an appreciable geoneutrino flux, while the Borexino detector had to collect over 2000 days of data to measure the geoneutrino signal with a $5.9\sigma$ discovery significance (see figure 1.10) [31, 32].

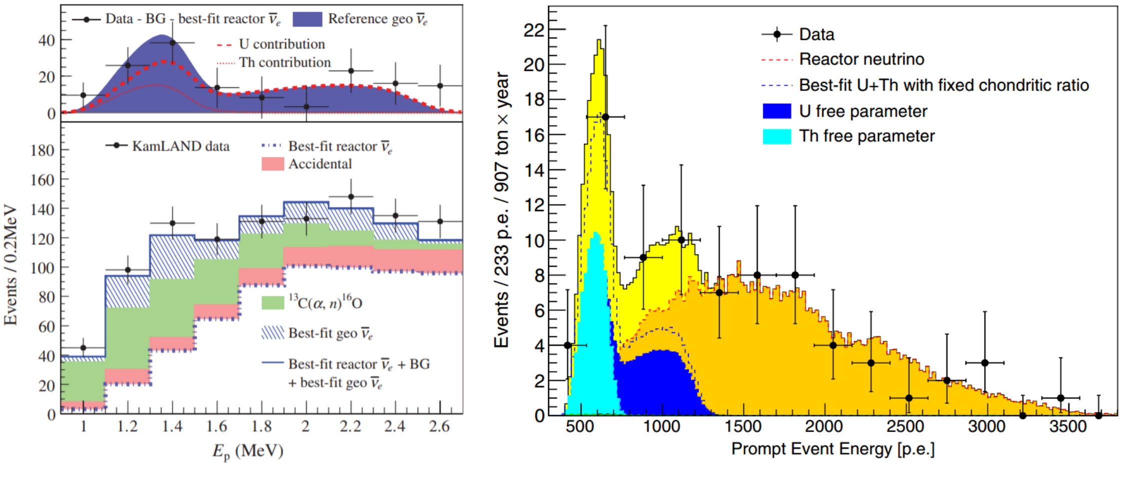

Figure 1.10. Best fits to the KamLAND (left) and Borexino (right) IBD candidate spectra. Reactor antineutrinos contribute a considerable background in both detectors, and $(\alpha, n)$ reactions on $^{13}C$ due to $\alpha$-emitting backgrounds produce additional background in KamLAND. Figure from [31, 32].

### 1.3.2 Reactor antineutrinos

Operational nuclear reactors have been instrumental in advancing the neutrino physics field. Recall that the Reines-Cowan Experiment used the Savannah River Plant near Aiken, South Carolina to make the first direct detection of neutrinos. Today, reactors are commonly used to make precision measurements of the neutrino oscillation parameters, as well as search for sterile neutrinos.

Nuclear reactors rely on the energy released in nuclear fission to convert water to steam, drive a steam turbine, and generate electricity. The nuclear reactor core contains fuel rods filled with fissionable nuclear isotopes, typically composed of $^{238}U$, $^{235}U$, $^{239}Pu$, and $^{241}Pu$. These isotopes have a non-negligible cross section for capturing neutrons, fissioning into two daughter isotopes and free neutrons, and releasing $O(200)$ MeV/fission in the form of kinetic energy and gamma radiation (see figure 1.11). While the released kinetic energy heats the water in the reactor, the free neutrons thermalize and capture on the fuel to produce more fissions and continue the neutron life cycle that maintains a steady reactor power state. A typical 3 GW thermal commercial reactor operating at full-power will undergo $O(10^{20})$ fissions/second [33].

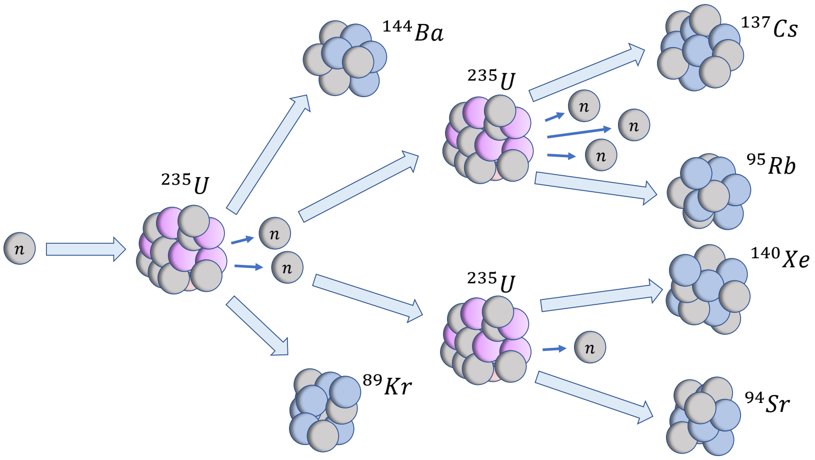

Figure 1.11. Diagram of the chain reaction occurring in fissionable isotopes in reactor fuel. Neutrons are captured by fissionable isotopes, which split and produce more neutrons to maintain the fission cycle. Different daughter isotopes are left after each fission, and are also often radioactive themselves.

The daughter isotopes produced in fission are often unstable, undergoing beta decay and emitting electron antineutrinos. The $U$ and $Pu$ isotopes in reactor fuel are relatively heavy isotopes and have a higher number of neutrons than protons; as such, the daughter isotopes left after fission are mostly neutron-rich. To approach a more even ratio of protons to neutrons, fission daughters undergo one or more beta decay processes; on average, about 6 beta decays will proceed from a single fission's daughters, meaning about 6 antineutrinos are emitted per fission [34]. The sum of all antineutrinos emitted from all daughter isotopes produces the observable reactor antineutrino flux, approximately $2 \times 10^{20}$ electron antineutrinos emitted every second per $GW_{th}$ for a reactor.

#### 1.3.2.1 Reactor antineutrino observation models

The number of antineutrinos observed at a distance $L$ from a reactor as a function of antineutrino energy $E_{\bar{\nu}}$ is modeled as [35, 9]

$$\frac{dN_\nu}{dE_\nu} = \sum_{i}^{reactors} N_p \, \epsilon(E_\nu)\sigma(E_\nu)\frac{P_{ee}(E_\nu, L_i)}{4\pi L_i^2} S_i(E_\nu) \ , \tag{1.25}$$

where $N_p$ is the number of the detector's proton targets, $\epsilon$ is the detector's detection efficiency, $\sigma$ is the cross section for the detection interaction (commonly inverse beta decay), $P_{ee}$ is the electron neutrino or antineutrino survival probability from a reactor $i$ to the detector, and $S_i$ is a parameterization of the reactor's antineutrino flux spectrum. $S_i$ is dependent on the fractional loading of each $U$ and $Pu$ fissile isotope, and is defined as follows:

$$S_{reactor} = \sum_{k=1}^{4} f_{k,reactor} \frac{dN_{\nu,k}}{dE_\nu} \ . \tag{1.26}$$

The $\frac{dN_{\nu,k}}{dE_\nu}$ distribution for each isotope $k$ is determined by measuring the beta decay spectrum following $U$, $Pu$ fissions. The beta decay energy spectrum is then used to estimate the antineutrino energy spectrum with energy conservation and models of nucleus de-excitation from beta decay [36, 37].

When deploying a neutrino detector, the location's reactor antineutrino spectrum is an important consideration as either a signal for potential physics measurements or as an irreducible background. For example, consider the expected antineutrino spectra for a 100% efficient detector with a $10^{32}$ proton target volume deployed at Davis, California and at SNOLAB in figure 1.12. Both spectra assume a 1-year deployment where all world reactors operate identically to the year 2015 according to the IAEA Power Reactor Information System (PRIS) database.

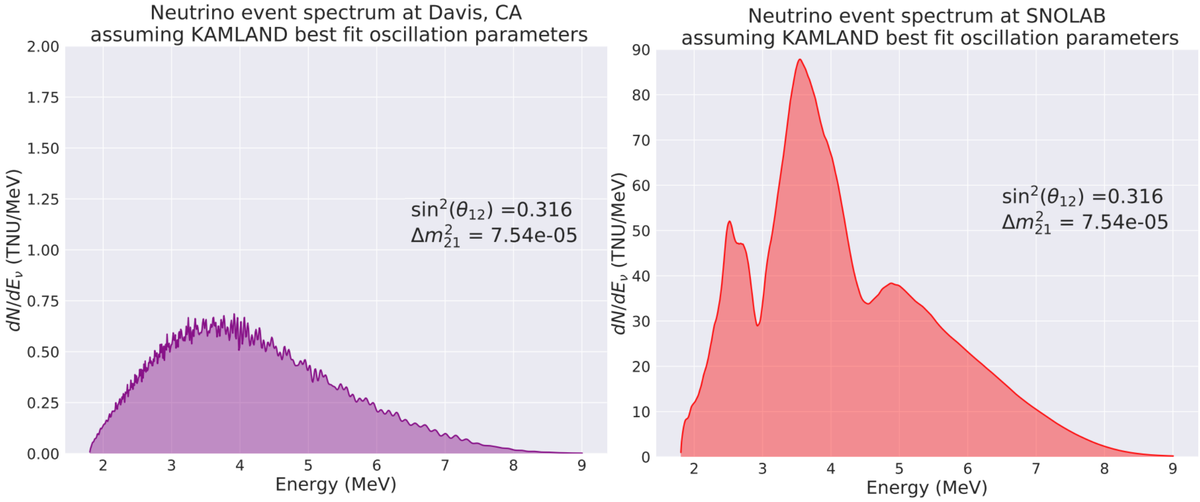

Figure 1.12. Comparison of the reactor antineutrino spectrum at SNOLAB to that at Davis, California for one year of observation. Reactors are assumed to have ran according to the 2015 operational schedule documented by the IAEA. The best-fit of $\Delta m^2_{12}$ and $\sin\theta_{12}$ from KamLAND, along with the PDG 2016 values for $\theta_{13}$ and $\Delta m^2_{13}$, are used to characterize the electron survival probability $P_{ee}$ [38, 39].

While there are few reactors near Davis, SNOLAB has three major nuclear reactor plants within a 300 km radius (Bruce, Darlington, and Pickering). The large reactor antineutrino signal makes SNOLAB an attractive location to measure neutrino oscillations, while Davis would be better for measuring something like geoneutrinos where minimizing the reactor signal reduces backgrounds.

### 1.3.3 Solar neutrinos

The various fusion processes occurring within the Sun result in the emission of neutrinos. For an example of neutrino emission in fusion, consider the simplest fusion process in young stars: the proton-proton $(pp)$ fusion process. The high temperature and density within a star provide the energy necessary to convert a proton to a neutron and then bind the two nucleons to form a deuteron, written as

$$p + p \rightarrow {}^2H + e^+ + \nu_e \,. \tag{1.27}$$

The deuteron formation also results in the emission of a positron and electron neutrino. Depending on a star's mass, composition, and age, this and many different fusion processes lead to the production and emission of neutrinos with different energy distributions.

The electron neutrinos produced in all fusion processes in the Sun form the total solar neutrino flux. The flux is most prominent in neutrino energies at $< 10\,MeV$, with different reactions producing either monoenergetic or continuous neutrino flux distributions, and originates in the Sun's core, where the temperature and density are the largest and the most fusion occurs. Predictions of the solar neutrino flux spectrum as of 2014 are shown in figure 1.13, informed by measurements of elemental abundances in the Sun's atmosphere, nuclear reaction rates, and helioseismic activity [40].

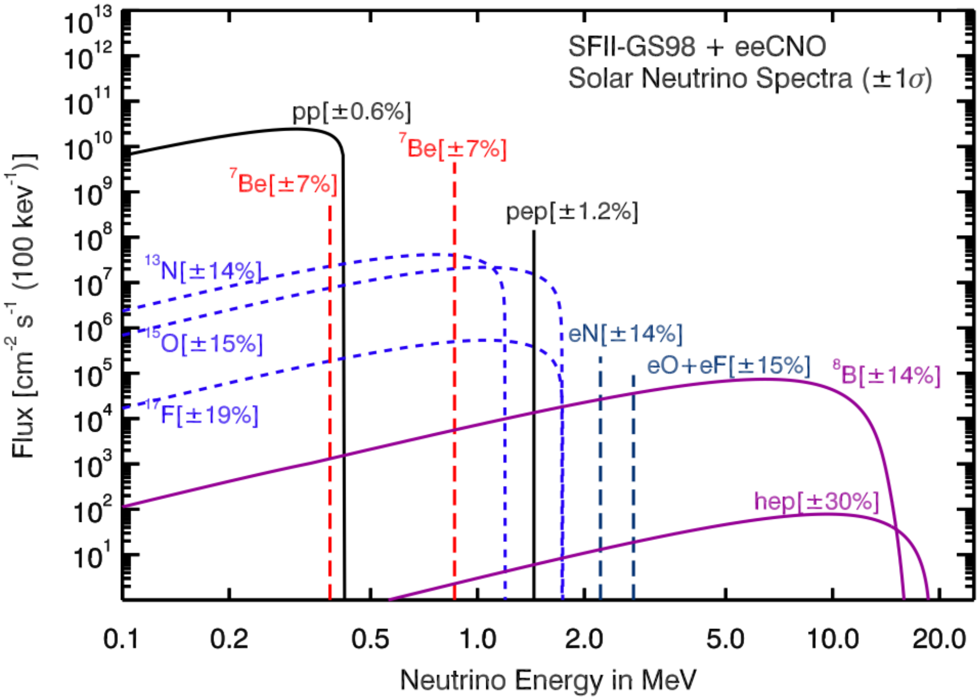

Figure 1.13. SFII-GS98 predictions of the solar neutrino flux due to the most prevalent fusion processes in the Sun. Neutrinos from electron capture on CNO-produced isotopes (eeCNO) are also shown. Colors utilized for readability. Figure from [40].

Measurements of the Sun's neutrino flux in different energy regimes are a valuable test for solar models. A compilation of solar neutrino flux measurements as compared to flux predictions from two prominent standard solar models is shown in table 1.3.3. Direct measurements of $^{8}B$, $^{7}Be$, and $pep$ fluxes are in agreement with predictions within statistical uncertainties, while measurements of the three prominent fluxes generated by the so-called "CNO cycle" are currently background-limited.

| Fusion process | GS98 | AGS09 | $cm^{-2}s^{-1}$ | Experimental results |
|---|---|---|---|---|
| pep | $1.44 \pm 0.012$ | $1.47 \pm 0.012$ | $\times 10^8$ | $1.6 \pm 0.3$ Borexino |
| $^7Be$ | $5.00 \pm 0.07$ | $4.56 \pm 0.07$ | $\times 10^9$ | $4.87 \pm 0.24$ Borexino<br>$5.82 \pm 1.02$ KamLAND |
| $^8B$ | $5.58 \pm 0.14$ | $4.59 \pm 0.14$ | $\times 10^6$ | $5.2 \pm 0.3$ SNO+SK+ Borexino+KamLAND<br>$5.25 \pm 0.16^{+0.011}_{-0.013}$ SNO LETA<br>$5.95^{+0.75}_{-0.71}(stat)^{+0.28}_{-0.30}(syst)$ SNO+ |
| $^{13}N$ | $2.96 \pm 0.14$ | $2.17 \pm 0.14$ | $\times 10^8$ | $< 7.4$ total CNO, Borexino |
| $^{15}O$ | $2.23 \pm 0.15$ | $1.56 \pm 0.15$ | $\times 10^8$ | |
| $^{17}F$ | $5.52 \pm 0.17$ | $3.40 \pm 0.16$ | $\times 10^8$ | |

Table 1.1. Table giving two prominent standard solar model neutrino flux predictions with comparisons to experimental results. Table modified from [41] with additional results from [42, 43].

#### 1.3.3.1 The solar abundance problem

An interesting point of tension in solar physics models that could be resolved with precise CNO cycle flux measurements is known as the solar abundance problem. The two prominent solar models, known as GS98 and AGS09, predict different ratios of metals (elements larger than hydrogen) and hydrogen in the Sun's photosphere (labeled as $(Z/X)_{solar}$). The GS98 model ($(Z/X)_{solar} \approx 0.23$)) provides speed-of-sound predictions consistent with helioseismic observations, while the AGS09 ($(Z/X)_{solar} \approx 0.18$)) provides a more accurate prediction of the Sun's atmospheric atomic and molecular profile [44, 41]. One consequence of the different metallicity predictions for GS98 and AGS09 is that CNO cycle neutrino fluxes are considerably different (see $C$,$N$, and $F$ rows in table 1.3.3). A successful measurement of the CNO flux could help inform which solar model is more accurate and provide a pathway to modifying the model in disagreement.

### 1.3.4 Supernovae

Supernovae are one of the most intense neutrino sources available in the universe. Because they are so weakly interacting relative to other matter, neutrinos produced in supernova processes have a much higher rate of escaping the collapsing star than any other particles produced during the collapse. The result is that nearly 99% of a star's gravitational binding energy ($O(10^{52})$ erg) is released in the form of neutrinos during a star's collapse, supernova explosion, and neutron star formation [45].

### 1.3.4.1 The supernova process

As stars age and lighter elements fuse into heavier ones, the further fusion of heavier elements requires more energy to proceed. This is because heavier elements generally have larger binding energies per nucleon (up to iron) as shown in figure 1.14. As a consequence of the reduced fusion rate, the total radiation pressure reduces and the star condenses inward under gravitational pressure. If the star has enough mass, the higher density (and higher temperature) at the core will initiate the fusion of the next heaviest element. This oscillation between condensing and reigniting fusion produces an onion-like layering in the star, with the heaviest elements at the center as shown in figure 1.15 [47].

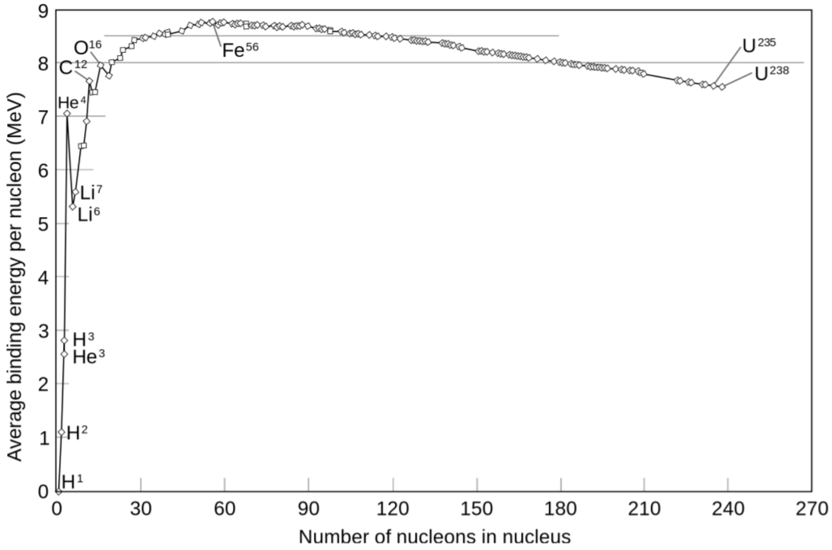

Figure 1.14. Distribution of binding energy per nucleon for several stable elements. Several elements relevant to fusion and radioactive elements are featured. Figure taken from [46].

If a core reaches the silicon-burning stage, an iron core begins to form. This marks the star's transformation into a pre-supernova star. Note that a star needs a mass greater than approximately $8M_{Sun}$ to begin forming an iron core. Fusion in a star stops at iron, as the fusion of iron to a higher mass isotope is an endothermic process and energetically unfavorable. As the net fusion in

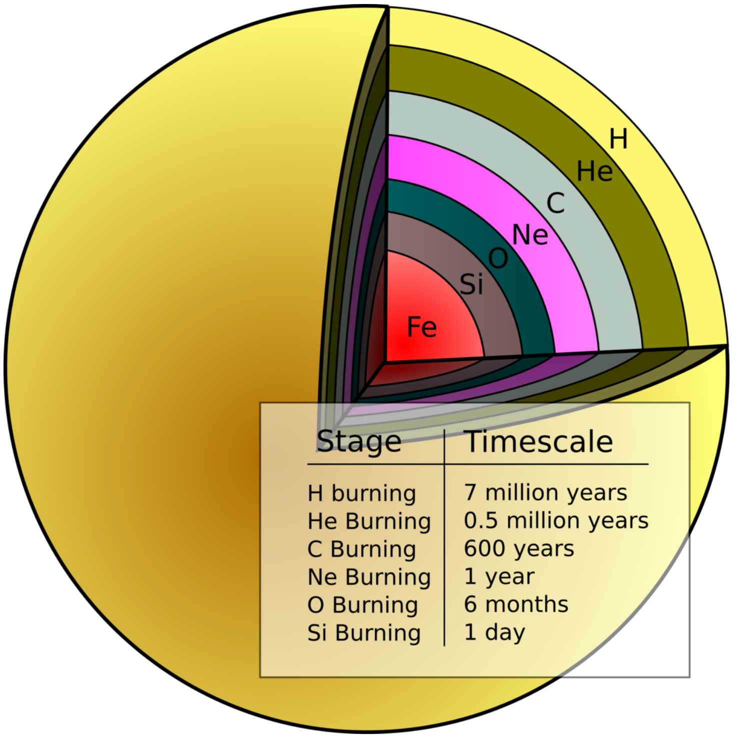

| Stage | Timescale |
|---|---|
| H burning | 7 million years |
| He Burning | 0.5 million years |
| C Burning | 600 years |
| Ne Burning | 1 year |
| O Burning | 6 months |
| Si Burning | 1 day |

Figure 1.15. Illustration of the onion-like structure that forms in pre-supernova stars, and approximate timescale for each burning stage. Figure taken from [47].

the star reduces, it continues to condense further until, according to the Pauli exclusion principle, the electron degeneracy limit prevents further collapse.

If the star has enough mass, iron will continue to form in the core and the density and temperature within the star will continue to climb. The extreme temperature and density drives electron capture on iron nuclei (written as $p + e^- \to n + \nu_e$) and photodisintegration of iron nuclei into helium and neutrons. As the number of electrons reduces in the core and crosses the Chandrasekhar Limit where even electron degeneracy can no longer maintain stability, the core rapidly collapses and a large $\nu_e$ burst is observed from rapid neutronization due to electron capture. Nuclear repulsion due to the strong force promptly halts the collapse, and is followed by a large outgoing shockwave and thermal explosion [48].

#### 1.3.4.2 Supernova neutrino emission models

A variety of processes occur within a developing supernova. A summary of the most prevalent neutrino and antineutrino interactions occurring in a supernova are given in table 1.3.4.2. One important feature to note is that, although proton-neutron conversions drive the production of

| Supernova process | Neutrino interaction |
|---|---|
| **Beta-processes** | |
| electron and $\nu_e$ absorption by nuclei | $e^- + (A,Z) \longleftrightarrow (A,Z-1) + \nu_e$ |
| electron and $\nu_e$ captures by nucleons | $e^- + p \longleftrightarrow n + \nu_e$ |
| positron and $\bar{\nu}_e$ captures by nucleons | $e^+ + n \longleftrightarrow p + \bar{\nu}_e$ |
| **“Thermal” pair production/annihilation processes** | |
| Nucleon-nucleon bremsstrahlung | $N + N \longleftrightarrow N + N + \nu + \bar{\nu}$ |
| Electron-positron pair production | $e^- + e^+ \longleftrightarrow \nu + \bar{\nu}$ |
| Plasmon pair-neutrino production | $\tilde{\gamma} \longleftrightarrow \nu + \bar{\nu}$ |
| **Reactions between neutrinos** | |
| Neutrino-pair annihilation | $\nu_e + \bar{\nu}_e \longleftrightarrow \nu_x + \bar{\nu}_x$ |
| Neutrino scattering | $\nu_x + \{\nu_e, \bar{\nu}_e\} \longleftrightarrow \nu_x + \{\nu_e, \bar{\nu}_e\}$ |
| **Scattering processes with medium particles** | |
| Neutrino scattering with nuclei | $\nu + (A,Z) \longleftrightarrow \nu + (A,Z)$ |
| Neutrino scattering with nucleons | $\nu + N \longleftrightarrow \nu + N$ |
| Neutrino scattering with electrons and positrons | $\nu + e^{\pm} \longleftrightarrow \nu + e^{\pm}$ |

Table 1.2. Table providing the prominent neutrino production and interaction processes found in supernova. Table taken from [49].

electron neutrinos and antineutrinos, all flavors of neutrino are observed from a supernova burst due to pair production processes.

Models of neutrino production and transport in supernova incorporate all of these processes to predict the total neutrino/antineutrino flux’s time and energy dependence. These models are invaluable for predicting the expected time window and energy profile that a neutrino detector must be designed to successfully observe.

For example, consider the simulated time evolution of a $27M_{Sun}$ supernova, shown in figure 1.16. A prompt $\nu_e$ burst is seen near $t \approx 0$ from rapid neutronization following the Chandrasekhar Limit crossing. Then, $\nu_e$ and $\bar{\nu}_e$ channels dominate the primary shockwave’s total flux, with a $\sim 50\%$ lower contribution from other flavor channels. The mean energy spectrum is greater than 10 MeV across the entire burst, well above most natural radioactive backgrounds

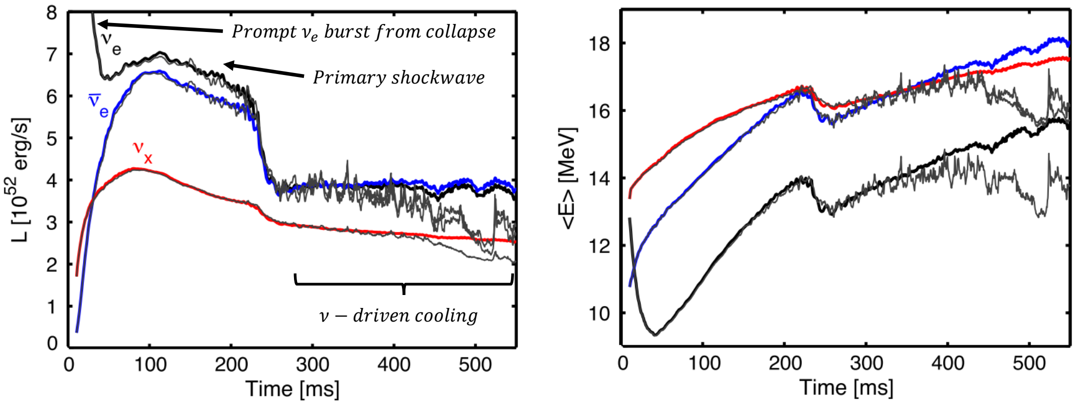

Figure 1.16. Simulation of integrated luminosity and mean energy spectrum for a $27 M_{Sun}$ supernova. The $\nu_e$, $\bar{\nu}_e$, and $\nu_x = \nu_\mu, \nu_\tau, \bar{\nu}_\mu, \bar{\nu_\tau}$ are shown for 3D simulations (color) and 2D simulations (gray). Figure modified from [50].

and neutrino sources. Finally, a steady neutrino/antineutrino flux follows the initial shockwave as the neutron star cools via neutrino emission, continuing for tens of seconds after the initial burst [51].

#### 1.3.4.3 Supernova 1987A observations

The 1987A supernova marked the first supernova observation where a neutrino signal was correlated with an optical signature. On February 24th, 1987, the optical signal of a supernova in the Large Magellanic Cloud (LMC) was observed around the world by several professional and amateur astronomers [45]. After searching for a possible correlated neutrino signal, the IMB and Kamiokande-II neutrino detectors identified a cluster of antineutrino events on February 23rd, 1987 well above rates expected during normal detector operation [52, 53]. After incorporating a 54-second systematic uncertainty in the absolute time, the Baksan collaboration also claimed observation of an event cluster in agreement with the IMB and Kamiokande-II signal times [54, 45]. The detector event times, with each data set's start of the burst assigned $t = 0$, is shown in figure 1.17.

Although the 1987A neutrino observations generally agreed with the supernova model predictions, the signal rates observed were not significant enough for fine model tuning. The Earth received a minuscule fraction of SN1987a's neutrino flux due to the 50 kpc distance from the LMC. Fortunately, astronomy observations suggest that a few core-collapse supernova occur

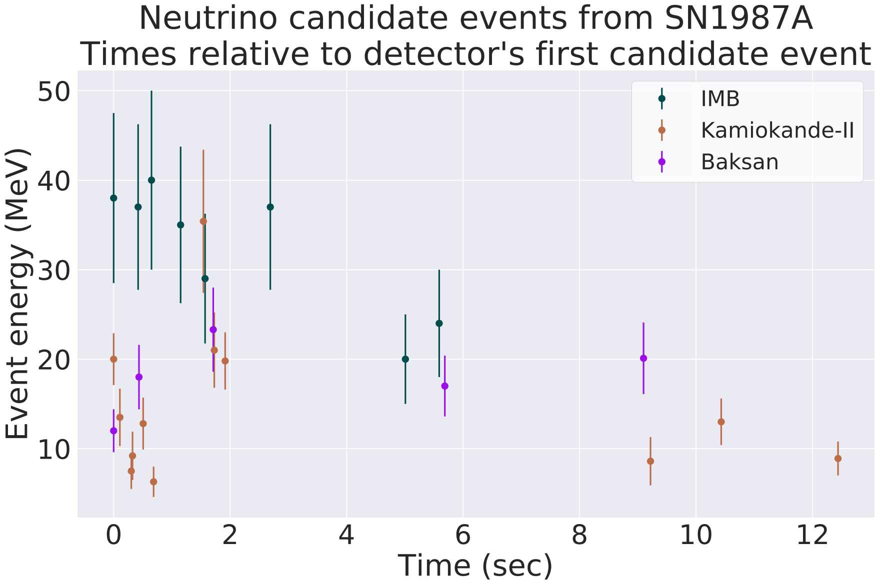

Figure 1.17. Candidate antineutrino events observed from SN1987a. Each detector saw its event cluster on February 23rd, 1987. Burst start times for each detector are: IMB - 7:35:41 UT, Kamiokande-II - 7:35:35 UT, Baksan - 7:36:12 UT. Event times and energies taken from [52, 53, 54].

per century in a Milky Way-like galaxy [55]; given the improvements in neutrino detection technology and the general increase in the number of operational detectors since 1987, the next intragalactic supernova should provide considerable insight to the supernova process.

#### 1.3.4.4 The Diffuse Supernova Neutrino Background (DSNB)

Given the combination of a supernova's tremendous neutrino/antineutrino emission and the vast number of stars in the universe, it is expected that the universe contains a steady neutrino and antineutrino flux known as the Diffuse Supernova Neutrino Background (DSNB). Since neutrinos and antineutrinos are weakly interacting and can travel large distances without interacting, few would argue that that the DSNB exists and should be present at Earth. The key question is whether or not the DSNB flux is large enough for present day neutrino detectors to extract the signal out of the detector backgrounds.

A recent paper provides an enlightening Fermi calculation which estimates the DSNB could be measurable with current or next generation of detectors. The DSNB neutrino detection rate at Earth can be approximately related to the SN1987a detection rate observed with [56]

$$\left[\frac{dN_\nu}{dt}\right]_{DSNB} \approx \left[\frac{dN_\nu}{dt}\right]_{87A} \left[\frac{N_{SN} M_{det}}{4\pi D^2}\right]^{-1}_{87A} \left[\frac{N_{SN} M_{det}}{4\pi D^2}\right]_{DSNB} . \tag{1.28}$$

Given the 1987a neutrino detection rate in Kamiokande-II, the mass difference between Kamiokande-II and Super-Kamiokande, the estimated rate of supernovas per galaxy, and the estimated number of galaxies, a Super-Kamiokande-like detector is estimated to observe

$$\left[\frac{dN_\nu}{dt}\right]_{DSNB} \approx 3\, year^{-1} . \tag{1.29}$$

Although several events/year is a small signal, detection is not an impossible feat. In 2003, Super-Kamiokande conducted a DSNB search with previous data taken and set limits on the expected DSNB IBD rate in SuperK, as shown in figure 1.18. A DSNB search has also been conducted using the KamLAND detector [57].

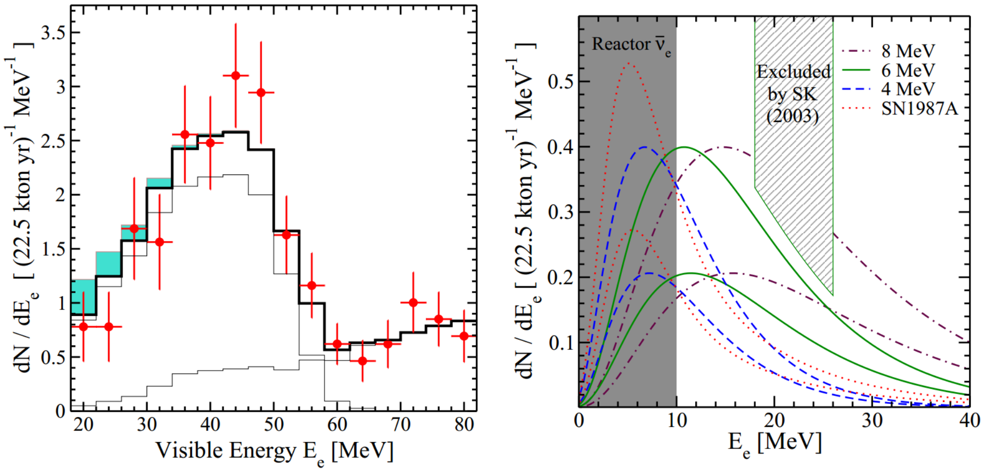

Figure 1.18. Left: DSNB candidate events for the 2003 SuperK DSNB search. The thick black line shows the expected atmospheric neutrino background, with the largest permitted DSNB signal shaded in light blue. Right: Exclusion region of DSNB flux as set by the SuperK DSNB search. Figures from [56].

Clearly, the limiting background for the DSNB measurement in water Cherenkov detectors is the atmospheric neutrino background. This background's significance, and ANNIE's relevance to reducing atmospheric neutrino event model uncertainties, is discussed in section 4.3.3.

### 1.3.5 Atmospheric neutrinos

Atmospheric neutrinos are produced as a result of cosmic ray interactions in the atmosphere and the decay of cosmic muons. High-energy particles (primarily hydrogen and helium) incident on the Earth's atmosphere can produce mesons such as $\pi^{\pm}$ and $K^{\pm}$. Considering a $\pi^{+}$ for example, the following decay chain can occur as the pion proceeds toward Earth:

$$\pi^{+} \rightarrow \mu^{+} + \nu_{\mu} \rightarrow e^{+} + \nu_{e} + \bar{\nu}_{\mu} + \nu_{\mu} \; . \tag{1.30}$$

The combination of cosmic meson and muon decay in the atmosphere results in a measurable flux of muon and electron neutrinos and antineutrinos. Tau neutrinos are also expected from neutrino oscillations and charm particle decays in cosmic-ray interactions, but the total tau flux is small compared to electron and muon flavor fluxes; the most sensitive measurement to date has been made by IceCube DeepCore [58].

Estimates for the atmospheric neutrino and antineutrino flux at several neutrino observatories are shown in figure 1.19. Each site's neutrino flux summed over all directions are shown for each site; parameters considered as inputs for the simulation include the cosmic ray flux/energy distributions, atmospheric composition and density (fluxes shown use the NRLMSISE-00 global atmospheric model, an empirical model based on best fits to data), geomagnetic field intensity, and neutrino oscillations in the atmosphere and in the Earth [59].

### 1.3.6 Accelerator neutrinos

In the last 50 years, neutrino and antineutrino beams produced at proton accelerator laboratories have become one of the most valuable tools for high-precision neutrino measurements. The neutrino production mechanism, although human-made, is similar to that of atmospheric neutrinos. High energy protons are produced in a proton accelerator and fired at a target, creating $\pi^{\pm}$ and $K^{\pm}$ mesons. The mesons of either $+$ or $-$ charge are then selected with a magnet, depending on whether the beam is set to neutrino or antineutrino production mode respectively. The selected mesons are then sent down a decay pipe to decay and produce neutrinos; any daughter particles remaining are stopped with a beam stop, while the neutrinos will proceed down the beamline.

Accelerator neutrino measurements are made on the same energy and distance scales as atmospheric neutrinos. Typical neutrino beam energies are on the order of 100s of MeV to

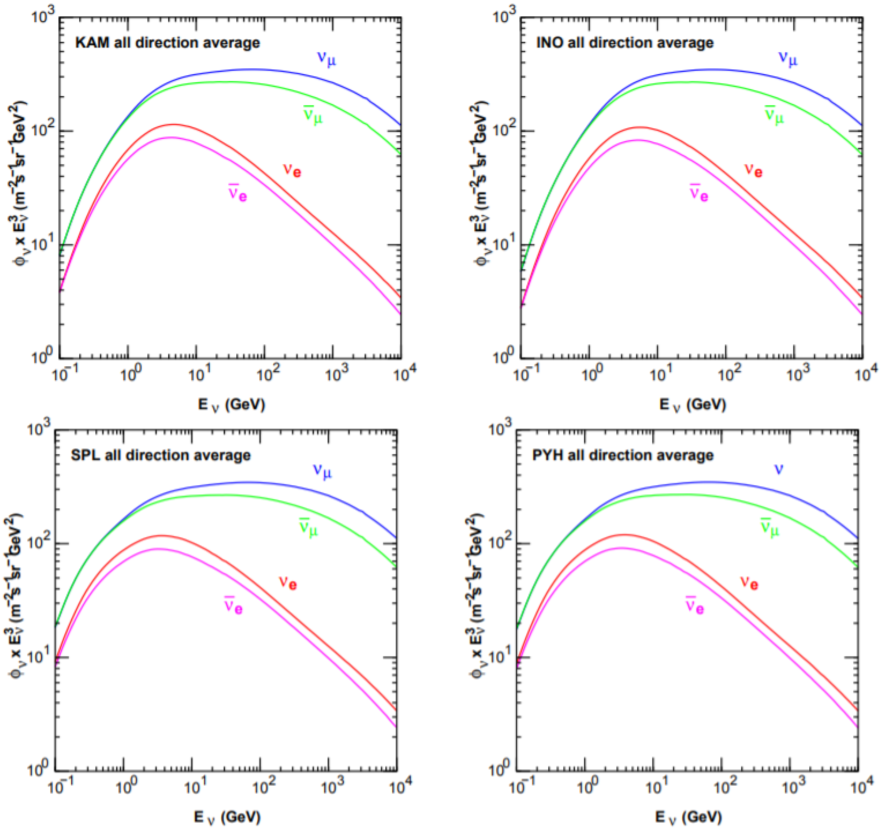

Figure 1.19. Simulation of the all-direction averaged atmospheric neutrino flux for a one year exposure at several sites. KAM stands for the Super-Kamiokande site in Japan, INO for the India-based Neutrino Observatory, SPL for the South Pole, and PYH for the Pyhasalmi mine in Finland. Figure from [59].

10s of GeV, although this can be tuned by varying the proton beam energy and target design. Neutrino detectors are often placed $O(100)$ meters away from the neutrino production target for short-baseline measurements, or can be placed $O(1000)$ km away from the target to observe neutrino oscillations in matter as they traverse the Earth's crust.

The prominence of the accelerator neutrino beam in neutrino physics today stems from the neutrino beam's predictability and tunability. Having a well-known neutrino flux and energy profile, knowledge of the incident direction of the neutrinos, and the ability to tune the beam to produce either neutrinos or antineutrinos are all invaluable for performing neutrino/antineutrino observations with minimal systematic uncertainties. An in-depth review of Fermilab's Booster Neutrino Beamline (BNB), including beam production process, detector positions in beam, and beam flux profile, is presented in section 5.2 and appendix C.

## 1.4 Water Cherenkov neutrino detectors

Given the low interaction rate of neutrinos, a particle detector with large target mass, high-efficiency event reconstruction, minimal detector backgrounds, and low cost are all key properties for developing an efficient yet feasible neutrino detector. To meet these demands, underground water Cherenkov detectors have been a dominant choice for the last 40 years of neutrino physics.

The history of Cherenkov detection is recent yet rich. One of the first proposals to image particles using Cherenkov radiation incident on a multiwire proportional counter was presented by Seguinot and Ypsilantis in 1977 [60]. Only a few years passed before large-scale water-based Cherenkov detectors utilized the photomultiplier tube (PMT) for Cherenkov radiation-based particle detection, with IMB and Kamiokande beginning operation in 1982 and 1983, respectively. Cherenkov detectors were initially deployed with the primary goal of observing proton decay. However, the capability of observing neutrinos and antineutrinos was quickly utilized, leading to the observation of SN1987a in IMB and Kamiokande and the discovery of neutrino oscillations by Super-Kamiokande, SNO, and KamLAND. More recent detector proposals often add additional features to the water Cherenkov formula, such as gadolinium doping for increased neutron detection efficiency or water-based liquid scintillator for improved energy resolution [61, 62]. Given the past success with, and future effort to improve, Cherenkov radiation detection with fast photosensors, the technique will likely remain prominent and popular for decades to come.

### 1.4.1 The discovery of Cherenkov radiation

The discovery of Cherenkov radiation dates to the early 20th century, when the study of radioactivity itself was still young. In the biography of Eva Curie, daughter of Pierre and Marie Curie, hints of Cherenkov radiation are referenced in the blue glow observed from Marie Curie's glass samples containing radium salts [63]. However, the phenomena was not studied systematically until Mallet first tried to study the emission spectrum of the light using a spectrograph [64]. However, the work was not developed experimentally from Mallet's end, and several key properties (polarization, asymmetry of emission spectrum) were not established in his work.

Independently and several years later in 1933, Cherenkov performed the optical experiments (as proposed by Vavilov) that established Cherenkov radiation as a distinct phenomena from standard luminescence. The experimental procedure hinged on observing light produced by exposing various liquids to a radium source's gamma radiation [65]. The critical discoveries were made by Cherenkov in 1936, wherein he measured that the radiation had a distinct polarization and was emitted only in the forward direction relative to the incoming gamma rays, as shown in figure 1.20.

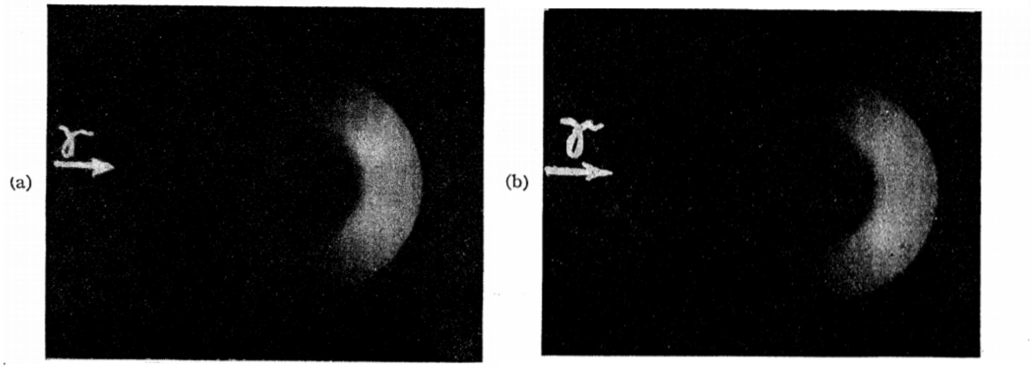

Figure 1.20. Original result providing evidence for the directionality of Cherenkov radiation. Radiation patterns for water (a, $n = 1.337$) and benzene (b, $n = 1.513$) are shown. Figure taken from [66].

Around the same time, Frank and Tamm also released a theory of the effect founded entirely on classical electromagnetic theory. Cherenkov, Frank, and Tamm shared the Nobel Prize in Physics in 1958 for their combined experimental and theoretical work in Cherenkov radiation.

### 1.4.2 Properties of Cherenkov radiation

Cherenkov radiation is light emitted when a charged particle moves through a dielectric medium at a velocity greater than the speed of light in the medium. As the charged particle moves through the medium, the particle's electromagnetic field polarizes the atoms of the medium as it passes by; effectively, the atoms' electrons follow the particle's electromagnetic waveform as it passes. The movement of these electrons due to polarization emits polarized radiation. If the particle is moving faster than the medium's phase velocity of light, the electromagnetic radiation emitted from electrons along the particle's track will form a coherent wavefront [64]. The effect is often compared to a sonic boom, wherein a pressure wavefront is formed by an object moving faster than the speed of sound in a medium.

The differential energy emission with respect to radiation frequency $\omega$ is given by the Frank-

Tamm result [67], written as

$$\left(\frac{dE}{dx}\right)_{rad} = \frac{(ze)^2}{c^2}\int_{n(\omega)>1/\beta} \omega\left(1 - \frac{1}{\beta^2 n^2(\omega)}\right) d\omega \ . \tag{1.31}$$

$n(\omega)$ is the index of refraction of the medium, $ze$ is the charge of the moving particle, and $c$ is the speed of light.

Differentiating with respect to $\omega$, converting from energy emission to number of Cherenkov photons, and converting from frequency to wavelength also provides insight to the Cherenkov emission spectrum shape [68]. Doing so yields

$$\left(\frac{d^2N}{d\lambda dx}\right) = \frac{2\pi\alpha z^2}{\lambda^2}\left(1 - \frac{1}{\beta^2 n^2(\lambda)}\right) \ , \tag{1.32}$$

where $\alpha$ is the fine structure constant ($\alpha = e^2/\hbar c \approx 1/137$). Notice that the Cherenkov emission spectrum intensity increases as the emission wavelength decreases, explaining Cherenkov radiation's characteristic blue hue in water. Equation 1.32 is plotted in the visible spectrum in figure 1.21. Figure 1.21 assumes the index of refraction of water $n(\lambda)$ as simulated in the RAT PAC simulation package [69]. For scale, integrating the graph in figure 1.21 predicts $\sim$ 850 Cherenkov photons are emitted per centimeter for a particle of charge $e$ passing through water with $\beta = 1$.

Note that the spectrum does not continue towards infinity for all light wavelengths $\lambda$. Notice that the power spectrum integral in equation 1.31 is only performed up to $n(\lambda) > 1/\beta$; at the condition where $n(\lambda) < 1$, no coherent Cherenkov wavefront is formed. Physically, this is the frequency cutoff at which the polarization of atoms in the medium no longer occurs as the driving frequency is too large (much like attempting to drive a harmonic oscillator off its characteristic resonant frequency). The point where $n(\lambda) < 1$ varies for materials; for water, $n(\lambda) < 1$ is first satisfied near 100 nm [70].

One key feature for event reconstruction via water Cherenkov detectors is the angle of emission for Cherenkov light. The angle of the Cherenkov wavefront relative to the particle's direction of travel, known as the Cherenkov relation, is given by

$$\cos\theta_C = \frac{1}{\beta n} \ , \ \beta > \frac{1}{n} \ . \tag{1.33}$$

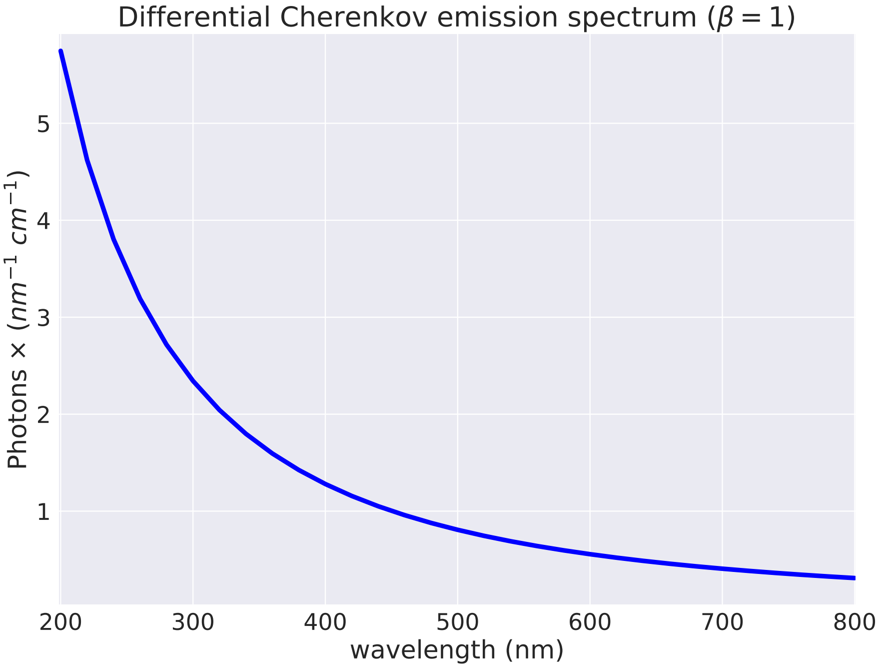

Figure 1.21. Differential Cherenkov emission spectrum for a charged particle passing through water at $\beta = 1$. The index of refraction $n(\lambda)$ is taken from the RATPAC simulation package [69].

$\theta_C$ is the Cherenkov angle, $\beta = \frac{v}{c}$, and $n$ is the index of refraction of the medium. The angle of the wavefront can be visualized intuitively by treating each position along the particle's track as an emission point for light emitted at $v_c = \frac{c}{n}$, as shown in figure 1.22.

In the context of a water-based Cherenkov detector, the resulting signal will appear as a ring or disc of light on the detector's photosensors (see figure 1.23 for a ring example). The resulting charge and time distribution of all detectors can be used to reconstruct the particle's initial production vertex.

A digression for calculating the Cherenkov radiation angle in water will be valuable in upcoming discussions on event reconstruction and particle identification. Consider a highly relativistic particle with $\beta \approx 1$ in water; given the index of refraction of water at $\lambda = 400\,nm$ is measured as $n = 1.34$ [71], the expected Cherenkov angle is approximately

$$\theta_C = \cos^{-1}\frac{1}{1.34} = 41.7^o \ . \tag{1.34}$$

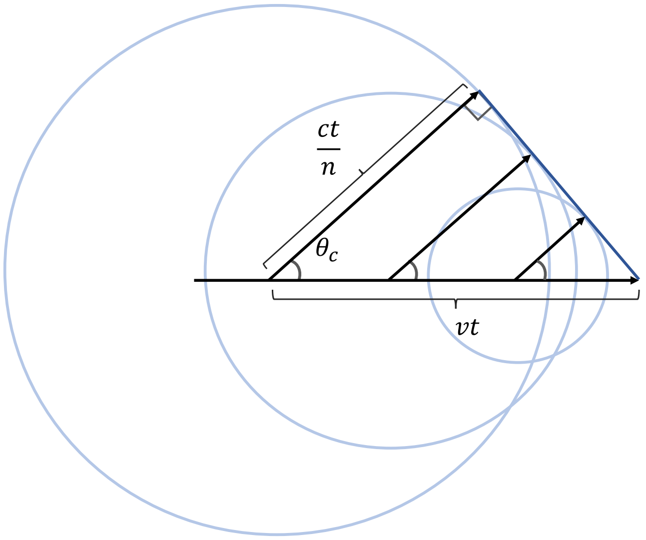

Figure 1.22. Visualization of the Cherenkov wavefront for a particle moving with velocity $v > \frac{c}{n}$.

Although more sophisticated algorithms can account for the variation in Cherenkov angle due to $n$'s dependence on $\lambda$, this Cherenkov angle is a common approximation for fast reconstruction and is quite accurate.

### 1.4.3 Summary of key water Cherenkov detector design features

To help construct a broad formula for successful water Cherenkov detection, consider the Sudbury Neutrino Observatory (SNO) which shared the 2016 Nobel prize in physics for confirming neutrino oscillations. SNO was a heavy water-based neutrino detector designed to observe solar neutrino electron scattering and inverse beta decay interactions. The detector was constructed at the 6800 foot level of the Creighton Mine in Lively, Ontario in Canada; the depth of the detector greatly reduces the rate of cosmic muons passing through the detector (approximately $3/\text{hour}$). The main detection volume is suspended in a 6-meter radius acrylic vessel, surrounded with 9438 PMTs to detect Cherenkov light from neutrino interactions. The PMTs are submerged in a secondary light water volume which acts as a buffer to reduce radioactive particles (primarily gamma rays) emitted from the detector cavern wall and PMT glass. Approximately 100 PMTs are also installed facing outward on the PMT frame; if Cherenkov light from a cosmic muon is detected, any physics interactions in the detector can be tagged as possibly being muon-related. An artist visualization of the SNO cavern and a candidate Cherenkov ring event are shown in figure 1.23.

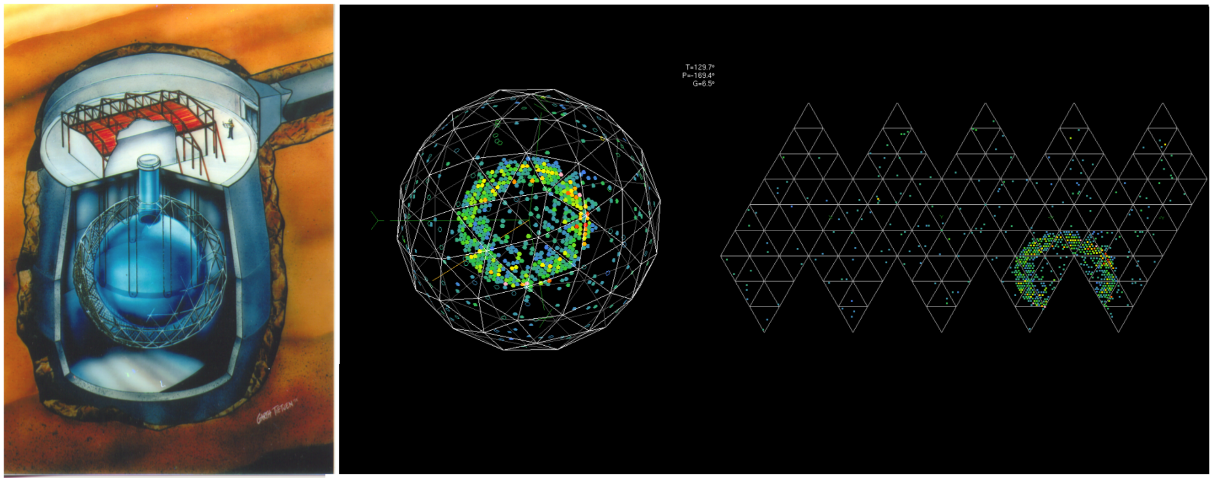

Figure 1.23. Left: Artist's rendition of the SNO detector. The detector cavern was excavated in Creighton mine at the 6800 foot level. Figure taken from [72]. Right: Candidate Cherenkov ring event in the XSNOED event display. The >9000 PMTs provide excellent ring resolution for particle ID and event reconstruction.

Although the SNO detector faced its own unique issues upon deployment and commissioning, traits emerge that are common to many water Cherenkov detectors. The features listed are primarily physics-related; all features must be weighed while also balancing the cost of detector deployment, neutrino source upkeep, and time needed to complete the measurement.

- *Neutrino source:* Different neutrino sources have different energies and will produce different energy particles after interacting. If a detector is too small, high energy particles may pass completely through, making energy estimation with Cherenkov radiation alone impossible. If a detector has too few PMTs, resolving the Cherenkov ring becomes more difficult.

- *Large detection volume:* The small cross section of neutrinos requires large detection volumes to observe a significant amount of events in detector. Typical masses are on the ton-kiloton scale. This issue can be bypassed by increasing the intensity of the neutrino source as well.

- *Detection medium transparent to Cherenkov photons:* Ton-kiloton scale detectors will have Cherenkov radiation travel on the meter-length scale before reaching a photodetector.

As such, the detection medium chosen must not readily absorb Cherenkov radiation in the wavelength range of photodetector sensitivity.

- *Photodetectors sensitive to Cherenkov photons:* The photodetectors chosen to image neutrino interactions utilize photocathodes deposited at the face of photodetectors, which must be able to convert Cherenkov-spectrum photons to photoelectrons. The photoelectrons produced are then amplified to produce a measurable charge signal. PMTs are a common detector choice for water Cherenkov detection, but additional technologies like Silicon PhotoMultipliers (SiPMs) and Large-Area Picosecond PhotoDetectors (LAPPDs) are also viable.

- *Cosmic background tagging/shielding:* Techniques for tagging detector events produced by cosmic backgrounds are generally needed for acceptable signal/background ratios. When possible, underground detector deployment also helps lower this background considerably.

- *Low radioactive backgrounds:* Detector signals due to radioactive contamination must be minimized. This is achieved with detector cleanliness standards, purification of the detection medium, selection of detector materials with low radioactivity, and detector shielding from outside radioactivity.

All points in this list were also taken into consideration when designing the ANNIE detector. For more details, see chapter 5.

# Chapter 2

# Open questions in neutrino physics

Since its discovery, the critical path to understanding the neutrino has rapidly evolved. In the earliest stages of neutrino physics, the most fundamental questions needed to be addressed, such as *can the neutrino be detected at all?* Fortunately, the neutrino was indeed detectable (albeit weakly interacting). Following the neutrino's discovery and confirmation of fixed helicity, things seemed about solved: the neutrino was a Weyl fermion (massless with fixed helicity), and there existd only the right-handed antineutrino and left-handed neutrino. Plenty of data was still needed to accurately model neutrinos and their interactions with matter, but the broad picture looked sensible.

The discovery of the solar neutrino problem and eventual resolution with the observation of neutrino oscillations completely rocked this foundation. The concept of a massive neutrino that exhibited flavor oscillations produced a plethora of fundamental questions that needed answering. *How massive are neutrinos? How do they oscillate? How much do they oscillate? Can this be fit into the Standard Model? What else is missing?* This chapter focuses on addressing the current status of the neutrino's fundamental questions, as well as how both experimentalists and theorists are attempting to answer them.

## 2.1 Neutrino oscillation parameters

Precision measurements of the PMNS matrix parameters and mass-squared differences are constantly ongoing to improve the modeling of neutrino oscillations. Recall that the neutrino oscillation probability in vacuum is completely described with the independent parameters

| Parameters | Common $\nu$ sources | Best fit (PDG 2018) |
|---|---|---|
| $\sin^2\theta_{12}$ | solar, reactor | $0.307 \pm 0.013$ |
| $\Delta m^2_{12}$ | solar, reactor | $-7.53 \pm 0.18 \times 10^{-5}\, eV^2$ |
| $\sin^2\theta_{23}$ | atmospheric,accelerator | $0.512^{+0.019}_{-0.022}$ |
| $\Delta m^2_{32}$ | atmospheric,accelerator (IH) | $-2.56 \pm 0.04 \times 10^{-3}\, eV^2$ |
| $\Delta m^2_{32}$ | atmospheric,accelerator (NH) | $2.51 \pm 0.05 \times 10^{-3}\, eV^2$ |
| $\sin^2\theta_{13}$ | reactor | $0.0212 \pm 0.0008$ |
| $\delta_{CP}$ | accelerator,atmospheric | NA |

Table 2.1. Particle Data Group 2019 best fit of neutrino oscillation parameters. For values associated with 2-3 angles and mass-squared differences the best-fit under the normal mass hierarchy hypothesis are shown. The inverted neutrino mass hierarchy (IH) and normal mass hierarchy (NH) best fit values are shown. Although PDG does have a best-fit average for $\delta_{CP} = 1.37^{+0.18}_{-0.16}$, the parameter has not been measured with discovery significance. Taken from [73].

$$\theta_{12}, \theta_{13}, \theta_{23}, \Delta m^2_{12}, \Delta m^2_{23}, \delta_{CP}\ . \tag{2.1}$$

$\Delta m^2_{13}$ is not included, as it is dependent on the $\Delta m^2_{12}$ and $\Delta m^2_{23}$ through the requirement that $\Delta m^2_{12} + \Delta m^2_{23} + \Delta m^2_{31} = 0$.

The best way to determine these parameters is using a suite of neutrino/antineutrino appearance/disappearance experiments with neutrino sources of varying neutrino flavor, energy, and baseline. Table 2.1 provides an overview of the neutrino sources used to measure the oscillation parameters, as well as the PDG 2019 best fit values for each parameter.

The mass-squared differences and mixing angles are often measured in pairs; $\Delta m^2$ and $\theta$ terms impact the neutrino oscillation frequency and amplitude, respectively, and are thus generally fitted simultaneously. The exception to this in table 2.1 is $\theta_{13}$; the short-baseline reactor measurements of $\theta_{13}$ generally constrain the $|\Delta m^2_{13}|$ value with best fits to $\Delta m^2_{12}$ and $|\Delta m^2_{23}|$ under a specific mass hierarchy hypothesis to increase the $\theta_{13}$ measurement's precision [74, 75].

Note that sign of the $\Delta m^2_{32}$ mixing parameter has not yet been determined, and is one major open question neutrino physics. The determination of this sign, which determines the neutrino mass hierarchy, is discussed in detail in section 2.2.

### 2.1.1 Measurements of "solar" oscillation parameters ($\Delta m^2_{12}$,$\theta_{12}$)

$\Delta m^2_{12}$ and $\theta_{12}$ are known colloquially as the "solar" parameters because they were first measured via solar neutrino fluxes. Given that SNO and Super-Kamiokande already measured the solar neutrino flux components, a first estimate of the neutrino oscillation parameters naturally followed. First attempts to model solar neutrino oscillations involved the two-flavor neutrino approximation with vacuum oscillations only; in this case, the electron neutrino survival probability $P_{ee}$ was fitted to the data. $P_{ee}$ is written as follows:

$$P(\bar{\nu}_e \to \bar{\nu}_e) \approx \left[1 - \sin^2\theta_{12}\sin^2\frac{\Delta m^2_{12}L(t)}{4E_\nu}\right] , \tag{2.2}$$

where $L(T)$ would be the approximate distance from the Earth to the Sun given the time of year. Notice this is just equation 1.24 with $\theta_{13} = 0$. This hypothesis did not fit the data well; instead, modifications to account for matter effects as the electron neutrinos oscillated out of the Sun were needed.

When calculating the survival probability of solar electron neutrinos as observed on Earth, the survival probability must be averaged over all neutrinos generated in the Sun's volume. Neutrinos generated at the Sun's center experience considerable matter effects while those at the lower density edge do not; additionally, solar neutrinos generated at the center with enough energy can also experience the Mikheyev-Smirnov-Wolfenstein (MSW) effect, an oscillation resonance that considerably alters the fraction of neutrino flavors observed at Earth. An in-depth discussion of oscillations in matter and the MSW effect can be found in appendix A.2 and section 2.2.1. The average survival probability for electron neutrinos from the Sun is described by the Parke formula, written as [6]

$$\bar{P}_{ee}(E_\nu) = \frac{1}{2} + \left(\frac{1}{2} - P_c\,\phi(A^0_{CC} - \Delta^2_m\cos 2\theta)\right)\cos 2\theta^{(i)}_M\cos 2\theta\ . \tag{2.3}$$

In equation 2.3, $A^0_{CC} = 2\sqrt{2}E_\nu G_F N^0_e$, $E_\nu$ is the neutrino's energy, $N^0_e$ is the electron number density at the center of the Sun, $\phi(x) = \frac{1}{2}(1 + x/|x|)$, and $P_c$ is the crossing probability at resonance (see appendix section A.2 for further discussion). Notice that the mean survival probability does not depend on the distance from the Sun.

The solar neutrino data observed thus far support a specific regime of $\Delta m^2_{12}$ and $\theta_{12}$ values known as the "Large mixing angle" (LMA) solution. The LMA solution refers to the case where $\sin^2\theta_{12}$ is relatively far from zero, and corresponds to a particular shape in the Parke formula. Keeping to the two-flavor approximation in the LMA regime, neutrinos with $E_\nu \lessapprox 2$ MeV do not pass through resonance, and the average survival probability simplifies to the following approximation in vacuum [6]:

$$\bar{P}_{ee}(E_\nu \lessapprox 2\,MeV) \approxeq 1 - \frac{1}{2}\sin^2 2\theta\ . \tag{2.4}$$

For $E_\nu \gtrapprox 2$ MeV, the MSW resonance is crossed adiabatically ($P_c \ll 1$) and equation 2.3 is approximately

$$\bar{P}_{ee}(E_\nu \gtrapprox 2\,MeV) \approxeq \frac{1}{2} + \frac{1}{2}\cos 2\theta^{(i)}_M \cos 2\theta\ . \tag{2.5}$$

The key feature in the MSW-LMA solution is the turning point in the oscillation probability around $2\,MeV$, which has been observed in the collective of solar neutrino measurements to date. A plot of several survival probability measurements across the solar neutrino energy regime are shown in 2.1 with $\bar{P}_{ee}$ in the MSW-LMA regime overlaid. The data agree strongly with the MSW-LMA description of neutrino oscillations in matter.

A recent Super-Kamiokande publication presents a useful case study of how $\Delta m^2_{12}$ and $\theta_{12}$ are extracted from solar neutrino data. After measuring 1664 days of $^8B$ solar neutrino interactions, the Super-Kamiokande collaboration compared the total extracted electron neutrino flux to that expected if neutrinos did not oscillate. Best fits to $P_{ee}$ were performed using a model-independent parameterization function of the form:

$$P_{ee}(E_\nu) = c_0 + c_1\left(\frac{E_\nu}{MeV} - 10\right) + c_2\left(\frac{E_\nu}{MeV} - 10\right)^2\ . \tag{2.6}$$

The SuperK fits to data, as well as the combined best SuperK+SNO fit to the oscillation parameters $\Delta m^2_{12}$ and $\theta_{12}$, are shown in figure 2.2. The dip in the oscillation probability between $3 - 10$ MeV is consistent in shape and scale with that presented in figure 2.1. Note that $\sin\theta_{13}$ is constrained using measurements made by reactor neutrino experiments (see section 2.1.3). This measurement also successfully determines the sign of $\Delta m^2_{12}$ (see section 2.2.1 for details).

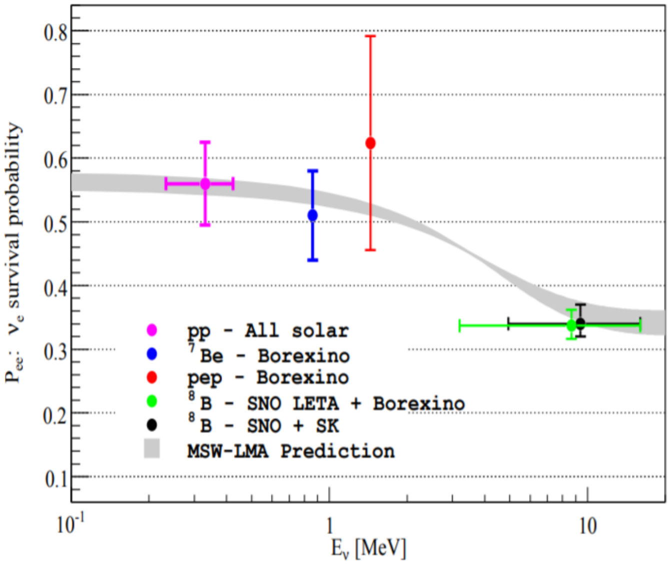

Figure 2.1. Measurements of the solar electron neutrino survival probability overlaid with the survival probability predicted with the LMA-MSW effect. Figure from [41].

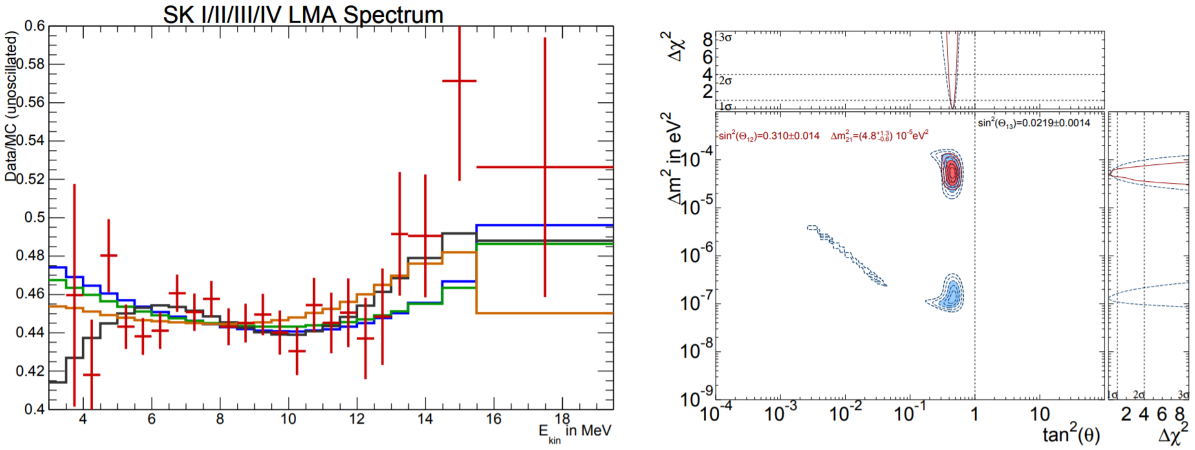

Figure 2.2. Left: SuperK I-IV recoil electron spectrum compared to the no-oscillation case. The green (blue) curve is the oscillation expectation using the SK (SK+SNO+KamLAND) best-fit oscillation parameters. The orange (black) curve is the best fit to SK data with the $P_{ee}$ form in equation 2.6 (cubic form of the function fit by SNO). Right: Best-fit solar neutrino oscillation parameters from SNO (blue) and SNO+SK combined (red). Solid contours mark the $3\sigma$ confidence level on the fit, and larger contours mark the $4\sigma$ and $5\sigma$ confidence levels. Figure from [76].

#### 2.1.1.1 $\Delta m^2_{12}$ and $\theta_{12}$ measurements with reactors

Neutrino detectors placed at $O(100)$ km from reactors can also produce accurate measurements of $\Delta m^2_{12}$ and $\theta_{12}$. Reactor antineutrino oscillation analyses benefit from the ability to neglect matter effects with with a $< 1\%$ uncertainty [9]. However, a detector's reactor antineutrino signal has contributions from all world reactors; an accurate analysis requires additional systematic analyses regarding reactor power states and reactor distances for each world reactor.

The KamLAND experiment currently has the most accurate measurement on $\Delta m^2_{12}$ and $\theta_{12}$ using reactor antineutrinos. The KamLAND procedure for fitting the electron antineutrino survival probability is discussed in section 1.2.4.2; figure 2.3 shows the total KamLAND antineutrino candidate dataset and the best fit to $\Delta m^2_{12}$ and $\theta_{12}$ under the three-oscillation hypothesis.

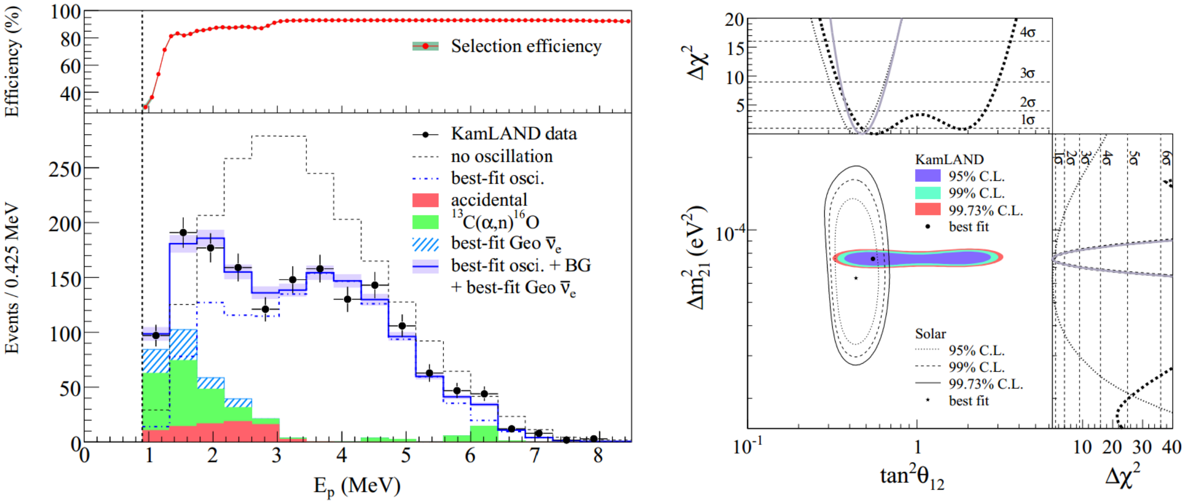

Figure 2.3. Left: Antineutrino candidate dataset at KamLAND as a function of reconstructed prompt energy with the best fit to the background and reactor signal model. Right: Best-fit oscillation parameters extracted from the KamLAND antineutrino dataset. The best combined solar fit at time of publication is also overlaid. Figure from [25].

Comparing the KamLAND best-fit $\Delta m^2_{12} = 7.58^{+0.14}_{-0.13}(stat)^{0.15}_{0.15}(syst) \times 10^{-5}\, eV^2$ to the SK+SNO best fit $\Delta m^2_{12} = 4.8^{+0.15}_{-0.8} \times 10^{-5}\, eV^2$, an interesting 1.6$\sigma$ tension exists. While the measurements do agree within uncertainties, additional measurements would be valuable in resolving or reinforcing this tension. The SNO+ experiment, the SNO detector repurposed as a $^{130}Te$-doped liquid scintillator-based detector for measuring neutrinoless double-beta decay, will be sensitive to its neighboring Canadian reactors and make another measurement of $\Delta m^2_{12}$ and $\theta_{12}$ in the coming years [77].

### 2.1.2 Measurements of "atmospheric" oscillation parameters ($\Delta m^2_{23}$,$\theta_{23}$)

The $\Delta m^2_{23}$ and $\theta_{23}$ oscillation parameters were first verified through the observation of atmospheric neutrinos. As discussed in section 1.3.5, a large flux of $\nu_e$, $\nu_\mu$, $\bar{\nu}_e$, and $\bar{\nu}_\mu$ neutrinos are produced in the Earth's atmosphere due to cosmic radiation. With accurate models of the atmosphere's neutrino production, the $\Delta m^2_{23}$ and $\theta_{23}$ parameters were fit by measuring the electron and muon neutrino spectra and searching for any deviations from the no-oscillation hypothesis.

The first atmospheric flux measurements demonstrating neutrino oscillations were made by the Super-Kamiokande collaboration. Candidate atmospheric neutrino events in SuperK were classified as either "e-like" or "$\mu$-like" based on the structure of the event's Cherenkov ring. The muon produced following $\nu_\mu$ charged-current interactions has a well-defined Cherenkov ring edge, while the electron produced in $\nu_e$ charged-current interactions is more blurred due to electromagnetic showering. While the $\nu_e$ flux observed agreed with expected atmospheric neutrino rates, a deficit was observed in the $\nu_\mu$ flux. The e-like and $\mu$-like event distributions with respect to the zenith angle are shown in figure 2.4.

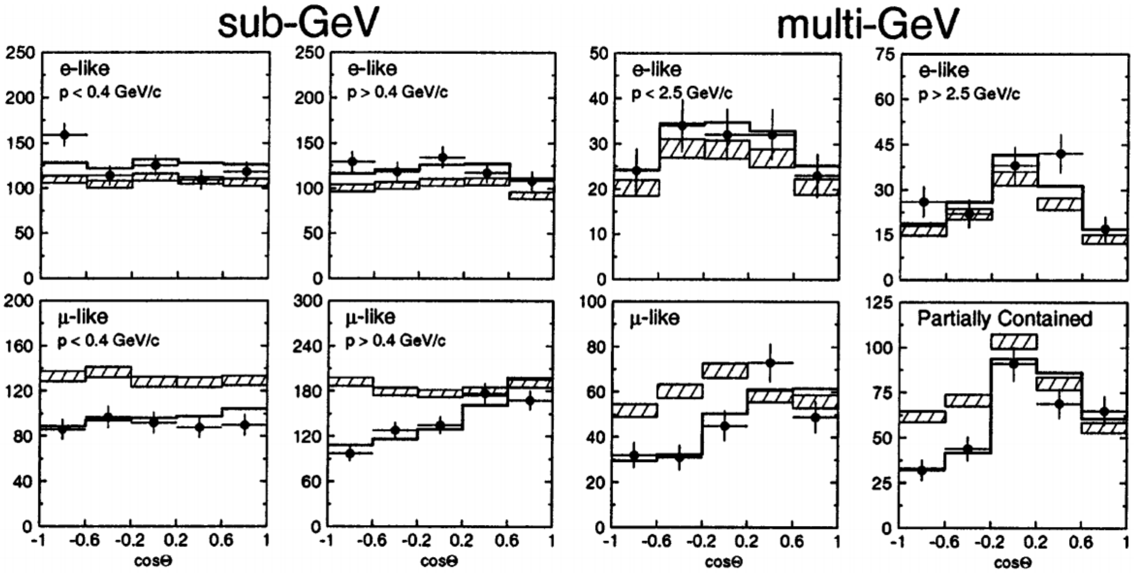

Figure 2.4. Candidate atmospheric neutrino events as published by the Super-Kamiokande collaboration. While the e-like event distributions agree with the no-oscillation hypothesis (hatched lines), the best-fit $\mu$-like distribution under a $\nu_\mu \to \nu_x$ hypothesis (bold line) shows a clear deficit. Figure from [21].

Given the disagreement from the no-oscillation hypothesis existed only in the $\nu_\mu$ flux, the atmospheric oscillation analysis was conducted under the two-flavor neutrino hypothesis, where $\nu_\mu \to \nu_x$ and $x$ is either a $\tau$ or some other sterile neutrino. The probability for a neutrino of flavor $\alpha$ to oscillate to flavor $\beta$ in vacuum would be given by [21]

$$P(\nu_\alpha \rightarrow \nu_\beta) = \sin^2 2\theta \sin^2 \frac{1.27\Delta m^2[eV^2]L[km]}{E_\nu[GeV]} \ . \tag{2.7}$$

The "atmospheric" oscillation parameters in equation 2.7 are related to the three-flavor model variables as $\Delta m^2 \sim \Delta m^2_{23} \approx \Delta m^2_{13}$ and $\sin^2\theta \sim \sin^2\theta_{23}$. The best-fit oscillations parameters to the data are shown in figure 2.5, with published values of $\sin^2 2\theta > 0.82$ and $5 \times 10^{-4} < \Delta m^2 < 6 \times 10^{-3}\, eV^2$ at 90% confidence level.

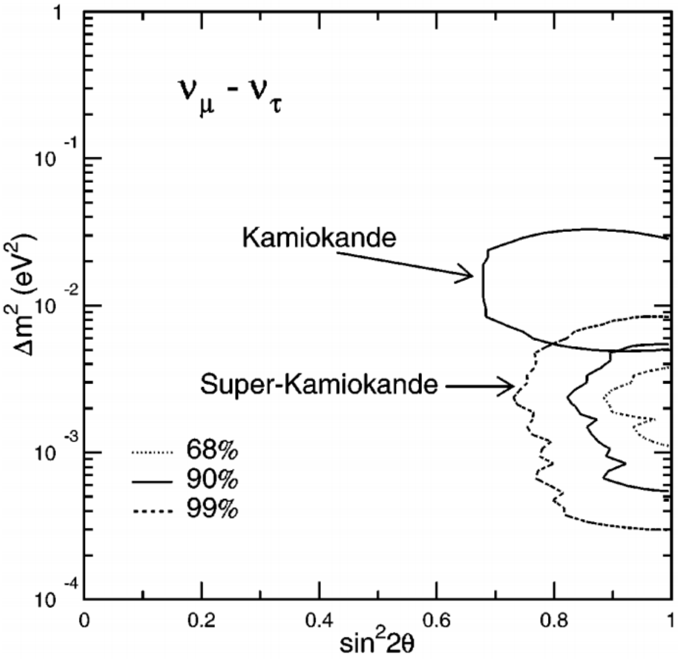

Figure 2.5. Best fit to the atmospheric oscillation parameters under a $\nu_\mu \rightarrow \nu_x$ hypothesis. Contours for confidence limits on the fit are also given. Figure from [21].

More recent publications from Super-Kamiokande perform fits to the atmospheric data with all three-flavor hypothesis oscillation parameters considered. When describing the oscillation probability with three flavors, several approximations can be used to simplify the expression in the atmospheric neutrino energy and baseline regime. [78]. The assumptions needed for simplification are:

1. Consider atmospheric neutrino energies ($\approx 1$ GeV) and baselines on the order of atmospheric neutrinos ($R_{Earth} \approx 6000$ km). Then, oscillation terms proportional to $\sin^2\theta_{12}$

are negligible since

$$\sin^2 \frac{1.27\Delta m_{12}^2 L[km]}{E_{nu}[GeV]} \approx \sin^2 \frac{(1.27)(7.54\times 10^{-5})(6\times 10^3)}{1} \ll 1 \ . \tag{2.8}$$

2. Since $\Delta m_{12}^2 \ll (\Delta m_{13}^2, \Delta m_{23}^2)$ and $\Delta m_{12}^2 + \Delta m_{13}^2 + \Delta m_{23}^2 = 0$, then $|\Delta m_{13}^2| \approx |\Delta m_{23}^2|$ .

Under these assumptions, the oscillation probabilities between $\mu$ and $e$ neutrinos in equation 1.20 can be approximated as [78]

$$P(\nu_e \rightarrow \nu_e) \approxeq 1 - \sin^2 2\theta_{13} \sin^2 \Delta_{31} \ , \tag{2.9}$$

$$P(\nu_\mu \rightarrow \nu_\mu) \approxeq 1 - 4\cos^2\theta_{13}\sin^2\theta_{23}(1 - \cos^2\theta_{13}\sin^2\theta_{23})\sin^2\Delta_{31} \ , \tag{2.10}$$

$$P(\nu_e \longleftrightarrow \nu_\mu) \approxeq \sin^2\theta_{23}\sin^2\theta_{13}\sin^2\Delta_{31} \ , \tag{2.11}$$

where $\Delta_{ij} = \Delta m_{ij}^2 L/4E_\nu$. For neutrinos coming upwards through the Earth, the oscillation probabilities are also modified to incorporate matter effects. The most recent Super-Kamiokande best fits with $\theta_{13}$ constrained by reactor measurements and in the normal mass hierarchy are $\sin^2\theta_{23} = 0.425^{+0.055}_{-0.036}$ and $|\Delta m_{32,31}^2| = 2.53^{+0.14}_{-0.31} \times 10^{-3}\, eV^2$ [78].

#### 2.1.2.1 $\Delta m_{23}^2$ and $\theta_{23}$ measurements with accelerator neutrinos

Precision measurements of $\Delta m_{23}^2$ and $\theta_{23}$ have also proceeded through the observation of neutrinos and antineutrinos produced in accelerator beamlines. The first observation of accelerator neutrinos was completed by the K2K collaboration, which observed $\nu_\mu \rightarrow \nu_\tau$ oscillations in a muon neutrino beam produced at KEK [79]. Additional measurements have been conducted by the MINOS experiment, the T2K experiment, and the NO$\nu$A experiments as well. The MINOS and NOvA results from measuring $\Delta m_{32}^2$ and $\sin^2\theta_{23}$ via $\nu_\mu$ and $\bar{\nu}_\mu$ disappearance and $\nu_\mu \rightarrow \nu_e$ appearance are described below.

For measurements of accelerator neutrino oscillations through $\nu_\mu$ or $\bar{\nu}_\mu$ disappearance, the two-flavor approximation is still utilizable; however, the survival probability expression can also be modified to better approximate the three-flavor model. The leading order terms in the $\nu_\mu$ and $\bar{\nu}_\mu$ survival probability take the same form as the two-flavor model, written as

$$P(\nu_\mu \to \nu_\mu) = 1 - \sin^2 2\theta \sin^2 \frac{1.27\Delta m^2[eV^2]L[km]}{E_\nu[GeV]} \ , \tag{2.12}$$

but with the following effective parameters substituted [80, 81]:

$$\sin^2 2\theta \to 4\sin^2\theta_{23}\cos^2\theta_{13}(1-\sin^2\theta_{23}\cos^2\theta_{13}) \ ,$$

$$\Delta m^2 \to \Delta m^2_{32} + \Delta m^2_{21}\sin^2\theta_{12} + \Delta m^2_{21}\cos\delta_{CP}\sin\theta_{13}\tan\theta_{23}\sin 2\theta_{12} \ ,$$

with additional matter-related modifications needed to account for travel through the Earth's crust.

The low $\nu_e$ and $\bar{\nu}_e$ backgrounds of an accelerator neutrino beam also provide the opportunity to measure oscillation parameters by searching for $\nu_e$ and $\bar{\nu}_e$ appearance. Given the $E_\nu \approx O(GeV)$ and $|\Delta m^2_{12}| \ll |\Delta m^2_{23}|$ approximations discussed in the previous section (which are also valid for most accelerator neutrinos), the $\nu_\mu \to \nu_e$ oscillation probability in matter is described approximately by [81]

$$\begin{aligned} P(\nu_\mu \to \nu_e) \approx \sin^2\theta_{23}\sin^2\theta_{23}\frac{sin^2\Delta(1-A)}{(1-A)^2} + \\ \alpha\tilde{J}\cos\Delta \pm \delta_{CP}\frac{\sin\Delta A}{A}\frac{\sin\Delta(1-A)}{(1-A)} + \\ \alpha^2\cos^2\theta_{23}\sin^2 2\theta_{12}\frac{sin^2\Delta A}{A^2} \ , \end{aligned} \tag{2.13}$$

where the appearance probability in matter has been expanded to second order in $\alpha \equiv \Delta m^2_{21}/\Delta m^2_{31} \approx 0.03$, $A \equiv \pm 2\sqrt{2}G_F n_e E_\nu/\Delta m^2_{31}$, $\tilde{J} \equiv \cos\theta_{13}\sin 2\theta_{13}\sin 2\theta_{12}\sin 2\theta_{13}$, $\Delta \equiv \Delta m^2_{31}L/4E_\nu$, and the plus (minus) signs correspond to oscillations for neutrinos (antineutrinos). For details on estimating oscillation probabilities using perturbative expansion to acquire equation 2.13, see appendix C of reference [82].

Equation 2.13 has several important features to consider when fitting the oscillation probability to accelerator neutrino data. In particular:

1. The oscillation probability is dependent on $\delta_{CP}$, and the sign of the term with $\delta_{CP}$ is opposite when using a neutrino or antineutrino beam. Thus, a comparison of neutrino to antineutrino oscillations in matter is sensitive to the value of $\delta_{CP}$.
2. The oscillation probability is dependent on $A$, whose sign changes when using a neutrino or antineutrino beam. Since the only term in $A$ whose sign can change is $\Delta m^2_{31}$, measuring the sign of $A$ determines the sign of $\Delta m^2_{31}$, as well as the neutrino mass hierarchy.

The above points explain the popularity of long-baseline accelerator neutrino oscillation measurements; they have the potential of simultaneously determining the neutrino mass hierarchy (see section 2.2) and the value of $\delta_{CP}$ (see section 2.1.4).

The MINOS experiment provides one useful example in measuring $\Delta m^2_{32}$ and $\sin^2\theta_{23}$ via accelerator neutrinos. MINOS has two detectors that both receive atmospheric neutrinos from Fermilab's NuMI beam line. The near detector is located 1.04 km from the NuMI proton target, while the far detector is located 735 km away in the Soudan mine in northern Minnesota. Both detectors are calorimeters composed of alternating layers of magnetized steel and scintillator. MINOS searched for neutrino oscillations in both the disappearance and appearance channels [83].

MINOS produced measurements of neutrino oscillation parameters utilizing both atmospheric and accelerator neutrinos. Results from the combination of both sources provided a slight preference for the inverted mass hierarchy, with best fits of $\Delta m^2_{32}$ and $\sin^2\theta_{23}$ shown in figure 2.6. The fit also yielded a value for $\delta_{CP}$, but discussion will be left for section 2.1.4.

The NOvA experiment has also recently published new results on the $\Delta m^2_{32}$ and $\sin^2\theta_{23}$ using accelerator-based neutrinos. NOvA also utilizes a near detector and far detector to measure neutrinos from the NuMI beam. Both detectors utilize arrays of liquid scintillator bars contained in PVC cells to detect the charged particles produced in neutrino interactions. Using a combination of neutrino-mode and antineutrino-mode accelerator data, the oscillation fit yields best-fit parameters $|\Delta m^2_{32}| = 2.48^{+0.11}_{-0.06} \times 10^{-3}\, eV^2$ and $\sin^2\theta_{23} = 0.56^{+0.04}_{-0.03}$ [84]. The best-fit parameters alongside measurements from other experiments is shown in figure 2.7.

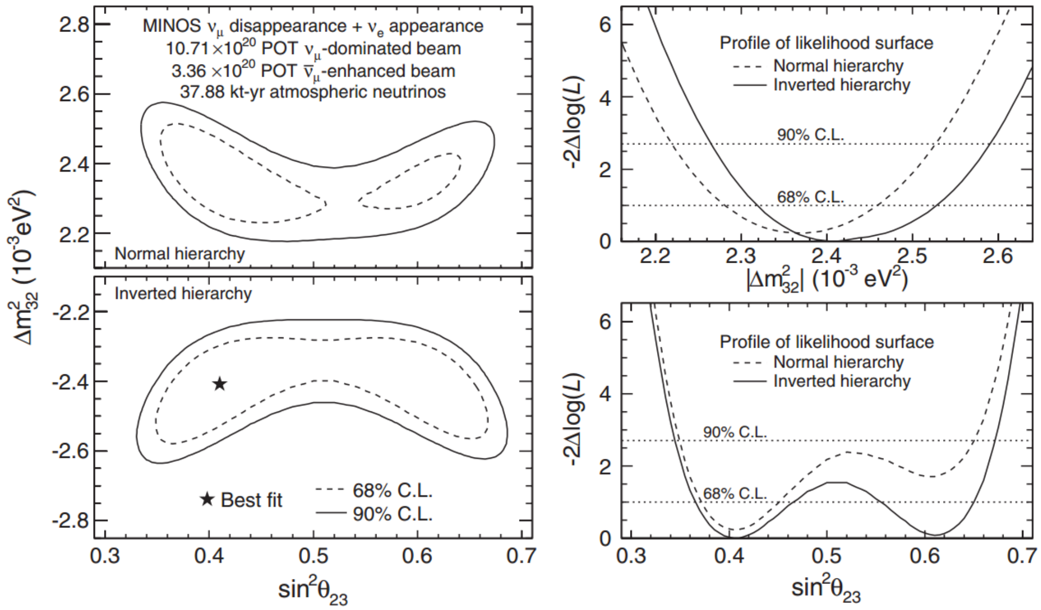

Figure 2.6. Best fits to the “atmospheric” neutrino oscillation in MINOS using combined results from atmospheric and accelerator neutrinos. The fit slightly favors the inverted mass hierarchy. Figure from [81].

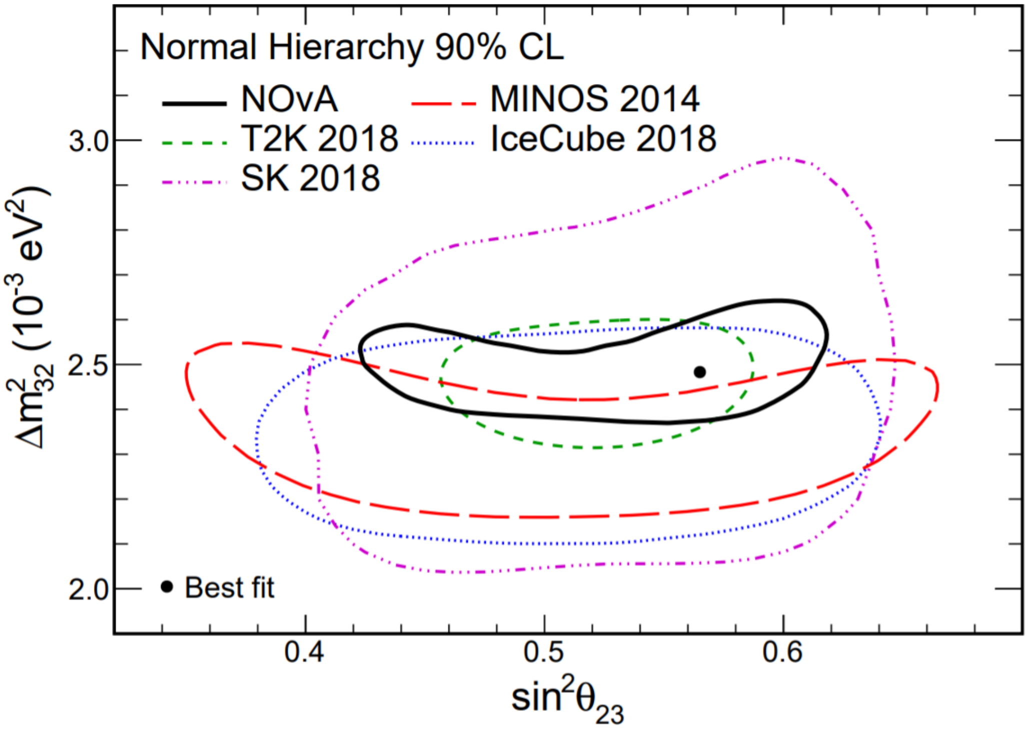

Figure 2.7. Best fits to the “atmospheric” neutrino oscillation in NOvA using antineutrino and neutrino-based accelerator data. Several other recent measurements are shown for reference. Figure from [84].

### 2.1.3 Measurements of $\theta_{13}$

When compared to solar, atmospheric, and reactor neutrino measurements, reactor-based measurements at baselines of $O(km)$ are particularly sensitive to measuring $\theta_{13}$. In the approximation that $\Delta m^2_{31} \approx \Delta m^2_{32} \equiv \Delta m^2_{atm}$, the electron antineutrino survival probability in vacuum under the three-flavor system is approximately given by [85]

$$P(\bar{\nu}_e \to \bar{\nu}_e) \approx 1 - \sin^2 2\theta_{13} \sin^2 \frac{1.27 \Delta m^2_{atm} L[km]}{E_\nu [GeV]} - \sin^2 2\theta_{12} \cos^4 2\theta_{13} \sin^2 \frac{1.27 \Delta m^2_{21} L[km]}{E_\nu [GeV]} \,. \tag{2.14}$$

However, in the regime where $L \approx 1$ km and $E_\nu \approx 10$ MeV, notice that

$$\sin^2 \frac{1.27 \Delta m^2_{21} L[km]}{E_\nu [GeV]} \approx \sin^2 \frac{(1.27)(7.54 \times 10^{-5})(1)}{1} \ll 1$$

and so equation 2.14 simplifies further to the expression fit in Daya Bay's first measurement of $\theta_{13}$ [74]:

$$P(\bar{\nu}_e \to \bar{\nu}_e) \approx 1 - \sin^2 2\theta_{13} \sin^2 \frac{1.27 \Delta m^2_{atm} L[km]}{E_\nu [GeV]} \,. \tag{2.15}$$

The Daya Bay experiment made the first discovery significance measurement of a non-zero $\sin^2 \theta_{13}$. Daya Bay consisted of six scintillator-based antineutrino detectors located in three different experimental halls (EH) relative to six commercial reactors at the Daya Bay powerplant near Shenzhen, China. By measuring the reactor antineutrino flux at several reactor baselines varying between $0.4$ to $1.7$ km, an oscillation in the electron antineutrino survival probability was confirmed with $5.2\sigma$ significance [74]. $\sin^2 \theta_{13}$ was measured to be $\sin^2 \theta_{13} = 0.092 \pm 0.016(stat.) \pm 0.005(syst)$ using the reactor data shown in figure 2.8.

Similar measurements of $\theta_{13}$ have been made by other short-baseline reactor experiments as well, including DoubleCHOOZ and RENO [75, 86].

### 2.1.4 Measurements of $\delta_{CP}$

The obvious outlier in table 2.1 is the Charge-Parity (CP) phase parameter, for which no measurement has been made with discovery significance. This is currently one of the most popular measurements to attempt in neutrino physics. Aside from being the last neutrino oscillation

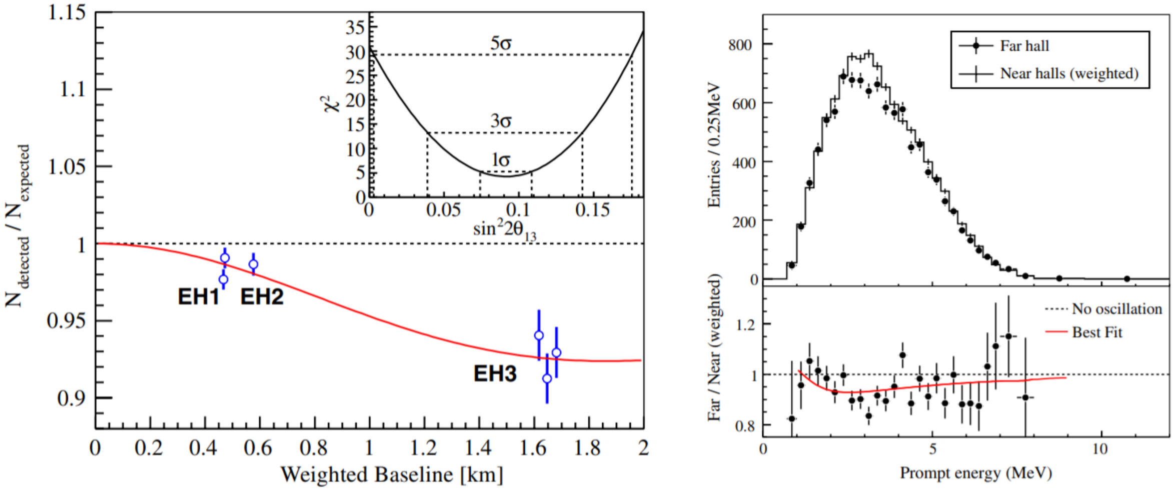

Figure 2.8. Left: Ratio of observed count rates to rates expected without oscillations in each scintillator detector. The best-fit oscillation probability is given by the red curve, with the $\chi^2$ versus $\sin^2\theta_{13}$ shown on inset. Right: Measured prompt energy spectrum for IBD candidate events in all three far hall detectors. Bottom is the ratio of observed counts to counts under the no-oscillation hypothesis. Figure from [74].

parameter with no discovery significance measurement, a non-zero CP phase measurement has exciting physics implications. Combined with the confirmation that the neutrino has Majorana mass terms, CP violation in the neutrino sector could provide the ingredients needed to explain the universe's matter-antimatter asymmetry via leptogenesis [87].

The most sensitive measurements of $\delta_{CP}$ have proceeded through the analysis of accelerator-based neutrinos after oscillating in matter. The most recent measurements have been made by the MINOS, T2K, and NO$\nu$A collaborations. Accelerator neutrino measurements can also be combined with atmospheric neutrino measurements to further constrain the $\delta_{CP}$ parameter space [78, 81]. The results from T2K are discussed as an example below, and the projected sensitivity of the Deep Underground Neutrino Experiment (DUNE) to $\delta_{CP}$ via both accelerator neutrinos and atmospheric neutrinos is also provided.

#### 2.1.4.1 CP phase measurement via accelerator neutrinos in T2K

Although Super-Kamiokande operates as a detector for low-background measurements like proton decay and the DSNB, the detector also acts as a far detector for accelerator neutrino oscillation measurements for the T2K collaboration. Super-Kamiokande sits 2.5° off-axis about 295 km from J-PARC's muon neutrino/antineutrino production point; the off-axis neutrino peaks at about 0.6 GeV and contains considerably less $\bar{\nu}_e$ contamination than an on-axis detector would. On-axis (INGRID) and $2.5°$ off-axis (ND280) near-field detectors also operate 280 meters from J-PARC's production point [88].

In 2018, T2K published the most sensitive CP phase measurement results to-date. The CP phase analysis focuses event selection on $\nu_\mu$ CCQE and $\bar{\nu}_\mu$ CCQE events from the J-PARC neutrino beam, and performs a best-fit for the neutrino oscillation parameters using the data. The best fit to the $\nu_\mu$ and $\bar{\nu}_\mu$ energy distributions are shown in 2.9. Constraints for the neutrino flux and interaction cross sections are obtained from fits to the near-detector data.

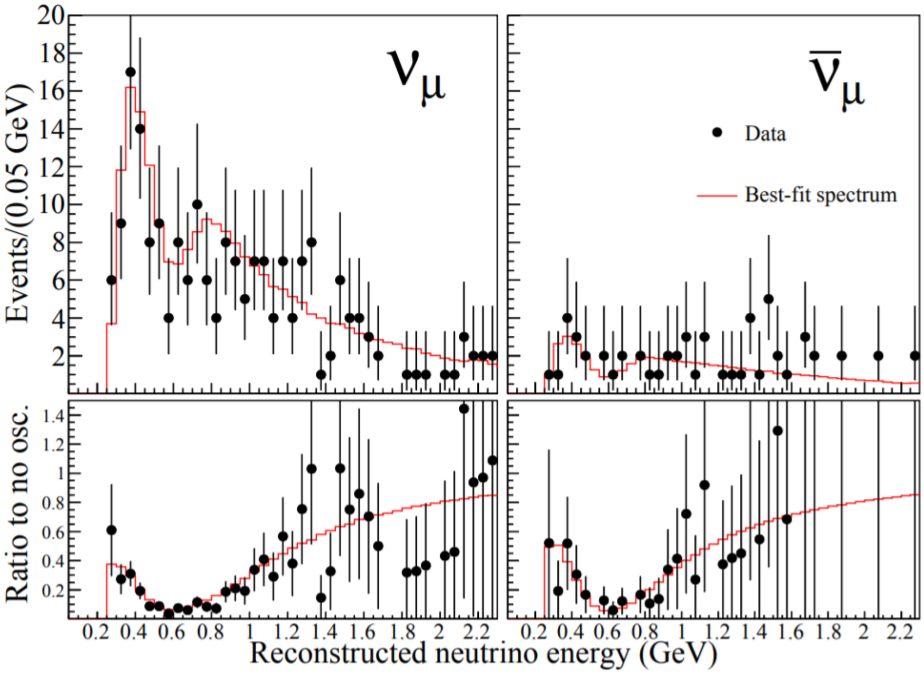

Figure 2.9. Best fit to the neutrino and antineutrino distributions observed in T2K from the J-PARC neutrino beamline. Figure taken from [88].

T2K's measurement of $\delta_{CP}$ proceeded in a similar fashion to that of the MINOS measurement discussed in section 2.1.2.1. A fit of $\theta_{23}$, $|\Delta m^2_{23}|$, and $\delta_{CP}$ are extracted by analyzing the muon neutrino oscillations in matter after propagating from J-PARC to SuperK. The best fit and confidence limits for the CP phase are evaluated using a marginal likelihood statistic, with further details on the fitting approach described in [89]. The marginal likelihood ratio $-2\Delta \ln \mathcal{L} = -2 \ln \frac{\mathcal{L}}{\mathcal{L}_{max}}$ ,which is used to compare the likelihoods from all tested oscillation parameters to the best-fit's likelihood $\mathcal{L}_{max}$, is shown in figure 2.10.

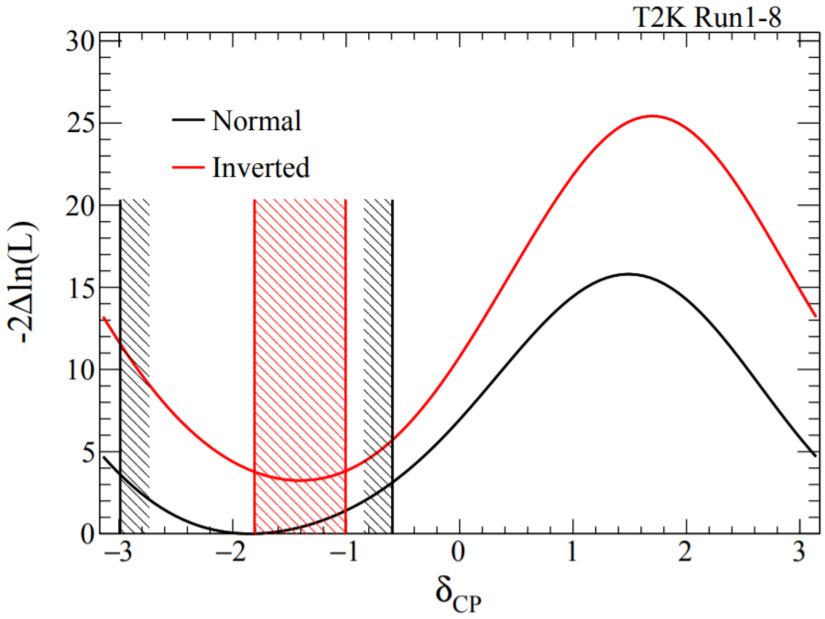

Figure 2.10. Maximum likelihood ratio for values of $\delta_{CP}$ as fit using T2K data. The $2\sigma$ confidence limits are shown in the shaded regions for the normal and inverted mass hierarchy assumption. Figure taken from [89].

Interestingly, the $\delta_{CP}$ parameters that would result in CP conservation are disfavored at $2\sigma$ in both neutrino mass hierarchies relative to the best fit to data. However, the best-fit $\delta_{CP}$ phase does not have the significance to claim the discovery of a non-zero $\delta_{CP}$ and CP violation in the neutrino sector.

#### 2.1.4.2 CP phase measurements in DUNE

Within the next decade, the Deep Underground Neutrino Experiment (DUNE) will be deployed as a long baseline detector at the Sanford Underground Neutrino Facility (SURF). DUNE is a Liquid Argon Time-Projection Chamber (LArTPC) detector, which will be composed of four 10-kiloton LArTPC modules. Utilizing a neutrino beam originating from Fermilab's future PIP-II neutrino line [90], DUNE's successful deployment will lead to a determination of the neutrino mass hierarchy and has the ability to measure $\delta_{CP}$ with discovery significance. DUNE will also be capable of other beam-independent measurements, including several modes of proton decay and supernova neutrino detection [91]. The details for DUNE's current design are detailed in several published Conceptual Design Reviews, which drive the discussion for this section.

DUNE will complete the primary $\delta_{CP}$ measurement through an analysis of both $\nu_{\nu}, \bar{\nu}_{\mu}$ disappearance and $\nu_e, \bar{\nu}_e$ appearance channels. Assuming three-neutrino mixing with matter effects accounted for, the probability of muon neutrino/antineutrino oscillation to electron neutrino/antineutrinos is shown with several $\delta_{CP}$ values at the approximate DUNE baseline in figure 2.11. The probability spectra show that different CP-phase parameters would lead to considerably different muon neutrino/antineutrino disappearance distributions in DUNE. Given suitable statistics and acceptable energy resolution, a precise $\delta_{CP}$ measurement is achievable [92].

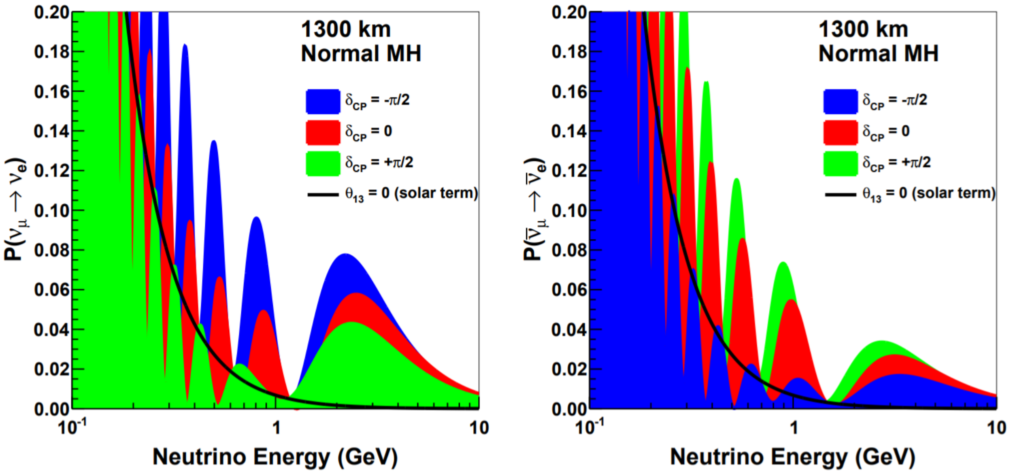

Figure 2.11. Muon neutrino (left) and antineutrino (right) disappearance probability distributions at the DUNE baseline. Oscillation probabilities shown are in the three-neutrino mixing case with constant matter density effects included. Figure taken from [92].

The sensitivity of DUNE's baseline detector design was quantified in the CDR via simulation. The GLoBES simulation package was used to predict DUNE's sensitivity to $\delta_{CP}$ given the predicted neutrino beam flux (estimated with a preliminary GEANT4 simulation of PIP-II), cross sections, and detector response parameters estimated using the DUNE Fast MC simulation. The simulated muon neutrino/antineutrino disappearance spectra for DUNE are shown in figure 2.12; the two-peak structure of the oscillation distribution from $1 - 10\,GeV$ in figure 2.11 is clearly visible.

The projected sensitivity to $\delta_{CP}$ given a combined fit of the simulated $\nu_\mu, \bar{\nu}_\mu, \nu_e, and \bar{\nu}_e$ data is shown in 2.13. Notice as $\delta_{CP}$ approaches either 0 or $\pi$, DUNE's measurement significance decreases; this reduction in sensitivity is inevitable, as a smaller $\delta_{CP}$ angle ultimately leads to smaller distortions of the neutrino and antineutrino spectra. However, the measurements made by T2K in figure 2.10 which indicate that $\delta_{CP} = 0, \pi$ is disfavored at $2\sigma$ provide a strong case

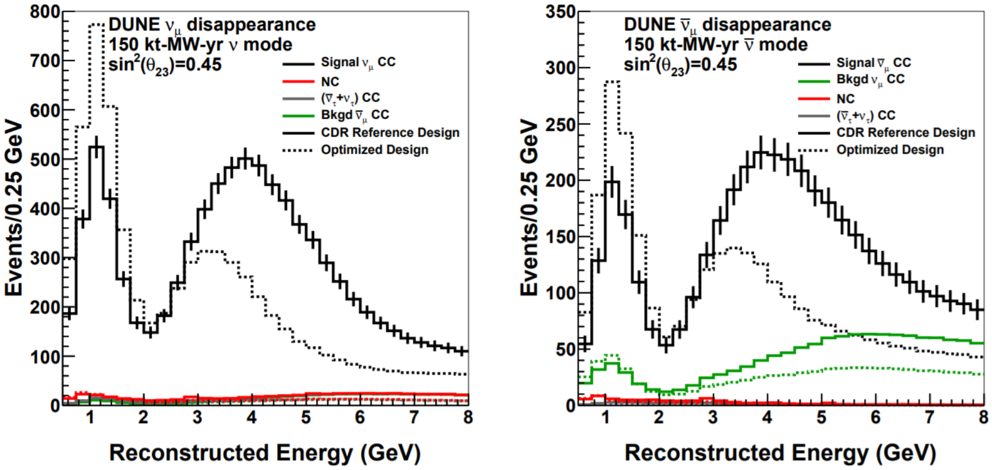

Figure 2.12. Muon neutrino (left) and antineutrino (right) CCQE event distributions for a simulated DUNE deployment. $\delta_{CP} = 0$ is assumed for the simulation. Figure taken from [92].

that the current DUNE design will make a successful $\delta_{CP}$ measurement.

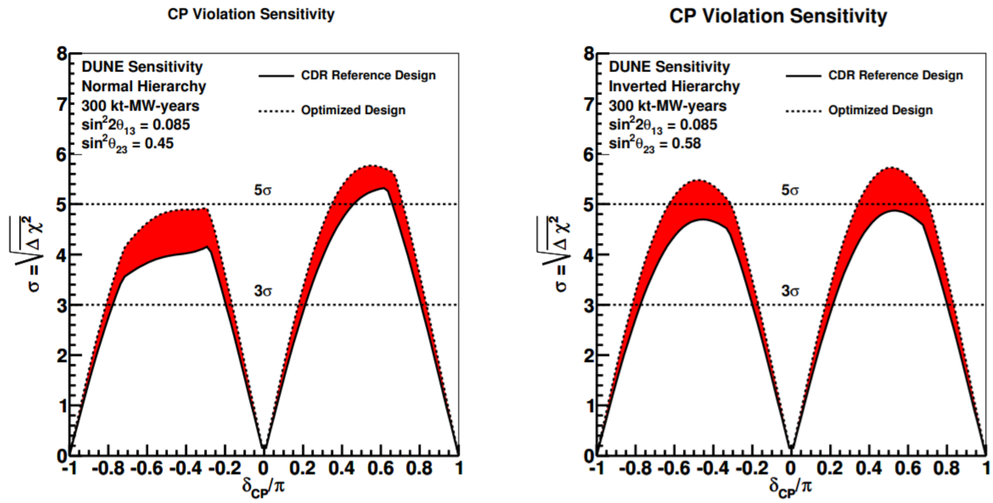

Figure 2.13. DUNE's projected sensitivity to measure $\delta_{CP}$ given different CP-phase values. The red band indicates the region of possible improvement based on optimization of the CDR reference design. Figure taken from [92].

## 2.2 Neutrino mass hierarchy

The neutrino mass hierarchy refers to the ordering of the neutrino masses $m_1$, $m_2$, and $m_3$ from heaviest to lightest. Consider again the mass-squared differences $\Delta m^2_{jk} = m^2_j - m^2_k$. In the three-flavor neutrino case, the following expression must be true:

$$\Delta m^2_{12} + \Delta m^2_{13} + \Delta m^2_{23} = 0\ . \tag{2.16}$$

This constraint brings to light a degree of freedom that must be determined: the *sign* of each term. The determination of each $\Delta$ term's sign is equivalent to determining the mass ordering of the $m_1$, $m_2$, and $m_3$ terms.

There are two main ways to determine the sign of each term in 2.17. The first option is to measure the absolute values of each $\Delta m^2_{jk}$ with incredible precision, then select the signs for each term such that the following holds:

$$\pm?\,|\Delta m^2_{12}| \pm?\,|\Delta m^2_{13}| \pm?\,|\Delta m^2_{23}| = 0\ . \tag{2.17}$$

Unfortunately, current measurements of the mass-squared difference values are not precise enough to determine the sign of these terms. Based on the uncertainties of the current best fits in 2.1, the increases in precision needed would also be challenging to achieve even with the next generation of neutrino detectors (although JUNO will attempt to do so using reactor antineutrinos [93]).

The second option is to determine the signs of $\Delta m^2_{32}$, $\Delta m^2_{21}$, and $\Delta m^2_{13}$ by measuring neutrino oscillations in matter. This turns out to be a more accessible task; in fact, the ordering of $m_1$ and $m_2$ has already been determined through solar neutrino observations (see below). However, it has not been determined whether $m_3$ is the heaviest (normal hierarchy) or lightest (inverted hierarchy) neutrino mass. Figure 2.14 provides a visual summary of the hierarchy question at hand.

### 2.2.1 The solar mass splitting hierarchy ($m_1$,$m_2$)

Solar neutrino observations provide a useful case study into how matter effects lead to the determination of a mass-squared difference's sign. For all fusion processes in the Sun, neutrinos are initially produced as fully electron neutrino-flavored. In the two-flavor oscillation model, as the electron neutrinos propagate outward, the effective oscillation angle $\theta_M$ in matter is related to the electron density in the Sun $N_e$ and the neutrino's energy $E_\nu$ via (see appendix A.2 for full derivation)

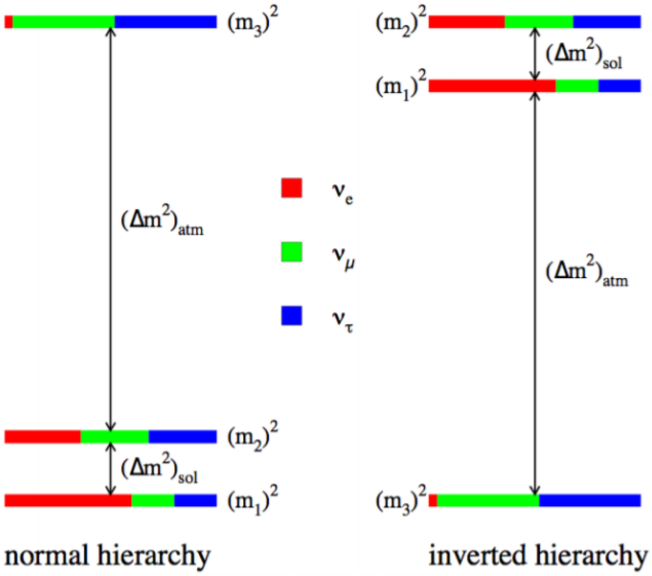

Figure 2.14. Visual representation of the neutrino mass hierarchy question. Although the absolute mass differences have been measured, the ordering of the neutrino masses has not. Figure from [94].

$$\tan 2\theta_M = \frac{\tan 2\theta_{12}}{1 - \frac{2\sqrt{2}E_\nu G_F N_e}{\Delta m^2_{12}\cos 2\theta_{12}}} . \tag{2.18}$$

As the neutrinos pass through the Sun, there is a particular $N_e$ density that results in a matter neutrino oscillation resonance corresponding to $\theta_M = \frac{\pi}{4}$; this results in a maximal probability to oscillate from $e$ flavor to $\mu$ flavor neutrinos. This phenomena is the Mikheyev-Smirnov-Wolfenstein (MSW) effect, and considerably modifies the ratio of $e$ and $\mu$ solar neutrinos observed on Earth as a function of neutrino energy. The sign of $\Delta m^2_{12}$ changes where in the neutrino energy spectrum this resonance occurs, and would change the survival probability $P_{ee}$ seen in figure 2.1.

### 2.2.2 The ordering of $m_3$

As discussed previously, most analyses focused on determining the ordering of $m_3$ emphasize measuring the sign of either $\Delta m^2_{13}$ or $\Delta m^2_{23}$. For accelerator-based measurements, a measurement of the antineutrino and neutrino oscillation probability changes the sign of terms in equation 2.13; with an accurate enough measurement, the sign of $A$, and thus the sign of $\Delta m^2_{23}$, can determine the mass hierarchy.

As seen in the T2K $\delta_{CP}$ fit in figure 2.10 and in the best-fit $\delta_{CP}$ value from NO$\nu$A in figure 2.15, current leading measurements favor the normal hierarchy mass ordering but only at a $\sim 2\sigma$ significance. However, more data are needed to confirm the mass hierarchy with discovery significance.

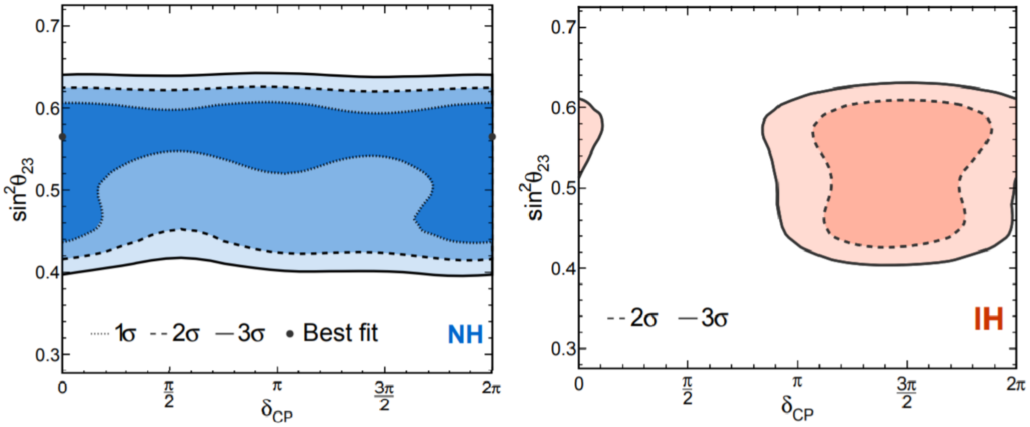

Figure 2.15. Best-fit of $\delta_{CP}$ made with the NO$\nu$A detector at Fermilab. The normal hierarchy solution is preferred in the best-fit neutrino oscillation parameters at a $1.9\sigma$ significance. Figure modified from [84].

Fortunately, upcoming neutrino experiments are expected to measure the neutrino mass hierarchy with discovery significance. In particular, the Deep Underground Neutrino Experiment (DUNE) anticipates a determination of the neutrino mass hierarchy at $5\sigma$ regardless of the $\delta_{CP}$ phase value [92].

## 2.3 Origin of neutrino mass

As discussed in chapter 1.2, the neutrino is treated as a massless particle in the Standard Model by ignoring the right-handed neutrino singlet. However, the confirmation of neutrino masses through measurements of non-zero mass-squared differences demands that some modification to the Standard Model be made. But how should the Standard Model be modified to include neutrino masses? And how does one know whether the modification is justified, or even correct? A brief overview on the competing Standard Model expansions and experimental paths to their verification is given below.

### 2.3.1 Dirac mass terms

One possible way of incorporating neutrino masses to the Standard Model is to simply add back in the right-handed neutrino component (i.e. the neutrino is a Dirac fermion). The neutrino mass would then be produced via the Higgs Mechanism just as with the other fermions (see appendix B.2.1) and lead to Dirac mass terms of the form

$$\mathcal{L}_D = m_D \bar{\nu}_R \nu_L \, + \, m_D \bar{\nu}_L \nu_R \, . \tag{2.19}$$

Although this modification is immediately achievable, the inclusion of the right-handed neutrino requires considerable parameter tuning to match experimental data, as right-handed neutrinos have not been observed; this is generally considered inelegant. For one example, observations of neutrino-nucleus scattering at CERN indicate that the ratio of the right-handed and left-handed neutrino current couplings to the weak quark currents would have to be $\sigma_R/\sigma_L \, < \, 0.009$ at $90\% \, CL$ [95]. The coupling to the Higgs would require even more aggressive tuning; if right-handed neutrinos are introduced to the Standard Model, neutrinos would have to couple to the Higgs $\sim \, 10^{22}$ times weaker than that of the top quark to have the proper mass as observed in experiments to date [96].

### 2.3.2 Majorana mass terms

Another path to including neutrino masses in the Standard Model is to treat the neutrino as a Majorana fermion. The Majorana fermion is a special solution to the Dirac equation where the fermion is its own charge conjugate; in terms of the fermion's left and right-chiral components $\nu = \nu_R + \nu_L$, the Majorana fermion condition that satisfies the Dirac equation is [97]

$$\nu_R \, = \, C \bar{\nu}_L^T \equiv \nu_L^C \, , \tag{2.20}$$

where the charge conjugation operator $C$ is related to $\gamma_0 C \, = UU^T$ for the unitary matrix $U$ that converts the gamma matrices to an entirely real representation [98]. Note that the neutrino is the only known fundamental lepton that could meet this condition due to its neutral charge. For neutrinos of Majorana type, the Lagrangian can now hold a Majorana mass term of the form

$$\mathcal{L}_M = m_M \bar{\nu}_L^C \nu_L \ . \tag{2.21}$$

Although this option seems appealing for modeling the neutrino mass, there is currently no experimental evidence that the neutrino is of Majorana type.

Note that if the neutrino is of Majorana type, neutrinos have additional phases introduced to the oscillation matrix, given by

$$U \rightarrow U = U_{PMNS} U_{Major} = U_{PMNS} \begin{pmatrix} e^{i\alpha_1} & 0 & 0 \\ 0 & e^{i\alpha_2} & 0 \\ 0 & 0 & 1 \end{pmatrix} \ . \tag{2.22}$$

However, the Majorana phases $\alpha_1, \alpha_2$ have no impact on the observable appearance or disappearance of neutrinos due to neutrino oscillations [6]. The current leading approach for confirming the neutrino is a Majorana fermion is through the observation of neutrinoless double-beta decay, discussed in section 2.3.4.

### 2.3.3 The seesaw mechanism

An interesting model of the neutrino which generates the low mass of left-handed neutrinos is called the *Seesaw Mechanism*. If the neutrino is of Majorana type, and *also* has Dirac mass terms via the existence of right-chiral neutrinos and left-chiral antineutrinos, then the neutrino mass Lagrangian can be written as [98]

$$\mathcal{L}_{mass} = m_D \bar{\nu}_R \nu_L \ + \ m_D \bar{\nu}_L^C \nu_R^C + m_L \bar{\nu}_L^C \nu_L + m_R \bar{\nu}_R^C \nu_R \ + \ h.c. \tag{2.23}$$

which can be represented in matrix form as:

$$\mathcal{L}_{mass} \sim \begin{pmatrix} \bar{\nu}_L^C & \bar{\nu}_R \end{pmatrix} \begin{pmatrix} m_L & m_D \\ m_D & m_R \end{pmatrix} \begin{pmatrix} \nu_L \\ \nu_R^C \end{pmatrix} + h.c. \tag{2.24}$$

Notice that a non-diagonal mass matrix $M$ has manifested in this form; this means that the $\nu_L$ and $\nu_R$ terms which couple to the $W$ and $Z$ bosons in interactions we observe are *not* the neutrino mass eigenstates. A similar phenomenon is observed in the quark families, which are related through the CKM matrix. Diagonalizing the mass matrix $M$ to be represented in the mass eigenbasis yields

$$M_{diag} = \begin{pmatrix} m_1 & 0 \\ 0 & m_2 \end{pmatrix} \ , \tag{2.25}$$

where

$$m_{1,2} = \frac{1}{2}\left[(m_L + m_R) \pm \sqrt{(m_L - m_R)^2 + 4m_D^2}\right] \ . \tag{2.26}$$

The case of interest comes from choosing $m_L = 0$ and $m_R \gg m_D$. In this limit, the mass of the $\nu_1$ field and the $\nu_2$ field become:

$$m_1 = \frac{m_D^2}{m_R} \ , \ m_2 = m_R\left(1 + \frac{m_D^2}{m_R^2}\right) \approx m_R \ . \tag{2.27}$$

With the eigenvalues $m_1, m_2$ solved for, the eigenvectors $\nu_1, \nu_2$ that solve the equation $M\nu_i = m_i\nu_i$ can also be found; in the limiting mass cases $m_L = 0$ and $m_R \gg m_D$ again, the mass eigenstates of the neutrino are

$$\begin{aligned} \nu_1 &\sim (\nu_L + \nu_L^C) - \frac{m_D}{m_R^2}(\nu_R + \nu_R^C) \ , \\ \nu_2 &\sim (\nu_R + \nu_R^C) + \frac{m_D}{m_L^2}(\nu_L + \nu_L^C) \ . \end{aligned}$$

In short, the $\nu_1$ mass eigenstate, which has the lighter mass of the two, is mostly composed of the left-chiral neutrino while the $\nu_2$ heavier mass eigenstate is composed primarily of the right-chiral neutrino. The values for $m_D$ and $m_R$ would then be tuned to give an $m_1$ consistent with the effective neutrino masses limited in current experiments, while $m_2$ would be too large to produce in any processes known in the universe today. This is the most natural mechanism that leads to the relatively small mass of the observed left-chiral neutrino and right-chiral antineutrino. As enticing as it is to take this mechanism as the standard, it relies on the presence of Majorana mass terms; this must be verified experimentally.

### 2.3.4 Search for the Majorana neutrino via neutrinoless double-beta decay

One possible experimental approach to confirming the neutrino is of Majorana type is through the observation of neutrinoless double-beta decay. Several nuclear isotopes, such as $^{130}Te$ and $^{136}Xe$, which cannot undergo single beta decay due to energy conservation can still (rarely) undergo two-neutrino double-beta decay ($2\nu\beta\beta$). However, if the neutrino is a Majorana fermion, the two neutrinos could effectively self-annihilate and result in the observation of two electrons and no neutrinos. The signal for $0\nu\beta\beta$ in a particle detector would be the emission of two electrons with total kinetic energy $K_e$ being equal to the decay's entire $Q$ value. See figure 2.16 for the $0\nu\beta\beta$ Feynman diagram and example energy signal signature.

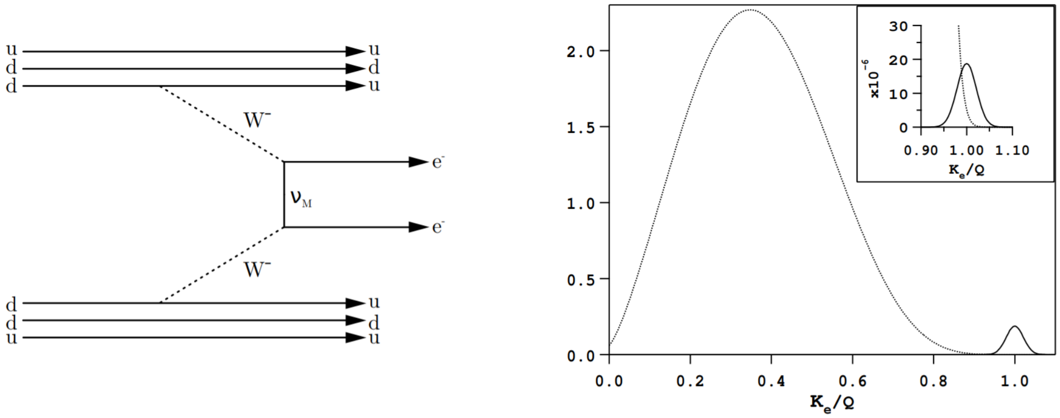

Figure 2.16. Left: Feynman diagram of neutrinoless double-beta decay possible if the neutrino is a Majorana fermion. Right: Example comparison of $2\nu\beta\beta$ and $0\nu\beta\beta$ decay electron energy spectra if $0\nu\beta\beta$ were $10^2$ times less likely to occur than $2\nu\beta\beta$ in a detector with 5% energy resolution. Figures from [99, 100].

Neutrinoless double-beta decay searches which contain no signal for $0\nu\beta\beta$ generally present results as a final limit on the half-life of the process, written as $T^{1/2}_{0\nu}$. Since $0\nu\beta\beta$ detectors operate for a finite amount of time, they only have a limited sensitivity to observing some number of $0\nu\beta\beta$ decays above background. As such, null results can be used to give a lower bound on the half-life of the $0\nu\beta\beta$ process. Given the $0\nu\beta\beta$ decay diagram shown in 2.16, Fermi's golden rule for particle decay can be used to model the half-life as

$$(T^{0\nu}_{1/2})^{-1} = G^{0\nu}|M^{0\nu}|^2|\frac{\langle m_{\beta\beta}\rangle}{m_e}|^2 \, , \tag{2.28}$$

where $G_{0\nu}$ is a directly calculable phase space factor, $M_{0\nu}$ is the model-dependent nuclear matrix element, and $\langle m_{\beta\beta}\rangle$ is the effective Majorana neutrino mass, given by

$$\langle m_{\beta\beta}\rangle = |\sum_i U_{ei}^2 m_i|^2 \,, \tag{2.29}$$

where $U_{e1} = \cos\theta_{12}\cos\theta_{13}e^{i\alpha_1}$, $U_{e2} = \sin\theta_{12}\cos\theta_{13}e^{i\alpha_2}$, and $U_{e3} = \sin\theta_{13}$.

Given the effective mass' dependence on the neutrino oscillation parameters, absolute neutrino masses, and unknown Majorana phases, the allowed effective mass parameter space is different for the normal or inverted neutrino mass hierarchy. The allowed parameter space for $\langle m_{\beta\beta}\rangle$ as a function of the lightest neutrino mass given the current uncertainties of the oscillation parameters is shown in figure 2.17. Several leading limits on the effective mass, calculated from the $T_{0\nu}^{1/2}$ measurement, are also shown [99].

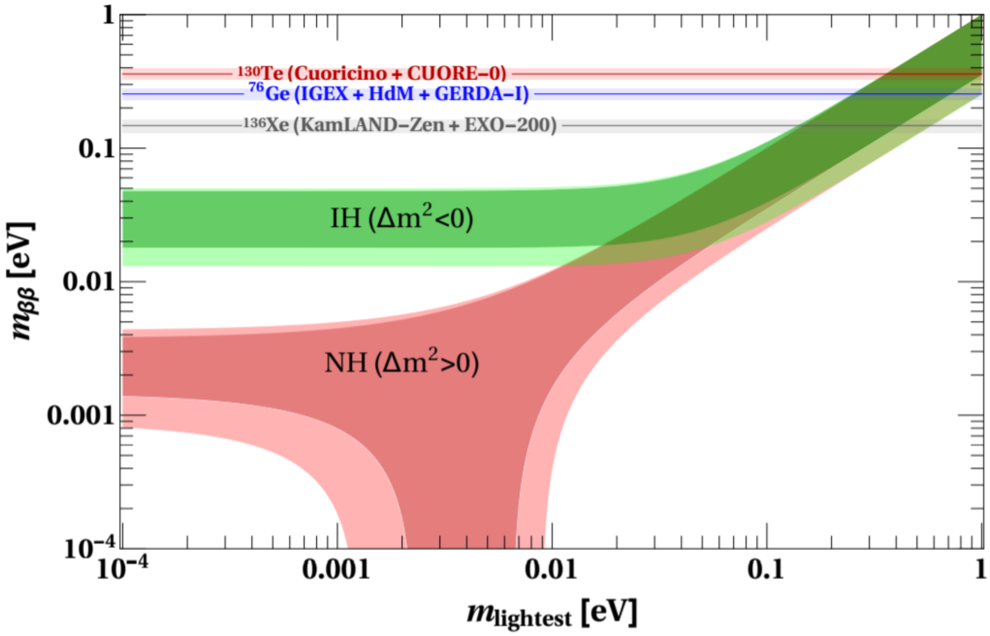

Figure 2.17. Range of allowed effective Majorana mass values given the current uncertainties in the neutrino oscillation parameters. Due to the effective Majorana mass' dependence on the absolute neutrino masses, the allowed phase space is different for the inverted and normal mass hierarchy. Horizontal bands on reported measurements are primarily due to the nuclear matrix element uncertainties and the allowed Majorana phase parameter space. Taken from [99].

Although no signal has been measured with discovery significance, many experiments have, are currently, and will continue the search for $0\nu\beta\beta$. Various detector types utilizing different double-beta decay isotopes have been deployed. The primary considerations for isotope and detector design choices include cost of detector and isotope production, potential to increase isotope loading, and energy endpoint of the double-beta decay spectrum.

## 2.4 Absolute neutrino masses

The absolute neutrino mass scale is also still an open question. Although neutrino oscillation measurements provide the squared mass *differences*, they cannot provide information regarding the absolute scale of the three masses $m_1$, $m_2$, and $m_3$. Fortunately, a combination of precise mass-squared difference measurements, knowledge of the neutrino mass hierarchy, and an additional measurement providing the absolute neutrino mass scale would provide the information needed to determine the neutrino mass values.

### 2.4.1 Beta spectrum endpoint measurements

One approach to acquiring the absolute mass scale is through the measurement of the effective electron neutrino mass. The most sensitive experiments to-date utilize a beta spectrometer to measure the beta energy spectrum from tritium decays. The decay process is written as follows:

$$^3H \rightarrow {}^3He + e^- + \bar{\nu}_e \; . \tag{2.30}$$

Given that the decay's energy release $Q$ is

$$Q = [m_{^3H} - m_{^3He} - m_e - m_{\nu_e}]c^2 \; , \tag{2.31}$$

the endpoint of the beta energy spectrum (i.e. where $KE_e = Q$) is directly relatable to the effective electron neutrino mass. The difference expected in the tritium beta spectrum endpoint given $m_{\nu_e} = 0$ and $m_{\nu_e} = 1$ eV is shown in figure 2.18. Given that $\nu_e = \sum_i U_{ei}\nu_i$ within the neutrino oscillation model, a measurement of the effective electron neutrino mass can then be related to the absolute neutrino masses via the relation

$$m_{\nu_e} = \sqrt{\sum_{i=1}^{3} |U_{ei}|^2 m_i^2} \; . \tag{2.32}$$

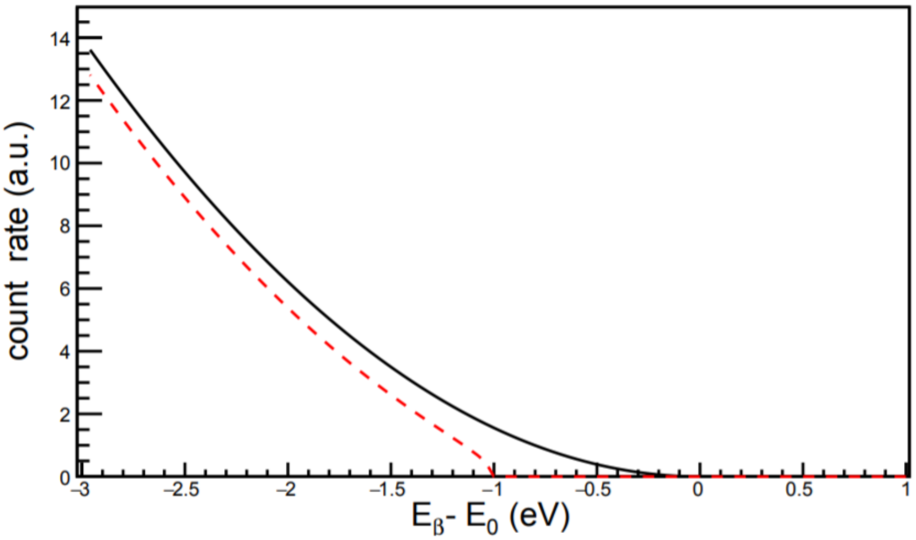

Figure 2.18. Difference in the electron kinetic energy probability distribution ($E_\beta$) and total decay energy ($E_o$) for tritium if the effective neutrino mass is $m_{\nu_e} = 0\, eV$ (black) and $m_{\nu_e} = 1\, eV$ (red). Figure from [101].

The current world-leading limit is set by the Karlsruhe Tritium Neutrino (KATRIN) experiment, who presented results at 2019 Topics in Astroparticle and Underground Physics. The KATRIN data shown in figure 2.19 limits the effective electron neutrino mass to $m_{\nu_e} < 1.1\, eV/c^2$ , $90\%\, CL$ [102]. The most sensitive measurement prior to KATRIN was performed by the Troitsk neutrino mass experiment, which set an upper limit of $m_{\nu_e} < 2.05\, eV/c^2$ , $95\%\, CL$ [103, 104].

### 2.4.2 Perturbations in CMB power spectrum

Measurements of the Cosmic Microwave Background (CMB) are also a path towards determining the absolute neutrino mass scale. Cosmological models predict the presence of relic neutrinos pervading the universe following the Big Bang. This Cosmic Neutrino Background (C$\nu$B) is composed of neutrinos that free-streamed following decoupling from other matter in the early universe. The total mass and number of active neutrino flavors in the C$\nu$B has a direct influence on the easily observed CMB power spectrum, and the neutrino mass can be constrained with fits to the spectrum. Recent limits set with Planck data constrain the total neutrino mass to $\sum_i^3 \nu_i < 0.14\, eV$ [105]. An in-depth review of the C$\nu$B's impact on the early universe and neutrino mass fits via cosmological data is available at [106].

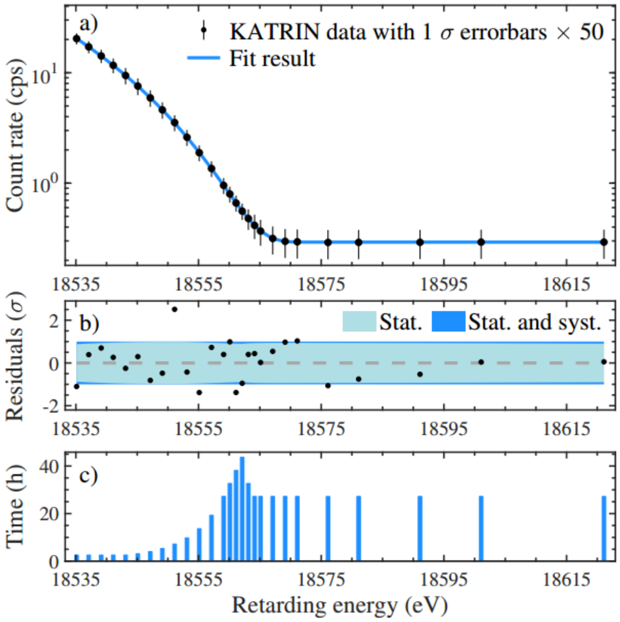

Figure 2.19. Tritium beta decay rates at specific electron emission energies selected by tuning an electrostatic potential's retarding energy $R(qU)$. The data yield the KATRIN limit of $m_{\nu_e} < 1.1\, eV/c^2$ , $90\%\, CL$ presented at TAUP 2019. The top panel shows the data relative to the best-fit model, the middle shows the data-MC residual, and the bottom shows the amount of time each data set was measured at. Figure from [102].

## 2.5 Sterile neutrinos

The search for the existence of a sterile neutrino flavor, a neutrino that does not interact via the weak force, is actively ongoing. If the sterile neutrino does exist, sterile neutrino production would have to proceed through physics beyond the Standard Model. One possible production mechanism would be through oscillations from Standard Model neutrino flavors to a sterile neutrino flavor (often referred to as the 3+1 scenario). A sterile neutrino flavor signal would manifest as a measurable deviation from the oscillation probabilities observed in the three-flavor scenario. Note that the presence of sterile neutrino oscillations would violate hypercharge, as sterile neutrinos have zero hypercharge and no color [107].

There are two sterile neutrino mass-scales of particular interest with current neutrino and cosmological observations: sterile neutrino flavors with $O(\Delta m^2 \sim eV^2)$ or $O(\Delta m^2 \sim keV^2)$ relative to the mass scale of the three active flavors. The $keV^2$-scale mass splitting is of significance as a possible warm dark matter candidate, while the $eV^2$-scale mass splitting could explain deficits in rates observed in short-baseline neutrino observations [107, 108]. For the $keV^2$-scale sterile neutrino state, direct detection is possible if the sterile neutrino does have some beyond Standard Model weak interaction that results in inelastic scatters with electrons or nuclei; given the expected low interaction rates, the low background environment in dark matter detectors are an ideal setting to search for sterile neutrinos in this manner [109].

Emphasis will be placed on short-baseline neutrino observations at the $eV^2$-scale, as direct detection efforts at this scale proceed through neutrino oscillation measurements. To model the sterile neutrino in the oscillation framework, four neutrino mass states ($m_1, m_2, m_3, m_4$) and four flavors ($e, \mu, \tau, s$) are utilized. The additional sterile parameters lead to new mixing angles and mass-squared differences; these new terms provide the parameter space for modeling neutrino oscillation features inconsistent with the three-flavor neutrino model.

The search for $O(\Delta m^2 \sim eV^2)$ sterile neutrinos became active following the observation of the "Gallium anomaly." Two Gallium-based solar neutrino experiments, GALLEX and SAGE, which detected solar neutrinos through the process

$$\nu_e +^{71} Ga \rightarrow^{71} Ge + e^- \ , \tag{2.33}$$

deployed intense electron neutrino sources ($^{51}Cr$ and $^{37}Ar$) to calibrate detector responses to neutrino interactions [110, 111]. The best combined fit ratio of observed electron neutrino events to expected neutrino events for the two experiments was [112]

$$R^{Ga} = 0.86^{+0.05}_{-0.05} \ , \tag{2.34}$$

indicating a $2.8\sigma$ smaller observed signal than the prediction.

This anomaly triggered active searches for neutrino deficits in other short-baseline neutrino experiments. Sterile neutrino oscillation searches at the $eV^2$ mass difference scale are generally performed in the short baseline limit (SBL) $L \approx O(m)$ and $E \approx O(MeV)$ (or identically $L \approx O(km)$ and $E \approx O(GeV)$ )[113]. The first limit is achievable using detectors meters away from reactor cores, while the second is achievable with detectors within a kilometer of accelerator neutrino production sources. In these limits, both $\sin^2 \frac{\Delta m^2_{12} L}{4E_\nu} \ll 1$ and $\sin^2 \frac{\Delta m^2_{23} L}{4E_\nu} \ll 1$. Effectively, any neutrinos produced have not had enough time to oscillate much through three-flavor means; in the three-flavor model, this can be summarized as

$$P_{3\nu}^{SBL}(\nu_\alpha \to \nu_\alpha) \approx 1 \ ,$$

$$P_{3\nu}^{SBL}(\nu_\alpha \to \nu_\beta) \approx 0 \ .$$

However, if a fourth sterile neutrino is present and at a much larger mass difference than $\Delta m^2_{solar}$ and $\Delta m^2_{atm}$ (say $\Delta m^2_{ster} \approx 1\,eV^2$), then the oscillation probabilities in a four-flavor scenario are dominated by the sterile-related oscillation terms, written as

$$P^{SBL}(\nu_\alpha \to \nu_\alpha) \approx 1 - 4|U_{\alpha 4}|^2(1 - |U_{\alpha 4}|^2)\sin^2\left(\frac{\Delta m^2_{41} L}{4E_\nu}\right) \ , \tag{2.35}$$

$$P^{SBL}(\nu_\alpha \to \nu_\beta) \approx 4|U_{\alpha 4}|^2|U_{\beta 4}|^2\sin^2\left(\frac{\Delta m^2_{41} L}{4E_\nu}\right) \ . \tag{2.36}$$

As more short-baseline experiments utilized this model to search for sterile neutrino oscillations, the mystery deepend as new data either reinforced or refuted the Gallium anomaly. Experimental evidence from experiments supporting and ruling out sterile neutrino oscillations in both the reactor and accelerator SBL configurations are summarized below.

### 2.5.1 Reactor-based searches

Reactor-based sterile neutrino searches fit for deviations in the observed $\bar{\nu}_e$ flux from reactors at $O(m)$ baselines. The detectors are generally small (on the order of a meter or two in dimension), and are typically designed to efficiently detect reactor antineutrinos via inverse beta decay interactions. They are often movable using an elevator or rail system, so the detector can measure the reactor flux at several positions relative to the reactor core. By searching for oscillations in a comparison of datasets taken at various distances, many of the systematic uncertainties, of particular importance is the model of the reactor antineutrino flux itself, are greatly reduced. Recent prominent short-baseline sterile neutrino searches include the DANSS measurement and NEOS + Daya Bay measurement [114, 115]. Results from the PROSPECT are also expected in the near future [116].

The DANSS experiment provides the most recent published results of a short baseline sterile neutrino search [114]. The DANSS detector is a $1\,m^3$ detector, composed of 2500 meter-long scintillator strips covered with Gd-loaded reflectors. Each strip contains a wavelength-shifting optical fiber connected to a silicon photomultiplier (SiPM) for light detection. DANSS detects reactor antineutrinos via the IBD signal; the gadolinium-doped reflectors boost the detector's neutron detection efficiency, thanks to gadolinium's large thermal neutron capture cross section and $\sim 8\,MeV$ de-excitation energy following capture.

DANSS measured the $\bar{\nu}_e$ flux at three different positions relative to the core center (10.7 m, 11.7 m, and 12.7 m) and searched for sterile neutrino oscillation signatures in the ratio of the neutrino distributions. The ratio of the top and bottom event distributions, as well as the oscillation parameter exclusion regions from comparing data from all three positions, are shown in figure 2.20. The best fit in the $4\nu$ flavor scenario is $\sin^2\theta_{14} = 0.05$ and $\Delta m^2_{14} = 1.4\,eV^2$, while a large portion of parameter space is also excluded under the null hypothesis that there are only three flavors of neutrino.

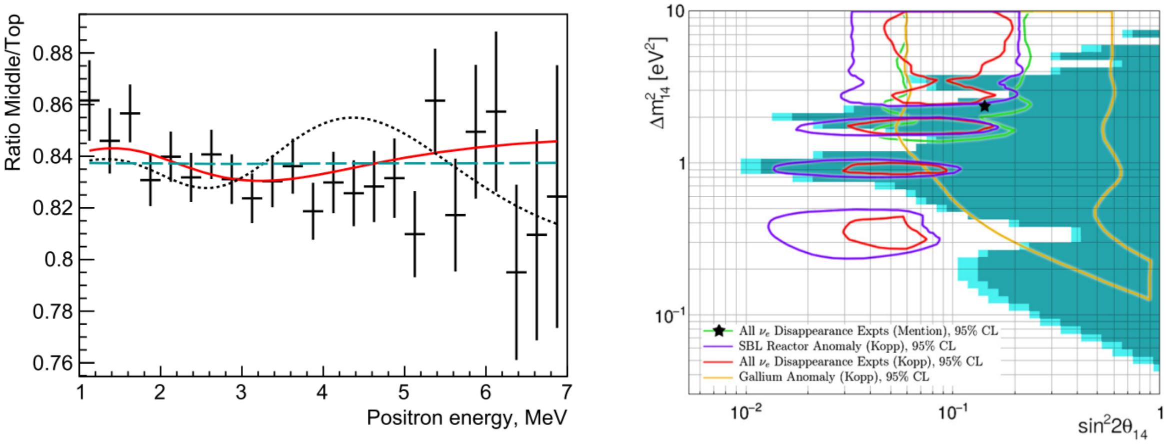

Figure 2.20. Left: Ratio of IBD rates for farthest to nearest position from the reactor core. The blue dashed curve shows the $3\nu$ prediction, the solid curve shows the best fit in the $4\nu$ scenario, and the dotted curve shows the best fit for the Reactor Antineutrino Anomaly (RAA) and Gallium Anomaly (GA) fit (starred in right). Right: Sterile oscillation parameter space excluded by the DANSS measurement at $90\%$ CL (cyan) and $95\%$ CL (blue). Allowed regions from a compilation of disappearance experiment results and the best fit from the RAA and GA are shown [117, 118]. Figures from [114].

### 2.5.2 Accelerator and atmospheric-based searches

Accelerator and atmospheric-based observations can search for sterile neutrino signals through both appearance ($\nu_\mu \rightarrow \nu_e$ or $\bar{\nu}_\mu \rightarrow \bar{\nu}_e$) and disappearance ($\nu_\mu$ or $\bar{\nu}_\mu$) measurements. While short-baseline reactor measurements are only sensitive to $\bar{\nu}_e$ interactions through the IBD process, neutrino detectors designed to reconstruct $O(GeV)$ interactions can be sensitive to $\mu$,$e$, or $\tau$-flavor charged-current interactions. This sensitivity to all flavors broadens the number of $U_{i4}$ components that can be measured in 2.35 and 2.36.

Interestingly, accelerator and neutrino-based measurements measuring the $\nu_\mu \rightarrow \nu_e$, $\bar{\nu}_\mu \rightarrow \bar{\nu}_e$ appearance and $\nu_\mu$ or $\bar{\nu}_\mu$ disappearance channels have conflicting results regarding sterile neutrino oscillations under a 4-flavor hypothesis. The LSND experiment was the first to provide indications of sterile neutrinos; the detector measured an excess of $87.9 \pm 22.4 \pm 6.0$ events in the $\bar{\nu}_e$ flux produced following the decay-at-rest of $\mu^+$ particles in the Los Alamos Neutron Science Center proton beam line [119]. The MiniBooNE experiment has also observed an excess of $\nu_e$ events at the Fermilab Booster Neutrino Beam (BNB) when operating in neutrino mode. The combined significance from the LSND and MiniBooNE results has a $6.0\sigma$ significance, with best fit to the sterile neutrino oscillation parameters in the 4-flavor hypothesis shown in figure 2.21 [120].

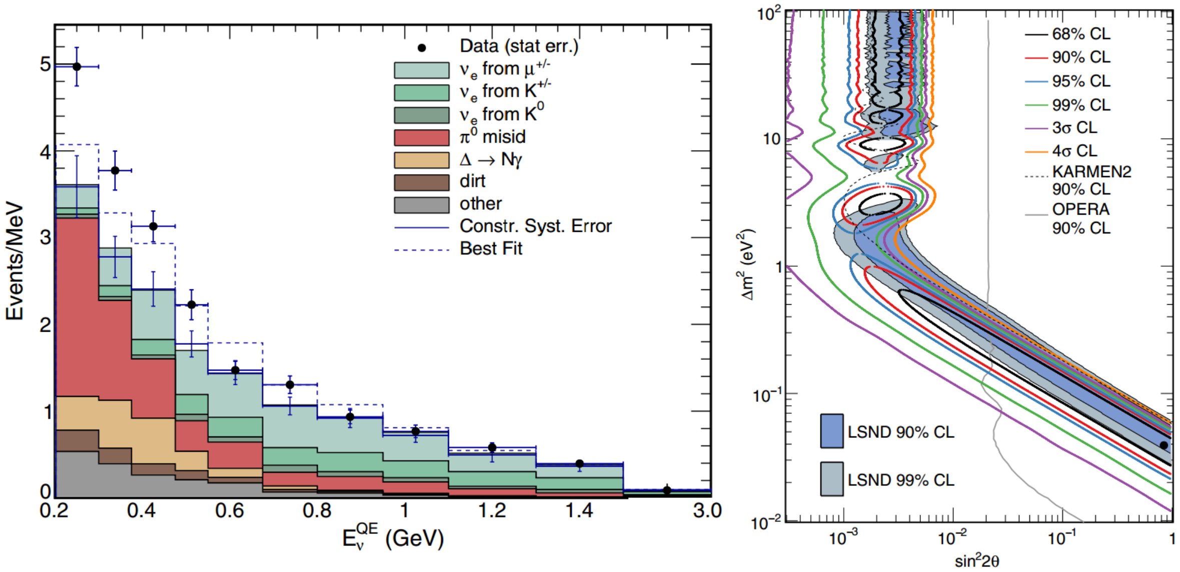

Figure 2.21. Left: Observed $\nu_e$ CCQE events in MiniBooNE (dots) with best background fit (histograms) for the neutrino mode dataset. Right: Allowed oscillation parameters under the 4-flavor hypothesis. Shaded regions show the allowed regions from LSND data. 90% CL exclusion limits from the KARMEN and OPERA experiments are shown. Figures from [120].

Of particular interest in figure 2.21 though is the best-fit parameters from LSND/MicroBooNE and the exclusion regions of KARMEN2 and OPERA. KARMEN and OPERA also searched for sterile neutrino oscillations in the $\nu_e$,$\bar{\nu}_e$ appearance channels; both exclude the best-fit region found with MicroBooNE's data fitted in the 4-flavor scenario at $90\% \, CL$ [121, 122]. Additional exclusions have been made by sterile oscillation searches in E776, NOMAD, and ICARUS, but do not conflict as blatantly with the MicroBooNE and LSND results. The disagreement observed in these experiments is currently unresolved.

The conflict in sterile neutrino oscillation measurements is exacerbated with a comparison of sterile neutrino searches in appearance and disappearance channels. A recent publication compares combined fits of accelerator-based appearance observations with short-baseline reactor, accelerator, and atmospheric disappearance observations. The disappearance observation includes results from short-baseline antineutrino disappearance measurements, atmospheric neutrino observations by IceCube, Super-Kamiokande, and DeepCore, as well as results from accelerator observations by NO$\nu$A, MiniBooNE, MINOS/MINOS+, and CDHS [113]. The combined fits are shown in figure 2.22.

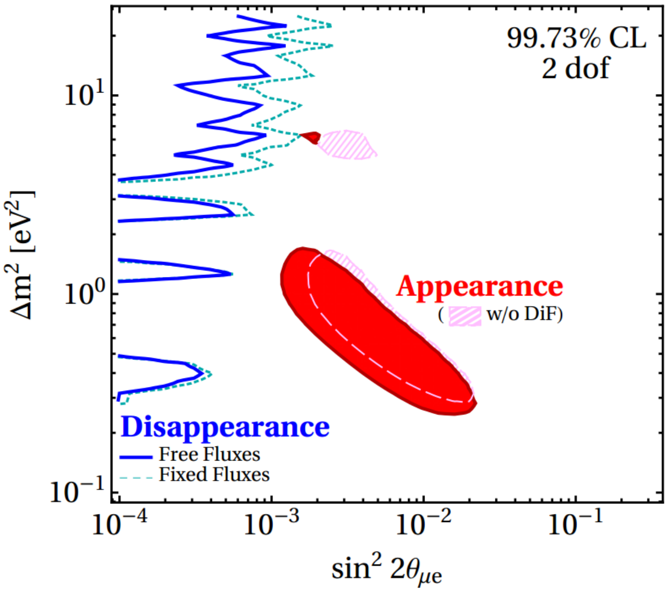

Figure 2.22. Sterile neutrino oscillation parameter space with a combination of appearance measurements (red) and the exclusion region from a combined analysis of disappearance measurements (blue) shown. Given that short-baseline reactor disappearance could be at least partially explained with an error in reactor flux modeling, exclusion regions are shown with reactor fluxes fixed (dotted blue) and free (solid blue) in the fit. Appearance fits with LSND's decay-at-rest neutrino measurement only (pink hatched) and decay-at-rest + decay-in-flight neutrino measurement (solid red) are also shown. Figure from [113].

The disagreement in sterile neutrino oscillation searches can be resolved in several ways.

Models of neutrino appearance and disappearance should be revalidated and improved in any ways possible to help resolve the current measurements. Additional data from both the appearance and disappearance channels could help determine where the discrepancy is as well. The ICARUS detector, the largest LArTPC detector ever built to-date (760 tons), has been moved from CERN to Fermilab's BNB line to make another measurement as part of Fermilab's Short-Baseline Neutrino program [123]. The Short-Baseline Near Detector (SBND), located just behind ANNIE in the BNB line, will also perform another sterile neutrino oscillation measurement in the coming years [124].

# Chapter 3

# GeV-scale neutrino interactions

Accurately detecting, reconstructing, and identifying GeV-scale neutrino interactions is a challenging process. Numerous neutrino-nucleon interactions are possible, neutrino-nucleon interactions must be modified to incorporate nucleus effects, and final-state interactions (FSIs) can occur within the nucleus following the neutrino's initial interaction. The intertwining of these effects is what makes successful event reconstruction and interaction identification so complex.

Why not steer clear and perform all neutrino experiments in the MeV-range? As seen in the previous chapter, the GeV-scale is debatably the most important neutrino energy regime for determining the neutrino mass hierarchy and $\delta_{CP}$ parameter. Additionally, there's rich physics to understand in the nuclear effects themselves. *How should neutrino-nucleon effects be modified to include nucleus effects? What kinds of interactions can happen in FSIs? How much do they differ for different nuclei?*

This chapter provides a crash course in the primary neutrino interactions at the GeV-scale. Neutrino-nucleon interactions are first covered, followed by the modifications needed to model neutrino-nucleon interactions inside a nucleus. A discussion on the modeling of FSIs via Monte Carlo approaches concludes the chapter.

## 3.1 GeV-scale neutrino-nucleon interactions

Prior to discussing neutrino interactions with nucleons, it is worth reviewing a simpler interaction with similar traits. Consider one of the simplest cases of neutrino charged-current interactions at the GeV scale: charged-current electron scattering, represented with

$$\nu_l + e^- \rightarrow l^- + \nu_e \; (l = e, \mu \, or \, \tau) \; . \tag{3.1}$$

In the limit where the total interaction energy transfer $Q^2$ is much less than the Z and W-boson masses ($Q^2 \ll M^2_{W,Z}$), the total cross section can be calculated from Fermi's golden rule at tree-level as approximately [125]

$$\sigma_{TOT} \approxeq \frac{2m_e G_F^2 E_\nu}{\pi} = \frac{G_F^2 s}{\pi} \; . \tag{3.2}$$

The key feature to note here is that the total cross section approximately increases linearly as the neutrino energy increases. Here lies yet another reason to perform GeV-scale neutrino experiments; more statistics are accumulated for GeV-scale neutrino sources than MeV-scale sources.

The total neutrino-nucleon interaction cross section shares the same general shape as in equation 3.2 with some modifications. The linear increase of the total neutrino-nucleon cross section is clearly visible in figure 3.1, but also has features deviating from this. The non-linearity of the $\sigma_{TOT}/E_\nu$ is primarily due to the presence of multiple types of interactions that contribute to the total cross section differently at different energies.

The primary contributions to the total neutrino cross section are charged-current quasielastic (CCQE) interactions, resonant interactions, and deep inelastic scattering. As the neutrino energy transfer increases, the final state of the interaction tends to get more complicated and more populated with particles; in turn, the interactions tend to get more challenging to reconstruct. A closer look at each of the dominant neutrino-nucleon interaction modes is warranted.

### 3.1.1 Charged-Current Quasielastic Scattering (CCQE)

Charged-current quasielastic (CCQE) scattering is one of the most valuable interaction types for neutrino experiments performed at the $O(GeV)$ energy scale. When possible, data analyses will often focus their event selection on accepting CCQE interactions and rejecting all others. The primary reasons for this are relatively straightforward event identification, higher efficiency for successful event reconstruction, and low uncertainties on the cross section.

When a CCQE interaction occurs, the neutrino or antineutrino incident on the nucleus will interact with a single nucleon:

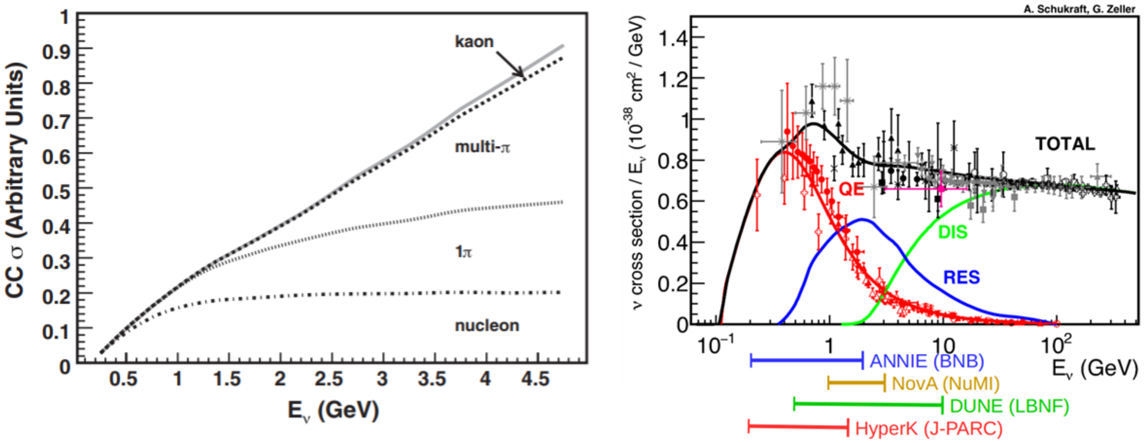

Figure 3.1. Left: Total neutrino-nucleon interaction cross section at $O(GeV)$. The cross-section contributions to the final-state particles are shown. Figure from [125]. Right: Total neutrino cross section in the GeV scale divided by neutrino energy, with the best fit of different interaction types overlaid. Several experiments and their sensitive energy range are shown below. Original figure from [125] .

$$\nu_l + n \to l^- + p \;, \tag{3.3}$$

$$\overline{\nu_l} + p \to l^+ + n \;. \tag{3.4}$$

For true CCQE events, the final state lepton and nucleon will leave the nucleus with no further interaction, and reconstructing the vertex position and neutrino energy with kinematics is straightforward. Detectors sensitive to protons, such as liquid argon time-projection chambers (LArTPCs), can use the proton and lepton signal from $\nu_l$ CCQE interactions to very accurately reconstruct the neutrino energy using conservation of momentum.

The most predominant model used to calculate the CCQE cross section is the Llewellyn-Smith model [126]. Many CCQE interaction models in the neutrino-nucleus context use this model as a starting point and expand to incorporate nucleus effects. For more details on how the neutrino interaction cross section is formulated for neutrino-nucleon interactions at tree level, see Appendix B.4.

### 3.1.2 Δ resonance

In baryonic resonance, a neutrino's interaction excites the nucleon into a higher mass baryon. In the Standard Model, different baryonic resonances are modeled as different excitation levels of the 3-quark systems composing protons and neutrons. These excited baryonic states have a very short lifetime (for example, a $\Delta(1232)$ resonance has a lifetime of $5.6 \times 10^{-24}$ seconds [15]), with de-excitations typically proceeding through the production of lighter hadrons such as the pion.

At the energy scales of ANNIE and T2K's neutrino beams, the $\Delta(1232)$ resonance is the most common baryonic resonance. The $\Delta(1232)$ decays via $\Delta \rightarrow N\pi$ with a branching ratio of $99.4\%$ [15]. These charged-current resonance interactions have final state particles of the forms:

$$\nu_l + p \rightarrow l^- + \Delta^{++} \rightarrow l^- + p + \pi^+ \tag{3.5}$$

$$\nu_l + n \rightarrow l^- + \Delta^{+} \rightarrow l^- + p + \pi^0 \tag{3.6}$$

$$\nu_l + n \rightarrow l^- + \Delta^{+} \rightarrow l^- + n + \pi^+ \tag{3.7}$$

$$\overline{\nu_l} + p \rightarrow l^+ + \Delta^{0} \rightarrow l^+ + p + \pi^- \tag{3.8}$$

$$\overline{\nu_l} + p \rightarrow l^+ + \Delta^{0} \rightarrow l^+ + n + \pi^0 \tag{3.9}$$

$$\overline{\nu_l} + n \rightarrow l^+ + \Delta^{-} \rightarrow l^+ + n + \pi^- \tag{3.10}$$

$$\tag{3.11}$$

Analysis of GeV-scale neutrino interactions will often use the pion's presence in the final state to separate baryonic resonance interactions from CCQE interactions.

The Rein-Sehgal model was one of the first to accurately model baryonic resonance and the relevant cross sections [127]. The Rein-Sehgal model first derives the cross section for baryonic resonance in terms of general nuclear matrix elements, and then utilizes the Feynman-Kislinger-Ravndal (FKR) model of the nucleus as quarks in a four-dimensional harmonic oscillator to calculate the matrix elements [128]. The Rein-Sehgal model was first validated by comparing the model's prediction of the cross section for $\Delta^{++}(1234)$ production to that measured by experiments at Argonne National Lab, Fermilab National Accelerator Laboratory, and CERN [129, 130, 131]. The model shows good agreement with data, as seen in figure 3.2.

### 3.1.3 Deep Inelastic Scattering (DIS)

Deep inelastic scattering (DIS) refers to high-energy neutrino scattering on an individual quark within a target nucleon. As seen in figure 3.1, this process becomes the dominant interaction type

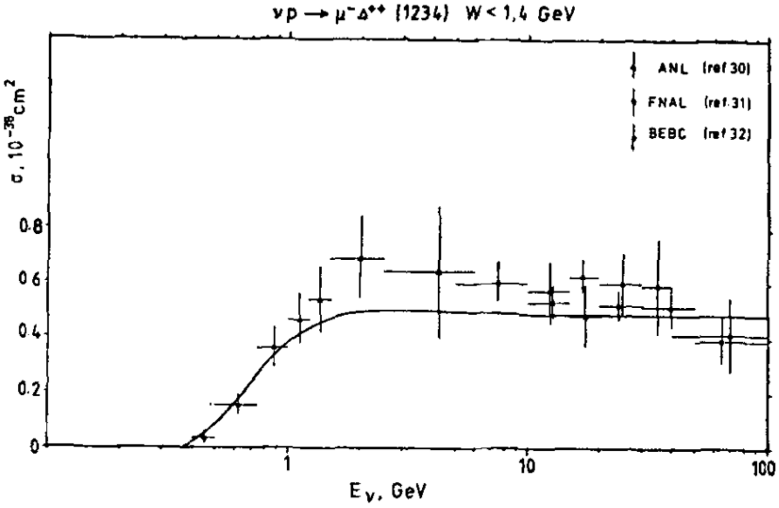

Figure 3.2. Calculated cross section of $\Delta^{++}$ resonance in neutrino-nucleon interactions using the Rein-Sehgal model. The theoretical cross section is in reasonable agreement with baryonic resonance observation from experiments utilizing hydrogen-based targets. Original data taken from [127].

at $E_\nu \approxeq 1\,GeV$. As the neutrino energy increases, more energy can be imparted to the interaction quark and provide the energy necessary to create hadronic showers. The DIS interaction at tree level is shown in figure 3.3.

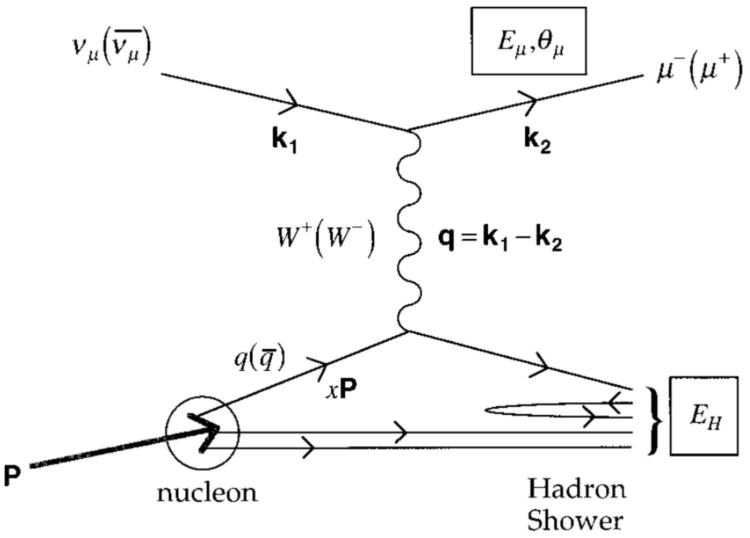

Figure 3.3. Feynman diagram of a neutrino deep inelastic scattering event at tree level. Figure from [132].

Given the vast phase space of particle production and momenta possible in DIS interactions,

| Invariants | General form | In lab frame |
|---|---|---|
| $\nu$ (energy transfer) | $(p \cdot q)/M$ | $E_H$ |
| $y$ (inelasticity param.) | $(p \cdot q)/(p \cdot k_1)$ | $E_H/(E_H + E_\mu)$ |
| $Q^2$ (neg. squared 4-momentum) | $-q^2$ | $(E_H + E_\mu)E_\mu\theta_\mu^2$ |
| $x$ (Bjorken scaling variable) | $Q^2/(2p \cdot q)$ | $\frac{(E_H+E_\mu)E_\mu\theta_\mu^2}{2ME_H}$ |
| $W^2$ (final state squared invariant mass) | $(p+q)^2$ | $M^2 + 2ME_H + Q^2$ |

Table 3.1. Common invariants used to express deep inelastic scattering cross sections. Expressions adapted to a table from [132].

DIS differential cross sections are typically represented using several interaction-invariant quantities associated with the hadronic vertex as a whole. These invariants are commonly used to simplify other cross-section representations as well, and are worth reviewing.

In the lab frame with a neutrino beam along the z-axis, the kinematic variables of different vertices in figure 3.3 are given in natural units $\hbar = c = 1$ by:

- $k_1 = (E_\nu, 0, 0, E_\nu)$
- $k_2 = (E_\mu, E_\mu \sin\theta_\mu \cos\phi_\mu), E_\mu \sin\theta_\mu \sin\phi_\mu, E_\mu \cos\theta_\mu$
- $p = (M, 0, 0, 0)$
- $q = k_1 - k_2$
- $E_\nu = E_\mu + E_H$

and the common invariant quantities used to characterize DIS cross sections are shown in table 3.1.3. The nuclear structure functions used to generalize the DIS cross section to nucleus targets are also described in terms of the invariants as well [133].

A recently published PhD thesis from the MINERVA collaboration shows the scale of the DIS cross section. The MINERVA detector at Fermilab uses a neutrino interaction volume composed of several layers of carbon, iron, and lead sandwiched between hydrocarbon scintillator detectors. The best fit of the DIS cross section using neutrino interactions originating from hydrocarbon-based and lead-based regions are shown in figure 3.4. It's interesting to note that the difference between the hydrocarbon and lead, which have considerably different size nuclei, is relatively small [134].

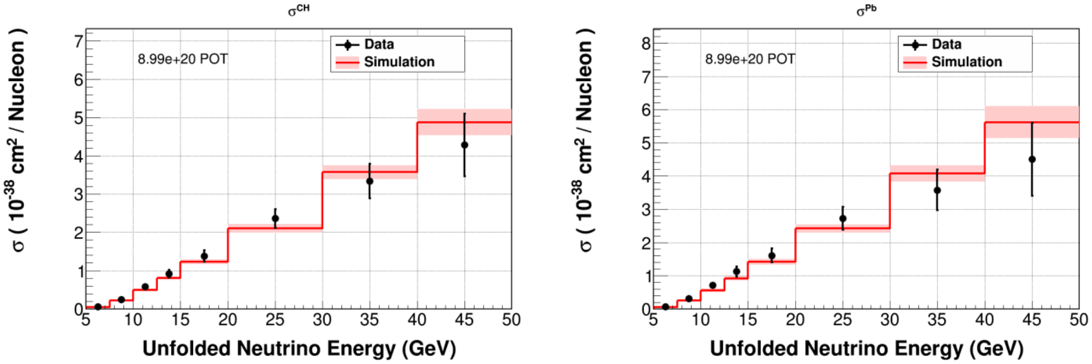

Figure 3.4. Best fit to the neutrino DIS cross section for interactions on hydrocarbon (left) and lead (right). The cross section approximately scales linearly with the reconstructed neutrino energy. Figures taken from [134].

#### 3.1.3.1 Neutral current scattering

Neutral current scattering is a subdominant contribution to the total cross section, but will be reviewed briefly. For a neutral current scatter of the form

$$\nu + N \to \nu + N \ , \tag{3.12}$$

where $N$ is the target nucleus, notice that no lepton is produced. Without an outgoing charged lepton, there is no prompt visible energy signal in the detection medium to reconstruct neutral current neutrino interactions. As such, neutral current interactions are primarily detected in the following manners:

- Additional FSIs within the nucleus could produce charged hadrons. An interaction with no charged lepton and FSI activity could indicate a neutral current interaction.
- If the $N$ nucleus is left an excited state after the interaction, de-excitation gammas could be produced. An interaction with no charged lepton but de-excitation gamma signals could indicate a neutral current interaction.

In general, most detectors have a relatively low sensitivity to neutral-current interactions.

The neutral-current differential cross section is modeled similarly to the charged-current case, but is only mediated by the $Z$ boson when applying the Feynman diagrams/rules. Ultimately, the neutral current cross section is described by a modified form of the Llewellyn-Smith model; however, more neutral current cross-section measurements would be useful to validate this model, as seen in figure 3.5.

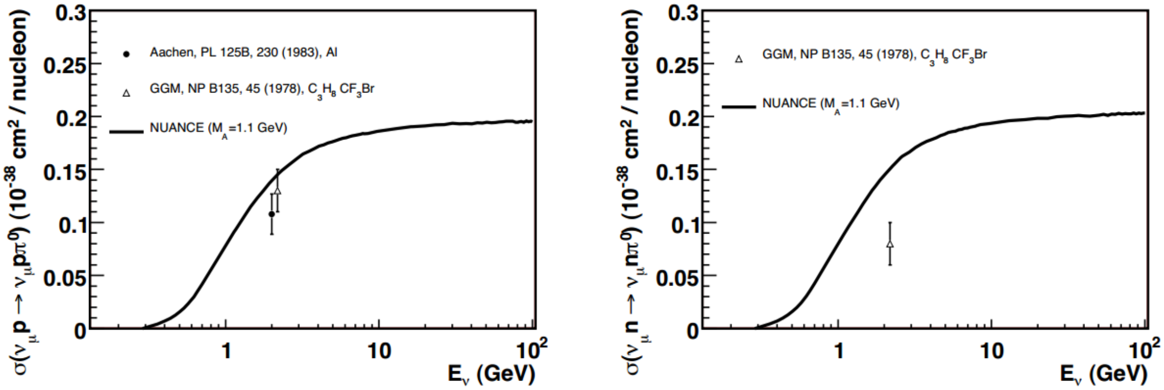

Figure 3.5. Current cross-section measurements of the $\nu_\mu p \rightarrow \nu_\mu p \pi^0$ (left) and $\nu_\mu n \rightarrow \nu_\mu n \pi^0$ (right) interactions. The neutral-current cross-section model from the NUANCE package is overlaid for reference [135]. Figures taken from [125].

## 3.2 From neutrino-nucleon to neutrino-nucleus interactions

With the surge in precise GeV-scale neutrino interaction data in the past several decades, consideration of the nucleus has become pivotal to accurately modeling neutrino interaction cross sections. When a neutrino interacts with a nucleon inside a nucleus, interactions with correlated pairs of nucleons (np-nh reactions) become possible. Mesons produced in neutrino-nucleon interactions can also mediate multinucleon interactions. FSIs also become possible in the context of a nucleus and detection medium filled with nuclei. The cross sections for these multinucleon effects also vary with the nucleus that a neutrino interacts with, as different nuclei have different nuclear excitation levels.

Given its complexity and demand, the development of models for neutrino-nucleus scattering and FSIs is an active and growing field. There are a zoo of nuclear models available [136], and application of the models is generally handled by simulation packages. Some of the most commonly-used event generators include GENIE, NuWro, and NEUT [137, 138, 139].

When constructing a neutrino-nucleus interaction model, most share a common neutrino-nucleon interaction starting point and diverge in how they incorporate effects from the nuclear medium. To give a picture of how these models are developed and validated, the relativistic Fermi Gas model and the Response Function formalism with Random Phase Approximation corrections are discussed below.

### 3.2.1 Neutrino-nucleus cross section formalism

A general framework for describing neutrino interactions with a many-body nucleus proceeds as follows [140]. Consider the charged-current interaction between a neutrino $\nu_l$ and nucleus $A$ producing a final nuclear state $X$, written as

$$\nu_l + A \to l^- + X \ , \tag{3.13}$$

If the neutrino carries an initial four-momentum $k \equiv (E, \mathbf{k})$ and scatters off a nuclear target to a lepton state $k' \equiv (E_l, \mathbf{k}')$, the differential cross section in the lab frame takes on the general form

$$\frac{d\sigma}{d\Omega_l dE_l} = \frac{G_F \cos\theta_C}{32\pi^2} \frac{|\mathbf{k}'|}{|\mathbf{k}|} L_{\mu\nu} W^{\mu\nu} \ , \tag{3.14}$$

where $G_F$ is the weak Fermi coupling constant and $\cos\theta_C$ is the Cabbibo angle. The $L_{\mu\nu}$ and $W^{\mu\nu}$ tensors contain the effects related to the lepton and nucleus structure, respectively, and are written as [141, 140]

$$L_{\mu\nu} = Tr\{\gamma_\mu (1+\gamma_5) \not{k} \gamma_\nu (1+\gamma_5) \not{k}'\} \ , \tag{3.15}$$

$$W^{\mu\nu} = \sum_X \langle 0| J^\mu |X\rangle \langle X| J^\nu |0\rangle \, \delta^{(4)}(p_0 + q - p_x) \ , \tag{3.16}$$

Where $\not{k} = \gamma^\alpha k_\alpha$, $|0\rangle$ and $|X\rangle$ represent the initial and final wavestates of the final nuclear state $X$, respectively, $J^\nu$ is the total nuclear current, and $q = k - k'$. This $W^{\mu\nu}$ tensor can also be decomposed into six real structure functions $W_i(Q^2), i = 1, ..., 6$. This cross-section formulation in the case where $A \to n$ and $X \to p$ produces the Llewellyn-Smith model cross section introduced in equation B.18 [142].

From this point, the derivation of the neutrino-nucleus cross section deviates based on whatever nuclear model is used to describe the nucleus' initial state and possible final state. In general though, each model takes the $W^{\mu\nu}$ nucleon tensor and upgrades it to a *nuclear* tensor $T^{\mu\nu}$ in whatever fashion the model uses to incorporate nucleus effects. The cross sections in the Relativistic Fermi Gas (RFG) model and a more general framework utilizing the Random Phase Approximation (RPA) are discussed below.

### 3.2.2 The Relativistic Fermi Gas (RFG) model

The Fermi gas model is the simplest of the nuclear models, but is applicable to a large range of nuclei and neutrino energies. In the simplest case, the protons and neutrons are treated as residing in a square potential well with constant potential within the well where different nuclei have different potential well heights. Note that the protons and neutrons are identifiable from each other, but individual protons and neutrons cannot be distinguished from each other. Most currently applied RFG models are variants of the relativistic Fermi gas model developed by Smith and Moniz [141].

In the RFG model, the nucleon tensor $W^{\mu\nu}$ defined in terms of structure functions $W_i(Q^2)$ are upgraded to a nuclear tensor in terms of nuclear structure functions [142]

$$W^{\mu\nu} \rightarrow T^{\mu\nu} = \int d\mathbf{p} f(\mathbf{p},\mathbf{q}) W^{\mu\nu}(p,q) \ , \tag{3.17}$$

where $p$ is the initial nucleon state's 4-momentum, $q = k - k'$, and $f(\mathbf{p},\mathbf{q})$ applies corrections related to the Fermi motion of nucleons in the nucleus. $f(\mathbf{p},\mathbf{q})$ is related to the momenta of the individual nucleons in the following manner:

$$f(\mathbf{p},\mathbf{q}) = \frac{1}{v_{rel}} \bar{n_i}(\mathbf{p}) \left[1 - n_f(\mathbf{p}+\mathbf{q})\right] \ , \tag{3.18}$$

where $\bar{n_i}(\mathbf{p})$ is the Fermi momentum distribution of the target nucleons, and the $1 - n_f(\mathbf{p} + \mathbf{q})$ factor is known as the unoccupation probability and is a correction for the Pauli blocking of outgoing nucleons. The $v_{rel}$ is a relative velocity of incident particles given by $v_{rel} = |(kp)|/(E_\nu M_t)$ where $M_t$ is the target nucleus mass. The Fermi momentum distribution $\bar{n_i}(p)$ has the general form [143]

$$f(k) = \frac{1}{1 + \exp(\frac{k - k_F}{a})} \,, \tag{3.19}$$

where $k_F$ is the mean Fermi momentum for the nucleus and $a = kT$.

A fit to the CCQE cross section corrected with the Relativistic Fermi Gas model is shown in figure 3.6. The neutrino-nucleus model fits the data relatively well for lighter nuclei targets at $\sim 1\,GeV$ and heavier targets up to $O(100)\,GeV$.

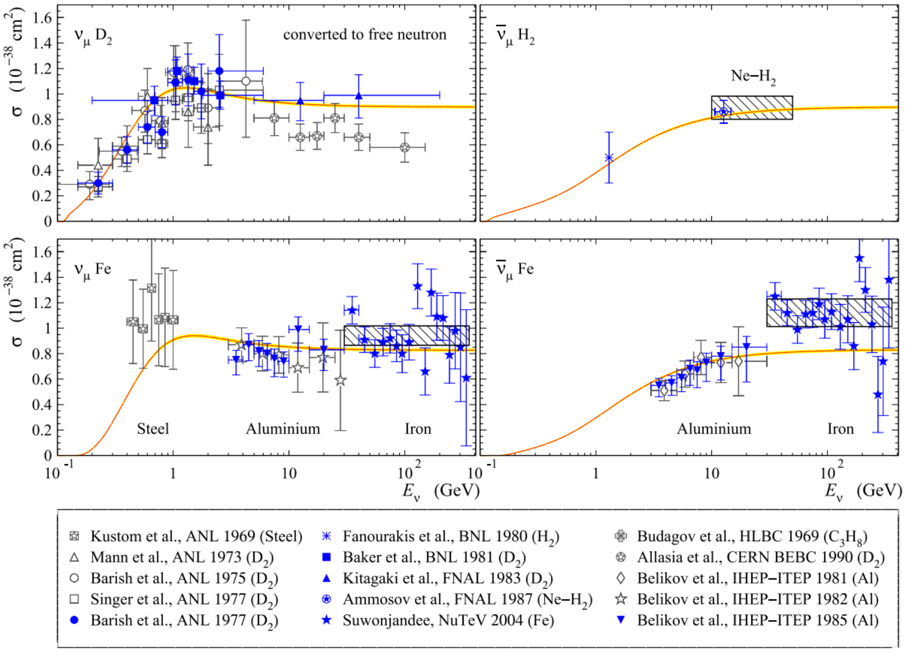

Figure 3.6. Left: Total $\nu_\mu$ and $\bar{\nu}_\mu$ CCQE cross sections measured by several experiments compared to the calculated CCQE cross section with RFG model corrections included. The solid red curve and shaded yellow band are calculated using an axial mass of $M_A = 0.999 \pm 0.011\,GeV$, the best fit from all measurements shown in blue. Gray points are excluded from the best fit of the axial mass. Original data taken from [142].

Although the RFG model replicates higher energy measurements of the CCQE cross section well, it results in poor fits to CCQE distributions for heavier nuclei at $< 1\,GeV$ . A publication by MiniBooNE finds disagreement between the RFG-predicted neutrino interaction counts in MiniBooNE (assuming the current best-fit axial mass $M_A$) and MiniBooNE data, as seen in figure 3.7 [144]. The RFG-predicted interaction distribution as a function of reconstructed $Q^2$ before tuning the axial mass (dotted line) and after tuning (solid line) are shown.

The disagreement of the RFG model with data can primarily be attributed to its lack of multi-

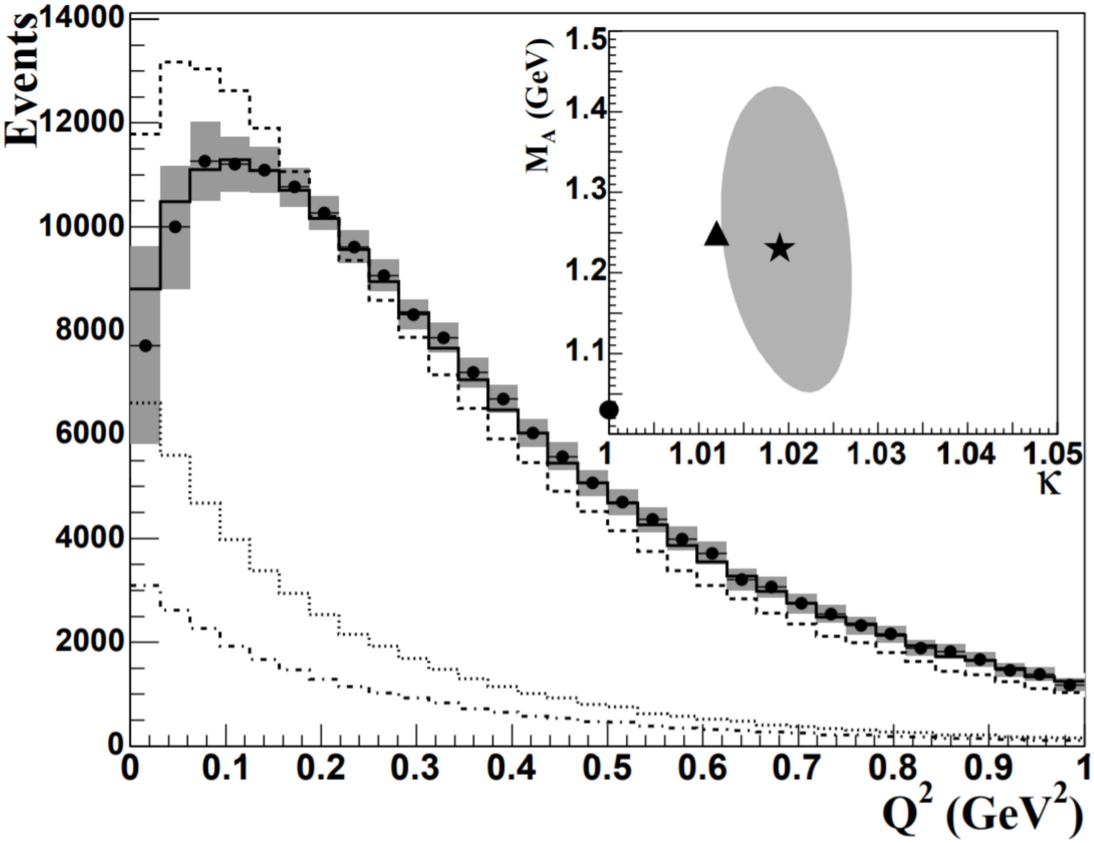

Figure 3.7. Best fit to MiniBooNE's reconstructed $Q^2$ for $\nu_\mu$ CCQE events using simulation data generated with the RFG model. The dotted line shows the simulation before fitting to the data, while the solid line shows after the fit. The inset shows the 68% CL contour for MicroBooNE's best fit axial mass $M_A$ before (star) and after (triangle) varying the backgrounds using the RFG model. The best-fit from MicroBooNE disagrees with the best-fit axial mass from other experiments (circle). Figure from [144].

nucleon interaction modeling and nucleon-nucleon correlations. Thus, either separate models of multinucleon cross sections and additional nuclear corrections are are needed to supplement the RFG cross section, or another neutrino-nucleus interaction model which generalizes to include multinucleon interactions is necessary.

### 3.2.3 Response function formalism with random phase approximation

General formulations of the nuclear tensor which utilize the Random Phase Approximation (RPA) are commonly referred to by the same name. In this generalized formalism, the $L_{\nu\mu}W^{\nu\mu}$ tensor is promoted to a sum of *response functions*, each corresponding to the amplitude of a particular type of interaction within the nucleus (1p1h, 2p2h, delta resonance, etc.). Response functions are evaluated by drawing Feynman diagrams of all processes that contribute to the neutrino's self-energy in the nucleus, cutting down the middle of the diagram, and taking only the imaginary part of the cut self-energy. Diagrammatically, the process is shown in figure 3.8.

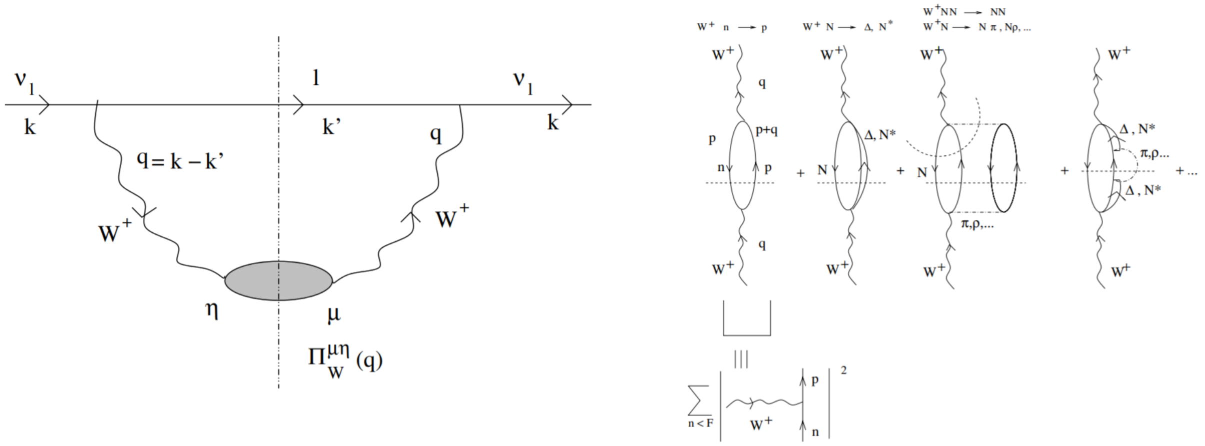

Figure 3.8. Left: Diagram of the neutrino's self-energy in nuclear matter. The $\Pi^{\mu\eta}_W(q)$ propagator is composed of all possible $W^+$-propagation diagrams inside the nucleus. Right: Several diagrams that can contribute to the $\Pi^{\mu\eta}_W(q)$ propagator on the left. The dotted lines represent where cuts are made to determine the final state of the interaction. Figures taken from [145].

This formalism is attractive because it allows for the incorporation of multi-nucleon interactions, as well as real and virtual meson exchange, but requires modifications to incorporate effects from the whole nucleus. Take for example the 1p1h term $W^+ n \to p$ in figure 3.8 on the right. To incorporate nuclear effects in the RPA, the 1p1h diagram is replaced by a sum of diagrams where nucleons interact via the Landau-Migdal potential. The detailed calculations for this model can be found in [145, 146, 147, 148, 149].

QE cross section predictions under the response function formalism with RPA corrections have better agreement with quasielastic measurements at $E_\nu < 1\,GeV$. Aside from agreeing with the MiniBooNE prediction of the total CCQE cross section, the model also accurately predicts cross section properties related to pion-producing interactions as well (see figure 3.9).

The improvements in the cross-section fit seen in figure 3.9 emphasize the importance of incorporating multinucleon interactions into cross-section models. In the MiniBooNE data, true CCQE interactions cannot be distinguished from np-nh interactions, mainly because identification of neutron knock-out is challenging. As such, the inclusion of np-nh into the interaction

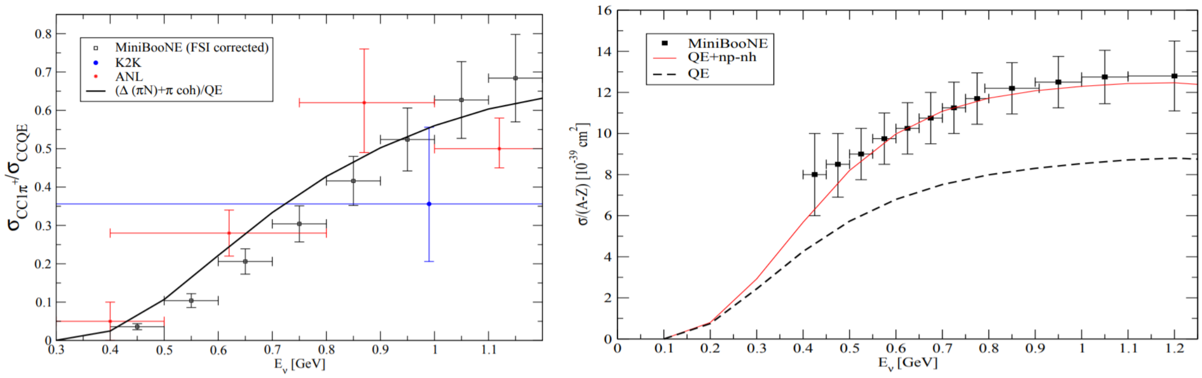

Figure 3.9. Left: Ratio of the total CC1$\pi$ cross section to the CCQE cross section as measured by several experiments, along with the calculated ratio using the response function formalism with RPA corrections. Right: Calculated cross section with np-nh corrections in the response function-RPA formalism compared to MiniBooNE data. Figures taken from [149].

model is necessary to correctly describe the data distribution.

### 3.2.4 Final State Interactions (FSIs)

Following the initial interaction inside a target nucleus, additional interactions with nucleons are possible as particles exit the nucleus. Interactions following the initial interaction are known as Final State Interactions (FSIs). Accurately modeling FSIs is key to producing an accurate model of any GeV-scale interactions, as the outgoing particles from an interaction can change drastically when FSIs occur.

The dominant contributors to the total FSI cross sections are:

- *Elastic scattering*: The nucleus is left in the ground state following the hadron's interaction, and the hadron remains the same charge.

- *Inelastic scattering*: The nucleus is left in an excited state or potentially undergoes breakup following an FSI.

- *Charge exchange*: The interacting particle changes charge in the interaction with a nucleon in the nucleus.

- *Pion absorption*: A pion is absorbed inside the nucleus. This interaction can lead to the ejection of one or multiple nucleons, and is often referred to as a "stuck pion" event.

- *Pion production*: Another pion is produced in the particle's interaction with a nucleon. For example, if the interacting particle is a pion, two pions would be observed outgoing from the nucleus.
- *Spallation*: A nucleon interacting with the nucleus knocks out several other nucleons. For example, the proton involved in the neutrino CCQE interaction can cause a spallation FSI and eject multiple protons/neutrons from the nucleus.

Although the response function formalism also has the ability to incorporate final state interactions to the cross-section model, Monte Carlo approaches that utilize well-measured cross sections of single nucleon interactions have seen success in modeling neutrino-nucleus FSIs.

#### 3.2.4.1 The IntraNuclear Cascade (INC) model

The most commonly used final state interaction model for post-neutrino interactions are the intranuclear cascade (INC) models [136]. INC models have rose to prominence primarily due to their success in accurately modeling pion-nucleon FSIs. When calculating the probability of an FSI's occurrence, the outbound particle is treated as if passing through a nucleus of mostly isolated neutrons and protons. The outgoing particle is moved step-by-step through the nucleus, with the probability of interaction being evaluated at each step. The mean free path $\lambda$ for the outgoing particle with energy $E$ and position $r$ in the nucleus is modeled as

$$\lambda(E,r) = \frac{1}{\sigma_{tot}(E)\rho(r)} \ , \tag{3.20}$$

where $\sigma_{tot}$ is the total cross section of possible interactions and $\rho(r)$ is the density of all nucleons within the nucleus. If the particle is found to interact at any step, the type of interaction that occurs is determined using the cross sections of each interaction that composes $\sigma_{tot}(E)$. Most data used to model the total cross section come from hadron-nucleus and photon-nucleus scattering experiments.

The GENIE simulation package, the neutrino-nucleus interaction simulation package primarily used at Fermilab and in ANNIE, has recently incorporated an INC model known as the hN model. In GENIE, densities of lighter nuclei (with nucleon count $A < 20$) are treated as Gaussians or modified Gaussians, while heavier nuclei are given the Woods-Saxon shape:

$$\rho(r) = N_0 \frac{1}{1 + e^{(r-c)/z}} \ , \tag{3.21}$$

where $N_0$ is a normalization factor, $c$ describes the approximate nuclear radius ($c \approx 1.2\, fm * A^{1/3}$) and $z$ describes the "surface thickness" of the nucleus [137].

# Chapter 4

# Final state neutrons following neutrino CC events

The study of the neutron multiplicity following neutrino interactions is critical to improving future GeV-scale neutrino measurements. Experimental efforts to measure neutron multiplicity will spearhead research and development efforts that ultimately improve neutron tagging techniques needed to separate quasielastic and inelastic neutrino interactions. Additionally, precision multiplicity measurements can help refine models of nuclear effects in neutrino interactions, which are necessary for validating and improving both np-nh and FSI cross sections.

The following chapter reviews energy reconstruction in CCQE interactions, and how the misidentification of non-CCQE events can produce biases in an analysis. The importance of neutron tagging as a tool for identifying non-CCQE events is then discussed in the context of several measurements, including cross-section measurements, proton decay, and the DSNB. The chapter closes with a discussion of the most recent neutron multiplicity measurements and how additional neutron multiplicity measurements by a detector like ANNIE (described in detail in chapter 5 would complement measurements already made.

## 4.1 CCQE event reconstruction

Given a known incident neutrino direction, the neutrino's incident energy in a CCQE interaction can be approximated through the lepton's reconstructed energy and direction alone. This is pivotal in accelerator neutrino experiments that must measure both neutrino and antineutrino CCQE interactions. For example, LArTPC detectors are sensitive to protons emitted from $\nu_l$-CCQE events and gadolinium-doped water Cherenkov detectors are sensitive to neutrons emitted from $\bar{\nu}_l$-CCQE events; however, neither are sensitive to both nucleon types. Thus, any measurements in either detector type using both the neutrino and antineutrino channel will need to perform event reconstruction without nucleon information.

Without proton/neutron information, the antineutrino/neutrino's energy in CCQE interactions can be approximately reconstructed using the following [150]:

$$E_{\nu_l,rec} = \frac{ME_l - \frac{m_l^2}{2}}{M - E_l + |\vec{p_l}|cos\theta_l} \ , \tag{4.1}$$

where $M$ is the nucleon mass, $E_l$ is the outgoing lepton energy, $|\vec{p_l}|$ is the lepton momentum, and $\theta_l$ is the outgoing lepton angle relative to the initial neutrino direction. The uncertainties in this reconstructed energy originate primarily from nuclear effects such as the nuclear binding energy of the target nuclei, the nucleon's Fermi Momentum within the target nucleus, and the outgoing proton energy.

### 4.1.1 Biases in reconstruction of CCQE-like events

Equation 4.1 is only valid for true CCQE interactions, and any non-CCQE interactions identified as a CCQE event will have a misreconstructed energy. For example, if protons or neutrons produced in np-nh interactions or FSIs go undetected, the non-CCQE event can be mistagged as a CCQE event. These incorrectly identified events are known as "CCQE-like" interactions, and must be quantified in any analysis.

To demonstrate the impact and implications of non-CCQE mistagging and misreconstruction, consider the effects of multinucleon interactions (np-nh interactions) on the neutrino's reconstructed energy studied in [150]. Given the relation between lepton energy and reconstructed energy in 4.1, the probability distribution that a neutrino's true energy is $E_\nu$ given a reconstructed $E_{\nu,rec}$ can be estimated with

$$F(E_\nu, E_{\nu,rec}) = c\frac{\Phi(E_\nu)}{\int \Phi(E_\nu) dE_\nu} \int_{E_\nu^{min}}^{E_\nu^{max}} \left[\frac{d^2\sigma}{d\omega d\cos\theta}\right]_{\omega=E_\nu-E_\mu, \cos\theta=\cos\theta(E_\mu,E_{\nu,rec})} dE_\mu \ , \tag{4.2}$$

where $\omega$ is the true energy difference between the neutrino and lepton, $\Phi(E_\nu)$ is the neutrino energy flux distribution, $\cos\theta(E_\mu, E_{\nu,rec})$ is the angle calculated in 4.1 for given values $E_\mu and E_{\nu,rec}$, and $\sigma$ is the total cross section for the interaction in consideration. $c$ is a normalization constant, and is chosen as the inverse value of the total flux $c = (\int \Phi(E_\nu)dE_\nu)^{-1}$ to give $F$ units of cross section divide by energy squared [150]. In general, $F(E_\nu, E_{\nu,rec})$ describes the possible $E_\nu$ values that could result in a measured $E_{\nu,rec}$. Given the simulated MiniBooNE and T2K ND neutrino fluxes, the energy spread for a measured $E_{\nu,rec}$ is shown in figure 4.1.

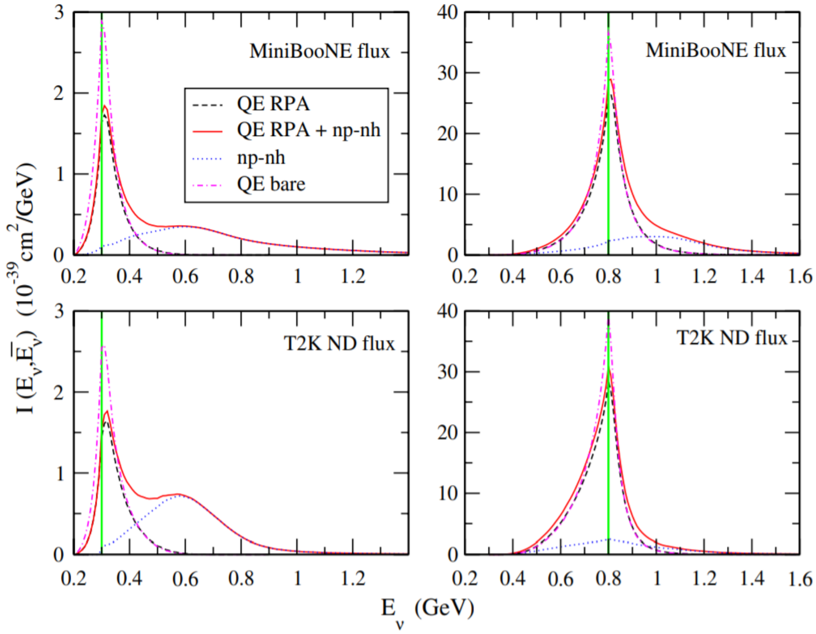

Figure 4.1. Distribution of a true neutrino energy $E_\nu$ given a measured $E_{\nu,rec}$ (green solid line). The top row assumes the neutrino flux at MicroBooNE, while the bottom row assumes the T2K near detector flux. The left column shows the distribution of true energies possible for $E_{\nu,rec} = 0.3\,GeV$, while the right column shows the true energies possible for a reconstructed energy $E_{nu,rec} = 0.8\,GeV$. The legend describes which distributions correspond to which input differential cross sections with different corrections. Original figure taken from [150].

Figure 4.1 demonstrates that significant misreconstruction is possible due to CCQE-like contamination. Any single reconstructed neutrino energy (the green lines in figure 4.1) actually has a large phase space of true neutrino energies which could have produced it. The potential for misreconstruction only grows as FSIs are also taken into consideration. Unavoidable energy resolution is present in all pure QE cases due to nuclear effects; however, the multinucleon interactions can result in a considerably larger error in the neutrino's reconstructed energy.

So what must be done to perform a CCQE-focused analysis in a world ripe with CCQE-like contamination? These "CCQE-like" events must either be tagged and removed from the CCQE dataset without fail, or they must be accurately modeled in simulation so the CCQE-like event contamination can be accurately quantified.

## 4.2 Neutron identification for CCQE-like event tagging

To quantify the reductions in CCQE-like contamination achievable with neutron tagging, consider the simulation of 1 GeV neutrino interactions on oxygen in the GENIE simulation package shown in figure 4.2 [137, 151]. Only interactions that yield 1 muon and no pions in the final state (CC$0\pi$) are shown.

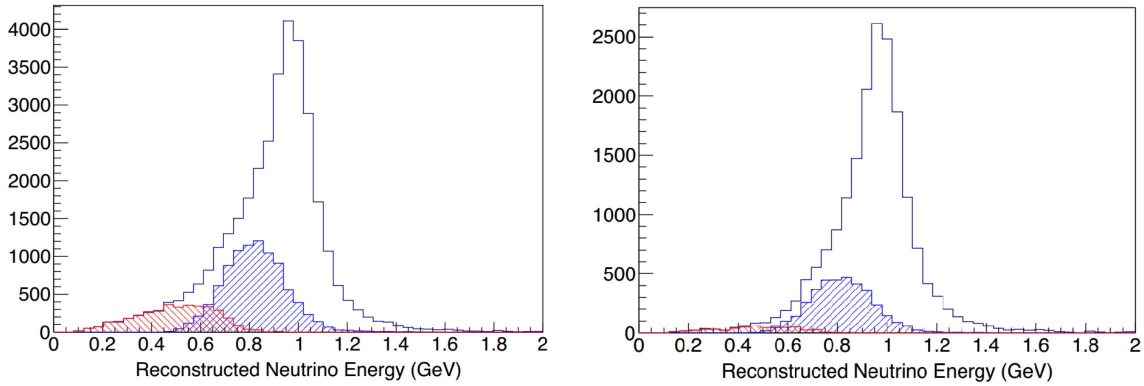

Figure 4.2. Comparison of 1 GeV $\nu_\mu$ $CC0\pi$ interactions on $^{16}O$. Interactions with (left) and without (right) outgoing neutrons are shown. The stuck pion (red) and 2p-2h (blue) contributions to the total distribution are explicitly shown. Selecting events with zero neutrons (right plot) results in a considerable reduction of stuck pion and 2p2h contamination; this lowers the fraction of interactions with a poorly reconstructed neutrino energy. Taken from [152].

In the ideal scenario, all neutrino interactions should reconstruct near 1 GeV (the true neutrino energy). The left plot in figure 4.2 shows that non-CCQE interactions have a bias to reconstruct at energies lower than 1 GeV. The right plot in figure 4.2 is the same simulated dataset as the left plot, but with all events containing a neutron in the final state removed. The stuck-pion contamination is almost completely removed, while an appreciable portion of 2p-2h contamination is also tagged; this results in an overall lower bias in the neutrino energy reconstruction. Detectors that can successfully tag final state neutrons can benefit from this background reduction when performing CCQE-based neutrino studies, or even use the neutrons to tag non-CCQE interactions for non-CCQE cross-section studies.

## 4.3 Impact of measuring neutron production in neutrino interactions

Most GeV-scale neutrino experiments stand to benefit from measurements of the number of neutrons knocked out of nuclei due to neutrino interactions (referred to as "neutron multiplicity"). Improving the modeling and tagging of neutron multiplicities can simultaneously lower CCQE-like contamination and reduce model uncertainties in any CCQE-like background subtraction performed. However, several measurements stand to markedly benefit from improved neutron multiplicity understanding and neutron tagging techniques.

### 4.3.1 GeV-scale interaction cross-section measurements

Measurements of interaction cross sections are highly dependent on accurate event reconstruction and interaction identification. Cross-section measurements proceed in neutrino detectors by relating the interaction rate in the detector to the *macroscopic cross section* $\sigma(E_\nu)$. The measured macroscopic cross section can then be used to test neutrino-nucleus models and help develop new models.

Consider, for example, a neutrino detector that will measure the total neutrino interaction cross section for events that produce no pions in the final state. The rate of an interaction per unit volume (denoted $R$) within a detector can be modeled as follows:

$$R_{CC0\pi}(E_\nu) = \sigma_{CC0\pi}(E_\nu)\Phi(E_\nu)\rho_N \ , \tag{4.3}$$

where $\Phi(E_\nu)$ is the fluence of incident neutrinos on a target per unit area per unit time and $\rho_N$ is the number of target nuclei per unit volume. Using this relation, detectors with a known number of nuclear targets placed within a well-characterized neutrino flux can make a measurement of the interaction cross section by measuring the rate of $CC0\pi$ events.

The challenge in measuring $R_{CC0\pi}(E_\nu)$ lies within experimentally tagging $CC0\pi$ events while quantifying the contamination of other interaction types. The rate $R_{CC0\pi}(E_{\nu,rec})$ measured in data must have systematic uncertainties in position and energy reconstruction, $CC0\pi$ tagging efficiency, and $CCN\pi$ contamination accounted for. An example of this is seen in T2K's measurement of the CC0$\pi$ cross section in figure 4.3. The neutrino data for the CC0$\pi$ dataset contains contributions from other interaction types which are fit using existing models.

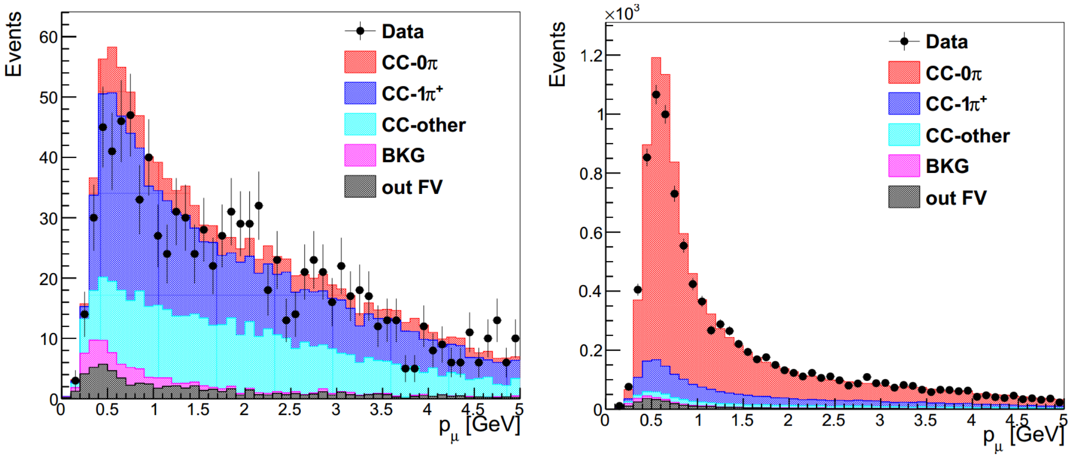

Figure 4.3. Data and MC best fit to CC0$\pi$ (left) and CC1$\pi^+$ (right) in sideband analyses. Generating accurate models via MC simulation relies on correct neutrino-nucleus interaction models and detector response models with tolerable uncertainties. Figure from [153].

Accurate neutron multiplicity measurements ultimately help reduce the uncertainties in estimating non-CCQE contamination with neutrons in the final state. The better the contamination is modeled, the lower the uncertainty on the contamination estimate. In the case above, accurate neutron multiplicity models could improve characterization of the “CC-other” category.

### 4.3.2 Background reduction in proton decay searches

Best fits to particle interaction cross-section data indicate that the coupling constants for electromagnetic, weak, and strong interactions run to different values as the interaction energy increases. One possible theory to describe this running of coupling constants is that all couplings converge into a single coupling constant at interaction energies on the order of $O(10^{16})\ MeV$ [154]. This convergence of all interaction types into one is known as the Grand Unified Theory (GUT). Numerous GUTs have been developed, but must ultimately be vetted and validated with experimental observations. Unfortunately, interactions at the energy scale of GUTs are not achievable with modern-day accelerators or naturally occurring processes. As such, direct experimental evidence for GUTs must be found elsewhere.

#### 4.3.2.1 Proton decay searches in water Cherenkov detectors

Since most GUTs share the common property that the proton is an unstable particle that can decay, the most popular experimental search which could validate GUTs is the observation of proton decay. Proton decay detectors are often composed of a detection medium with a large amount of protons, such as a hydrocarbon-based liquid scintillator or water. This is not an absolute, however, as proton decay could also occur inside nuclei if it does occur. These detectors will focus event selection on predicted proton decay modes, of which many result in an energy signal near the mass of the proton.

In water Cherenkov detectors, some of the most popular predicted decay modes are

$$p \rightarrow e^+\pi^0 \tag{4.4}$$

and

$$p \rightarrow \mu^+\pi^0 \tag{4.5}$$

primarily for their distinct Cherenkov cone patterns. However, kaon-producing decay modes are also common to search for. Nucleon decay occurring inside a nucleus could also leave the daughter nucleus in an excited state; decay searches such as that performed in SNO+ can search for the de-excitation's gamma signal [155].

Note that the majority of proton decay modes in water do not include neutrons in the final state. Clearly, no neutrons should be emitted if the hydrogen nucleus in a water molecule undergoes either decay in equations 4.4 or 4.5. Additionally, it is estimated that less than 10% of proton decays occurring in the oxygen nucleus should have an associated neutron [152]. When considering the oxygen nucleus using the nuclear shell model, the oxygen nucleus has eight protons lying in the $1s$, $1p$, and $2s$ shells. Only in the decay of a $1s$ proton is the $^{15}N$ daughter nucleus expected to have the excitation energy necessary for neutron emission ($11.24$ MeV) [156, 157].

In short, rejecting events coincident with a neutron signal could help remove common proton decay backgrounds while retaining over 90% of the expected proton decay signal in water Cherenkov detectors.

#### 4.3.2.2 Proton decay atmospheric neutrino background

Due to the match of the proton mass with the peak in the atmospheric neutrino flux energy distribution, atmospheric neutrinos form one of the dominant backgrounds of most proton decay modes. Revisiting the atmospheric neutrino spectra models in 1.19, a considerable fraction of atmospheric neutrino events could result in a visible energy consistent with proton decay. To make matters more complicated, charged-current neutrino or antineutrino interactions could exactly mimic the signals shown in equations 4.4 and 4.5 via FSIs or resonance interactions.

One example of this background's presence is found in a recent Super-Kamiokande proton decay search. Figure 4.4 shows that the simulation predicts numerous atmospheric neutrino events in the proton decay search region of interest.

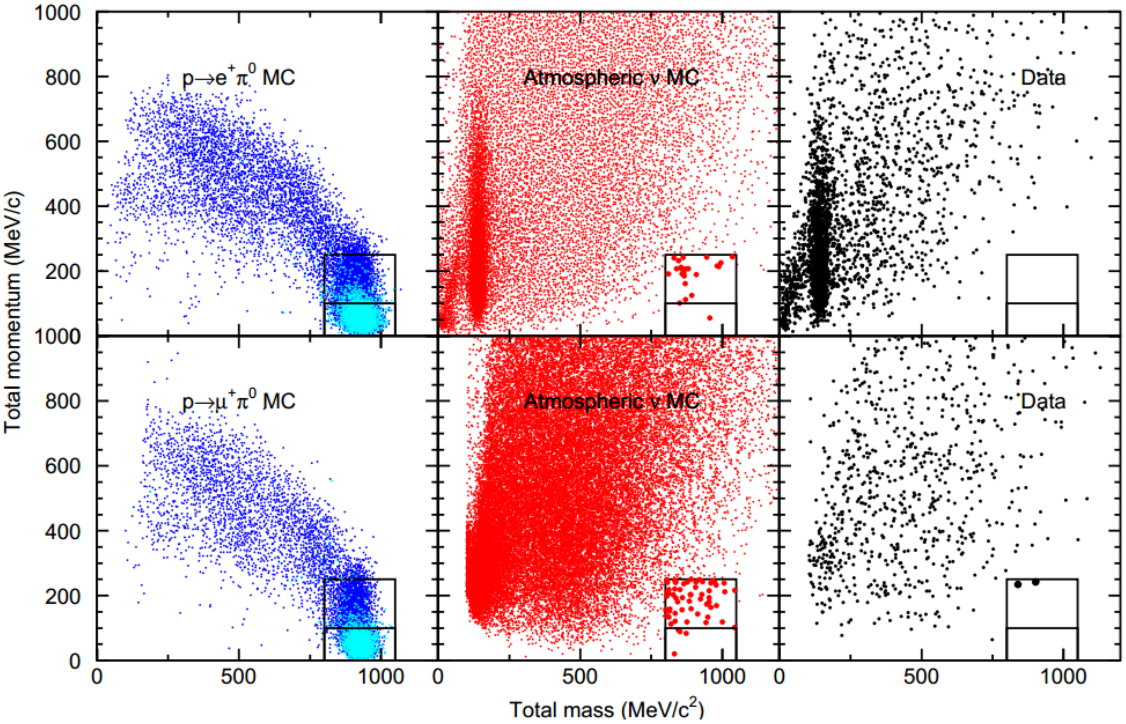

Figure 4.4. Simulatied energy distributions of proton decay (left) and atmospheric neutrinos (center) compared to Super-Kamiokande data (right). Boxes drawn into plots identify the region of interest used for the Super-Kamiokande proton decay search. Original data taken from [158].

One way to reduce the atmospheric neutrino background is through rejection of proton decay candidate events that are coincident with neutron activity. Atmospheric neutrino interactions can result in the ejection of neutrons from the nucleus through np-nh interactions, FSIs, or neutron evaporation from an excited final-state nucleus. As such, tagging neutrons aids in rejecting atmospheric neutrino events while sacrificing only a small portion of the expected proton decay signal.

### 4.3.3 Background reduction in DSNB searches

Atmospheric neutrinos also form the primary background for intermediate energy signals in DSNB searches, and can be mitigated with neutron tagging techniques. Recall that the 2003 Super-Kamiokande DSNB search focused on measuring the DSNB's $\bar{\nu}_e$ component by searching for events with the inverse beta-decay signal, written as

$$\bar{\nu}_e + p \to n + e^+ \ . \tag{4.6}$$

The signal is a delayed coincidence where the prompt event is an electron-like Cherenkov cone and the delayed signal is the 2.2 MeV de-excitation gamma following the neutron capture on a proton in water. Atmospheric muon neutrino interactions can mimic this signal. Consider an atmospheric neutrino charged-current interaction which produces a muon below Cherenkov threshold (known as an "invisible muon"). If the muon decays in the detector volume as follows:

$$\mu^- \to e^- + \bar{\nu}_e + \nu_\mu \ , \tag{4.7}$$

then the electron produced (known as a Michel electron) could generate a prompt Cherenkov signal that, paired with a delayed neutron capture signal, could result in a false DSNB coincidence signal. The predicted DSNB $\bar{\nu}_e$ flux spectrum for several characterization parameters shown in figure 4.5 indicates where atmospheric neutrinos are the dominant background.

### 4.3.4 CP violation measurements with atmospheric neutrinos

A recent proposal has been made to measure $\delta_{CP}$ using sub-GeV atmospheric neutrinos in DUNE [160]. Atmospheric neutrinos will enter into the DUNE detector at all incident angles; however, neutrinos that pass through varying depths of the Earth's crust will have different oscillation probabilities due to matter effects. As shown in figure 4.6, these matter effects, combined with a non-zero $\delta_{CP}$ value, will result in different oscillation probabilities of $\nu_\mu$ to/from $\nu_e$. With this in

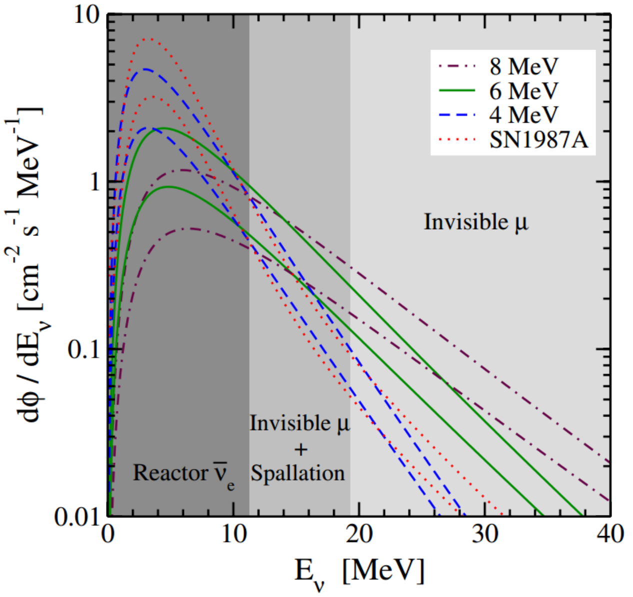

Figure 4.5. Expected DSNB neutrino flux distributions for several. The DSNB is modeled by a Fermi-Dirac spectrum with some mean neutrino emission energy; different mean energies are shown, with the widths of each spectrum representing uncertainties in the observed cosmic supernova rate. The prominent detector backgrounds are shown in the shaded gray regions. Figure taken from [159]

mind, a measurement of the $\delta_{CP}$ phase could be done by fitting the neutrino survival probability spectrum to atmospheric $\nu_\mu, \nu_e$ events in DUNE for several incident angles.

To quantify the feasibility of this measurement in DUNE, a simulation study was performed [160]. The atmospheric neutrino flux is simulated using the NRLMSISE00 atmospheric model presented in figure 1.19, while atmospheric neutrino interactions on argon were simulated using the NuWro event simulator. Momentum and angular resolutions due to event reconstruction were incorporated by smearing the momentum and angular distributions with the projected reconstruction uncertainties in DUNE. The projected sensitivity assumes perfect $\nu_\mu/\nu_e$ separation, as well as perfect classification of $CCNp0\pi$ interactions, where $N$ is the number of protons produced following the charged-current event. For a 400 kton-year exposure (10 years of running for the baseline 40-kton design), and assuming $\delta_{CP} = \frac{3\pi}{2}$ and $\sin^2\theta_{23} = 0.5$, the projected sensitivity to $\delta_{CP}$ is given in figure 4.7.

This measurement in DUNE would benefit from improved models of neutron multiplicities. Since liquid argon detectors have a difficult time detecting neutrons, DUNE will have to rely on accurate modeling of neutron multiplicities and their projected impacts on energy recon-

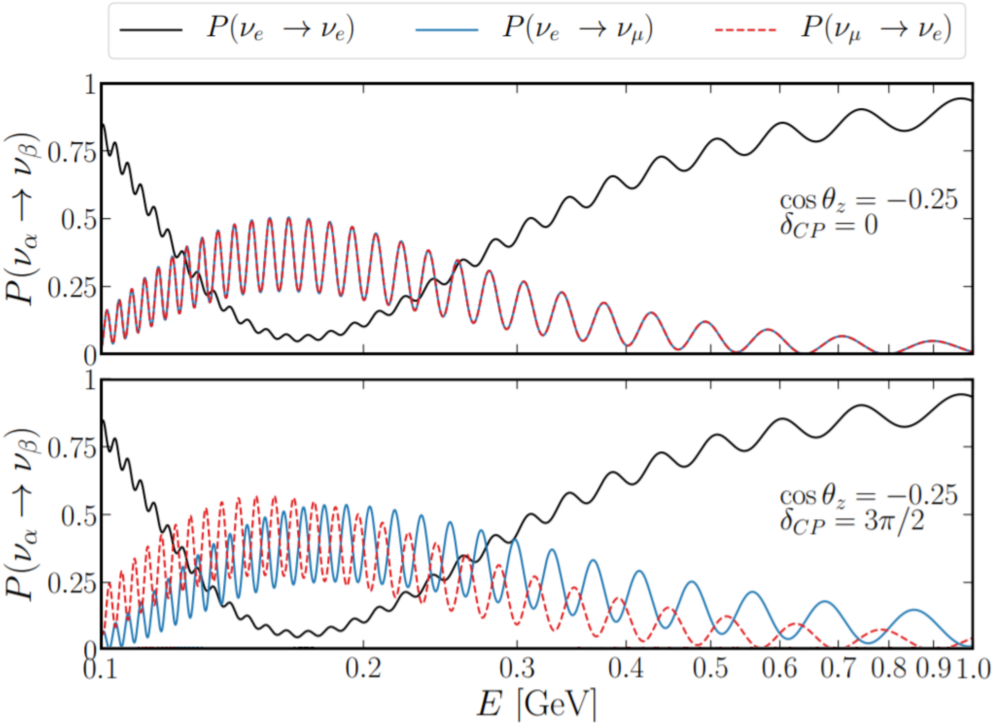

Figure 4.6. Oscillation probability distributions for $\delta_{CP} = 0$ (top) and $\delta_{CP} = \frac{3\pi}{2}$ (bottom). Figure taken from [160].

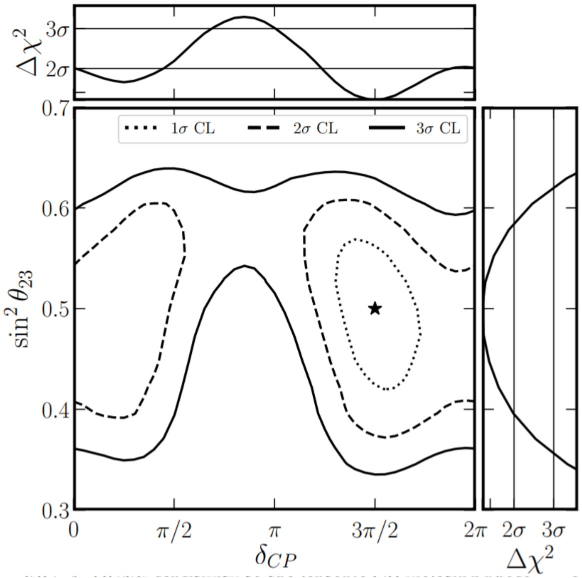

Figure 4.7. Projected sensitivity of DUNE to $\delta_{CP}$ and $\sin^2\theta_{23}$ using only sub-GeV atmospheric neutrinos. The input values for the neutrino oscillation simulation are marked with the star ($\delta_{CP} = \frac{3\pi}{2}$ and $\sin^2\theta_{23} = 0.5$). Exclusion bounds at several confidence limits are drawn. Figure taken from [160].

struction for any $CCNp0\pi$ events which also produce neutrons via np-nh interactions or FSIs. Improvements in the neutron multiplicity model used could reduce the uncertainties in energy reconstruction and event classification.

## 4.4 Current neutron multiplicity data

To improve both the modeling of neutron multiplicities and techniques used to tag neutrons, new neutron multiplicity data in different mediums is pivotal. Neutrinos interacting with Different elements will likely produce different neutron multiplicities; any neutron multiplicity model should be validated against as many different target nuclei as possible. Some of the most prominent neutron multiplicity measurements in common detector designs are reviewed below, along with a discussion on the successes and shortcomings of each dataset in the context of improving neutron multiplicity models.

### 4.4.1 Liquid argon (ArgoNeuT)

One of the most prominent detectors for neutrino beam physics, both now and in the future, is the Liquid Argon Time-Projection Chamber (LArTPC). Currently, LArTPC detectors like MicroBooNE, ICARUS, and LArIaT are being utilized for cross-section measurements, neutrino oscillation measurements, and the characterization of LArTPC response to hadrons produced in neutrino interactions. Additionally, the DUNE experiment will deploy within the next decade. Given the possible impact on numerous current and upcoming experiments, any advances in measuring and understanding the neutron multiplicity following neutrino-argon interactions is valuable.

The ArgoNeuT detector, a LArTPC detector located at Fermilab, has demonstrated the ability to observe $O(MeV)$ particle interactions by detecting gamma radiation emitted following nuclear de-excitation of, or neutron inelastic scattering off of, Argon [161]. In ArgoNeuT, the gamma radiation's interactions are identified by searching for small charge depositions in a cluster of TPC wires. Figure 4.8 shows the results from ArgoNeuT's search for gamma activity occurring in muon neutrino charged-current events.

Detecting neutrons with $< 100\,MeV$ of kinetic energy is a challenging task in LArTPC detectors, and the successful result is an important step towards effectively performing MeV-

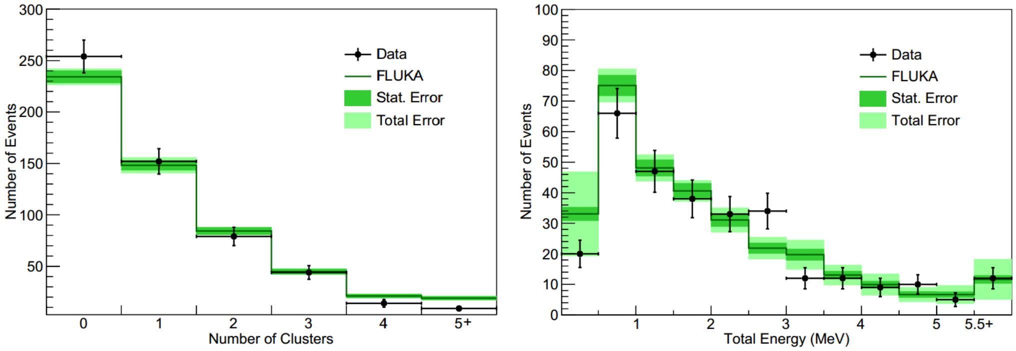

Figure 4.8. Cluster count distribution and reconstructed energy of cluster events in the ArgoNeuT detector. The detector's observed cluster distributions are consistent with those predicted from nuclear de-excitation and neutron inelastic scattering in FLUKA. Figure from [161].

scale neutron physics in liquid argon detectors. The simulation's agreement with data is a good validation of FLUKA's neutron interaction model in liquid argon. The measurement's main shortcoming is the detection approach is not sensitive to boil-off neutrons, as these neutrons wouldn't have enough kinetic energy to produce a gamma through inelastic scattering on argon.

### 4.4.2 Water Cherenkov (Super-Kamiokande)

The atmospheric neutrino contamination in Super-Kamiokande's proton decay search also served as a signal for performing neutron multiplicity measurements. First, a neutron multiplicity measurement of proton decay candidate events as a function of visible energy was made [158]. Since no neutrons are expected for proton decays, any events with a non-zero neutron multiplicity should be due primarily to atmospheric neutrino contamination. As such, comparing this distribution to simulated neutron multiplicity distributions provided a measurement of atmospheric neutrino neutron multiplicities (shown in figure 4.9).

Although Super-Kamiokande found that their data were consistent with their neutron multiplicity model within uncertainties, there are limitations for using their data to then refine existing multiplicity models. First, since the neutrino source was atmospherics, the incident direction of the neutrino was not known; this means that the neutrino's incident energy could not be accurately reconstructed (as is possible with a beam experiment). Additionally, Super-Kamiokande's detector signal could not indicate whether the atmospheric was a neutrino or an antineutrino, whereas the fractional presence of both is well-characterized in a neutrino beam.

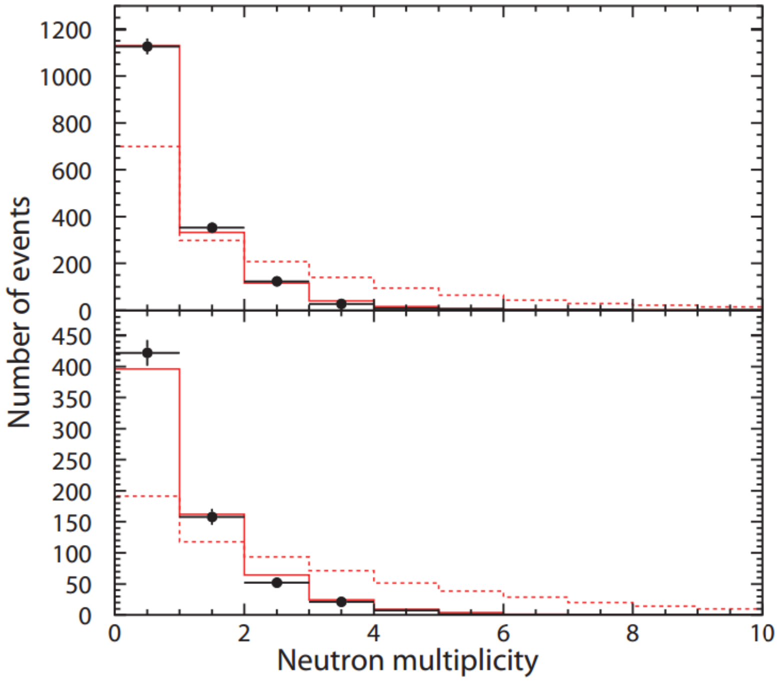

Figure 4.9. Neutron multiplicity distribution for candidate $p \rightarrow e^+\pi^0$ (top) and $p \rightarrow \mu^+\pi^0$ (bottom) events within the Super-Kamiokande detector. The presence of interactions with a non-zero neutron multiplicity is due to atmospheric neutrino interaction contamination. The dotted red histogram shows the true multiplicity of neutrons in the atmospheric neutrino MC, and the solid red histogram shows the multiplicity of successfully tagged neutrons in the atmospheric neutrino MC. Taken from [158].

### 4.4.3 Liquid scintillator (Minerva)

Liquid and solid organic scintillator-based detectors are also efficient at neutron multiplicity searches. Scintillator detectors have a high photon yield to energy deposition ratio, making detection of low energy physics interactions possible. For reference, the SNO+ experiment's scintillation cocktail emits approximately 10000 photons/MeV [77]. Following a charged-current neutrino interaction, neutrons are primarily detected via their inelastic scatters on protons in the organic scintillator or by the 2.2 MeV gamma emitted following a neutron capture on a proton.

The Minerva experiment has made a recent measurement of the neutron multiplicity from muon antineutrino interactions on hydrocarbon [162]. The Minerva detector, located in the NuMI beamline at Fermilab, is composed of an array of liquid scintillator-filled pipes routed with optical fiber to collect the scintillation light produced following particle interactions. Any neutron inelastic scatters appear as isolated energy depositions in several neighboring scintillator bars. The neutron multiplicity as a function of clustered energy deposition is shown in figure 4.10.

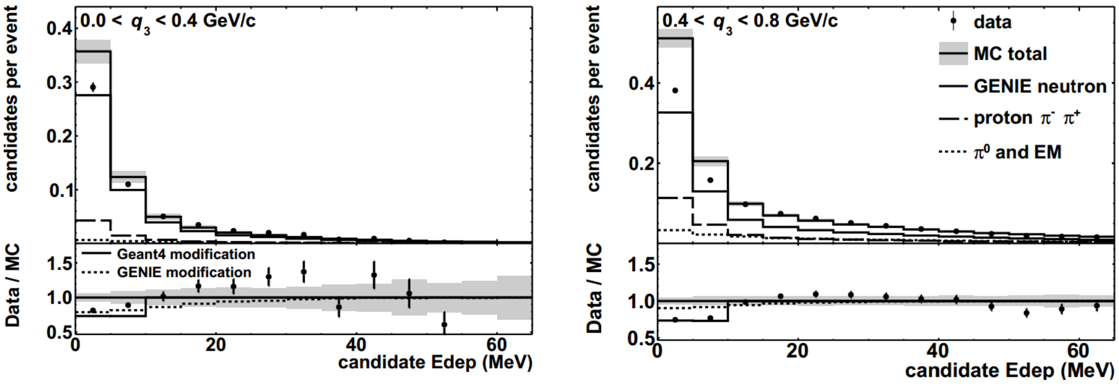

Figure 4.10. Neutron candidate multiplicity distribution as a function of energy deposition in the Minerva detector. A discrepancy in the data and MC simulation is apparent in the $E_{dep} < 10\,MeV$ region. Taken from [162].

A clear discrepancy in the $E_{dep} < 10\,MeV$ region is apparent in figure 4.10. To investigate the source of this low-energy discrepancy, the neutron candidate distribution was re-binned as a function of time-of-flight relative to the reconstructed antineutrino vertex interaction time (see figure 4.11). The data/MC discrepancy at $E_{dep} < 10\,MeV$ appears to be due to an excess of protons, $\pi^{\pm}$, and $\pi^0\,EM$ signal in the simulation relative to the data.

The Minerva measurement is a great example of a neutron multiplicity measurement as a function of observed energy. The time-of-flight information also provides approximate information on the energy of the neutrons produced in the neutrino interactions. The Minerva multiplicity measurement would be complementary to similar measurements in a neutrino beam of different energy regimes (Minerva lies in the NuMI beam line, with neutrinos produced mostly at energies $2-20$ GeV [163]) as well as with a detector medium containing different target nuclei. Take oxygen for example; since carbon and oxygen are both lighter elements, a comparison of the Minerva's neutron multiplicities in a water-based detector would assist in validating and tuning FSI models for nuclei in the same mass range.

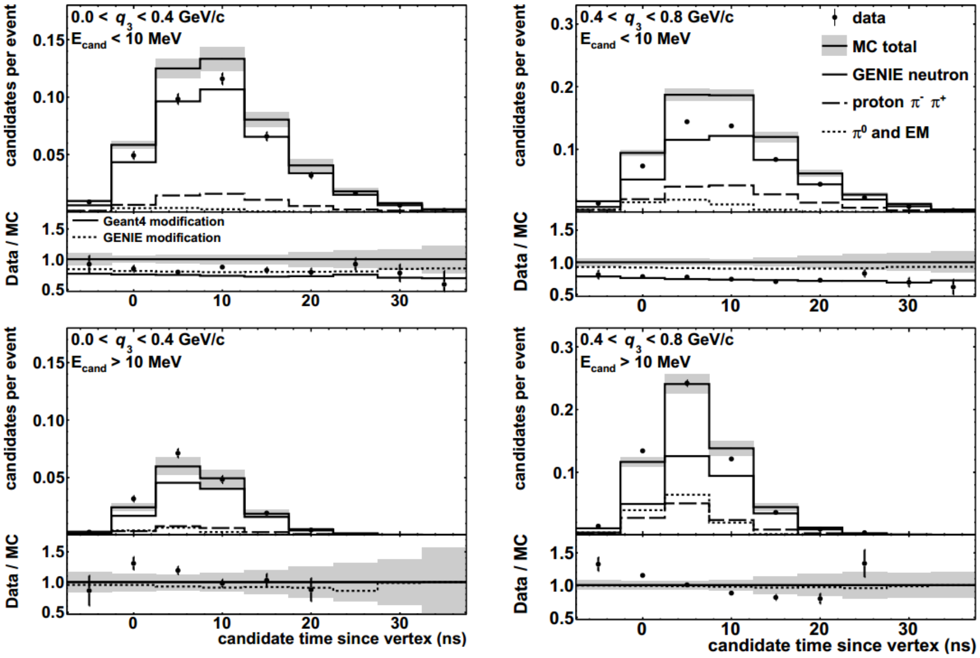

Figure 4.11. Neutron candidate multiplicity distribution as a function of time-of-flight relative to the interaction vertex time. The discrepancy between data and simulation in the $E_{dep} < 10\,MeV$ region appears isolated to the centroid of the time-of-flight distribution and could be mostly resolved by rescaling the simulation's rate of proton $\pi^+, \pi^-$ and $\pi^0/EM$-based contamination. Taken from [162].

# Chapter 5

# The ANNIE experiment

As discussed in chapter 4, there is a clear demand for new detectors that are capable of measuring neutron multiplicities from neutrino interactions. Neutron multiplicity measurements across a variety of different nuclei will help validate models of neutron-producing interactions, such as np-nh and final state interactions. Measurements of the neutrino-oxygen neutron multiplicity are particularly important for tagging atmospheric neutrino backgrounds in water Cherenkov detectors. Development of neutron detection techniques will also lead to improved neutrino-nucleus interaction reconstruction.

The ANNIE detector is designed to meet this demand. ANNIE is a gadolinium-doped water Cherenkov detector located in Fermilab's Booster Neutrino Beam (BNB) line, and will make a measurement of the number of neutrons produced following GeV-scale neutrino interactions on oxygen. ANNIE will also utilize new detector technologies, specifically gadolinium-doped water and Large-Area Picosecond PhotoDetectors (LAPPDs), to improve the reconstruction of neutrino-nucleus interactions and the neutrons produced. Along the way, ANNIE will also measure neutrino interaction cross sections, with an emphasis on the total cross section, charged-current interactions with zero pions ($CC0\pi$), and charged-current interactions with one pion ($CC1\pi$).

The following chapter provides an overview of ANNIE's neutron multiplicity detection technique, and a closer technical look at each ANNIE subsystem. Details on the improvements resulting from gadolinium doping and LAPPD utilization are discussed in the tank subsystem section.

## 5.1 Measuring neutrino neutron multiplicities in ANNIE

To perform the neutron multiplicity measurement, ANNIE has five primary components:

- The Fermilab Booster Neutrino Beam (neutrino source)
- The ANNIE water tank (neutrino interaction medium)
- The Front Anti Coincidence Counter (FACC; tags muons produced in the dirt upstream)
- The Muon Range Detector (muon track and energy reconstruction)
- The data acquisition electronics

Each component and its orientation in the ANNIE hall are shown in figure 5.1.

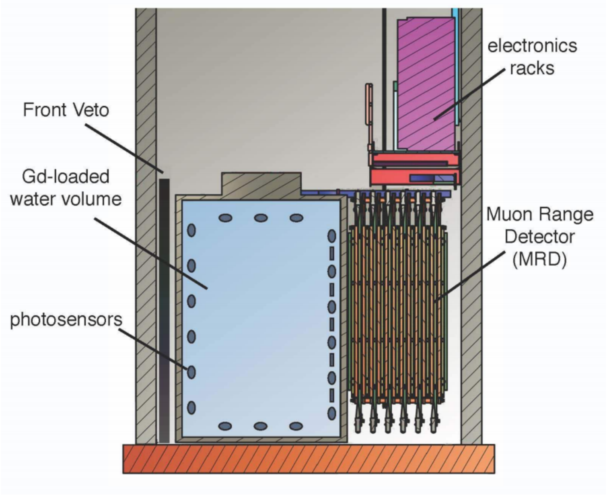

Figure 5.1. Cross section of the ANNIE detector with a breakdown of the key detector components. The neutrino beam crosses from left to right through the Front Anti-Coincidence Counter (FACC, labeled as "Front Veto" in diagram), ANNIE tank, and MRD. Figure taken from [152].

To summarize how the ANNIE detector will conduct its neutron multiplicity measurement, an example neutrino charged-current interaction is shown in figure 5.2. When a charged-current neutrino interaction occurs in the ANNIE tank volume, any charged particles produced in the interaction will emit Cherenkov light if moving faster than the speed of light in water (typically muons, pions, and electrons in ANNIE). The Cherenkov light emitted will produce a time and charge signal in the tank PMTs, which is utilized to reconstruct the neutrino event. Additionally, muons are generally produced with enough energy to exit the tank; forward-directional muons will pass through the muon range detector for muon energy and track reconstruction.

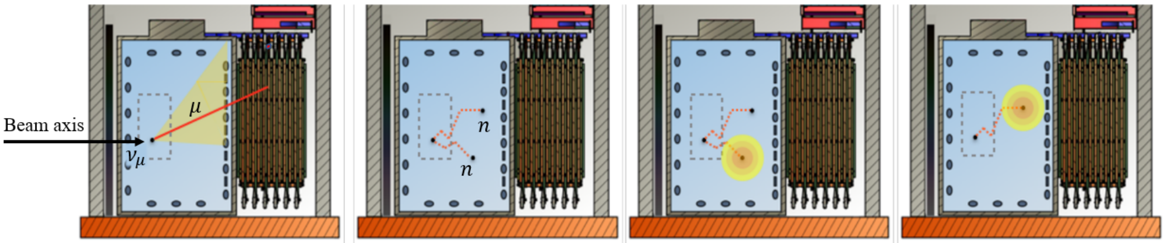

1. Muon neutrino from Booster Neutrino Beam interacts with nucleus in target volume; muon stops in MRD

2. Neutrons produced (if any) undergo thermalization in target volume

3. Neutrons capture on gadolinium; gadolinium's de-excitation signal (Cherenkov light from ~8 $MeV$ gamma cascade's Compton scatter electrons) is detected

Figure 5.2. Breakdown of a single charged-current neutrino interaction in the ANNIE detector, and a description of each component's role in the event's reconstruction. Figure from [152].

Following the initial interaction, any neutrons produced will scatter through the water volume and eventually thermalize. Some time later (characteristic capture time of 30 $\mu s$ for a $0.2\%$ gadolinium sulfate concentration by weight), the neutron will capture on a gadolinium atom. The gadolinium atom will be in an excited state post-capture, and de-excite through the emission of a gamma cascade with total energy $\sim 8\,MeV$. The gamma radiation will scatter on electrons in the water, producing more Cherenkov light.

In short, neutron multiplicities of neutrino interactions are measured in ANNIE by counting the flashes of light (i.e. number of neutron captures on gadolinium) that occur within the ANNIE tank volume following a charged-current neutrino interaction.

## 5.2 The Booster Neutrino Beam (BNB)

The Booster Neutrino Beam (BNB) line is one of two active neutrino production beamlines currently at Fermilab, and is the primary neutrino source for ANNIE. The beamline was originally developed for use in the Booster Neutrino Experiment (BooNE), but other past, present, and future experiments such as MicroBooNE, SciBooNE, ICARUS, SBND, and ANNIE also utilize its beam. A top-down view is shown in figure 5.3 to provide scale and locational references to Wilson Hall, as well as ANNIE's location relative to the target (marked as a green star). The ANNIE detector is located 100 meters downstream from the production target.

An overview of the BNB's primary components is displayed in figure 5.4. To produce neutrinos in BNB, protons are accelerated to energies of 8.89 GeV via Fermilab's Booster Accelerator

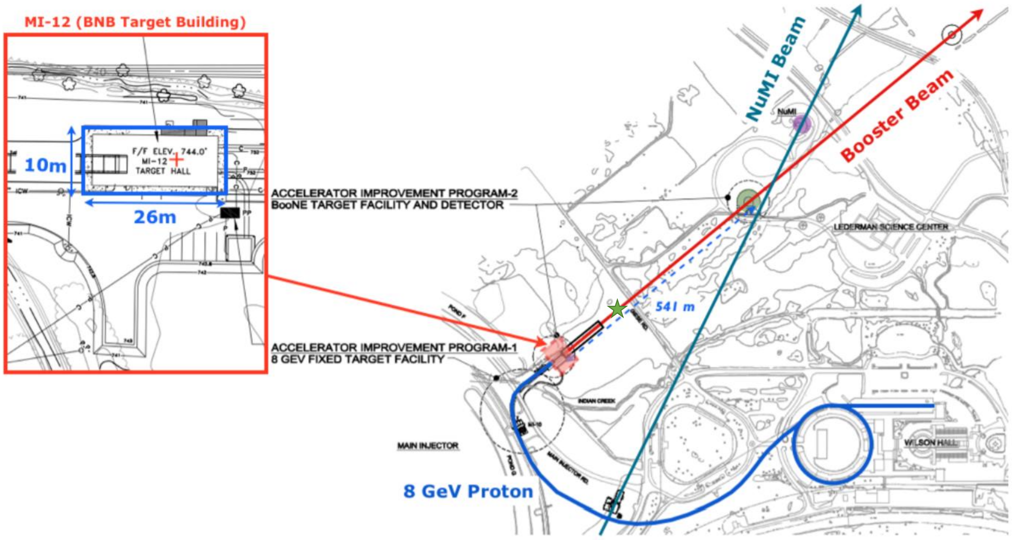

Figure 5.3. Drawing of the Booster Neutrino Beam line at Fermilab. The green star marks the approximate location of the ANNIE hall from the production target. Figure modified from [164].

and fired at a beryllium target. Secondary mesons ($\pi^{\pm}$, $K^{\pm}$, $K^{0}$) are produced via interactions in the target. Pions are then selected for positive or negative charge via an electromagnet (known as the horn). These pions decay in the following decay pipe, producing muon neutrinos or antineutrinos depending on the pion's charge. The BNB delivers beam dumps to the ANNIE hall at a rate of roughly 5 Hz, where each beam dump contains 84 bunches spread throughout a $1.6\,\mu s$ window [165].

The BNB currently operates in neutrino mode at Fermilab, and will for the foreseeable future. In neutrino mode, the magnetic horn selects negatively-charged pions produced in the target. Residual contamination from other secondary mesons are still present and must be accounted for when profiling the final neutrino beam. After selecting pions with the horn, the beam is collimated using a concrete collimator 259 cm downstream from the target. The pions then pass through a decay region and undergo the decay

$$\pi^{-} \rightarrow \mu^{-} + \nu_{\mu} \ , \tag{5.1}$$

providing the desired muon neutrino. The secondary muons are stopped using absorber targets at the end of the decay pipe.

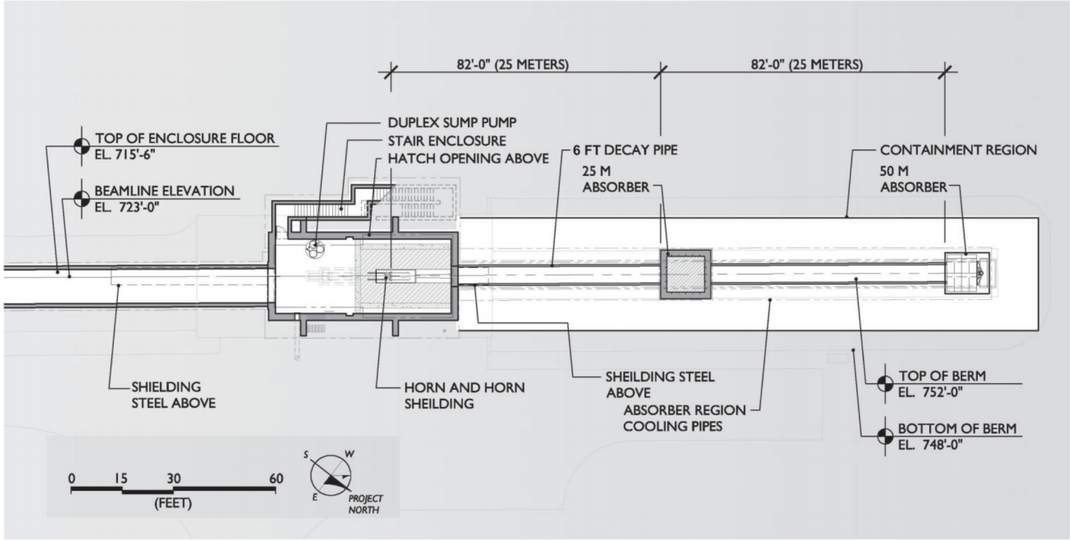

Figure 5.4. Summary of the Booster Neutrino Beam target hall's main components. Taken from [166].

A detailed overview of the neutrino production process is summarized in appendix C.

### 5.2.1 BNB beam profile

Key properties of the BNB, including neutrino flavor fractions and energy distributions, are determined through simulation. A full Monte Carlo simulation of the production target, magnetic horn, and secondary particle production was developed by the MiniBooNE collaboration, and has also been utilized by MicroBooNE for beam modeling [166, 167]. When measuring the cross sections of various neutrino interactions, analyses of ANNIE data will utilize the same software to estimate the neutrino beam properties in the ANNIE hall.

Given the beam properties are not expected to change drastically between MicroBooNE's detector position to ANNIE's, a brief overview of the MiniBooNE neutrino flux predictions is informative. When protons strike the beryllium target in the production hall, the neutrino flux is determined by the decay of mesons in the BNB decay pipe. The contributions of each meson's decays to the total $\nu_\mu$ and $\bar{\nu}_\mu$ flux when operating in neutrino mode are shown in table 5.1.

Notice that the pions produced in the beryllium target largely determine the muon neutrino and antineutrino content. The simulated energy distribution of the BNB in neutrino mode is shown in figure 5.5. BNB neutrinos have a mean energy of approximately $700\,MeV$.

|  | Decay mode | $\nu_\mu$ | Decay mode | $\bar{\nu}_\mu$ |
|---|---|---|---|---|
| Flux ($\nu$/cm$^2$/POT) | $5.19 \times 10^{-10}$ |  | $3.26 \times 10^{-11}$ |  |
| Frac. of total |  | 93.6% |  | 5.86% |
| Composition | $\pi^+$: | 96.72% | $\pi^-$: | 89.74% |
|  | $K^+$: | 2.65% | $\pi^+ \to \mu^+$: | 4.54% |
|  | $K^+ \to \pi^+$: | 0.26% | $K^-$: | 0.51% |
|  | $K^0 \to \pi^+$: | 0.04% | $K^0$: | 0.44% |
|  | $K^0$: | 0.03% | $K^0 \to \pi^-$: | 0.24% |
|  | $\pi^- \to \mu^-$: | 0.01% | $K^+ \to \mu^+$: | 0.06% |
|  | Other: | 0.30% | $K^- \to \pi^+$: | 0.03% |
|  |  |  | Other: | 4.43% |

Table 5.1. Contributions of each meson channel to the total $\nu_\mu$ and $\bar{\nu}_\mu$ fluxes in the BNB beam line derived from simulation. The first particle listed in each production mode is a parent particle produced by a proton or neutron interaction within the production target. Flux contributions are valid for the BNB operating in neutrino mode. $\nu_e$ and $\bar{\nu}_e$ fractional contributions are also simulated, but are not shown. Table from [166].

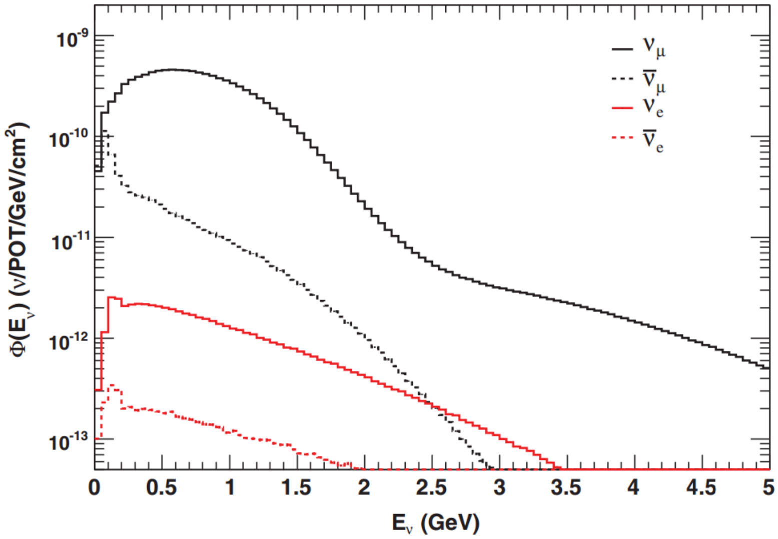

Figure 5.5. Energy distribution of the simulated BNB neutrino mode flux at MicroBooNE. Although the beam is dominated by the $\nu_\mu$ flux, the antineutrino and electron flavor components are also present. Figure taken from [166].

## 5.3 ANNIE water tank

The ANNIE water tank is an upright cylinder with a height of 13 feet and diameter of 10 feet. When fully filled, the tank holds a volume of 26 tons of water. The PMT/LAPPD support structure hangs inside the ANNIE tank. The entire support structure is wrapped with several layers of black low-density polyethylene, optically separating the tank volume into an "internal volume" (active detection medium instrumentated with tank PMTs) and an "external volume" (which could be used to veto cosmics with a detector upgrade). The ANNIE tank is made of standard steel, and lined with a white PVC liner distributed by Kentain. The PVC liner prevents leaching of heavy elements from the tank's steel and eliminates risk of corrosion in the tank. Of particular importance, past experiments have shown that iron leaching into Gd-doped water can negatively impact the Gd-doped water's transparency [168]. A white liner was chosen to maximize reflections in the external volume, which would improve the efficiency of cosmic muon tagging through the addition of outward-facing PMTs.

### 5.3.1 PMT/LAPPD support structure and tank lid

A stainless steel support structure is utilized to mount the tank photomultiplier tubes and LAPPDs. The support structure is made of 304 stainless steel, and is attached directly to the lid of the ANNIE tank. All steel was passivated, electropolished, and teflon-taped to minimize leaching of impurities into the tank water. The support structure contains 8 horizontal panels which form an octogonal structure in the inner volume. Between each panel, 8 rails are installed; LAPPDs can be deployed at any position along each rail. Combining the side panels with the top and bottom panels, ANNIE can mount 136 inner PMTs and 16 outer PMTs total. Currently, 132 inner PMTs and no outer PMTs are mounted due to time and budget constraints. A CAD drawing of the support structure resting in the ANNIE tank, which was used to inform design and fabrication, is shown in figure 5.6.

The tank lid acts as the primary interface between the detector hall and the detector volume. Four large ports (colored orange in figure 5.6) are used as PMT cable and LED fiber entry/exit points. Five calibration ports are also located on the lid. 8 rectangular ports provide access to the LAPPD rail mounts. A central hatch (holds the 4 PMTs on the right side of figure 5.6) can be removed for the deployment of larger apparatuses; this was used to deploy the scintillator

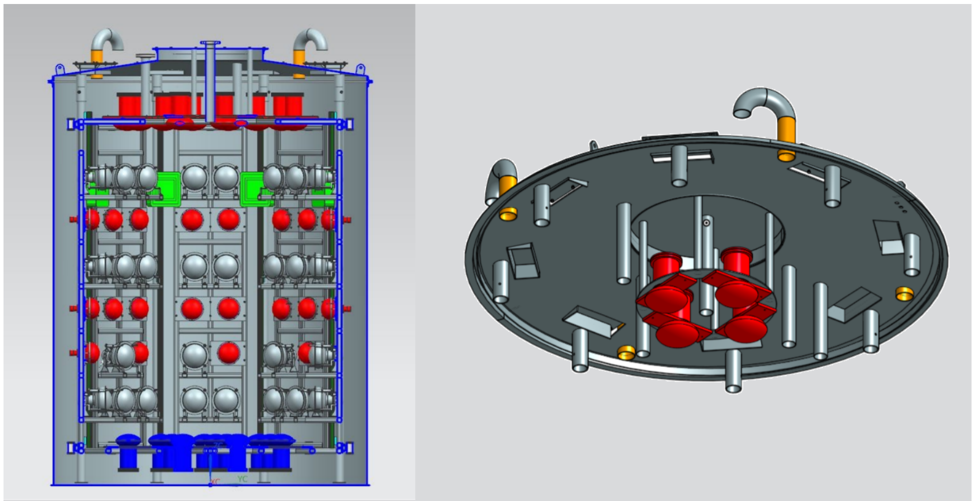

Figure 5.6. CAD drawing of the ANNIE support structure resting inside the ANNIE tank (left) and the tank lid (right). PMTs are also shown in the diagram where they are mounted on the structure. The support structure is bolted onto on the lid and suspended in the ANNIE tank. Figures from [169].

volume for characterizing neutron backgrounds in the ANNIE engineering run (ANNIE phase I).

Three PVC tubes are also installed in the lid for recirculation and nitrogen bubbling. Nitrogen is constantly bubbled into the tank to displace oxygen in the water, which can increase light attenuation in the tank and result in organic growth in the tank volume. The PVC tubes run along the support structure and do not shadow any PMTs in the inner volume.

### 5.3.2 Tank PMTs

The ANNIE tank is instrumented with four different types of photomultiplier tubes. The 20 PMTs placed at the tank bottom are 10-inch Hamamatsu R7081 PMTs previously used in the LUX experiment's muon veto [170]. The 20 PMTs mounted on the tank's top panel and hatch are new 11-inch ETEL prototype tubes. The remaining PMTs mounted around the inner structure's wall are a combination of brand new 8-inch Hamamatsu R5912 PMTs, 10" Hamamatsu R7081 PMTs used in the WATCHBOY experiment [171], and four 10" Hamamatsu R7081-100 high quantum efficiency PMTs that will eventually be used in the WATCHMAN demonstration [172]. For a detailed review of the general characteristics of photomultiplier tubes, see [173].

To provide a more symmetric charge response to single photons in the ANNIE tank volume, all PMT voltages were selected so the photodetectors have a similar gain. PMT gain matching was first performed on a test stand at Fermilab and then re-performed in-situ using LEDs. For a more in-detailed discussion of the in-situ PMT gain calibration, see section 6.2.

### 5.3.3 Large Area Picosecond PhotoDetectors (LAPPDs)

Large Area Picosecond PhotoDetectors (LAPPDs) are a developing photodetector technology for next-generation neutrino detectors. The LAPPD has an $8 \times 8$-inch photosensitive area that converts photons to electrons with a similar quantum efficiency to that of PMTs (20-25$\%$ QE). LAPPDs can achieve photoelectron amplifications of up to $10^7$ gain, and also demonstrate millimeter-level position resolution with $< 100$ picosecond photon time resolution. An in-depth study of the performance of several LAPPDs can be found at [174].

In the 2020-2021 beam year, ANNIE will install 5 LAPPDs on the support structure to improve the reconstruction of charged-current interactions. Muon neutrino charged-current event reconstruction in ANNIE relies primarily on detecting Cherenkov radiation from the final-state muon; by adding LAPPDs in the ANNIE tank, the timing resolution on Cherenkov light detection improves reconstruction of the muon track. Preliminary simulation studies utilizing the current default ANNIE reconstruction algorithms indicate a factor of two improvement in vertex reconstruction is possible [175]. Note that no LAPPD data is included in this thesis, as they were not installed for initial commissioning and data-taking.

### 5.3.4 Gadolinium-doped water

The addition of gadolinium to the ANNIE water tank improves the neutron multiplicity measurement on two key fronts: an improved neutron capture detection efficiency and a shorter time difference between neutrino interaction and neutron capture/detection.

Following a thermal neutron capture, gadolinium (specifically $^{155}Gd$ or $^{157}Gd$ de-excites and emits a total of 7-8 MeV energy in gammas [176]. The final result is more visible Cherenkov light following the gammas' Compton scatters on electrons in the water. The resulting signal is larger than most naturally-occurring radioactive backgrounds resulting from contaminants such as the $^{238}U$ or $^{232}Th$ chains.

Gadolinium also has a large thermal neutron capture cross section; as such, neutrons will preferentially capture on gadolinium even when gadolinium is in low concentration. Given that the effective cross section of a homogeneous mixture of two materials A and B is

$$\sigma_{eff} = \frac{N_A}{N}\sigma_A + \frac{N_B}{N}\sigma_B \ , \tag{5.2}$$

a considerable fraction of neutron captures would still occur on hydrogen in water if the neutron capture cross sections of $H$ and $Gd$ are of comparable size. Fortunately, the thermal neutron cross sections of natural gadolinium is $\sim 49,000$ barns (primarily due to large capture cross sections on $155$ and $157$-gadolinium), a considerably larger value than hydrogen's cross section at $0.33$ barns [177, 178, 179]. As such, only a small addition of gadolinium is needed to drastically increase the detection medium's neutron capture cross section.

The addition of gadolinium in ANNIE also reduces the time between when a neutron is produced and when it captures in the tank. For gadolinium sulfate concentrations of approximately 0.2% by mass, a reduced neutron capture time (≈30 $\mu s$) is expected relative to pure water (≈200 $\mu$s). Similar reductions in capture time have been observed in past gadolinium-doped detectors, including Double CHOOZ and Daya Bay [180, 177]. For reference, the mean neutron capture time in the six Daya Bay detectors was measured to be $\tau = 33.46\,\mu s$ with all liquid scintillator detectors loaded with 0.1% gadolinium by mass [85]. A first measurement of ANNIE's neutron capture time using an AmBe source is also presented in this thesis, and was found to be $\tau = 37 \pm 7\,\mu s$ (see section 8.5.2).

Larger concentrations than 0.1% gadolinium by mass are generally not used. The addition of more gadolinium has two main effects: increasing the fraction of neutron captures on gadolinium and shortening the mean capture time. Generally, adding more than 0.1% gadolinium by mass in water has diminishing returns for both effects and becomes cost-inefficient, as described below.

Shortening the mean capture time to even less than $30\,\mu s$ can increase the contamination of backgrounds in neutron captures. As the capture time constant decreases to below $30\,\mu s$, more neutrons will capture in the same time range as Michel electrons produced in muon decays (muon lifetime is 2.2 microseconds [15]) and PMT afterpulsing instrumentals (seen to occur $6 - 10$ microseconds after a high energy event; see the afterpulsing peak in calibration data in figure 8.10). There's no need to reduce the capture time further than $30\,\mu s$ if the result is to increase backgrounds.

Further increasing the concentration of gadolinium yields diminishing returns on the number of captures on gadolinium rather than water. Consider 1 gram of 0.1% Gd-doped water. The number of gadolinium atoms and hydrogen atoms in the sample is

$$\begin{aligned} N_{Gd} &= \tfrac{0.001}{157}\, mol\, Gd_{nat}\ , \\ N_H &= \tfrac{0.999*2}{18}\, mol\, H\ . \end{aligned} \tag{5.3}$$

This results in an effective cross section of

$$\sigma_{eff} = \frac{N_{Gd}}{N_{Gd}+N_H}49000 + \frac{N_H}{N_{Gd}+N_H}0.33 = 3.14\, b\ . \tag{5.4}$$

The fraction of captures on $Gd$ given this effective cross section is the gadolinium contribution to $\sigma_{eff}$ divided by $\sigma_{eff}$ itself, and is

$$f_{Gd,cap} = \frac{1}{\sigma_{eff}}\frac{N_{Gd}}{N_{Gd}+N_H}49000 = 0.90\ . \tag{5.5}$$

Thus, 90% of neutron captures already occur on gadolinium for water doped with 0.1% gadolinium by mass. From this point, larger amounts of gadolinium must be added to acquire only percent-level increases gadolinium capture fraction. This is cost-prohibitive, and higher concentrations of gadolinium can also negatively impact water transparency.

#### 5.3.4.1 Gadolinium sulfate for Gd-loading

The ANNIE collaboration has chosen to load gadolinium via the addition of gadolinium sulfate ($Gd_2(SO_4)_3$) at 0.2% concentration by mass. This compound is an electrolyte, dissolving into its $Gd^{+3}$ and $SO_4^{-2}$ constituents when placed into a solvent like water. $Gd_2(SO_4)_3$ was selected for use in ANNIE for its low corrosiveness and low absorption of light at $> 300\, nm$. An absorption curve of 0.2 % $Gd_2(SO_4)_3$ in $18M\Omega$ DI water is compared to pure DI water in figure 5.7. The absorption of light begins to increase below 300 nm, but ANNIE's PMTs are not sensitive to light in this region; above 300 nm, gadolinium doping has a small impact on the absorption length relative to pure water detector, with no observable difference above 350 nm.

There are several alternative gadolinium compounds that could be used for doping, but were not considered for use in ANNIE. Studies for gadolinium compound compatibility with water Cherenkov detectors have been performed in the past for Super-Kamiokande, with the leading

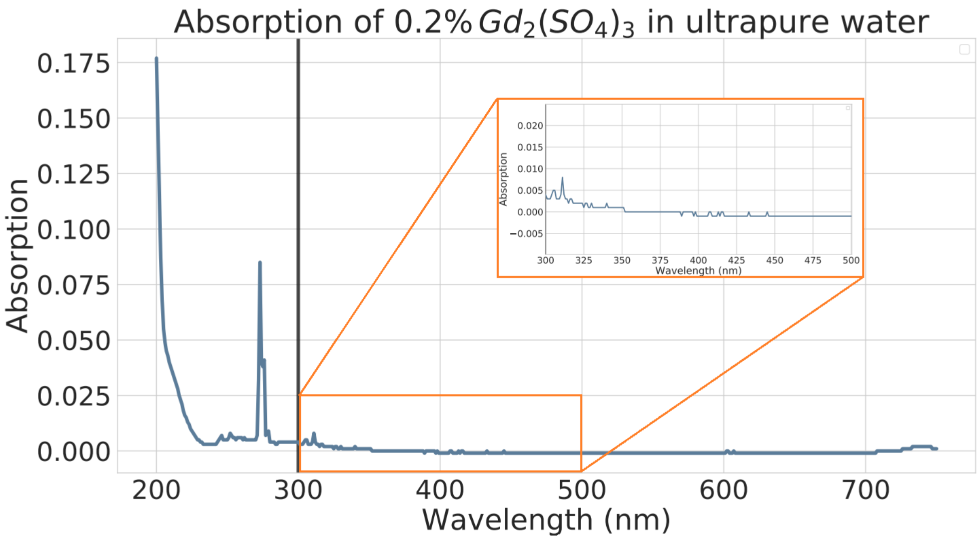

Figure 5.7. Absorption of 0.2% $Gd_2(SO_4)_3$-loaded ultrapure water relative to ultrapure water. The inset shows the absorption curve in the wavelengths of maximum sensitivity common for PMTs.

competitors being $GdCl_3$ and $Gd(NO_3)_3$ [181]. $GdCl_3$ was ruled out for use in ANNIE because the $Cl^{-1}$ ions formed in solution are corrosive and would increase the risk for rust formation on the PMT support structure. $GdCl_3$ is a good candidate for detectors that have little risk for corrosion, such as the WATCHBOY detector which is primarily composed of acrylic [171]. $Gd(NO_3)$ is not corrosive, but is effectively opaque for the entire UV region below $350\,nm$; this reduces the fraction of UV-range Cherenkov light seen by PMTs, hindering the detector's performance.

### 5.3.5 ANNIE water purification system

Gadolinium-doped water purification is more complex than pure water purification and cannot employ all of the same purification techniques. Gadolinium-doped water must be purified without removing any gadolinium or sulfate ions from the water; the gradual removal of gadolinium would steadily increase the mean neutron capture time in a Gd-doped water detector, while the removal of sulfates could create a basic solution that would encourage the formation of $GdOH$ and result in gadolinium dropping out of solution. As such, more aggressive pure water purification techniques, such as distillation or reverse osmosis (RO), are no longer an option.

Gadolinium-doped water purification systems developed and deployed prior to ANNIE helped inform the design of ANNIE's purification system. The Evaluating Gadolinium's Action on Detector Systems (EGADS) 200-ton detector served as a first testing ground for upgrading Super-Kamiokande to a Gd-doped detector. EGADS was developed to quantify the impact that gadolinium doping would have on the Super-Kamiokande detector's performance. EGADS also served as a testbed for a small-scale Gd-doped water purification system utilizing ultrafilters and nanofilters. The primary objective of the system was to remove impurities both larger and smaller than the the gadolinium and sulfate ions, a technique known as "molecular bandpass filtering".

Although the EGADS purification system demonstrated success, ANNIE has different demands and design constraints relative to EGADS/SuperK. Since space is limited in the ANNIE hall and the ANNIE tank is only 26 tons, a smaller purification system than that used by EGADS was needed. The ANNIE water purification system is briefly summarized below, but more details are available at [182].

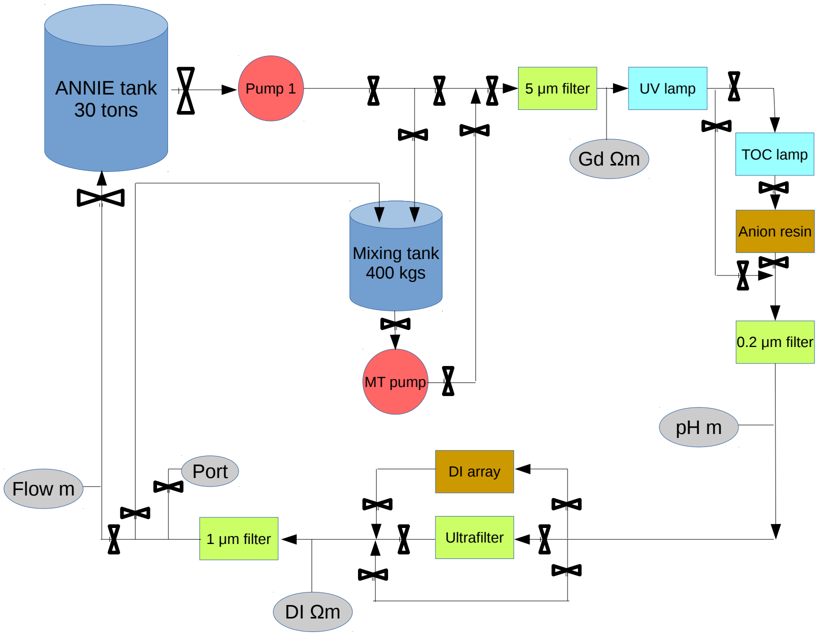

Figure 5.8. Flow diagram of the ANNIE water purification system. Figure taken from [183].

A diagram of the ANNIE water purification system is shown in figure 5.8. The initial feed from the ANNIE tank is first passed through a 5 $\mu m$ micron filter to remove larger particulates. Flow is then directed into a UV lamp, used to kill bacteria with 254 nm UV light. If desired, flow can then be passed through a TOC lamp, emitting 185 nm UV light, to break the carbon bonds of organic impurities, such as plastics leached from detector components. The anion resin follows, and is primarily used to capture nitrates and anionic impurities remaining from organics broken up by the TOC lamp. In a pure water operational mode, the TOC lamp and anion resin are bypassed and flow is directed to a mixed bed DI resin array that removes anions and cations, producing ultrapure water with resistivities of $18-20\ M\Omega$. An ultrafilter ($\sim$ 30 nm pore size) is also installed to remove any iron in colloidal form, such as bacterial iron or larger iron-based organic compounds. A final $1\ \mu m$ filter removes any particulates collected from the water system's components. A secondary loop contains a mixing tank, used to stir gadolinium sulfate into the ANNIE water system.

Water quality is monitored through an array of sensors built into the system and external Raspberry Pis. Flow rate, water acidity, and water resistivity readings are available through digital displays on the water system's front panel. This panel, along with the rest of the hall, is monitored with an array of Raspberry Pi cameras, whose photos are transferred to the ANNIE web sever for monitoring during shift. Several Raspberry Pis also have water sensors attached, which send alarms to the ANNIE shift slack if a leak ever develops in the water system.

## 5.4 Muon Range Detector (MRD) and Front Anti-Coincidence Counter (FACC)

The MRD and FACC are the most pivotal systems to muon detection in ANNIE. The Front Anti-Coincidence Counter (also referred to as the FACC, the "front veto", or the Front Muon Veto (FMV)) is responsible for tagging muons produced upstream of the ANNIE tank, as muons not generated via neutrino interactions in the tank can contaminate the charged-current neutrino interaction dataset. The MRD's primary use is to detect and reconstruct any muons produced in the tank volume via charged-current neutrino interactions. The two subsystems pair to veto non-tank muons and reconstruct neutrino interaction-based muons.

### 5.4.1 FACC overview

The FACC is used to reject events originating from muons produced upstream of the ANNIE tank. The FACC is composed of 26 plastic scintillator paddles, mounted in two rows of 13 paddles. The FACC was built from components of the Collider Detector at Fermilab (CDF) [184]. If any FACC paddle triggers in coincidence with a beam spill, the event can be flagged as a non-neutrino interaction. The FACC's data readout is integrated into that of the MRD as seen in figure 5.13. The refurbished and installed FACC is shown in figure 5.9.

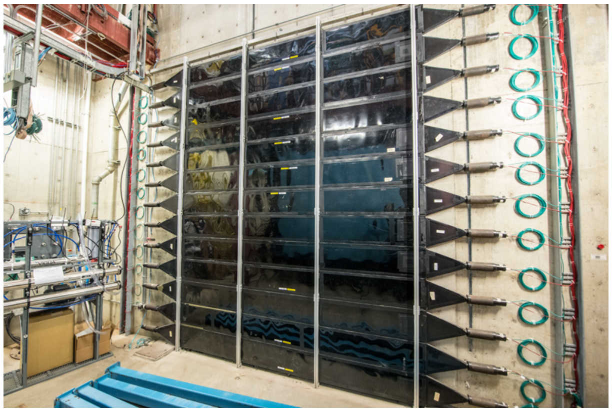

Figure 5.9. Picture of the FACC system with the ANNIE tank removed. The paddles reside upstream from the ANNIE tank (not yet installed in figure) for maximal solid angle coverage of the ANNIE tank.

### 5.4.2 MRD overview

The Muon Range Detector (MRD) resides behind the ANNIE water tank just downstream of the beam, and is used to track muons produced by charged-current neutrino interactions. The MRD is composed of 307 plastic scintillator paddles coupled to 2-inch PMTs. There are eleven rows of paddles, with each row being either horizontally or vertically oriented. Each row of paddles is separated with iron plates to help slow the traversing muon, and can be moved to any desired position on the pink frame via a mounted pulley system (see figure 5.10).

As a muon passes through the MRD, the muon's direction and penetration depth can be determined to reconstruct the muon's momentum. A muon must be fully contained in the MRD to effectively reconstruct the muon track; fortunately, the MRD is sensitive to a broad range of muon energies consistent with the BNB neutrino energy spectrum. A GEANT4-based simulation of muons generated in the ANNIE tank and passing through the MRD demonstrates this in figure 5.11. Muons with energies between 200-1200 MeV will stop somewhere in the MRD, depending on the muon's angle of incidence. As such, a large portion of muons produced from BNB-based charged-current neutrino interactions should be fully reconstructable in the MRD

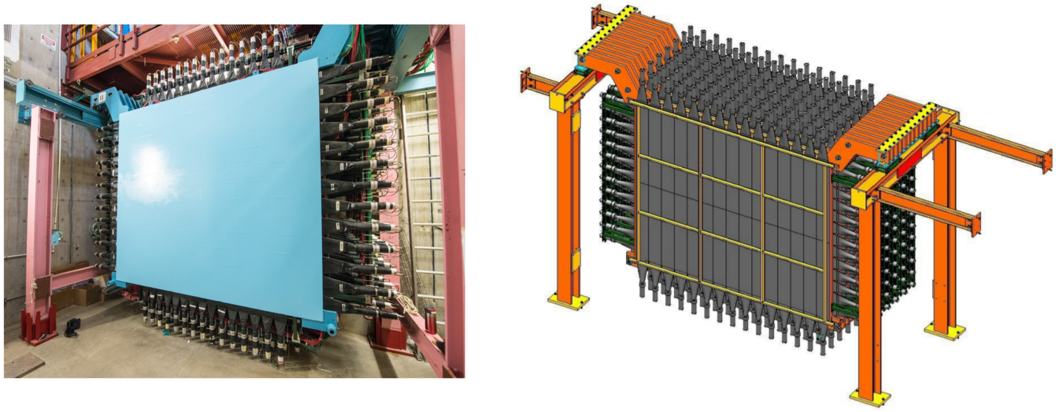

Figure 5.10. Front view of the MRD (left) and schematic of the MRD paddle positions (right).

(recall the BNB energy spectrum peaks at 700 MeV, seen in figure 5.5).

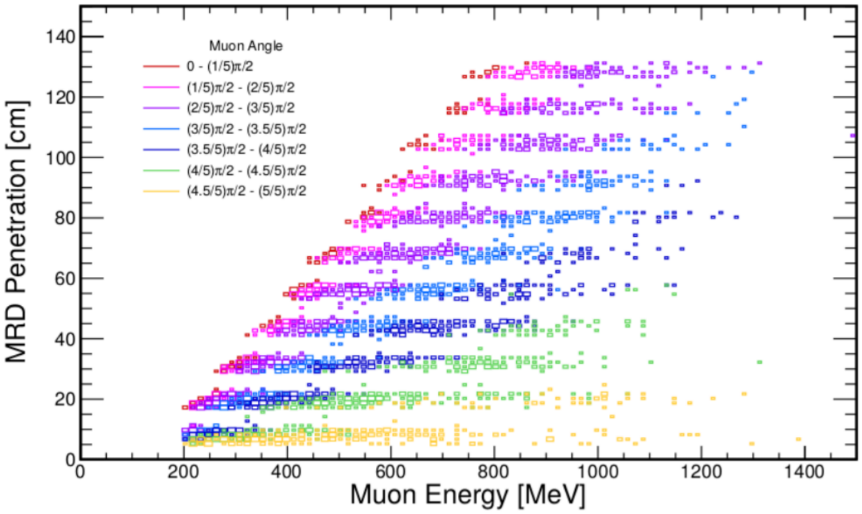

Figure 5.11. Penetration depth of tank-based muons into the MRD. Results for muons of different incident angles relative to the beam axis (color-coded) are shown. The MRD is sensitive to muons originating from the ANNIE tank with energies between 200-1200 MeV. Figure from [169].

## 5.5 ANNIE data acquisition (DAQ) electronics

The ANNIE data acquisition electronics are responsible for collecting and storing data from the ANNIE photomultiplier tubes and LAPPDs. The acquisition of data from tank PMTs, MRD PMTs, and LAPPDs is conducted by three separate DAQ subsystems. A single Central Trigger Card (CTC) records all trigger types and timestamps that triggered data acquisition in any subsystem to facilitate combining the datastreams in post-processing. The tank PMT data acquisition is performed with three VME crates, each filled with Analog to Digital Converter (ADC) cards which store full PMT waveforms. The MRD data acquisition is performed with two CAMAC crates filled with discriminators and Time to Digital Converter (TDC) cards, which store timestamps of when any discriminator channel crosses a preset voltage threshold. The LAPPD data acquisition is currently in development, and will not be discussed in this thesis.

In a beam run configuration, neutrino beam data acquisition is triggered by a pulse from the Resistive Wall Monitor (RWM). The RWM is coupled directly to an inductor in the BNB hall, and sends an analog pulse to the ANNIE hall for every beam spill incident on the beryllium target. Two microseconds of tank PMT waveforms are acquired for every RWM pulse trigger; the readout is extended to $\sim 70$ microseconds if any single tank PMT detects a pulse consistent with at least 5 photoelectrons. Four microseconds of MRD TDC data is acquired for every RWM pulse. See section 9.2 for more information on the beam profile relative to the acquisition window in each subsystem.

The control of data acquisition is managed through two DAQ servers located in the ANNIE hall. The DAQ server communication used to configure the CTC, VME CPU boards, and CAMAC CPU boards is performed using the ToolDAQ framework. The DAQ server is also used to start/stop runs and adjust run configurations. A chain of tools in ANNIE's ToolAnalysis framework are used to combine raw CTC, Tank PMT, and MRD/FACC data into single events which can be used for physics analyses.

The following sections detail the electronics subsystems associated with the tank PMTs and the MRD/FACC PMTs. The LAPPD data acquisition electronics are currently still in development, and will not be covered.

### 5.5.1 Tank PMT electronics and DAQ

The Tank PMTs are powered by a CAEN SY527 crate with A374P control cards. Each tank PMT's high voltage setpoint is individually configurable. A LABVIEW-based GUI was developed to interface with both the Tank PMT and MRD/FACC HV electronics through serial port communication, making remote control straightforward for ANNIE shifters.

The Tank PMT waveform collection workflow is shown in figure 5.12. The tank PMT cables are connected to pickoff boxes, which provide the PMT high voltage and extract the PMT signal. All pickoff box connections are impedance-matched to the 50$\Omega$ impedance of the tank PMTs. PMT waveforms are digitized using custom K0T0 4-channel 12-bit 500 MHz ADC cards. The K0T0 cards have a 2 nanosecond time resolution and voltage readout resolution of $2.415\,V/2^{12}$ ADC counts. Each VME crate housing the ADC cards contains one CPU board; the CPU board collects PMT data from the ADC cards via the VME backplane, and transfers the data to the DAQ servers for storage and eventual processing.

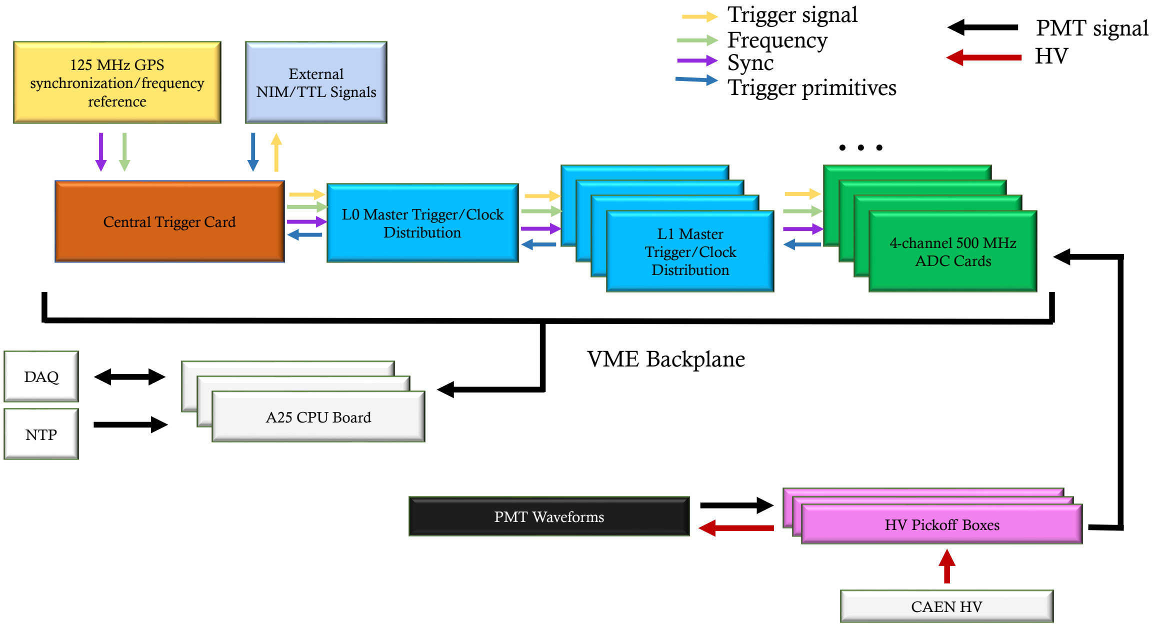

Figure 5.12. Diagram of the ANNIE Tank PMT dataflow. Figure modified from [185].

The CTC forms the foundation for triggering data acquisition in ANNIE's tank PMTs. A 125 MHz GPS clock reference is sent to the CTC, which distributes sync signals to all ADC cards to keep all ADC card times in-sync. The CTC is connected to all ADC cards through a set of Trigger/Clock distribution boards, which act as the pathway for delivering sync signals and timing as well as receiving trigger primitives. Triggers to collect data from all ADC cards are generated based on any combination of logic based on signals collected through external NIM/TTL signals (beam signals, LED trigger signals, AmBe source signals, etc.) and the ADC card trigger primitives (number of PMTs hit or number of PMTs *not* hit). When the CTC determines data acquisition should occur, trigger signals are sent to all ADC cards and any desired

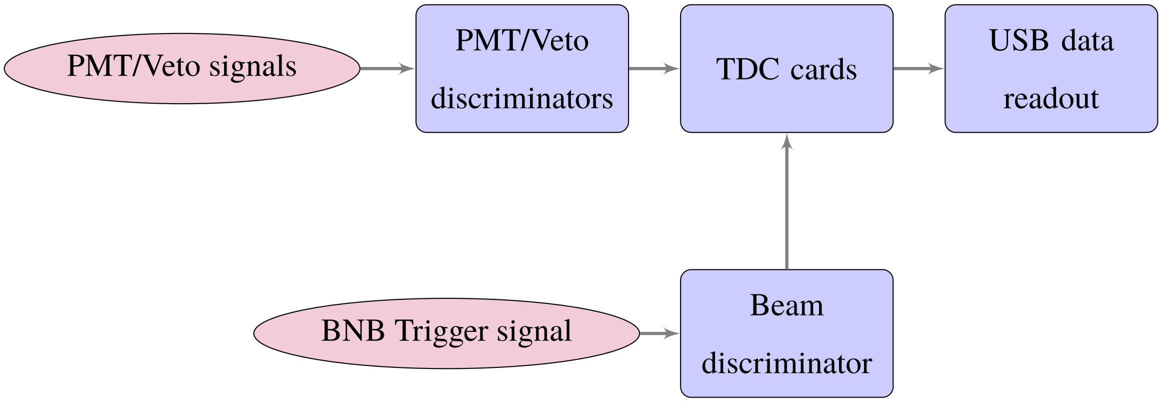

Figure 5.13. Data flow for MRD electronics.

external electronics (such as the LEDs).

### 5.5.2 MRD/FACC electronics and data acquisition

The MRD and FACC PMTs are powered by A LeCroy crate filled with LeCroy 1440 HV supply boards. Each channel's voltage setpoint is individually configurable, with a $V_{max} = 2.5\,kV$ and $I_{max} = 2.5\,mA$. All HV is controlled through the same LABVIEW-based GUI as used for the tank PMT HV control.

The MRD/FACC data flow is shown below in figure 5.13. PMT signals from the MRD and FACC PMTs are fed into LeCroy 4413 discriminators mounted in a NIM crate. The output from the PMT discriminators are fed to an array of 250 MHz LeCroy time-to-digital converter (TDC) cards. As such, only hit time information is collected from the MRD channels. Readout from all TDC cards is triggered by an 8-channel discriminator, which distributes trigger pulses to each TDC card when it receives an RWM pulse. TDC data is read out through a NIM crate-USB interface card by the DAQ servers and stored locally for future processing.

# Chapter 6

# Calibration and monitoring

Detector calibration and monitoring are essential tasks for safe detector operation and successful analysis of detector data. While calibration is the utilization of well-understood or controllable physical processes to quantify a detector's performance, monitoring is the continual tracking of the detector's state over time to confirm the validity of past calibration as it pertains to future data. Calibration and monitoring prior to, and during, data-taking are key to relating a detector's signal to known physics interactions and benchmarking detector performance for observing these interactions. This process is critical for comparing any physics analysis performed with detector data to measurements made with other detectors, a necessary step in making multiple measurements of the same physical processes.

This chapter describes the procedures utilized to calibrate and monitor the ANNIE detector. Calibration sources and their properties are first described, followed by a description of the calibration procedures performed on the ANNIE tank electronics. The chapter closes with a brief discussion of the monitoring techniques used to track the water quality and transparency in the ANNIE tank.

## 6.1 Calibration sources

A suite of calibrations were performed in the ANNIE detector using a combination of well-characterized light sources and radioactive sources. The main calibration sources utilized for commissioning ANNIE include controlled light sources for characterizing ANNIE's photodetectors and an Americium-Beryllium source to study ANNIE's response to neutron captures on gadolinium. Through-going muons are also used to quantify the total charge observed due to Cherenkov light per unit of energy deposition (see section 9.5.1).

### 6.1.1 Stationary LED fibers

The ANNIE tank needed in-situ light sources for performing calibration and monitoring studies. I designed and constructed six Optical Fiber Modules (OFMs) installed on the ANNIE inner structure for light injection.

A cross-sectional diagram of the OFMs is shown in figure 6.1. An optical fiber is installed in polypropylene tubing, which provides protection and rigidity to the fiber. The fiber is glued into an acrylic disk, which acts as the OFM's light injection window. The acrylic disk is then glued to a PVC tube, and the tube is filled with epoxy to provide additional support to the optical fiber. Stainless steel zip ties are used to attach the OFM to the ANNIE frame.

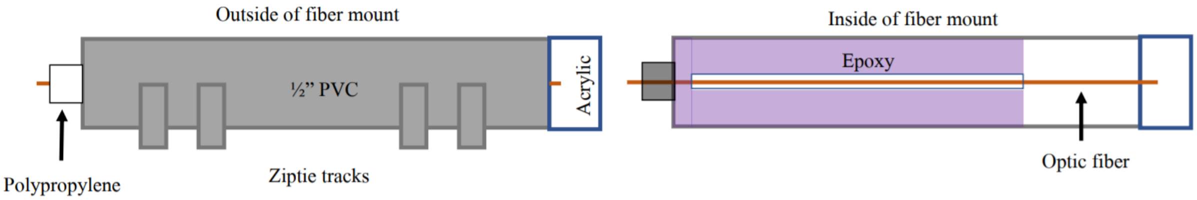

Figure 6.1. Cross section of an ANNIE optical fiber module. All materials were chosen for gadolinium compatibility and durability throughout ANNIE's operation.

The optical fiber is a $700\,\mu m$ diameter multimode optical fiber ($300 - 2000\,nm$ bandwidth) purchased from Thorlabs. The fiber was chosen for its large Numerical Aperture (0.5 NA), which provides the injected light a broad diffusion angle upon exiting the fiber, as well as its material compatibility with gadolinium-doped water as tested at UC Davis.

Each OFM is mounted at one of six different positions inside the ANNIE tank. Four OFMs are mounted on side panels facing across the ANNIE PMT volume, one OFM is mounted on the bottom panel looking upward, and one is mounted at the top of panel 8 at an angle looking directly to the tank bottom. A panel map with LED positioning is shown in figure 6.2, and a picture of the PMT structure with the OFM positions illustrated is in figure 6.3.

Six LEDs are connected to each optical fiber and used to inject light into the ANNIE tank. LED intensities are set based on the intensity read out by a photodiode installed on the LED

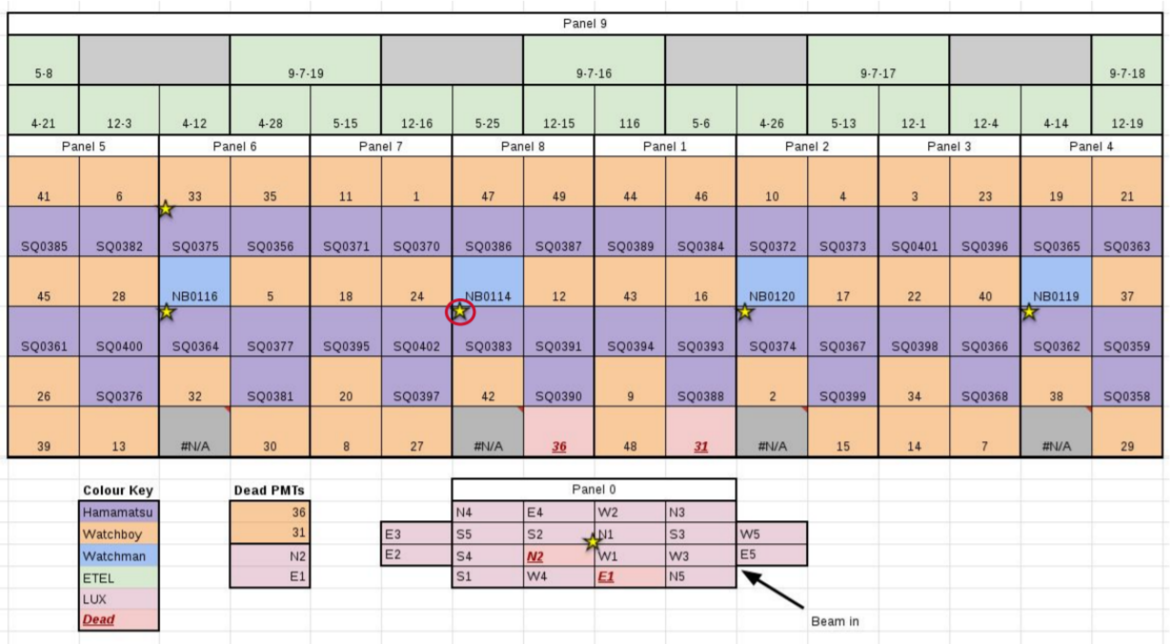

| Panel 9 | | | | | | | | | | | | | | | |
|---|---|---|---|---|---|---|---|---|---|---|---|---|---|---|---|
| 5-8 | | | 9-7-19 | | | | 9-7-16 | | | | 9-7-17 | | | | 9-7-18 |
| 4-21 | 12-3 | 4-12 | 4-28 | 5-15 | 12-16 | 5-25 | 12-15 | 116 | 5-6 | 4-26 | 5-13 | 12-1 | 12-4 | 4-14 | 12-19 |
| Panel 5 | | Panel 6 | | Panel 7 | | Panel 8 | | Panel 1 | | Panel 2 | | Panel 3 | | Panel 4 | |
| 41 | 6 | 33 | 35 | 11 | 1 | 47 | 49 | 44 | 46 | 10 | 4 | 3 | 23 | 19 | 21 |
| SQ0385 | SQ0382 | SQ0375 | SQ0356 | SQ0371 | SQ0370 | SQ0386 | SQ0387 | SQ0389 | SQ0384 | SQ0372 | SQ0373 | SQ0401 | SQ0396 | SQ0365 | SQ0363 |
| 45 | 28 | NB0116 | 5 | 18 | 24 | NB0114 | 12 | 43 | 16 | NB0120 | 17 | 22 | 40 | NB0119 | 37 |
| SQ0361 | SQ0400 | SQ0364 | SQ0377 | SQ0395 | SQ0402 | SQ0383 | SQ0391 | SQ0394 | SQ0393 | SQ0374 | SQ0367 | SQ0398 | SQ0366 | SQ0362 | SQ0359 |
| 26 | SQ0376 | 32 | SQ0381 | 20 | SQ0397 | 42 | SQ0390 | 9 | SQ0388 | 2 | SQ0399 | 34 | SQ0368 | 38 | SQ0358 |
| 39 | 13 | #N/A | 30 | 8 | 27 | #N/A | ***36*** | 48 | ***31*** | #N/A | 15 | 14 | 7 | #N/A | 29 |

| Colour Key |
|---|
| Hamamatsu |
| Watchboy |
| Watchman |
| ETEL |
| LUX |
| ***Dead*** |

| Dead PMTs |
|---|
| 36 |
| 31 |
| N2 |
| E1 |

| | Panel 0 | | | | |
|---|---|---|---|---|---|
| | N4 | E4 | W2 | N3 | |
| E3 | S5 | S2 | N1 | S3 | W5 |
| E2 | S4 | ***N2*** | W1 | W3 | E5 |
| | S1 | W4 | ***E1*** | N5 | |

Figure 6.2. Panel map of PMTs in the ANNIE tank with the approximate LED positions marked with a star. Each box corresponds to an approximate PMT position and its cable label. Panel 0 is the bottom panel, panels 1-8 are the side panels, and panel 9 is the top panel.

| LED Properties | Value |
|---|---|
| Emission wavelength (nm) | 468 |
| Duration of light pulse (ns) | 5-20 |
| Pulse repetition frequency (Hz) | 1-1000 |
| Width of amplitude spectrum (%) | 1.3 |
| Error of flash energy control (%) | 0.5 |
| Error of flash energy stabilization (%) | 0.3 |

Table 6.1. Key properties for the ANNIE LEDs. Further details available at [187].

electronics board, and can either fire at fixed frequency or be externally triggered by the ANNIE DAQ. A general overview of the relevant LED properties is provided in table 6.1 [187].

### 6.1.2 Cosmic muons and "dirt muons"

Cosmic muons and so-called "dirt muons" act as a valuable calibration source for ANNIE's response to GeV-scale muons. As seen in figure 6.4, most cosmic muons observed at sea level

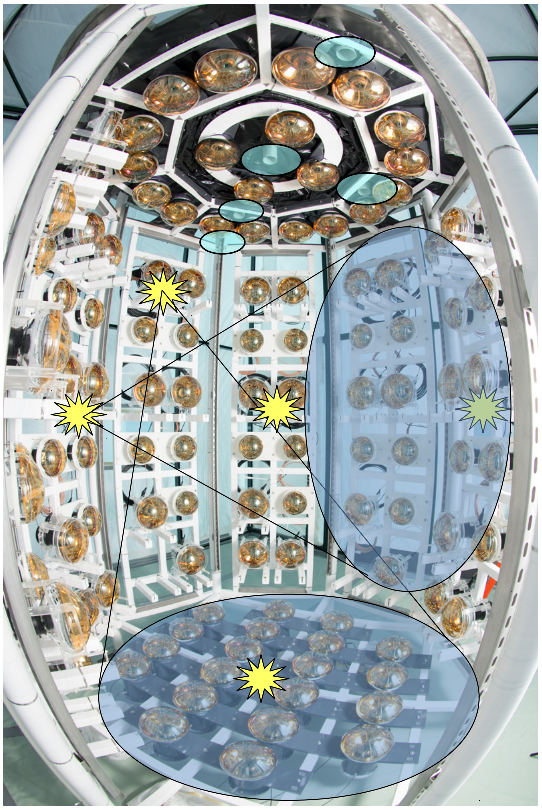

Figure 6.3. Picture of the ANNIE inner structure with stars marking the LED OFM mounting positions. One LED OFM is not shown, which is mounted approximately at the point where the photo was taken. Picture from [186].

have energies at the GeV-scale [188]. This energy regime overlaps nicely with muon energies anticipated following muon neutrino charged-current interactions in the BNB beam line. Furthermore, muon neutrino charted-current interactions that occur in the dirt in front of the ANNIE tank (known as dirt muons) can also produce GeV-scale muons utilizable for calibration purposes.

The ionization energy loss per unit distance traveled in a medium for muons can be characterized using the Bethe-Bloch equation. To first order however, GeV-scale muons have a constant energy deposition per distance traveled in a medium and are minimum-ionizing particles (MIPs) [189]. In this case, ANNIE's detector response to minimum-ionizing muons in both the ANNIE tank and MRD can be approximately characterized using through-going cosmic and dirt muons of known path length.

The energy deposition of a minimum-ionizing muon per unit path length varies depending

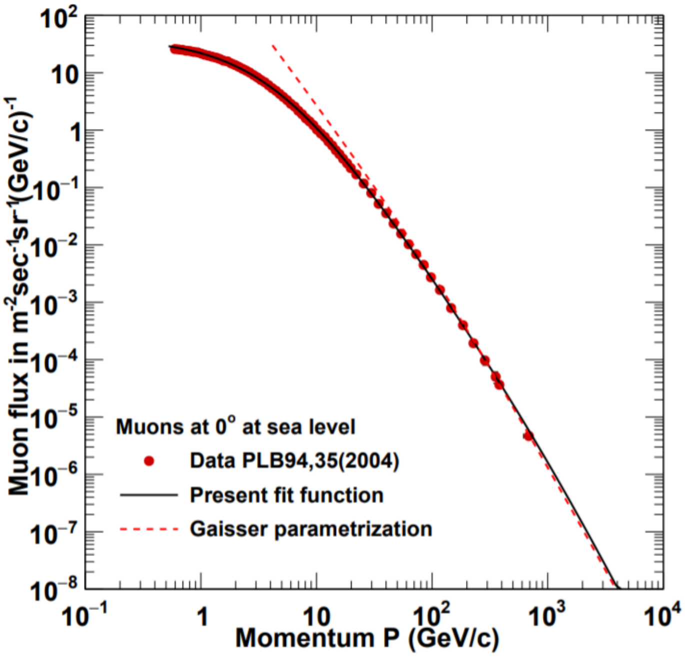

Figure 6.4. Flux distribution as measured at sea level at Earth for muons with zenith angle $0^o$. The best fit is a power law parameterization of the form $I \propto I_0(E)^{-n}$, where $I_0$ is the vertical muon flux integrated over energy. Figure from [188].

| Material | ANNIE component | $\rho$ $(g/cm^3)$ | $-\langle dE/dx \rangle_{min}$ $(MeV cm^2/g)$ | $E_{\mu c}$ $(GeV)$ |
|---|---|---|---|---|
| Iron (Fe) | MRD steel layers | 7.874 | 1.451 | 345 |
| Water ($H_2O$) | ANNIE tank water | 1.000 | 1.992 | 1032 |
| Polystyrene ($[C_6H_5CHCH_2]_n$) | Scintillator paddles | 1.060 | 1.936 | 1183 |
| Air (dry, 1 atm) | ANNIE hall | $1.205 \times 10^{-3}$ | 1.815 | 1114 |

Table 6.2. Muon energy loss information for several detector materials in ANNIE. $E_{\mu c}$ is the energy at which electronic and radiative losses become equal and the minimum-ionizing particle approximation breaks down considerably. Table numbers from [189].

on the medium being traversed. The $dE/dx$ for minimum ionizing particles in several materials in the ANNIE detector is provided in table 6.2 [189].

### 6.1.3 AmBe source

Neutrons emitted from an Americium-Beryllium (AmBe) source are utilized to characterize ANNIE's response to neutron captures on gadolinium. An AmBe source is a mixed composition of $^{241}Am$ and $^{9}Be$. When an Americium atom undergoes alpha decay to $^{237}Np$, the following reaction is possible:

$$\alpha +^{9} Be \; (\alpha, n) \; \rightarrow \; ^{12}C* + n \; \rightarrow \; ^{12}C + \gamma(4.44\,MeV) \; + n \; . \tag{6.1}$$

Past measurements of AmBe sources indicate that the ratio of AmBe interactions with a prompt $4.4$ MeV gamma to all interactions producing a neutron is $R = 0.58$ [190, 191, 192]. Thus, an AmBe source regularly emits a prompt 4.44 MeV gamma in coincidence with a single neutron. With the right configuration, the gamma signal can be utilized to trigger the ANNIE detector and acquire data that can contain a neutron capture on gadolinium with the expected $\sim 30\,\mu s$ characteristic neutron capture time.

The ANNIE AmBe source has an Americium activity of 100 $\mu Ci$. The typical efficiency of $\sim 10^{-4}$ for the $(\alpha, n)$ interaction and a 4.44 MeV de-excitation gamma produces approximately 100 tagged neutrons per second [193].

#### 6.1.3.1 Triggering scheme

A single AmBe source data aqcuisition is triggered by the 4.44 MeV de-excitation gamma to detect the correlated neutron. A Bismuth Germanium Oxide (BGO) scintillation crystal is mounted above the AmBe source and instrumented with two Silicon PhotoMultipliers (SiPMs), referred to as the “AmBe source SiPMs”. When a 4.44 MeV $\gamma$ scatters in the BGO crystal, a burst of light ($\sim$ $8500$ photons/MeV) is detected by the AmBe source SiPMs which trigger the ANNIE data acquisition. When the AmBe neutron thermalizes and captures on gadolinium in the detector volume, the tank PMTs will observe the Cherenkov light produced by de-excitation gamma rays scattering off electrons in the water. A diagram of a single AmBe source acquisition is shown in figure 6.5.

#### 6.1.3.2 Source enclosure

The ANNIE AmBe source uses an acrylic housing to waterproof and protect all source components during deployment. The acrylic housing has a removable lid that is sealed using a double gasket design with four acrylic screws. The AmBe source itself is double-encapsulated in two stainless steel layers to ensure containment if one cover layer fails. A small steel plate separates the BGO crystal and AmBe source to reduce scintillation noise that could result from X-rays

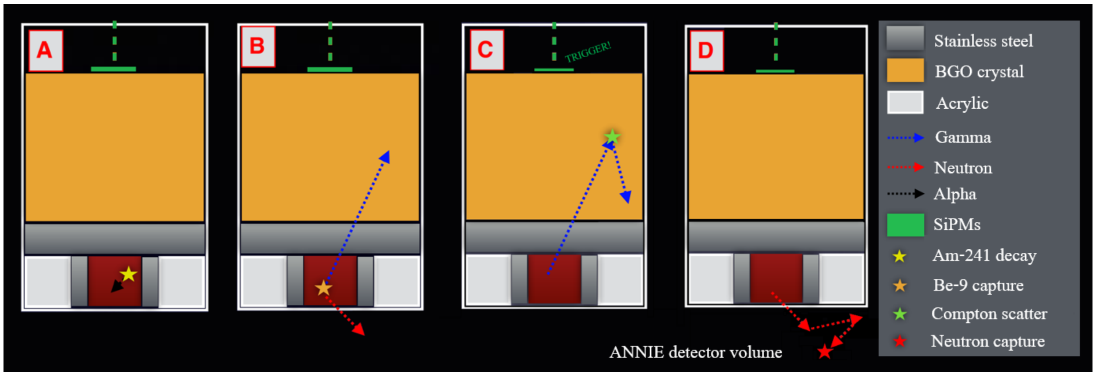

Figure 6.5. Diagram visualizing the principle of operation for the ANNIE AmBe source. When a 4.44 MeV gamma is produced by the AmBe source and scatters in the BGO crystal, the produced scintillation light is observed by the AmBe source SiPMs and triggers ANNIE data acquisition. Any neutron that thermalizes in the tank and captures on gadolinium is observed by the photodetectors. Figure modified from [194].

produced by $^{237}Np$. A photo of the AmBe source components is shown in figure 6.6.

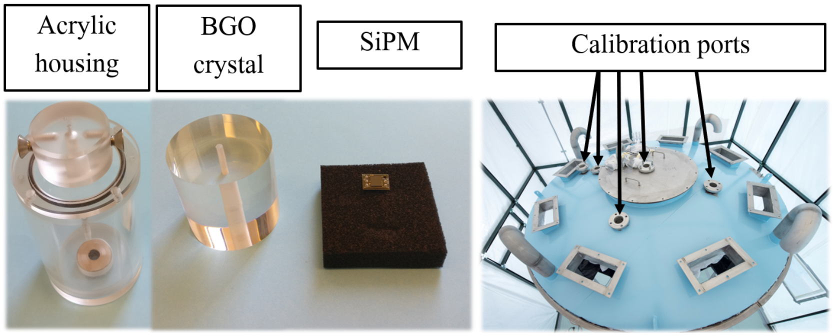

Figure 6.6. Pictures of the ANNIE AmBe source housing and components (left) and the ANNIE calibration ports (right).

When deployed in the ANNIE tank, the entire housing is surrounded with a black polyethylene bag. The bag optically isolates the BGO crystal from the tank volume, preventing BGO scintillation light from producing photoelectrons in the tank PMTs. The housing and black bag fit into any of the five calibration ports installed in the ANNIE tank lid.

#### 6.1.3.3 SiPM

The AmBe source utilizes two 60035 J-series SiPMs from ON Semiconductors to detect scintillation in the BGO crystal. Typical operating conditions and specifications for the J-series SiPMs are given in table 6.3. The AmBe source SiPMs are operated in a slow-pulse mode, resulting in longer pulses ($\sim \mu s$) that provide the option to perform pulse shape discrimination for signal/background separation. An example SiPM pulse from an ANNIE calibration run is shown

| Parameter | Value |
|---|---|
| Active area | 6 mm × 6 mm |
| Number of microcells | 22,292 |
| Typical breakdown voltage ($V_{BD}$) | 24.2 - 24.7 V |
| Typical overvoltage OV ($V_{op} = V_{BD} + OV$) | 2.5-6 V |
| Typical gain for OV ranges | 2.9 - 6.3 $\times 10^6$ |
| Typical dark count rate for OV ranges | 50-150 kHz/mm$^2$ |
| Peak quantum efficiency wavelength | 420 nm |
| Typical QE for OV ranges and peak QE $\lambda$ | 30-38 % |

Table 6.3. Several relevant properties for the AmBe source SiPMs. Further details are available at [195].

in figure 6.7.

Single pulse in SiPM 1 from through-going muon (Run 1612)

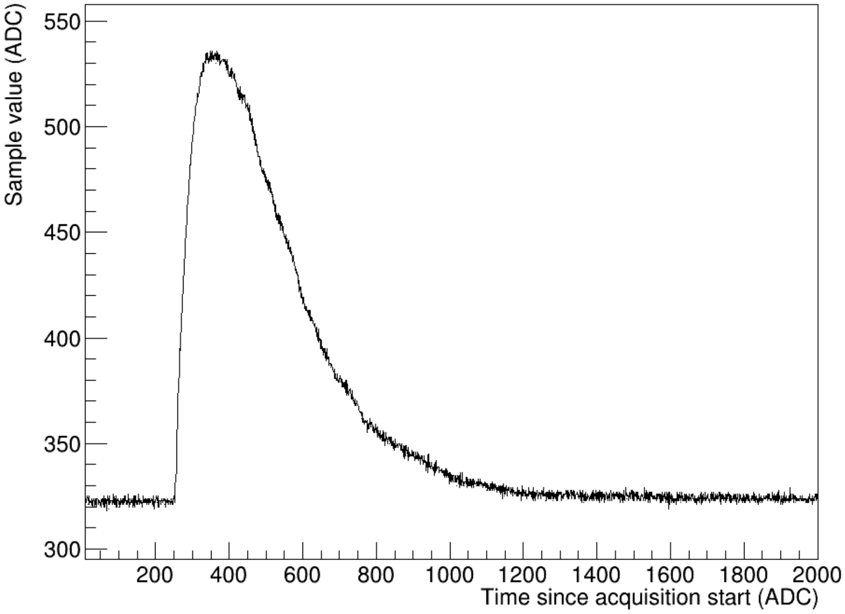

Figure 6.7. Example SiPM pulse acquired during an ANNIE calibration run. The SiPMs operate in a "slow pulse" configuration, resulting in pulse widths on the order of 1-2 microseconds.

Note that while SiPM gains similar to those of conventional PMTs ($O(10^7)$) are achievable at much lower operating voltages than PMTs, the dark count rate for SiPMs at room temperature

($50 - 150$ kHz/$mm^2$) is much higher than that for conventional PMTs ($<10$ kHz per PMT). As such, SiPMs require triggering thresholds corresponding to multi-photoelectron events to have acceptable signal-to-background ratios when acquiring data.

The bias voltage and charge trigger thresholds of the AmBe source SiPMs were optimized on a teststand by maximizing the fraction

$$f_{SB} = \frac{R_{source}}{R_{no\,source}} \;, \tag{6.2}$$

where $R_{source}$ is the triggering rate with the AmBe source installed and $R_{no\,source}$ is the triggering rate with no source. The $R_{no\,source}$ triggers were primarily due to cosmic muons passing through the BGO crystal. The signal-to-noise ratio on the teststand for these settings was maximized at $R_{SB} = 25$ for a bias voltage of $29\,V$; total charge seen in source vs. no source data is shown in figure 6.8.

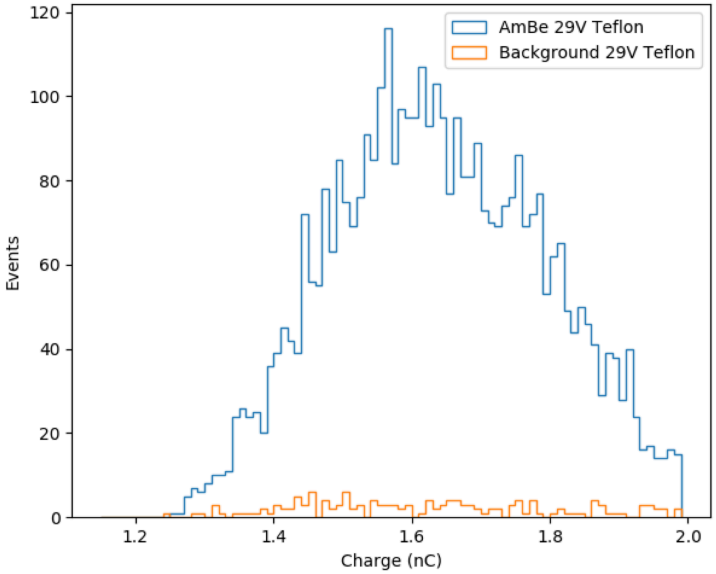

Figure 6.8. Distributions of the total AmBe source SiPM charge observed with and without the AmBe source on the teststand. Acquisitions with total charges in the range $1.2\,nC < C_{tot} < 2.0\,nC$ are shown. The rate of events is much higher for data taken with the source installed. The background distribution is primarily due to through-going muons.

$V_{bias} = 29\,V$ was selected as the default point for AmBe calibration runs, and results in a high trigger purity in ANNIE tank deployments when combined with a tank activity cut to reject through-going muons (see sections 8.2 and 8.3).

## 6.2 PMT gain calibration

The primary goal of PMT gain calibration is to determine the total charge produced following the amplification of a single photoelectron conversion, and to determine how this total charge changes as a function of the voltage applied to the PMT's base. This information is pivotal to extracting the number of photoelectrons detected by a PMT during data acquisition (and thus, how much light was incident on the PMT). Matching gains of all PMTs in a detector also makes the detector's response to physics interactions more uniform across the detector. PMT gain calibration must be performed individually for each PMT, as each PMT has a unique gain vs. voltage curve.

The gain calibration of all PMTs in the ANNIE tank was conducted using the six LEDs and OFMs described in section 6.1.1. After installing the OFMs, I conducted the ANNIE PMT gain calibration campaign. This involved tuning the LED intensities to single photoelectron levels, taking LED calibration runs at various PMT voltages, extracting the single photoelectron charge for each PMT, and gain-matching all PMTs.

### 6.2.1 Estimation of total charge in PMT pulses

Single photoelectron pulses were extracted from calibration runs where all six LEDs were fired. The intensity of the LEDs were set such that there was a single pulse for approximately one in every ten triggers; this ratio ensured that the probability of observing more than one photoelectron in any single trigger was adequately suppressed. Each LED pulsed once per acquisition, and each LED was pulsed 150 nanoseconds after another to ensure stable PMT baselines were achieved prior to each LED's flash. The LED light arrival times were different for every PMT due to cable delay corrections and light transit time from the LED to the PMT positions, and were manually found for each PMT. The total hit time distribution for a single PMT during a calibration run is shown in figure 6.9.

Prior to characterizing PMT pulses due to LED light, the PMT's waveform baseline was estimated. For each individual LED pulse window, the PMT waveform's baseline was estimated using 30 waveform samples prior to the LED pulse window. The baseline and variation in the waveform baseline was estimated by taking the mean and standard deviation of these samples.

In the LED pulse window, pulses were characterized by integrating the PMT's voltage signal

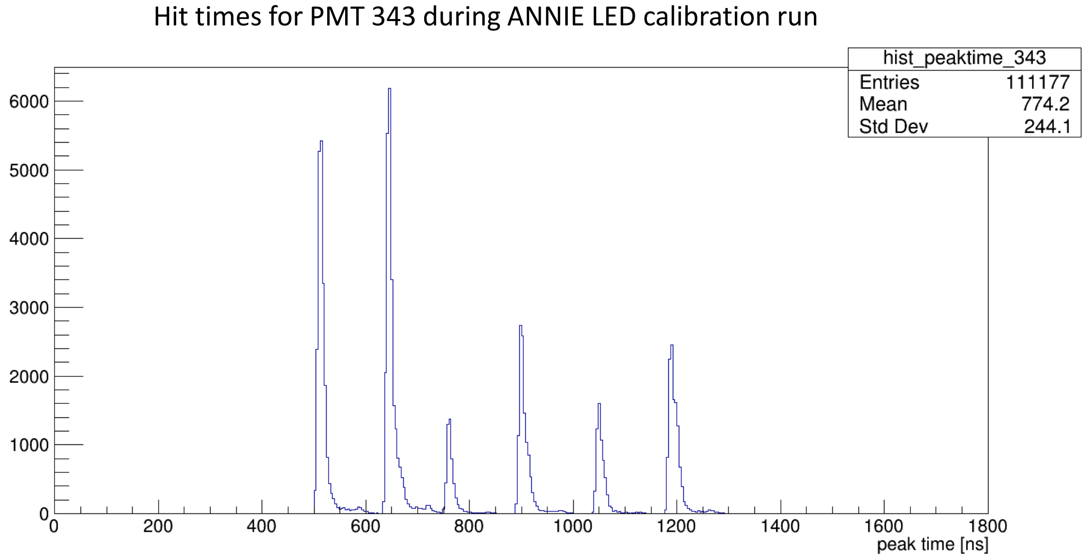

Figure 6.9. Hit time distribution for a single photomultiplier tube in an ANNIE calibration run. Six distinct hit populations are visible, each due to the successive pulsing of one LED 150 nanoseconds after the previous LED. A single PMT will see different levels of light from each LED, causing different amplitudes in each LED's hit time distribution.

around the maximum peak observed in the LED window. This algorithm was adopted from the ANNIE PMT teststand data analysis and incorporated into the ANNIE analysis software framework. First, the waveform sample with the highest analog-to-digital conversion (ADC) count was found in the LED pulse window. The waveform was then integrated to the left and right of this maximum until the waveform had a value less than 10% the maximum peak on each side. A diagram of the entire baseline and pulse estimation procedure is shown in figure 6.10.

The total voltage measured for a photoelectron pulse can be converted to a total charge using the signal cable's impedance. According to Ohm's law,

$$I\left(t\right)R = V\left(t\right) \ , \tag{6.3}$$

where $V$ is the voltage on the PMT observed above the baseline estimation, $I$ is the current through the PMT, and $R$ is the resistance of the PMT base. Integrating both sides and dividing by the resistance yields

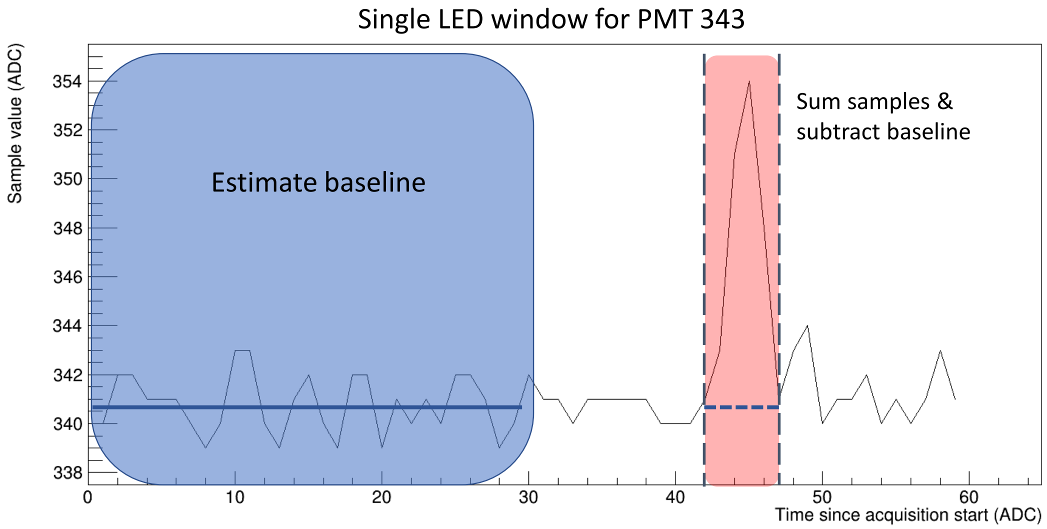

Figure 6.10. Diagram of the pulse extraction process for LED calibration. The waveform's baseline is estimated using 30 samples prior to the LED flashing window. The maximum of the LED pulse window is taken as the characteristic pulse, and integrated to either side until reaching an ADC value at or below 10% of the maximum peak.

$$\int_{t_i}^{t_f} I(t)dt = Q_{tot} = \frac{1}{R}\int_{t_i}^{t_f} V(t)dt \ . \tag{6.4}$$

Thus, the total charge produced given one single photoelectron's production can be found by integrating the total PMT voltage observed for a single photoelectron pulse and dividing by the signal cable's impedance. Given the PMT signal voltage waveforms are discretized in the analog-to-digital conversion process, equation 6.4 takes the form

$$Q_{tot} = \frac{\alpha_V}{R}\sum_{i=0}^{N}(A_i - A_{BL})\Delta t \ , \tag{6.5}$$

where $N$ is the number of bins in a digitized pulse, $A_i$ is the digitizer ADC count measured in bin $i$, $A_{BL}$ is the estimated baseline ADC value, $\alpha_V$ is the conversion from ADC count to voltage ($2.415\,V$ per $2^{12}$ ADC counts for the ANNIE digitizers), and $\Delta t$ is the time per digitizer bin (2 ns for the ANNIE digitizers).

### 6.2.2 Single photoelectron charge characterization

Each PMT's single photoelectron gain is extractable by fitting the charge distribution observed for many LED pulses with a model of the expected features given instrumental noise, signal amplification, and multi-photoelectron pulse contamination. The model used to fit the charge distributions observed in ANNIE's PMTs has the form

$$\begin{aligned} Q(x) = A_{ped} \cdot Gauss(x, \mu_{ped}, \sigma_{ped}) + Be^{-\frac{x-a}{\tau}} H(Q - \mu_{ped}) + \\ A_{1PE} \cdot (Gauss(x, \mu, \sigma) + Gauss(x, f_\mu \cdot \mu, f_\sigma \cdot \sigma)) + \\ A_{2PE} \cdot \Big( Gauss(x, 2\mu, \sqrt{2}\sigma) + Gauss(x, (1 + f_\mu) \cdot \mu, \sqrt{1 + f_\sigma} \cdot \sigma) \Big) \ , \end{aligned} \tag{6.6}$$

where

$$Gauss(x, c, d) = e^{-\frac{(x-c)^2}{2d^2}} \ . \tag{6.7}$$

The terms $A_{ped}, \mu_{ped}, \sigma_{ped}, B, a,$ and $\tau$ model the pedestal, and were constrained using fits to background runs where no LEDs were flashing. The heavyside step function $H(Q - \mu_{ped})$ ensures that the exponential component is only fit to any charge bins with $Q > \mu_{ped}$. The Gaussian terms dependent on $f_\mu$ and $f_\sigma$ model incomplete amplification of photoelectrons in the PMT dynode; similar terms were used in the PMT fitter used by the DEAP collaboration [196]. $f_\mu$ is constrained to be in the range $[0, 1]$ to ensure the partial amplification mean is less than the full-amplification mean. The one-photoelectron and two-photoelectron amplitudes $A_{1PE}$ and $A_{2PE}$ were allowed to float freely in each fit.

An example fit to a charge distribution from the ANNIE in-situ calibration is shown in figure 6.11. The model is in good agreement with the typical charge distributions observed in the LED calibration runs.

### 6.2.3 Gain matching

Each PMT's gain vs. voltage distribution was extracted to inform voltage setpoints for physics data-taking. LED calibration data was taken with all PMTs operating in the voltage range 1000-1900 V in increments of 50 V, and the single photoelectron gain was extracted at each voltage setpoint. An example gain vs. voltage curve is shown in figure 6.12.

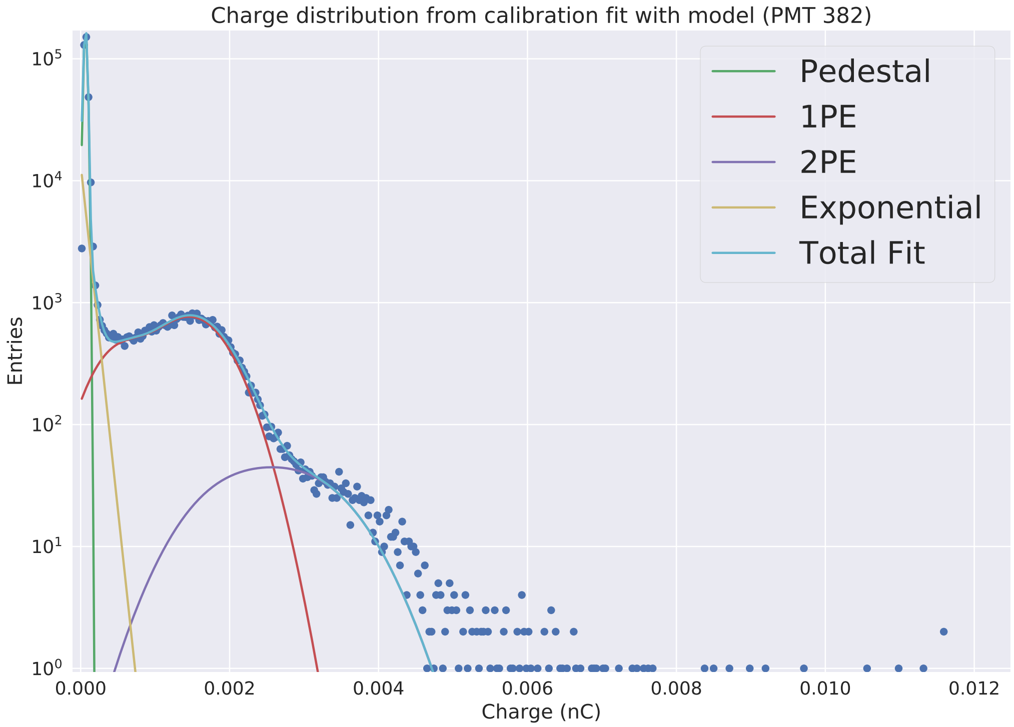

Figure 6.11. Example charge distribution measured for a single PMT in an ANNIE calibration run. The best fit for each component of the model in equation 6.6 are shown.

The ANNIE PMT operating voltages were selected for physics data-taking to match the PMT single photoelectron gains at approximately $7 \times 10^6$. A single photoelectron gain of $7 \times 10^6$ corresponds to a mean charge of 1.12 pC per photoelectron. The ANNIE detector PMT gain distribution is shown in figure 6.13.

A mean detector gain of $7 \times 10^6$ was chosen to provide a good balance of peak-to-valley (PV) ratios and tolerable dark rates. The PV ratio is the ratio of the number of samples at the 1-photoelectron peak to the valley between the 1-PE peak and the pedestal. At gains of $\sim 7 \times 10^6$, the the PVs are mostly 1.5-2 throughout the detector. The PV ratios for all PMTs are shown in figure 6.14.

The PMT dark count rates were quantified with an AmBe-type run with the AmBe housing placed in a dark box. Cosmic muons passing through the BGO crystal would trigger data acquisition, effectively triggering random acquisitions of tank PMT data. The first 20 microseconds of each acquisition window was ignored to reject any PMT hits correlated with cosmic activity

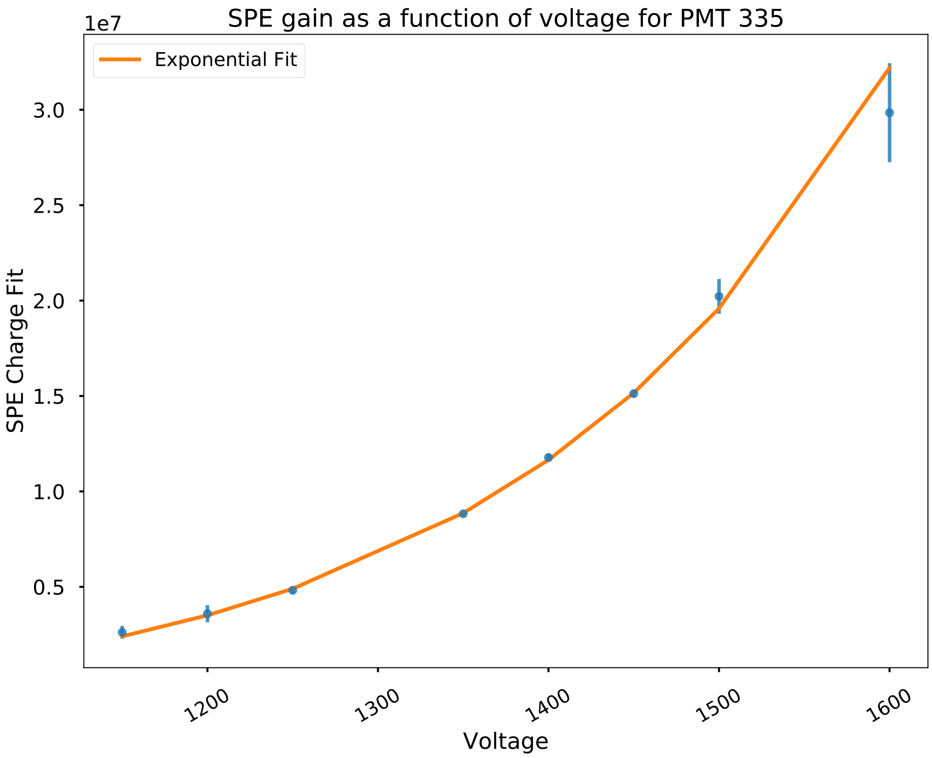

Figure 6.12. Example gain vs. voltage distribution for a PMT in ANNIE. The uncertainties shown are uncertainties in the model fit. The gain trend is exponential, as expected for photomultiplier tubes.

(mainly muon-produced Cherenkov light and PMT afterpulsing). The total acquisition time for this run was approximately one second. As seen in figure 6.15, the dark rates of most PMTs are kept below 15 kHz.

Several PMTs were set to operate at considerably lower gain setpoints than $7 \times 10^6$, resulting in lower dark rates than the other tubes. This was necessary for several of the ETEL tubes, as any higher of a voltage setpoint resulted in current instabilities which could alter the tube's photoelectron response. Instability in the base current would also occasionally cause the tube to cross the current alarm threshold and be powered down by the HV control.

## 6.3 PMT timing calibration

The ANNIE tank is composed of several different types of PMTs, each with different cable length, cable composition, and dynode structure; as such, each PMT can have different pulse

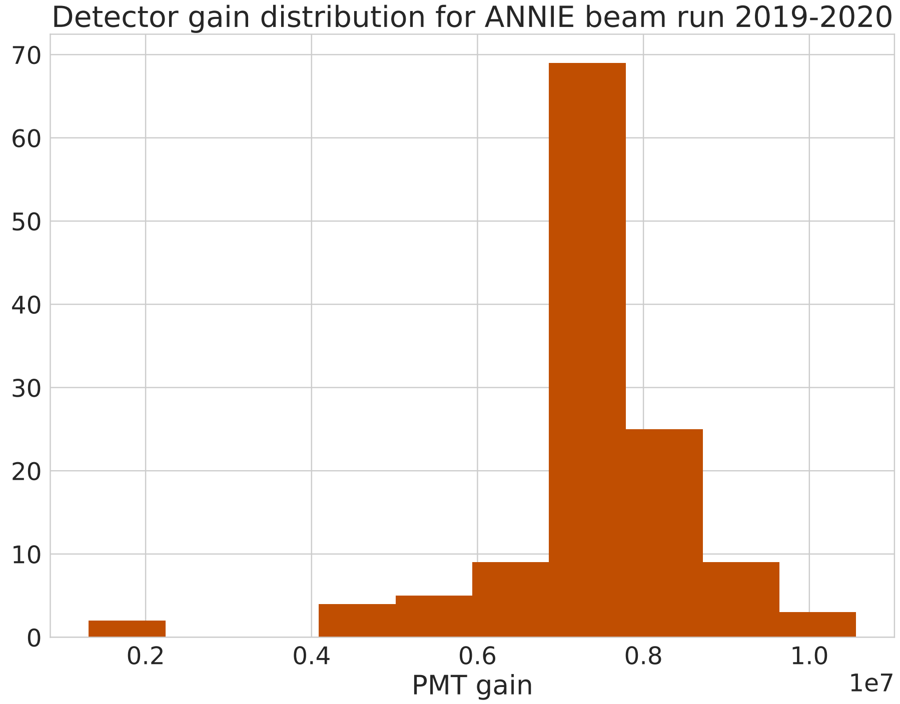

Figure 6.13. Distribution of PMT single photoelectron gains as extracted using the fit in equation 6.6. The ANNIE PMTs are gain-matched at $\sim 7 \times 10^6$ for the 2019-2020 beam run.

arrival times at the ADC card's readout for identical photon arrival times at the photocathode. To use PMT hit times for event selection and reconstruction, corrections must be applied for the differences in each PMT's signal propagation time. Signal propagation variation between different photodetectors and their cables is generally measured using light sources such as LEDs or lasers. I used light produced at the OFMs to calibrate the differences in PMT signal timing. These timing differences were then removed in calibration and analysis data using digital delays set by the ADC cards.

The differences in PMT signal arrival time were quantified using the LEDs and OFMs as follows. Consider an LED pulse fired at time $t = 0$ into OFM $j$. The time at which an ADC card would detect a pulse from PMT $i$ is given by

$$t_{p;i,j} = t_{fiber,j} + \frac{L_{ij} n}{c} + t_{elec,i} \ , \tag{6.8}$$

where $t_{fiber,j}$ is the time for the LED pulse to propagate to the OFM, $L_{ij}$ is the path length

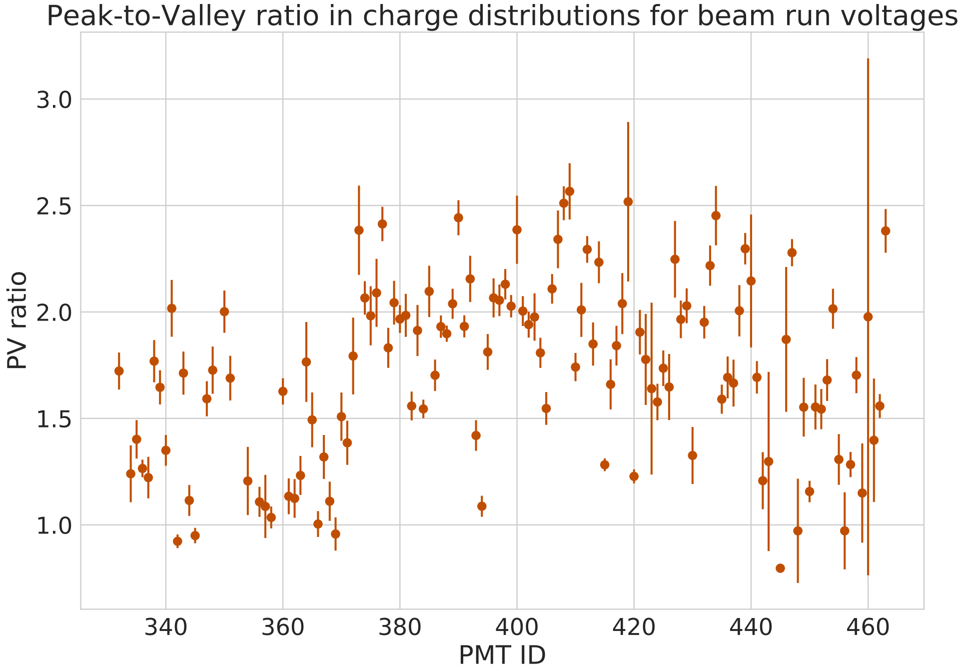

Figure 6.14. Peak-to-valley ratio distribution for the PMTs in ANNIE. Uncertainties are taken as the standard deviation of the 5 lowest bins in the valley and the 5 maximal bins in the 1-PE peak.

between the PMT and OFM, $n$ is the index of refraction in water, $c$ is the speed of light in vacuum, and $t_{elec,i}$ is the PMT-dependent signal propagation time (composed mainly of signal cable propagation time and the time for electrons to propagate through the PMT dynode). The difference in signal propagation between PMT $i$ and PMT $k$ as estimated with LED $j$ is thus written as

$$\Delta t_{elec,ikj} = t_{p;i,j} - t_{p;k,j} + (L_{ij} - L_{kj})\frac{n}{c} \ , \tag{6.9}$$

where $t_{p;i,j}$ and $t_{p;k,j}$ are pulse arrival times measured in calibration data and $L_{\alpha\beta}$ are estimated given the known positions of any PMT $\alpha$ and LED $\beta$ . The value of a $t_{p;\alpha,\beta}$ term is estimated using a weighted mean of the hit time distribution measured by PMT $\alpha$ from LED $\beta$. An example of the PMT hit time distributions and how the terms defined relate to these distributions is shown for two different PMTs in figure 6.16.

Unfortunately, the $L_{\alpha\beta}$ parameters were not yet known at the time of the first signal delay

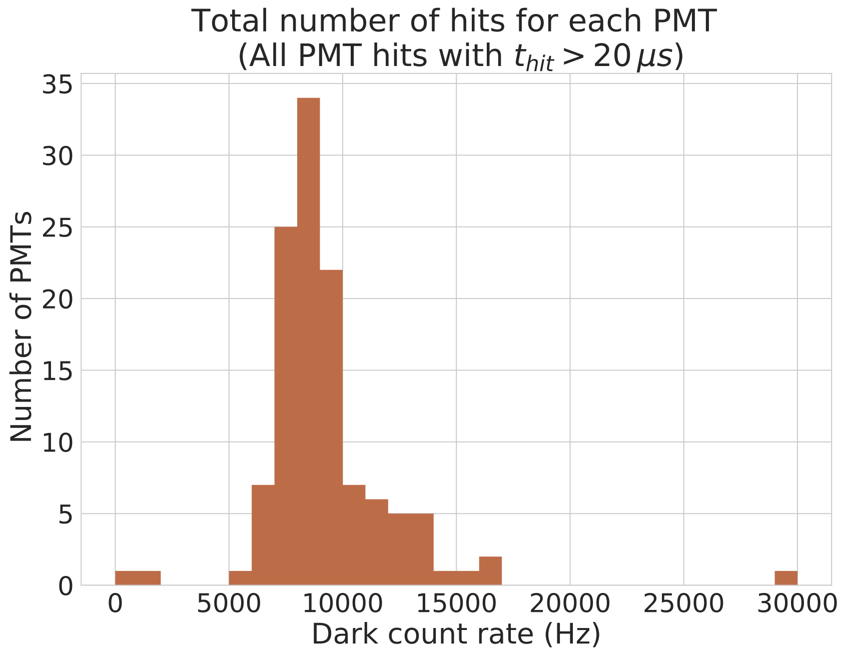

Figure 6.15. Dark count rates for all PMTs read out during an AmBe background run. The AmBe housing had no source installed and was placed in a dark box outside the ANNIE tank. The dark rate for most tubes is kept below 15 kHz.

estimates. For a first cable delay approximation, all $L_{\alpha\beta}$ terms were approximated as the ANNIE tank diameter; to quantify an uncertainty with this assumption, the signal delay difference between a PMT $i$ and PMT $k$ and its uncertainty were estimated using all six LEDs as follows:

$$\begin{aligned} \tilde{\Delta} t_{ik} &= \frac{\sum_{k=0}^{5} \Delta t_{ikj}}{k} \ , \\ \delta \tilde{\Delta} t_{ik} &= \sqrt{\frac{\sum_{k=0}^{5} (\Delta t_{ikj} - \tilde{\Delta} t_{ik})^2}{5}} \ . \end{aligned} \tag{6.10}$$

Figure 6.17 show the first estimates of the signal delay differences in the ANNIE PMTs. All signal delay differences are shown relative to a single PMT $k$, which has the shortest signal delay estimate (defined as time zero). Each point in the plot represents a single $\tilde{\Delta} t_{ik}$ while the error bar represents the uncertainty $\pm \delta \tilde{\Delta} t_{ik}$. The uncertainty is dominated by the unknown $L_{\alpha\beta}$ terms.

A Monte Carlo approach was taken to determine the average expected spread of hit clusters due to signal arrival time uncertainties. For each PMT, ten thousand samples were drawn from a Gaussian with a standard deviation equal to the PMT's signal delay uncertainty. A Gaussian was fit to the total distribution to estimate a mean standard hit cluster deviation due to the signal time delay uncertainties. The best fit to the simulated distribution is shown in figure 6.18. The best

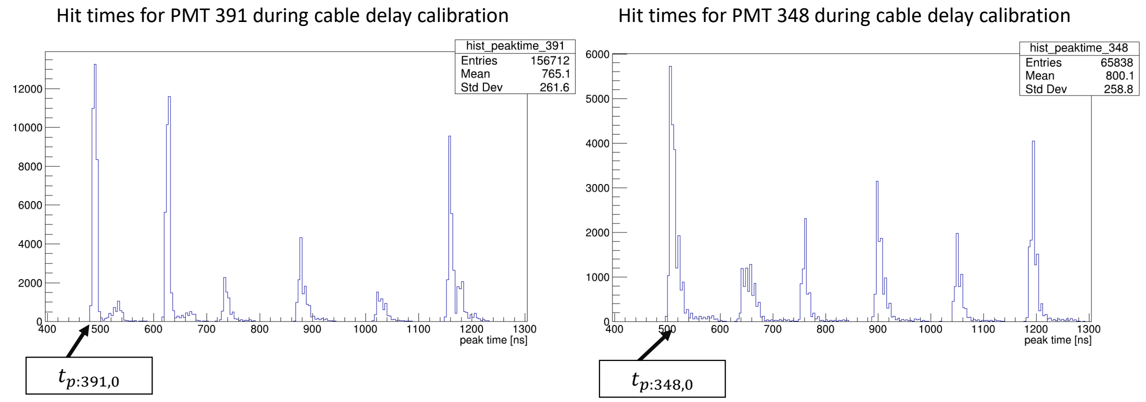

Figure 6.16. Calibration data from two PMTs used for signal delay estimation. The pulse arrival times as described in equation 6.8 are labeled for two PMTs and a single LED. The quantity $t_{p;i,j}$ is estimated by taking the weighted mean of all bins in the PMT $i$'s hit time distribution for LED $j$. A second peak due to reflections is observed for some LED pulse regions, and is ignored when defining LED $j$'s hit window.

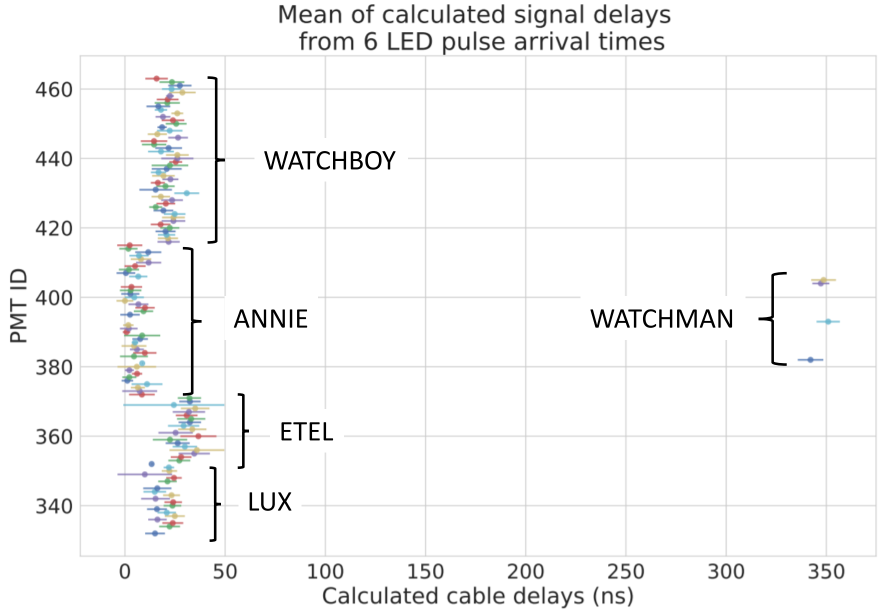

Figure 6.17. Estimate of all PMT signal delays using ANNIE LED calibration data. The point and uncertainty shown for each PMT is the mean and standard deviation of the signal time delay estimated using each LED independently. The WATCHMAN tubes have a much larger delay than other PMT populations due to their relatively long cable lengths. The uncertainty is dominated by the the unknown $L_{\alpha\beta}$ term between each LED $\alpha$ and PMT $\beta$.

fit standard deviation is $\sigma = 4$ ns, but all hits should conservatively lie within any time window $\geq 50$ ns.

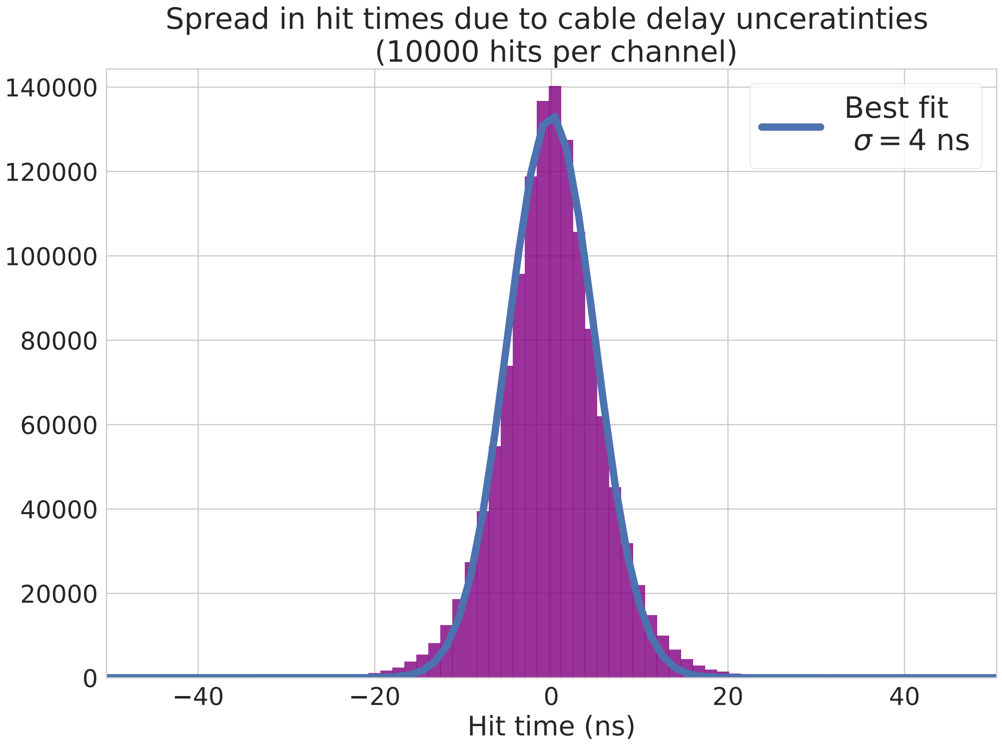

Figure 6.18. Simulated distribution of hit times for all ANNIE PMTs given the cable delay uncertainties in figure 6.17. The best fit standard deviation for a Gaussian is $\sigma = 4$ ns, but a cluster window of $\geq 50$ ns should capture all PMT hits without loss.

To reiterate, the uncertainties in each LED's signal time delay estimation is dominated by the uncertainty in the PMT and LED positions (the $L_{\alpha\beta}$ term in equation 6.9) and the LED pulse firing time. Most PMT signal delay estimates have an uncertainty within $\pm 10\,ns$. This uncertainty is acceptable for triggering the detector for data acquisition, but sub-nanosecond uncertainty is needed for event reconstruction. In the coming months, the signal delay differences will be measured to sub-nanosecond precision using a deployed light diffuser ball illuminated with a fast pulse laser.

## 6.4 Water quality monitoring

Water transparency and quality in the ANNIE tank must be actively monitored during detector operation. Changes in the water transparency correspond to changes in the detected amount of Cherenkov light, which can lead to variations in detector response to the same physical processes over time. These changes must be tracked and applied to data analyses. Additionally, active monitoring of the water's state helps ensure the water purification system is operating as expected and inform when filters and ionic resins should be rinsed or replaced.

The water quality properties actively monitored in ANNIE include resistivity, acidity, and transparency. Techniques for monitoring these values, and a brief discussion of why each should be monitored, are given below.

### 6.4.1 Acidity and conductivity measurements

The conductivity of the tank water is a useful property for monitoring the gadolinium sulfate concentration and ionic contamination. Changes in resistivity can indicate that the gadolinium sulfate is dropping out of solution (decrease in conductivity) or that additional ionic impurities are leaching into the tank water (increase in conductivity). Resistivity is monitored through a sensor installed in the water purification system and has remained steady since the loading of $0.2\%$ gadolinium sulfate by mass.

Acidity is also monitored to ensure gadolinium sulfate is still suspended in the tank. If the tank water's pH becomes basic (a pH of $> 7$), the gadolinium can begin to form gadolinium oxide (GdOH); GdOH is not soluble in water and will drop out of solution. The tank pH is measured with a single probe installed at the top of the tank, and has stayed within a pH of $4.10 - 4.15$ since filling ANNIE to the nominal gadolinium loading.

### 6.4.2 UV-Vis spectrophotometry

UV-Vis spectrophotometer measurements are used to quantify absorption levels in the ANNIE tank water. UV-Vis spectrophotometers typically use a light source with a wide emission spectrum (commonly tungsten-halogen lamps) to quantify the attenuation of light through a sample. The UC Davis neutrino group uses a Shimadzu 1800-series spectrophotometer which can measure the absorption of light in the 190-1000 nm range through samples with a length of either 1 cm or 10 cm [197]. A sample is generally compared to a baseline sample, such as ultrapure water, to remove systematic uncertainties such as scattering in the sample container.

The ANNIE tank water's absorption spectrum is measured at UC Davis at regular intervals to track water quality changes. Several UV-Vis spectrophotometry measurements for the ANNIE tank water at different stages in gadolinium loading are shown in figure 6.19.

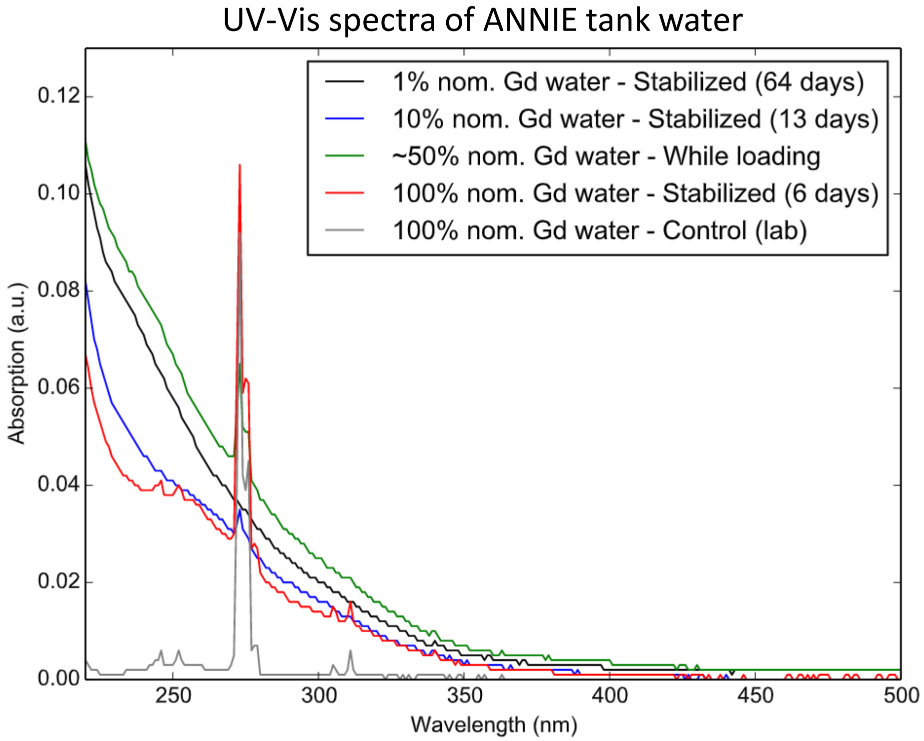

Figure 6.19. Several UV-Vis spectrophotometry measurements taken of the ANNIE tank water throughout gadolinium loading. Measurements were made at UC Davis using a 10 cm UV-Vis cell. Absorption in the tank would increase after adding more gadolinium, but gradually decrease over time as the Gd-doped water was purified. Figure from [183].

The absorption of the water has remained steady since the full gadolinium sulfate loading. The exponential-like increase at wavelengths $< 300\,nm$ is primarily due to plastics leaching into the water. The peak at $\sim 275\,nm$ is an absorption peak from the gadolinium sulfate, and acts as a good indicator that the gadolinium sulfate is still suspended in water. The important wavelength range to monitor for Cherenkov radiation detection is at wavelengths $> 300\,nm$; this is where most PMT photocathodes have can convert photons to photoelectrons). The ANNIE tank water has remained relatively transparent at $> 300\,nm$.

### 6.4.3 Relative water quality monitoring

Although absolute water quality monitoring is pivotal to making systematic corrections in the final data analysis and tuning detector simulations, UV-Vis spectrophotometry measurements have a longer lead time and take personnel to access the detector and take a water sample. I

| PMT ID | Cable label | Voltage setpoint (V) |
|---|---|---|
| 356 | ETEL 117 | 1267 |
| 357 | ETEL 701 | 1600 |
| 364 | ETEL 135 | 1408 |
| 365 | ETEL 136 | 1367 |
| 367 | ETEL 103 | 1553 |
| 368 | ETEL 129 | 1400 |
| 370 | ETEL 128 | 1448 |

Table 6.4. Voltage setpoints for PMTs used in initial transparency monitoring.

developed an additional approach to monitoring the ANNIE tank water quality which provided immediate feedback and required no access to the ANNIE hall.

This technique involved measuring the relative water transparency over time using the LEDs and OFMs. At daily intervals, the bottom OFM was flashed with LED light at a high intensity (the same intensity every measurement) such that the PMTs at the top of the tank detected multi-PE levels of light. If the transparency of the ANNIE tank water varied over time, the average photoelectrons observed per LED flash would also vary. The ANNIE tank is effectively being utilized as an attenuation arm, where reduced levels of light at the top of the tank indicated a loss in the water's transparency due to increased scattering/attenuation.

In the first several months of operation, seven top tubes (ETEL-brand tubes) were used to measure the total number of photoelectrons observed per LED flash. The bottom OFM (attached to LED 6) was set to an intensity such that the on-board photodiode read a total current of 3500 ADC counts. The seven tubes were selected because their default operating voltages prior to gain calibration provided acceptable gains ($> 1 \times 10^6$). The seven PMTs used and their operating voltages are shown in table 6.4.

The mean photoelectrons seen by the top seven ETEL tubes per LED flash in the first two months of commissioning are shown in 6.20. The mean photoelectron count seen in the top tubes per LED flash is defined as

$$PE_{tot/flash} = \sum_{i=1}^{7} c_i Q_i \ , \tag{6.11}$$

where $Q_i$ is the mean charge observed by PMT $i$ per flash of the LED, and $c_i$ is the charge-to-PE conversion estimated with gain calibration. The uncertainties in the total PE observed are related to the uncertainty in $c_i$ and the uncertainty in the number of photons produced per LED flash (see table 6.1).

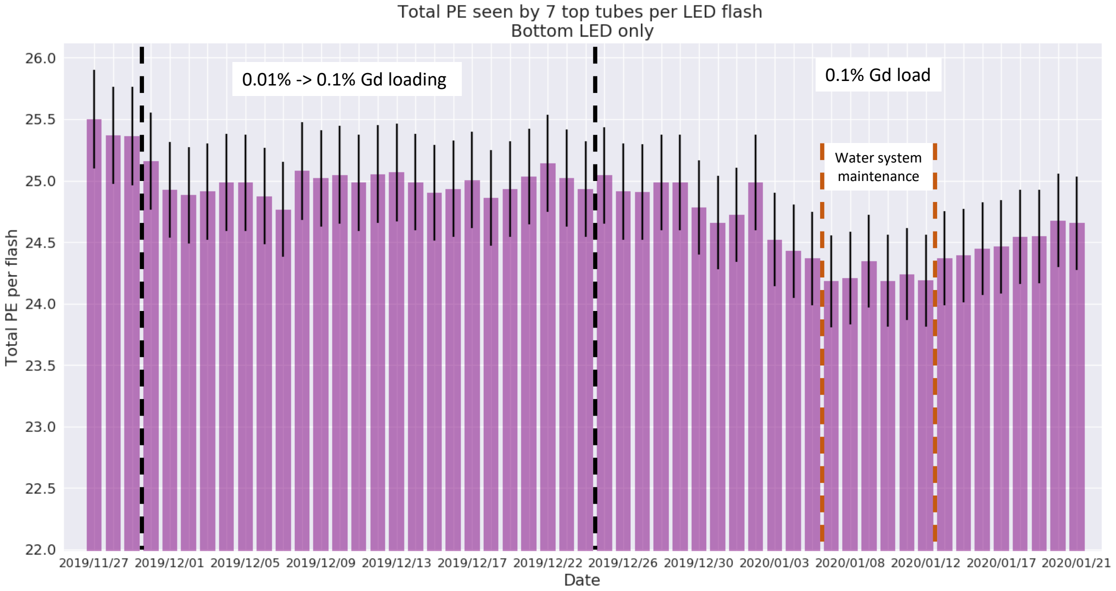

Figure 6.20. Mean number of photoelectrons seen by the top PMTs per LED flash in ANNIE. Variation in the observed photoelectron count

An initial drop in detected light was observed due to the initial addition of gadolinium, but remained stable throughout loading to the full $0.2\%$ nominal gadolinium sulfate concentration. A steady decrease in detected light was observed at the beginning of 2020; after a water system maintenance where the ionic resin was flushed, the transparency steadily recovered.

# Chapter 7

# Data processing

Several data processing steps were necessary to extract physics events from the ANNIE raw data. Raw waveform data from ANNIE's photodetectors was processed to extract signal pulses, also referred to as "hits", caused by incident light. Following hit identification, a cluster finding algorithm was used to find PMT hits coincident in time, which generally result from a light-producing physics interaction inside the tank. Each cluster was then characterized with a set of cluster classifiers to help identify what kind of interaction caused the cluster. This chapter briefly describes the data processing algorithms developed to analyze both AmBe calibration data and neutrino beam data.

## 7.1 Baseline estimation

Each ADC channel in ANNIE has a different baseline voltage reading in the presence of no signal; this baseline had to be quantified for every data acquisition and every channel during data acquisition. A more sophisticated baseline estimation algorithm was utilized than in the gain calibration analysis; the reason was to reduce incorrect baseline estimation caused by increased PMT pulse activity (mainly associated with calibration sources and the neutrino beam). ADC waveform baselines were estimated in each channel using the "ze3ra" algorithm, an algorithm created for ZE3RA (ZEPLIN 3 Reduction Analysis), which is utilized in the ZEPLIN-III experiment. This algorithm was also used for baseline estimation in ANNIE phase I, and is described in detail in [198].

The ze3ra algorithm is summarized briefly below. A region of PMT waveform is split into M regions each with N samples. The mean and standard deviation for region $j$ is calculated using

$$\begin{aligned} \mu_j &\equiv \tfrac{1}{N}\textstyle\sum_{k=1}^{N} x_{j,k} \ , \\ \sigma_j^2 &\equiv \tfrac{\sum_{k=1}^{N}(x_{j,k}-\mu_j)^2}{N-1} \ , \end{aligned} \tag{7.1}$$

Where $x_{j,k}$ is waveform sample $k$ in the $j$th region. Then, a ratio $R$ of each neighboring region $j$ and $j+1$'s standard deviation is formed and defined as

$$R_j \equiv \begin{array}{ll} \sigma_j^2/\sigma_{j+1}^2 & \sigma_j > \sigma_{j+1} \\ \sigma_{j+1}^2/\sigma_j^2 & \sigma_j \leq \sigma_{j+1} \ . \end{array} \tag{7.2}$$

If the ADC values from the $j$th and $j+1$th regions contain independent, simple, random samples drawn from populations of the same variance, then $R$ should follow an F distribution. A test statistic $P_j$, which represents the probability of observing a deviation of $R_j$ from 1 at least as extreme as that observed, can then be written as follows:

$$P_j \equiv 2(1 - F_{N-1,N-1}(R_j)) \ , \tag{7.3}$$

where $F_{n,m}(R_j)$ is the cumulative distribution function of $R_j$ assuming regions $j$ and $j+1$ have $n$ and $m$ degrees of freedom, respectively. A $P_{crit}$ value is defined such that if $P_j \leq P_{crit}$, then $R_j$ fails the hypothesis that the regions $j$ and $j+1$ share the same mean and standard deviation, and region $j+1$ is rejected from the regions.

If $L$ regions pass the ze3ra test, each of these (labeled $l$) are then used to estimate the baseline mean and standard deviation terms

$$\begin{aligned} x_0 &= \tfrac{1}{L}\textstyle\sum_{l=1}^{L} \mu_l \ , \\ \sigma_{x_0} &= \left(\tfrac{N-1}{NL-1}\textstyle\sum_{l=1}^{L} \sigma_L^2\right)^{1/2} \ , \end{aligned} \tag{7.4}$$

The ze3ra algorithm has several benefits over performing a simple mean and standard deviation estimation of the baseline. If a pulse occurs in the baseline estimation window, the ze3ra test should indicate the sub-window is anomalous and exclude it from the baseline estimation. Additionally, a larger number of rejected sub-windows is indicative that the baseline estimation could be less accurate, and the baseline uncertainty could be adjusted accordingly.

The values used for the analysis of data shown in the rest of this chapter are as follows: $N = 10$, $M = 15$, and $P_{crit} = 0.01$. The $N$ and $M$ values were selected to keep the first baseline estimation within the first $300$ ns of an acquisition; this minimized contamination of the baseline region with either beam activity or AmBe source activity. $P_{crit}$ was kept the same as in ANNIE Phase I, and could potentially be re-optimized in future analyses.

The ze3ra algorithm was used at regular intervals in each acquisition to account and correct for any drift in the baseline. Some ADC channels demonstrated an oscillating baseline due to noise from the PMT HV power supply. This noise consistently demonstrated a frequency of $20$ kHz. To correct for this varying baseline, the ze3ra algorithm is re-performed every 4 microseconds as shown in figure 7.1.

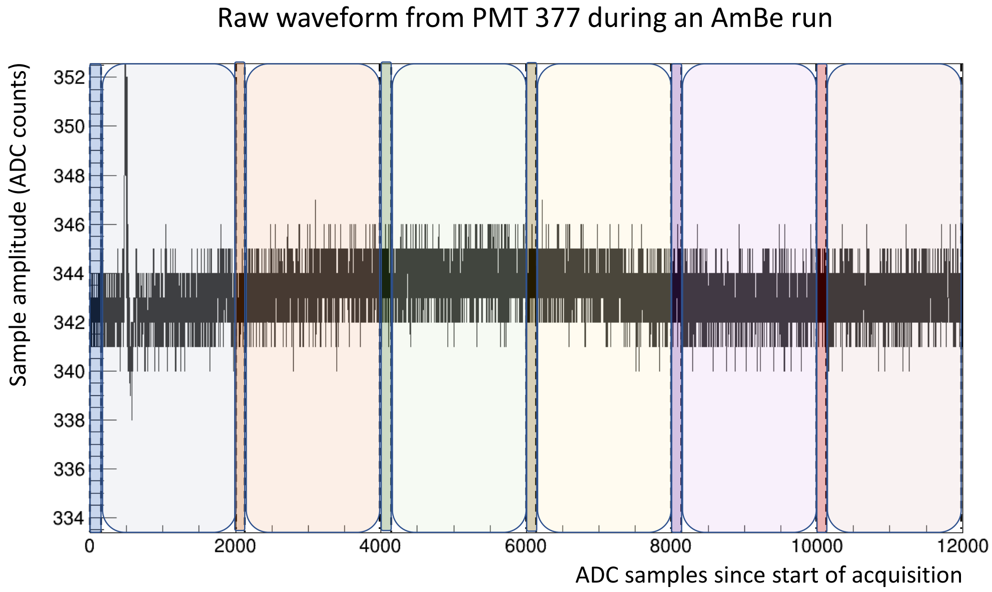

Figure 7.1. Example of an ADC channel demonstrating noise from the PMT power supply. The dark colored windows indicate where the ze3ra algorithm is performed, while the light-shaded regions indicate where the baseline estimation is utilized.

In the future, the baseline in the entire acquisition window could also be characterized using a sinusoidal fit. The amplitude and phase of the sinusoidal wave would be free to float, while the frequency would be constrained by measurements of the power supply noise frequency.

## 7.2 PMT hit finding

Hit finding in AmBe source and beam data proceeded in a different manner than used during the detector gain calibration. While the expected location of PMT pulses was known in LED calibration runs, pulses from neutron captures or neutrino interactions could occur anywhere in AmBe and beam run acquisitions.

A general pulse-finding algorithm was developed to search for pulses in every ADC channel acquisition. Consider a single ADC acquisition window whose baseline has been estimated as discussed in section 7.1. If a waveform acquisition crosses a set threshold above the estimated baseline, a "pulse" is marked in the acquisition. Five samples behind the threshold crossing and all samples following the threshold crossing until the acquisition returns to a value within the baseline's uncertainty were summed. A diagram demonstrating this process is shown in figure 7.2. The sum of all samples in the pulse was converted to charge as described in equation 6.4. The hit time is defined as the time at which the maxima of the pulse sample window was measured.

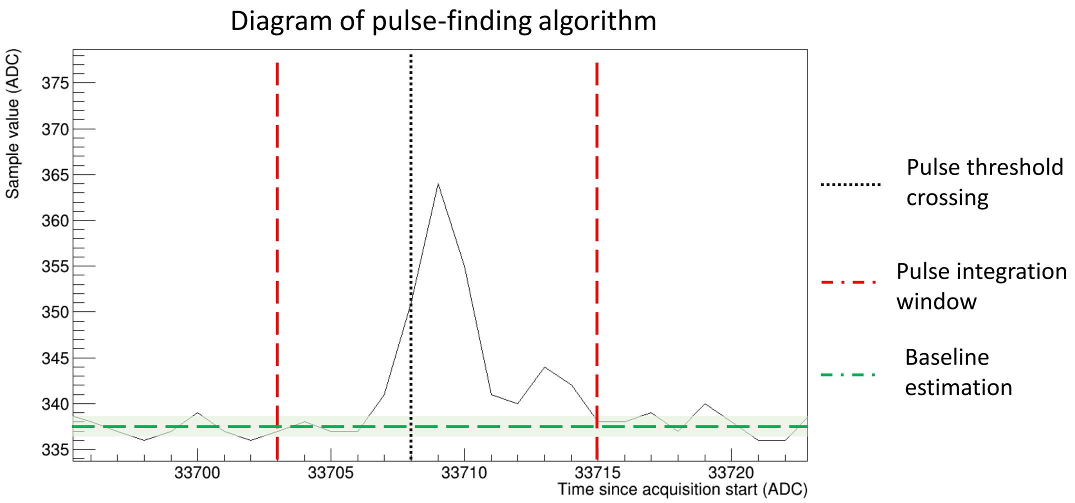

Figure 7.2. Diagram demonstrating the characterization of a pulse in an acquisition. All samples are summed following the threshold crossing until the waveform returns to the estimated baseline region. Five samples prior to the threshold crossing are included in the pulse characterization window.

The threshold for identifying a single photoelectron pulse was determined by measuring the pulse amplitudes observed on all tubes in LED calibration runs. Based on this data, a default of 7 ADC counts above baseline was utilized for all channels. In the future, channel thresholds in the hit finder will be set on a per-channel basis as well.

## 7.3 PMT hit cluster finding and classification

Physics interaction candidates in PMT hit data were found using a cluster-finding algorithm. A scan of all hits in a single acquisition was performed; if five or more hits were found within a 50 nanosecond time window, a hit cluster object was created. The 50 nanosecond window was selected based on the estimated signal delay uncertainties shown in figure 6.18. The 5 hit threshold was chosen to mimic the 5 photoelectron (PE) threshold utilized in preliminary neutron detection efficiency studies, but could be lowered for future studies [152]. The cluster's "hit cluster time" is characterized as the mean time of all hits in the cluster, while the "hit cluster PE" is the sum of the number of photoelectrons seen by all tubes in the cluster.

Several cluster classifiers were developed to help characterize clusters as signal or background, and are briefly described below.

### 7.3.1 Charge balance

The charge balance classifier is formed using the total charge seen on all tubes in a cluster. For a single cluster, the charge balance value is defined as

$$CB = \sqrt{\frac{\sum_i^N Q_i^2}{Q_{sum}Q_{sum}} - \frac{1}{N}}\,, \tag{7.5}$$

where $N$ is the number of phototubes, $Q_i$ is the total charge seen by tube $i$ in the cluster, and $Q_{sum} = \sum_i^N Q_i$ is the total cluster charge. If the charge is distributed evenly in PMTs within the cluster, the charge balance parameter CB approaches zero. On the other hand, if a single tube sees all the charge in a cluster, CB approaches one. The charge balance cut was also used in the WATCHBOY detector to characterize neutron captures on gadolinium, as shown in figure 7.3 [199]. I implemented the charge balance parameter as a classifier in the ANNIE analysis framework for analyses presented in the following analysis chapters.

### 7.3.2 PE point vector

The PE point vector acts as a rudimentary characterization of the directionality of clusters containing a Cherenkov cone or disk. For a cluster, the PE point vector is defined as

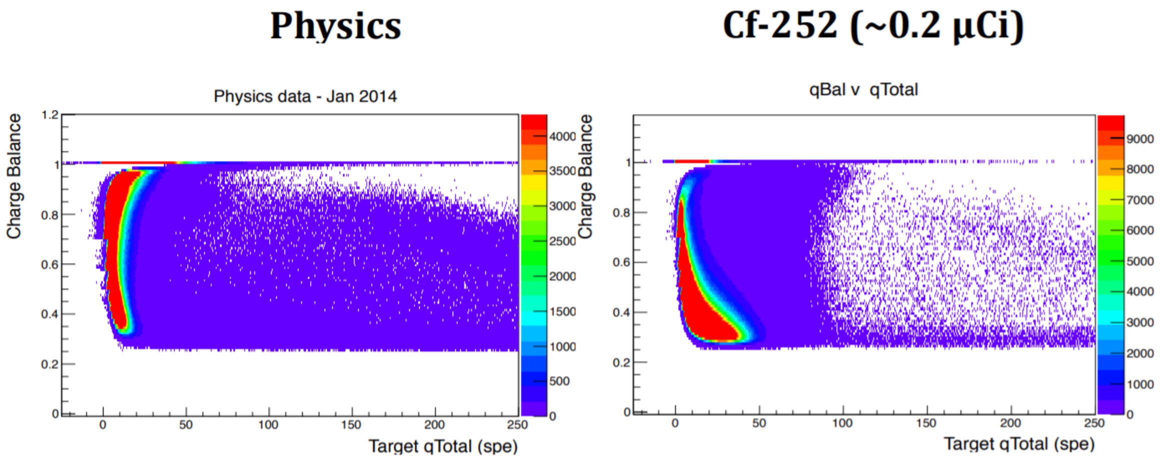

Figure 7.3. Charge balance parameter plotted against total charge for events in WATCHBOY. Neutron captures as observed in a Californium-252 deployment have a charge balance parameter distribution closer to zero than the physics data shown. Figure from [199].

$$\vec{PE} = \sum_i PE_i \left(\hat{x}_i + \hat{y}_i + \hat{z}_i\right) \ , \tag{7.6}$$

where $PE_i$ is the number of photoelectrons seen by PMT $i$ and $(x_i, y_i, z_i)$ is the direction to PMT $i$ in the tank. For events with an asymmetric charge distribution, the PE point vector will point towards the PMTs which measure a higher PE count, as seen in figure 7.4.

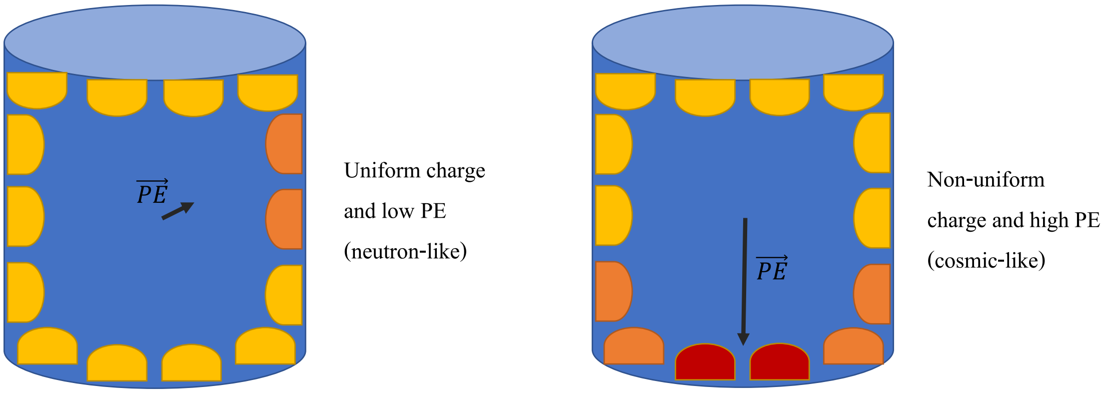

Figure 7.4. Figure demonstrating the expected difference in PE point directionality based on different hypothetical PE distributions. The PE point could be used to classify clusters as pointing downstream (positive z-direction), towards the ground (negative y-direction), or neutron-like (non-directional), for example.

### 7.3.3 MRD hit cluster and track finding

Clusters of MRD hits were also found during data processing. An MRD cluster is composed of a minimum of 4 paddle hits within a 40 nanosecond time window. A minimum of four hits is required to increase the track reconstruction efficiency and reduce contamination from clusters resulting from noise in the MRD paddle PMTs. An MRD' cluster's "cluster time" is characterized as the mean time of all paddle hits in the cluster, while the "cluster nhit" is the number of MRD paddles hit in the cluster. No MRD cluster PE exists, as the charge of each MRD paddle PMT is not measurable.

MRD clusters were then given to an MRD track reconstruction algorithm, which estimates particle track parameters including MRD entry point, length, and energy loss. The MRD track reconstruction algorithm is based on a cellular automation algorithm used in the SciBooNE SciBar detector [200, 201, 202, 203].

# Chapter 8

# Neutron detection efficiency

Any estimate of the neutrino interaction neutron multiplicity on oxygen using ANNIE beam data will require systematic corrections for ANNIE's neutron detection efficiency. The neutron detection efficiency is a necessary correction factor for converting from the number of neutrons observed in the ANNIE tank to the number of neutrons that were actually produced in an interaction. The uncertainties associated with ANNIE's neutron detection efficiency must also be quantified and propagated into the neutron multiplicity analysis as well.

This chapter provides an overview of ANNIE's first AmBe source calibration campaign and the analysis developed to extract ANNIE's neutron detection efficiency. Prior to describing the data analysis, an overview of the source deployment positions and acquisition rates is presented. Cross-checks of the data quality to confirm that the AmBe data contains signals consistent with neutron captures on gadolinium are also presented. Extraction of the neutron detection efficiency using a toy Monte Carlo approach is described and presented, as well as the prominent sysetematic uncertainties and corrections needed for analyzing ANNIE's AmBe source data.

## 8.1 AmBe source deployment positions

The AmBe source was deployed at four different positions during the neutron detection efficiency campaign. Preliminary simulation studies indicated that the neutron capture detection efficiency can vary from nearly 100% to 20% depending on the neutron production position [152]. As such, AmBe deployments at different positions in the ANNIE tank were necessary to quantify the actual positional variation. All positions are shown approximately as deployed in the ANNIE

| Position label | Source coordinates (x,y,z) [cm] |
|---|---|
| Position 0 | (0,0,0) |
| Position 1 | (0,0,75) |
| Position 2 | (0,0,102) |
| Position 3 | (0,100,102) |

Table 8.1. AmBe source positions deployed in the ANNIE tank calibration campaign. The positive z-direction points down the beamline, while the positive y-direction points towards the tank top.

tank in figure 8.1. More source positions will be measured prior to the start of the 2020-2021 BNB beam run.

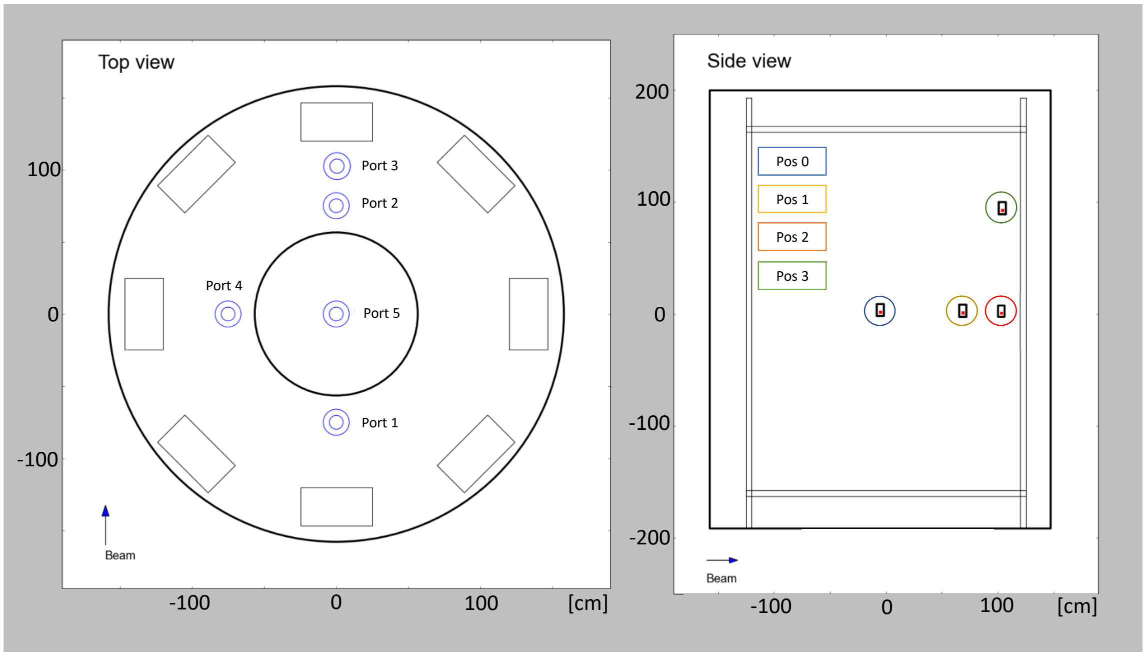

Figure 8.1. Left: Top-down view showing the five calibration port positions on the ANNIE lid. Right: Approximate AmBe source deployment positions in ANNIE tank during initial calibration campaign. Positions are known inside the tank to $\pm 5\,cm$ uncertainty.

The exact coordinates of the AmBe source are shown in table 8.1. Positions are known inside the tank with a $\pm 5\,cm$ uncertainty. This positional uncertainty will be considerably reduced following analysis of the ANNIE frame infrared scan data.

## 8.2 AmBe source data acquisition overview

AmBe data acquisition was triggered using coincident pulses in the AmBe source SiPM ADC channels. The ANNIE DAQ was configured to trigger PMT waveform acquisition if both SiPM channels measured two consecutive samples 10 ADC counts above baseline (10 ADC samples = 5.9 mV threshold). The distribution of AmBe source SiPM pulse heights from runs 1594-1596 are shown in figure 8.2. The main peak at 10 mV is primarily due to 4.4 MeV $\gamma$s from the AmBe source, while the higher amplitude events in the tail are mostly due to through-going muons.

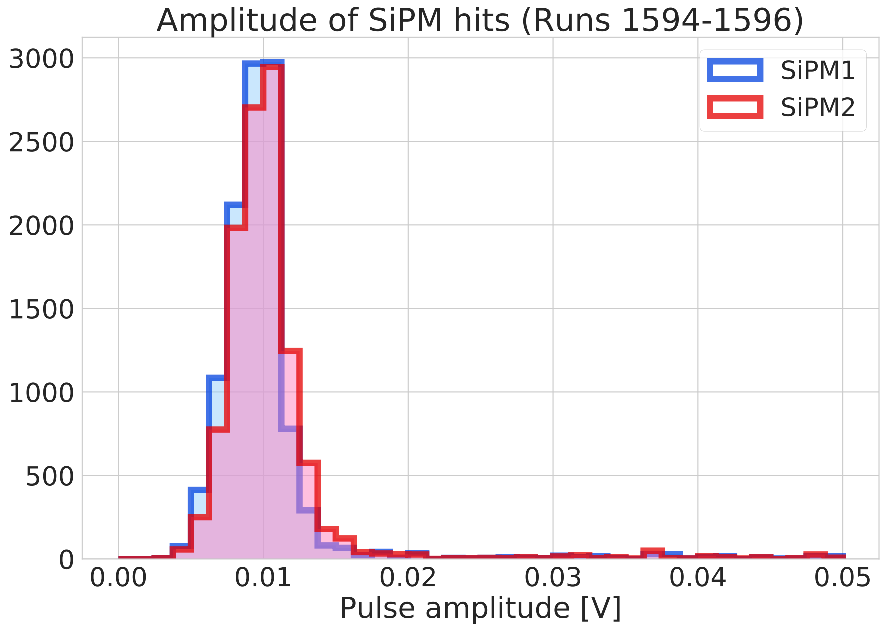

Figure 8.2. Distribution of AmBe source SiPM pulse amplitudes in AmBe calibration data with source installed. The 6 mV threshold set by the DAQ is apparent. The primary peak is due to 4.4 MeV $\gamma$s from the AmBe source, while higher amplitude pulses are contributed to through-going muons.

Once triggered, the ANNIE DAQ acquired a 67 microsecond-long waveform from all ADC channels. The AmBe source SiPM waveforms were also collected, and were used to characterize the SiPM pulses that initiated the data acquisition trigger. Trigger pulse peaks typically occurred at 500 nanoseconds in the acquisition window as seen in figure 8.3. This timing offset was manually set to ensure the full AmBe source SiPM pulses were visible in the two-microsecond prompt window. Note that the trigger initiation time, defined by a fixed threshold crossing in the SiPM voltage readings, does not correspond to the SiPM pulse peak time; the width of the pulse time distribution is due to this difference, as well as the SiPMs operating in a slow-pulse mode. Since AmBe source SiPM pulses are on the order of 1-2 microseconds wide (see figure 6.7), the uncertainty on the peak time is relatively large.

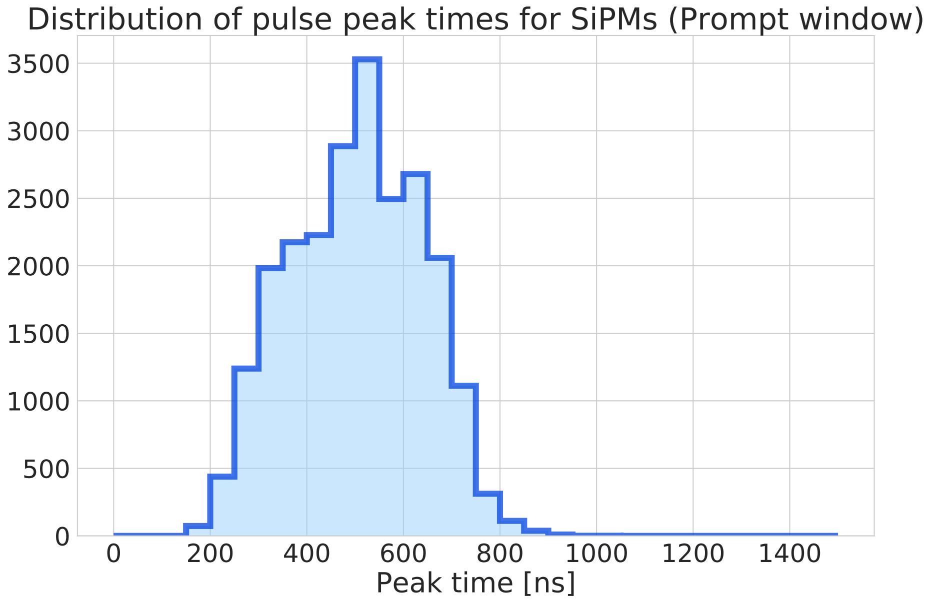

Figure 8.3. Distribution of AmBe source SiPM pulse peak times in calibration data with the source installed. A large standard deviation in the mean peak time is primarily due to the SiPMs being operated in slow-pulse mode (high charge resolution, but lower peak time resolution).

Following a DAQ trigger, a trigger hold-off prevents any additional triggers from being sent to the DAQ for 0.6 seconds. Readout of the ANNIE ADC card FIFO buffers takes approximately 0.5 seconds; a 0.6 second hold-off prevents multiple acquisition triggers from overflowing the ADC card FIFO buffers and causing data loss. A 0.6 second holdoff limits the max AmBe data acquisition rate to $1.67$ Hz.

Five sets of AmBe runs were taken during the calibration campaign and are described in table 8.2. One set of runs was taken with the AmBe housing deployed, but without the AmBe source installed, to characterize detector backgrounds in calibration data. The dominant background is expected to result from cosmic rays both triggering data acquisition in the prompt window and producing tank PMT signals in the delayed window. Note that the BNB beam was on throughout AmBe data-taking, so some beam-related backgrounds may also be present in the AmBe data.

Notice that the trigger rate for runs with the source installed are much higher than the run

| Position | Source installed? | Run numbers | Num. triggers | Livetime estimate [s] | Trigger rate estimate [Hz] |
|---|---|---|---|---|---|
| Position 0 | Yes | 1594-1596 | 12990 | 8648 | 1.50 |
| Position 0 | No | 1611,1612 | 23260 | 74528 | 0.31 |
| Position 1 | Yes | 1636-1638 | 17600 | 11798 | 1.49 |
| Position 2 | Yes | 1642-1645 | 21240 | 14478 | 1.47 |
| Position 3 | Yes | 1651,1652 | 10370 | 7470 | 1.38 |

Table 8.2. Description of AmBe calibration data taken and used for the following analysis. Position 0 data was taken without the source installed, and was used to characterize backgrounds for all source positions.

with no source. Comparing the central source positions, a trigger rate of 1.5 Hz is observed with the source installed while the background "no source" data has a trigger rate of 0.3 Hz. This was expected due to the increased trigger rate caused by the AmBe source's 4.43 MeV gamma rays.

## 8.3 Prompt window data quality cuts

Three preliminary cuts were applied to the prompt window (defined as $< 2\,\mu s$ in an acquisition) to remove acquisitions triggered by backgrounds, such as cosmic muons. If an acquisition failed any of the preliminary cuts, the acquisition was rejected. First, each AmBe source SiPM is required to have one and only one pulse in the entire acquisition. This cut prevented contamination of neutrons from additional AmBe decays (whose 4.43 MeV gamma would cause another trigger in the BGO) as well as through-going cosmics that produce scintillation light in the BGO crystal. Second, any event with a tank PMT hit cluster, referred to as a "tank cluster", in the prompt window was removed from the analysis. This cut removed acquisitions triggered by through-going cosmic muons, whose Cherenkov light would also produce a PMT hit cluster in the tank. Finally, any acquisition containing a tank cluster with a cluster PE $> 150$ was rejected. This cut helped reject any through-going cosmic activity in both the prompt and delayed ($> 2\,\mu s$) windows.

The reductions in data for the central source dataset and central background dataset due to preliminary cuts are shown in table 8.3. Comparing the signal and background rates after applying all cuts, the purity of source-based triggers is expected to be $> 99\%$. Note that source-

| Cut applied | Trigger count [source] | Trigger count [no source] |
|---|---|---|
| None | 12990 | 16160 |
| SiPM cut | 11667 | 8539 |
| Prompt tank cut | 10751 | 246 |
| $> 150$ PE cut | 9934 | 233 |
| Trigger rate after cuts [Hz] | 1.15 | 0.005 |

Table 8.3. Triggers remaining following the application of data quality cuts on the central source runs 1594-1596 and central background run 1612. The trigger rate after applying preliminary cuts is provided in the final column. The trigger rate of background-based acquisitions drops dramatically while signal-based triggers are mostly preserved.

based triggers include both triggers from 4.4 MeV $\gamma$s and false triggers from neutron captures near the housing, which must be accounted for with a systematic correction.

## 8.4 Delayed window charge balance cut

A charge balance cut (also referred to as $CB$ below) was applied to the delayed window tank clusters (tank clusters with $t_c > 2\,\mu s$) to remove instrumental-based clusters observed in both the signal and background datasets. The charge balance distribution for the central position with the AmBe source installed is shown in figure 8.4. Three distinct populations are present in charge balance parameter space; one with $CB > 0.9$ (referred to as "high charge balance clusters"), one with $0.4 < CB < 0.6$ (referred to as "mid-range charge balance clusters"), and one with $CB < 0.4$ (referred to as "low charge balance clusters").

To inform a charge balance cut that will remove backgrounds while preserving the neutron signal, the charge balance distribution of the background data was also plotted (see figure 8.5). The high and mid-range charge balance populations dominate the background dataset, while the low charge balance population is nearly nonexistent. This indicates that the low charge balance population ($CB < 0.4$) in the source dataset is primarily due to AmBe neutrons.

For all delayed tank clusters in the following analyses, a charge balance requirement of $CB < 0.4$ was placed on both the signal and background data. This removed the anomalous clusters due

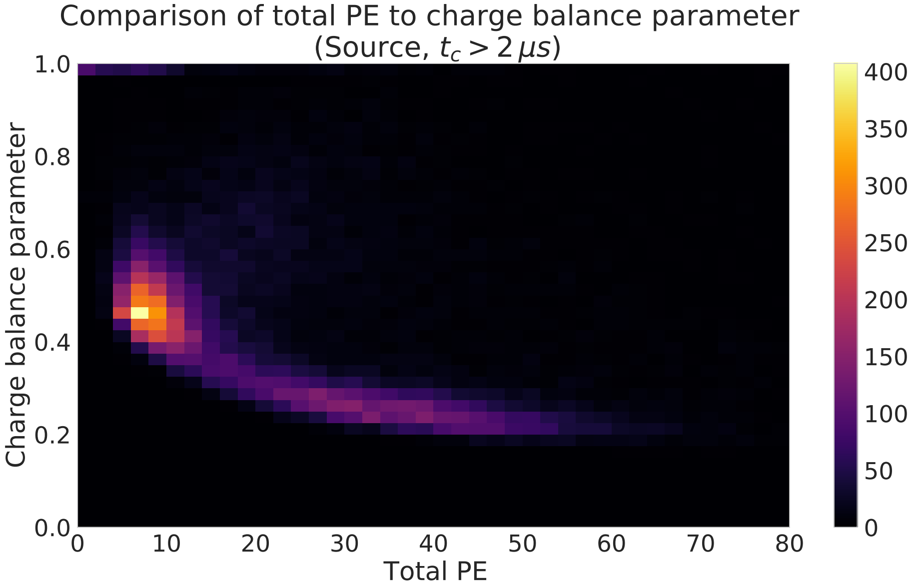

Figure 8.4. Charge balance distribution for all delayed window tank clusters in the source data taken at position 0. No preliminary cuts are applied to the data. Three charge balance populations are apparent in the source data. The charge balance population with $CB > 0.9$ is small relative to the other two populations and difficult to see by eye.

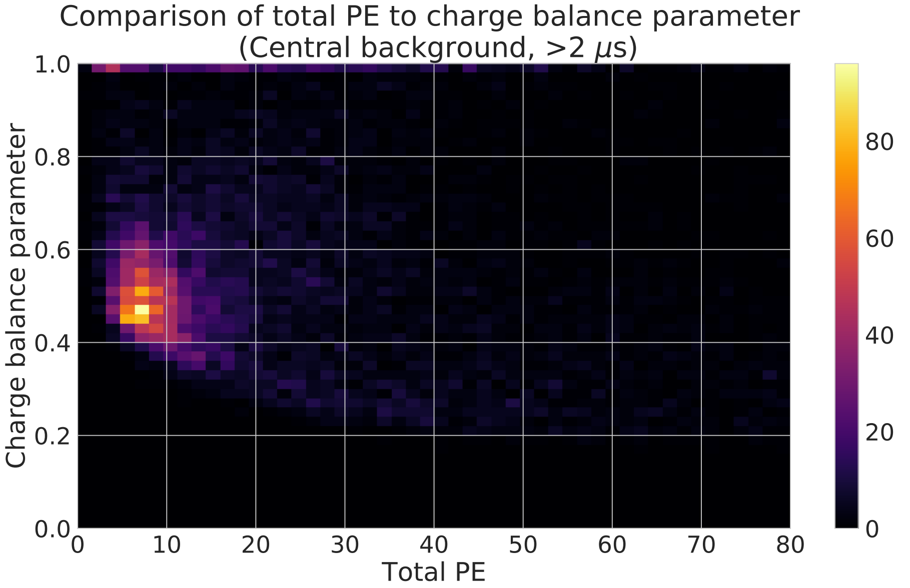

Figure 8.5. Charge balance distribution for all delayed window tank clusters in the background data taken at position 0. No preliminary cuts are applied to trigger selection. The high-range charge balance ($CB > 0.9$) and mid-range charge balance ($0.4 < CB < 0.6$) populations dominate the background data.

to backgrounds and instrumentals while sacrificing only a small fraction of neutron candidates in the source data.

### 8.4.1 Origin of PMT hit clusters in charge balance populations

The origin of PMT hit clusters with a charge balance of $CB > 0.4$ is explored below. The characteristics of the high charge balance population ($CB > 0.9$) and mid-range charge balance population ($0.4 < CB < 0.6$) will be emphasized.

The charge balances for all PMT hit clusters in the central source data as a function of time in the acquisition are shown in figure 8.6. While the high charge balance population is spread evenly through the acquisition window, the mid-range charge balance population is mostly localized to the time window between $6 - 10$ microseconds. PMT afterpulsing is expected in this time window; it is likely that the mid-range charge balance population is primarily due to afterpulsing. This charge balance region could provide a good population of events for characterizing hit clusters caused by afterpulsing in future analyses.

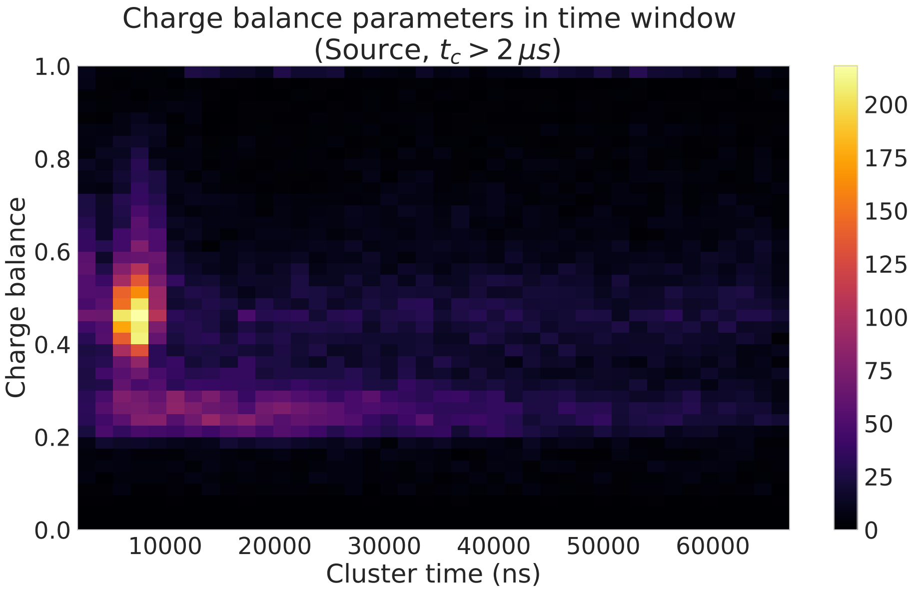

Figure 8.6. Charge balance distribution for all delayed window tank clusters in the source data taken at position 0 as a function of cluster time in the acquisition. No preliminary cuts are applied to the data. A peaked distribution emerges in the 6-10 microsecond window, which is expected to be due to PMT afterpulsing.

The very high charge balance clusters ($CB \sim 1$) are instrumental-based backgrounds, and are a combination of afterpulsing and misidentification of pulses due to extreme baseline ringing following a large energy deposition in the tank. Muons produced in neutrino charged-current interactions produce a large amount of Cherenkov light, which may cause the voltage baseline in tubes to ring sinusoidally. If the baseline is estimated in a trough of the sinusoidal baseline ringing, the peak of the baseline can be misidentified as numerous pulses. Fortunately, these instrumental clusters are rare and easily removed with a charge balance cut; however, the presence is worth noting as baseline ringing may be unavoidable following high energy neutrino interactions in beam data.

Plotting the photoelectron distribution for all tubes in clusters with $CB > 0.9$, these instrumentals appear localized to several tubes in the ANNIE tank (see figure 8.7). In particular, the tubes contributing to these high charge balance events are the four WATCHMAN tubes (PMT IDs 382,393, 404, and 405), two ETEL tubes (PMT IDs 361 and 362) and a WATCHBOY tube (PMT ID 414). Additional instrumental cuts targeting these specific tubes, paired with more sophisticated baseline estimation algorithms, may be needed in future analyses.

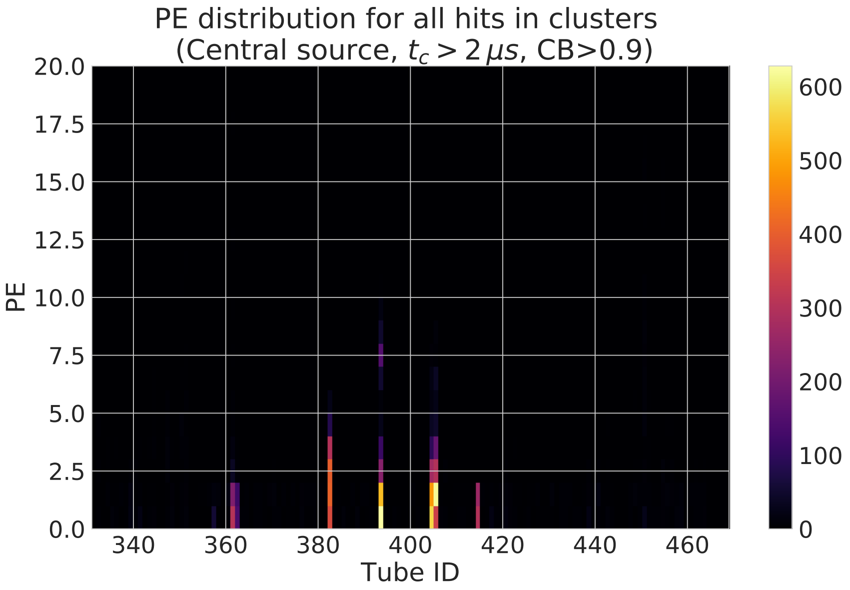

Figure 8.7. PE distribution of delayed clusters with $CB > 0.9$ in the central source data. No preliminary cuts are applied to the data. The clusters are entirely composed of low-PE hits in the four WATCHMAN tubes (PMT IDs 382,393, 404, and 405), two ETEL tubes (PMT IDs 361 and 362) and a WATCHBOY tube (PMT ID 414).

The PE distribution for each PMT ID in the mid-range charge balance clusters (expected to be due to afterpulsing) is shown in figure 8.8. Few afterpulsing hits are seen in the ETEL tubes (mounted at the top of the tank), which is expected for through-going cosmic muons primarily going in the downward direction. Tubes contributing to the $CB \sim 1$ clusters also contribute a large number of hits in the afterpulsing clusters.

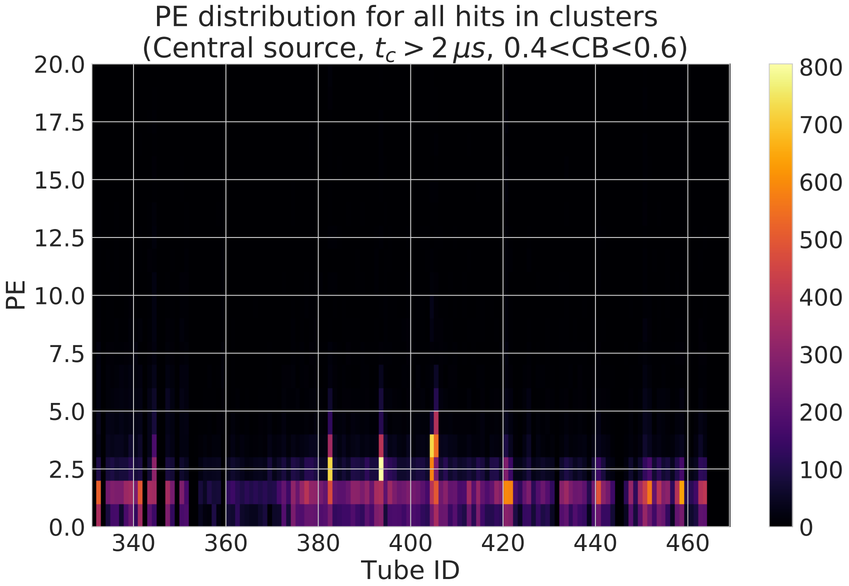

Figure 8.8. PE distribution of delayed clusters in central source data. No preliminary cuts are applied to the data, and delayed clusters with time $t_c > 2\,\mu s$ and $0.4 < CB < 0.6$ are shown. Less afterpulsing is seen in the top-mounted ETEL tubes.

For reference, the low charge balance cluster ($CB < 0.4$) PMT hits are uniformly distributed in the ANNIE tank, as seen in figure 8.9. This is expected for neutron captures, and supports that PMT hit clusters with $CB < 0.4$ are predominantly neutron candidate events.

## 8.5 Validation of AmBe data quality

Prior to conducting a neutron detection efficiency analysis, the AmBe dataset quality was cross-checked with several studies. All plots shown in this section compare the central runs (position 0) with and without the AmBe source installed unless noted otherwise.

### 8.5.1 Hit cluster time distributions

It is informative to preview the hit cluster distributions in data prior to applying all preliminary cuts. The distribution of all hit clusters seen in the central AmBe source runs are shown in figure 8.10. The single SiPM pulse cut was still applied to ensure that the AmBe source SiPM pulses for the event trigger were clean and properly reconstructed.

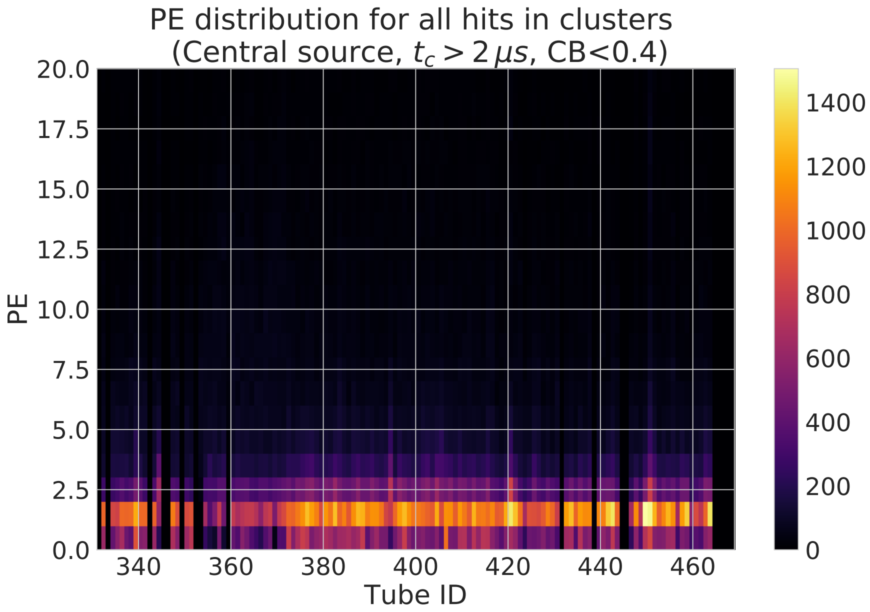

Figure 8.9. PE distribution of delayed clusters in central source data. No preliminary cuts are applied to the data, and delayed clusters with time $t_c > 2\,\mu s$ and $CB < 0.4$ are shown. PMT hits are mostly distributed evenly throughout the ANNIE tank.

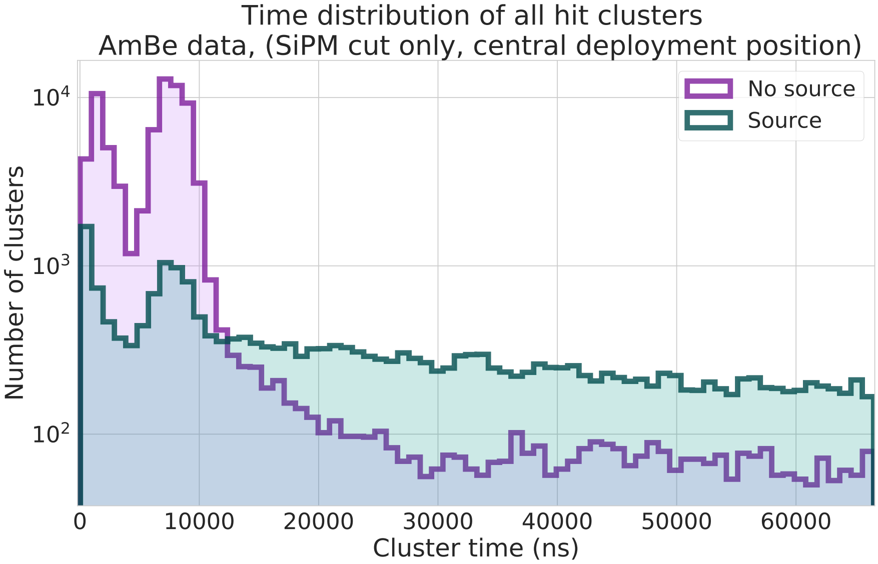

Figure 8.10. Tank cluster time distribution for AmBe central data with and without the source installed. Both datasets contain a tank cluster spike in the first microsecond of the acquisition, consistent with the SiPM trigger time. The tank cluster distribution peak in both datasets between $6-10$ microseconds is due to afterpulsing following high-PE cosmic events in the prompt window.

Both datasets demonstrate a large population of tank PMT hit clusters in both the first microsecond and between $6-10$ microseconds into the acquisition window. The cluster population in the first microsecond is primarily due to through-going muons that produce scintillation light in the BGO crystal; an event display of one candidate cosmic muon in the AmBe data is shown in figure 8.11. The peak at $6 - 10$ microseconds is primarily due to afterpulsing in the PMTs following through-going muons.

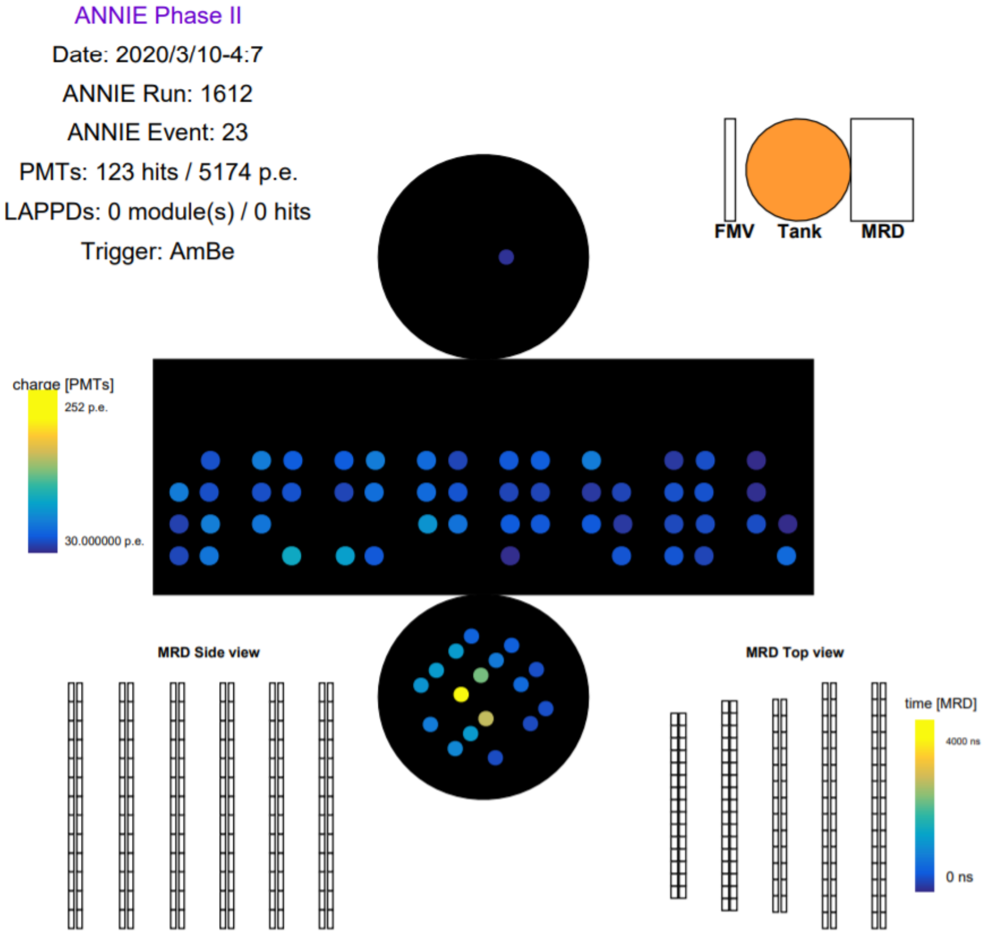

Figure 8.11. Event display for a prompt cluster correlated in time with AmBe source SiPM pulses in the central AmBe background run. A 30 PE threshold is set to emphasize the PMTs within the Cherenkov disk. The charge deposition is primarily in the bottom tubes, indicating the event is likely a downward-going cosmic muon.

The same data from figure 8.10 with all data quality cuts applied are shown in figure 8.12. The dramatic reduction in the size of the background run dataset indicates that most triggers in the background data are correlated with a cluster of PMT hits in the tank. On the other hand, most source data acquisitions have no tank PMT hit clusters in the prompt window. This is expected, as triggers from true 4.4 MeV $\gamma$s should have no PMT hits in the tank region since the

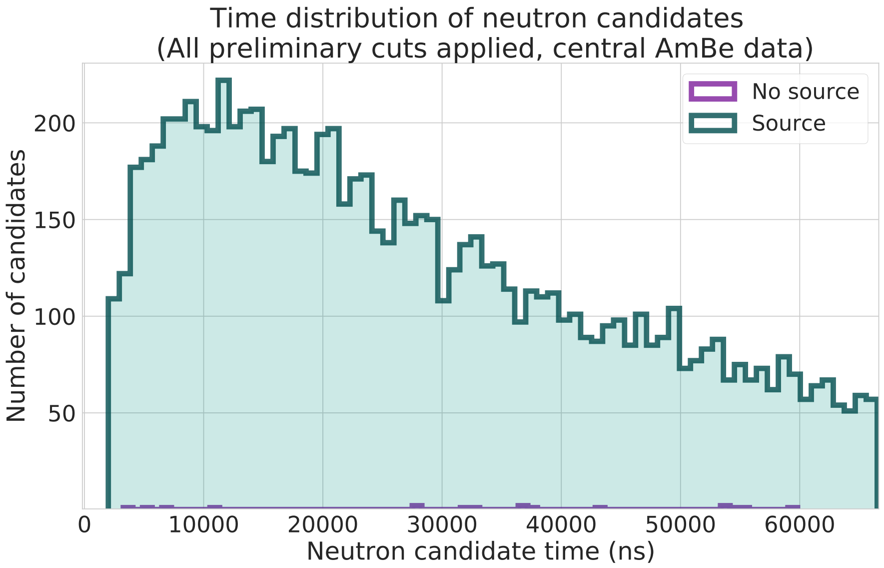

Figure 8.12. Tank cluster time distribution for AmBe central data with all preliminary cuts applied. The application of the preliminary cuts rejects the majority of "no source" acquisitions, reducing the statistics in the background data considerably. The majority of acquisitions with the source installed are preserved and the neutron capture distribution is apparent.

source housing is optically isolated with a black sheet.

Note that although figure 8.12 background distribution may seem to indicate that there should be no flat background in the source data, the dramatic reduction of background counts is mostly due to lowering the statistics of the background dataset. A background consisting of clusters from contamination such as cosmic muons, beam-related events, and background neutrons is still expected in the source data.

### 8.5.2 Delayed cluster time distribution and neutron capture time extraction

To estimate the neutron capture time using the source data's delayed tank cluster distribution, the data were fit with an exponential plus a flat background. The fit is performed in the region from [15,67] microseconds, as the AmBe source neutrons take some time to thermalize prior to potentially capturing on gadolinium in the tank. The best fit is shown in figure 8.13.

The best fit neutron capture time is $37 \pm 7\,\mu s$ with a goodness-of-fit $\chi^2/ndof = 29/35$. This capture time is in agreement with the expected neutron capture time for a gadolinium-doped water detector loaded with $0.2\%$ gadolinium sulfate by mass (see section 5.3.4). The current

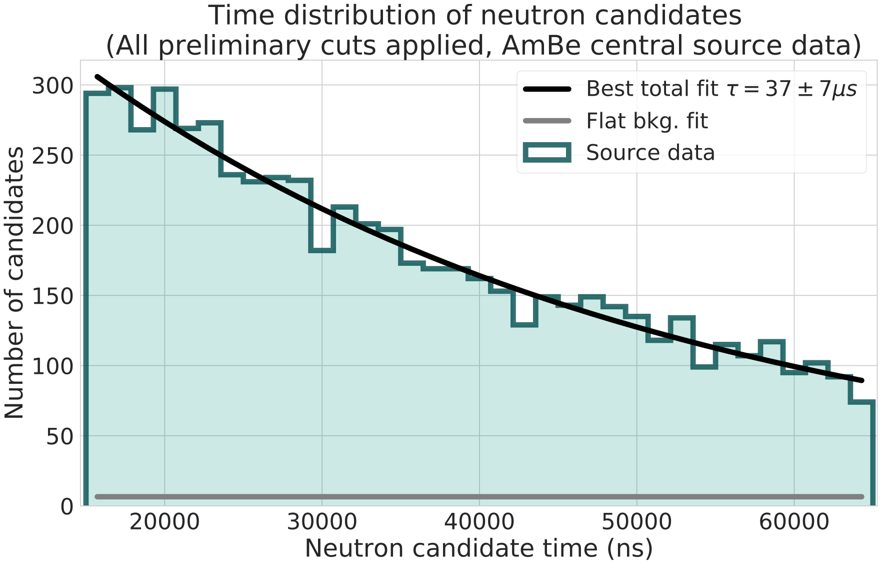

Figure 8.13. Neutron candidate distribution with the best fit flat background plus exponential model. The goodness-of-fit is $\chi^2/ndof = 29/35$. The neutron capture time is in agreement with that expected for the current gadolinium loading.

measurement is statistics-limited, and will have lower uncertainties with the collection of more central data in future calibration runs.

### 8.5.3 Neutron candidate PE distribution

The delayed neutron candidate PE distribution for the central AmBe source data and the central AmBe background data are shown in figure 8.14. No tank cut is applied to the background data to increase the statistics of the background data tank cluster dataset. To exclude afterpulsing, only background datatank clusters occurring at $t_c > 12\,\mu s$ are shown. The background distribution has a similar shape to the source data's neutron candidate PE distribution, suggesting that a decent fraction of background neutron candidates are uncorrelated neutrons.

### 8.5.4 Comparison of data to ANNIE RATPAC simulation

Detector response simulations of the ANNIE tank and MRD have been developed in two GEANT4-based simulation packages. The first simulation package is WCSim, a detector response simulation package that branched off of a simulation package used by the Super-Kamiokande collaboration. The second package is RATPAC (Reactor Analysis Tools Plus Additional Code), which is currently in use by several collaborations including WATCHMAN, SNO+, and Theia [69].

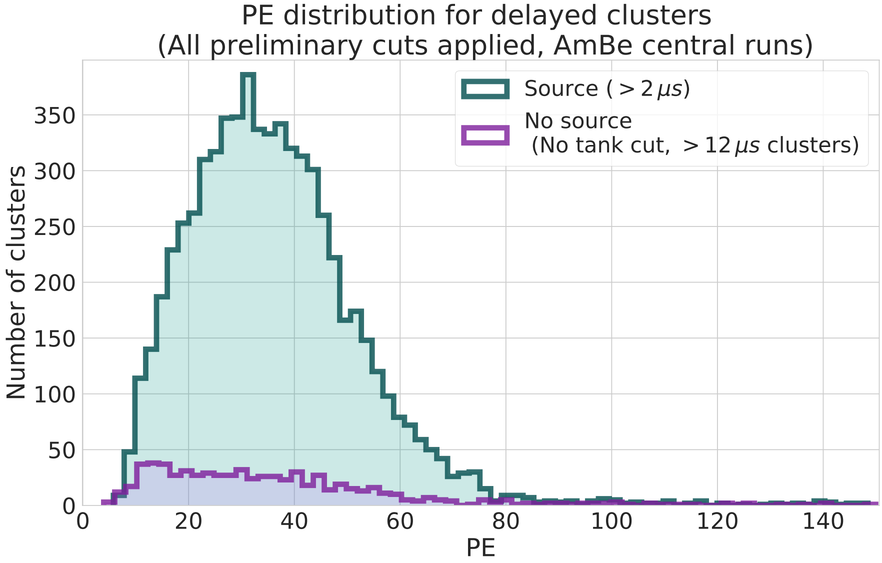

Figure 8.14. Cluster PE distribution for AmBe central runs. The prompt tank cut and $> 150$ PE cut are not applied to the background data to increase the dataset's statistics. Background data tank clusters with $t_c > 12\,\mu s$ are only shown to remove PMT afterpulsing contamination.

Simulations of ANNIE's AmBe data calibration runs were performed with the first default version of RATPAC developed for the ANNIE collaboration (ANNIE RATPAC V1.0). ANNIE RATPAC is developed and maintained in the ANNIE collaboration github repository [204]. The AmBe source housing and the expected AmBe neutron energy profile have been implemented in RATPAC (see figure 8.15). The water transparency in simulation is modeled according to UV-Vis spectrophotometer measurements described in 6.4.2. The gadolinium sulfate concentration is modeled as $0.2\%$ by weight, but will be tuned after the gadolinium concentration in the tank is assayed. Given some parameters, such as the individual PMT charge response curves and an exact mapping of the PMT positions, must still be tuned in the simulation, some differences between data and simulation are expected.

A simulated AmBe source deployment with ten thousand neutrons was performed to compare to the AmBe calibration source data. The neutron candidate capture time predicted in the default RATPAC simulation is compared to the background-subtracted AmBe source data in figure 8.16. The simulation contains a slightly higher fraction of neutron captures in the time window $t < 20\,\mu s$, but is generally in good agreement with the calibration data. It is possible that the simulation's gadolinium sulfate concentration of $0.2\%$ by weight is too high, resulting

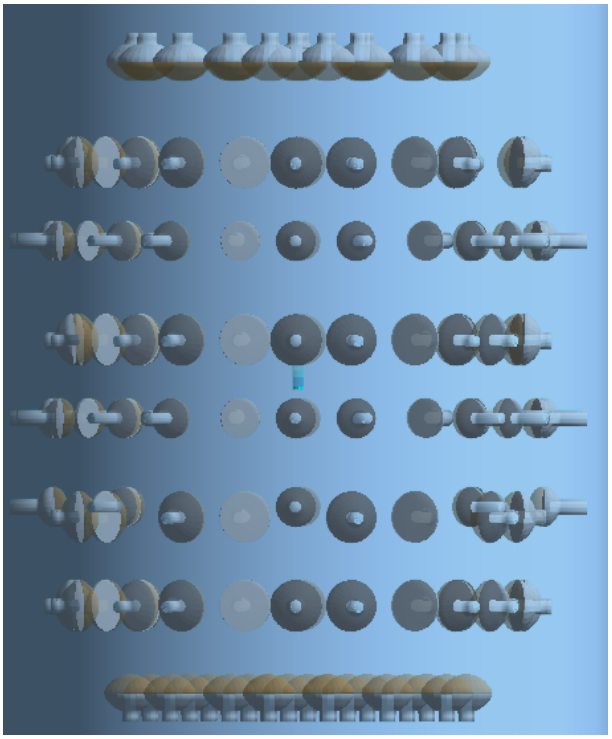

Figure 8.15. Visualization of the AmBe source housing simulated in the ANNIE tank in RAT-PAC. Figure credit: Vincent Fischer.

in too short of a decay time constant (and a smaller fraction of neutron captures at later times). An assay of the ANNIE tank's final gadolinium concentration must be performed in the future to cross-check this possible discrepancy.

The neutron candidate PE count distribution where $PE_{tot} > 20$ is shown in figure 8.17. The data and simulation PE distributions for the lower PE range are in disagreement and are not compared; the disagreement is due to a systematic loss of neutrons in data caused by the cluster finder needing a minimum of five PMT hits to define a cluster. This five PMT hit threshold could be lowered at the cost of larger data files and increased processing time.

In the higher PE range, an interesting feature around 60-80 PE appears in the simulation which is not seen in data. One possibility is that the gadolinium de-excitation model in the default RATPAC simulation package does not reflect the actual de-excitations of gadolinium, and should be updated. This disagreement will be further investigated in upcoming Data/MC comparison studies.

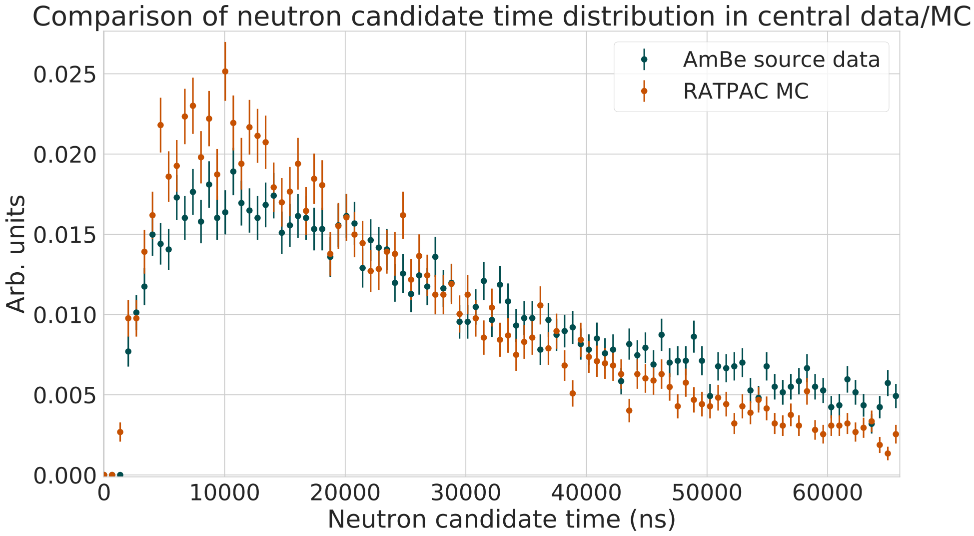

Figure 8.16. Visualization of the AmBe source housing simulated in the ANNIE tank in RATPAC. The default simulation is in good agreement with the AmBe data, but does have a larger fraction of captures for $t_c < 20\,\mu s$. This discrepancy may be caused by an overestimation of the gadolinium concentration in the simulation.

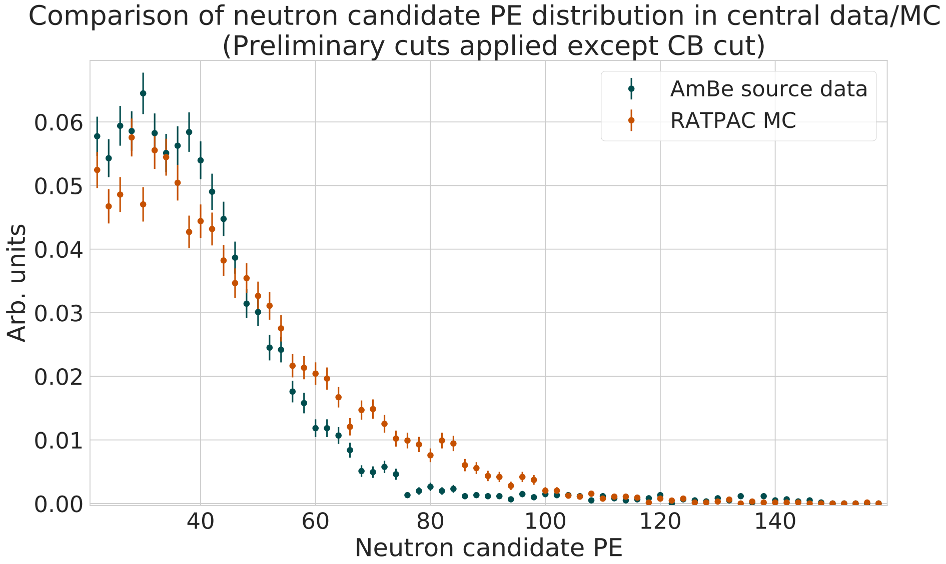

Figure 8.17. PE distribution as seen in the default RATPAC AmBe simulation data and the ANNIE source deployment data. A feature at 60-80 PE is present in the simulation that is not observed in the actual source data.

## 8.6 Extraction of neutron detection efficiency

The neutron detection efficiency was extracted from the neutron multiplicity distribution of the AmBe source data. The neutron candidate multiplicity per trigger in the AmBe source data is shown in figure 8.18.

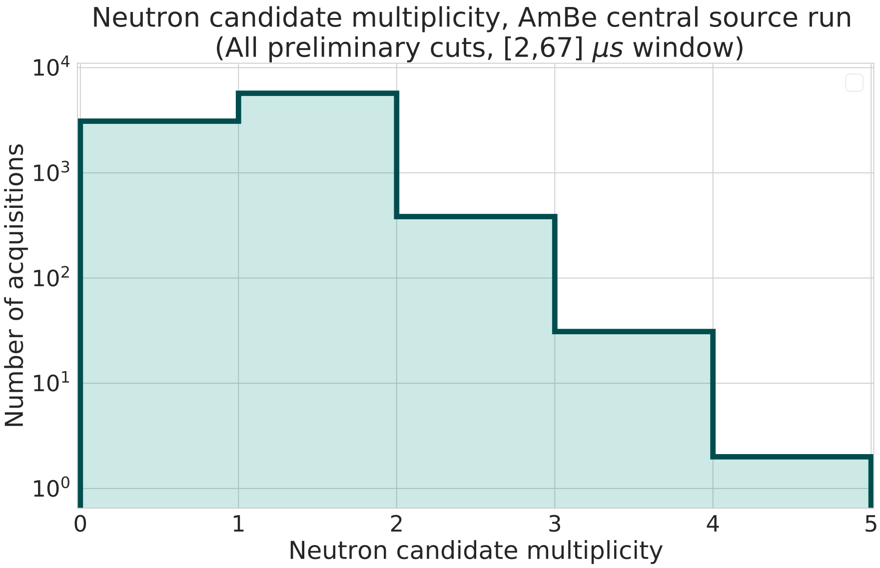

Figure 8.18. Histogram of the number of neutron candidates detected per acquisition in the ANNIE source data. The presence of acquisitions with multiplicity greater than one suggests the presence of backgrounds.

In a background-free scenario with all triggers resulting from 4.4 MeV $\gamma$s, the neutron detection efficiency would simply be

$$\epsilon_n = \frac{Num.\ triggers\ with\ neutron\ candidate}{Num.\ triggers}\ . \tag{8.1}$$

However, the presence of background contamination and triggers due to neutron activity from the AmBe source would have caused the naive counting analysis in equation 8.1 to yield an incorrect detection efficiency. I developed and performed an analysis which extracts the neutron detection efficiency in the presence of backgrounds.

Two different models were developed through which the neutron efficiency was extracted. One model utilizes the background data to model the background component of the multiplicity distribution, while another models the background's contribution to the multiplicity as resulting from a purely uncorrelated background. Ultimately, the results from both models were used to produce a final efficiency estimate and estimate the uncertainty of the background models.

### 8.6.1 Multiplicity model

The multiplicity distribution model utilizes a toy Monte Carlo approach to produce a distribution based on the input background model and neutron detection efficiency (labeled $\epsilon_n$). Consider a single Monte Carlo throw of the neutron candidate multiplicity distribution, labeled $M$. The neutron multiplicity for this single throw is given by

$$M = \delta_S + N_B \ , \tag{8.2}$$

where $\delta_S$ is the AmBe decay's correlated neutron and $N_B$ is the number of background neutron candidates detected.

$\delta_S$ is either 0 or 1, and is determined with a random draw $x$ between $[0, 1]$ and is defined as

$$\delta_s(x) = \begin{matrix} 1 \ , \ \ x \leq \epsilon_n \\ 0 \ , \ \ x > \epsilon_n \ , \end{matrix} \tag{8.3}$$

where $\epsilon_n$ is the neutron detection efficiency in the model.

$N_B$ is a random draw from the background multiplicity distribution model. A random draw is performed by forming the cumulative distribution $C_B$ of the background multiplicity distribution, firing a random number $x$ in the range [0,1], and getting the value returned from $C_B(x)$. In the data-driven background model, $N_B$ is sampled using the background multiplicity distribution measured in the AmBe background run (see figure 8.19). In the uncorrelated background model, $N_B$ is drawn from a Poisson distribution of mean background rate $\lambda_N$, given by

$$Pois_B(x; \lambda_n) = \frac{\lambda_n^x e^{-\lambda_n}}{x!} \ , \tag{8.4}$$

where $\lambda_n$ is a free parameter that must also be fit.

Using one million throws of $M$ for a fixed $\epsilon_n$ and either the background data multiplicity distribution or a Poisson background of rate $\lambda_n$, a multiplicity profile $P_{model}$ is formed. The model distribution $P_{model}$ for the input parameters is normalized then tested with a goodness-of-fit test against the AmBe source data's normalized multiplicity distribution.

In the data-driven background model, the goodness-of-fit $\chi^2_{DD}$ is defined as

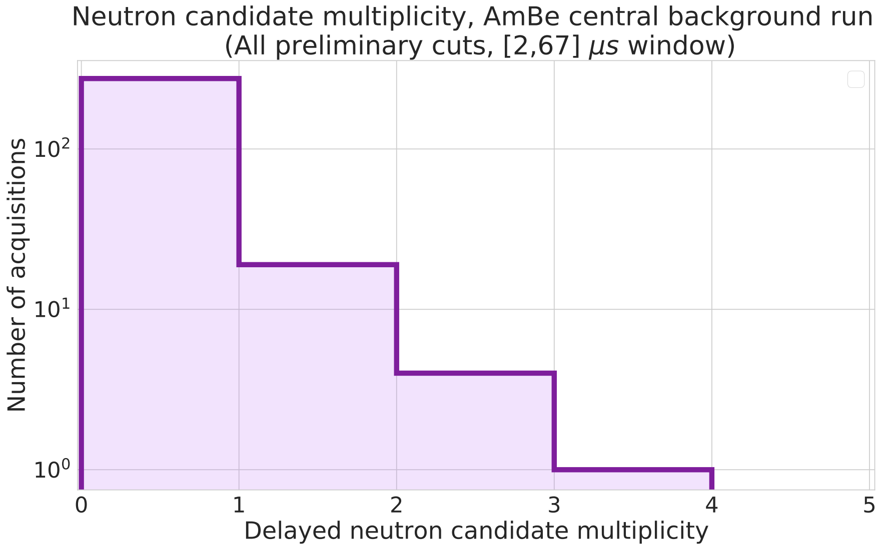

Figure 8.19. Neutron candidate multiplicity in AmBe background run. All preliminary cuts have been applied to the dataset. The multiplicity distribution is drawn from to produce $N_B$ values in the data-driven multiplicity model.

$$\chi^2_{DD}(\epsilon_n) = \sum_{i=1}^{N} \left( \frac{P_{data}(i) - P_{model}(i)}{\sqrt{\sigma^2_{s,i} + \sigma^2_{b,i}}} \right)^2 , \tag{8.5}$$

where $\sigma_{s,i}$ is the statistical uncertainty of multiplicity bin $i$ in the source data and $\sigma_{b,i}$ is the statistical uncertainty of bin $i$ in the background data. The best fit neutron efficiency $\epsilon_n$ is determined by scanning the entire probability space $\epsilon_n \, \forall \, [0, 1]$ in a profile likelihood fashion.

In the Poisson background model, the goodness-of-fit $\chi^2_{Pois}$ is defined as

$$\chi^2_{Pois}(\epsilon_n, \lambda_n) = \sum_{i=1}^{N} \left( \frac{P_{data}(i) - P_{model}(i)}{\sigma_{s,i}} \right)^2 , \tag{8.6}$$

where $\sigma_{s,i}$ is the statistical uncertainty of multiplicity bin $i$ in the source data. The best fit neutron efficiency $\epsilon_n$ and background rate $\lambda_n$ are determined by scanning the entire probability space for both variables in a profile likelihood fashion.

The variation of the $\chi^2$ parameter as a function of profile variables was used to quantify the uncertainties in the best fit model parameters. The $\epsilon_n, \lambda_n$ parameters that yielded the lowest goodness-of-fit parameter $\chi^2_{min}$ was taken as the best fit efficiency. The confidence limit for the best-fit neutron detection efficiency was taken as the range of $\chi^2$ values where the following expression is valid [205]:

$$\chi^2 - \chi^2_{min} \leq \Delta\chi^2 \ , \tag{8.7}$$

where $\Delta\chi^2$ is a function of the confidence limit and the number of parameters being simultaneously fit. For a confidence interval of 68.3%, $\Delta\chi^2 = 1$ when fitting a single parameter and $\Delta\chi^2 = 2.3$ when simultaneously fitting two parameters [205].

### 8.6.2 Neutron efficiency estimates for central source data

A comparison of the best-fit multiplicity models described in section 8.6.1 to the central source data (position 0) are shown in figure 8.20. Both models are in agreement with the data at lower cluster multiplicities, but diverge at the higher multiplicity bins. For all source positions, the uncorrelated background model fit underestimates the high multiplicity tail, while the data-driven background model fit overestimates the tail. This suggests that background-related neutron candidates observed in the AmBe source data:

- Are not entirely uncorrelated-in-time backgrounds (since the Poisson background model underestimates the source data distribution)

- Contain less backgrounds than that found in the background dataset (since the background-driven model overestimates the source data distribution)

The $\chi^2_{DD}$ profile for the data-driven fit to the position 0 source data is shown in figure 8.21. The best fit detection efficiency was found to be $\epsilon_n = 0.64$ with $\chi^2/ndof = 4/5$. The low statistics of the background set results in a larger uncertainty for the data-driven model fit and broadens the goodness-of-fit profile.

The uncorrelated background model's goodness-of-fit is in higher tension with the position 0 source data ($\chi^2/ndof = 11/5$) but agrees well with the data-driven model fit (also has best fit $\epsilon_n = 0.64$). The goodness-of-fit profile as a function of $\epsilon_n$ and $\lambda_n$ are shown in figure 8.22. The likelihood profile for the uncorrelated background model is two-dimensional, as both the detection efficiency $\epsilon_n$ and the background rate $\lambda_n$ were varied to find the best fit to the data.

To better illustrate the uncertainty in both the neutron efficiency parameter and the background rate parameter, the same goodness-of-fit profile in figure 8.22 is projected along the $\epsilon_n$ and $\lambda_n$ axes at the minimum $\chi^2$ in figures 8.23 and 8.24.

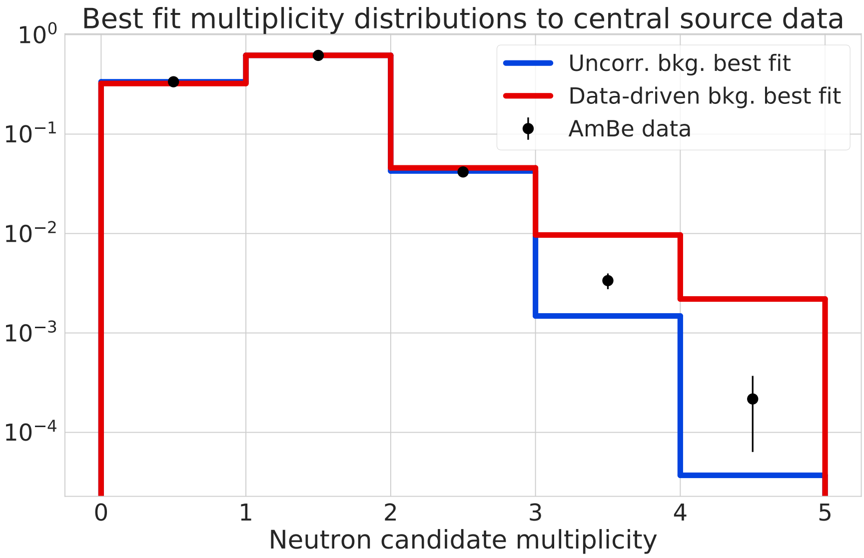

Figure 8.20. Best fit neutron candidate multiplicity models for the central source data. The data-driven model overestimates the higher cluster multiplicity tail while the uncorrelated background model underestimates the distribution tail.

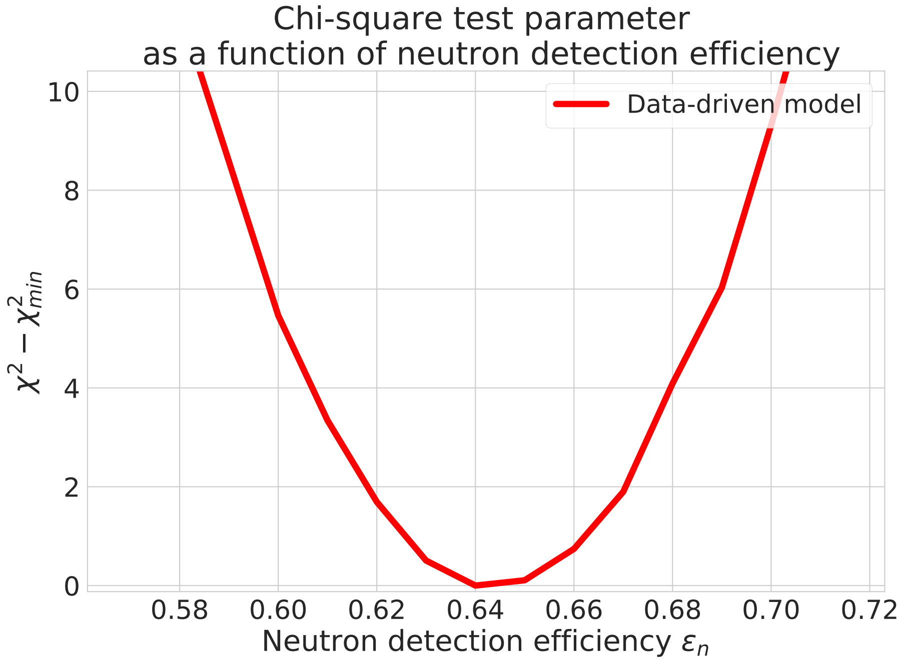

Figure 8.21. Goodness-of-fit profile for the data-driven multiplicity model as the neutron detection efficiency $\epsilon_n$ is varied. The best fit neutron detection efficiency is $\epsilon_n = 0.64$, with $\chi^2/ndof = 4/5$.

Note that the neutron detection efficiency estimate from the uncorrelated background model fit has smaller uncertainties than that of the data-driven model fit. This is expected, as the data-

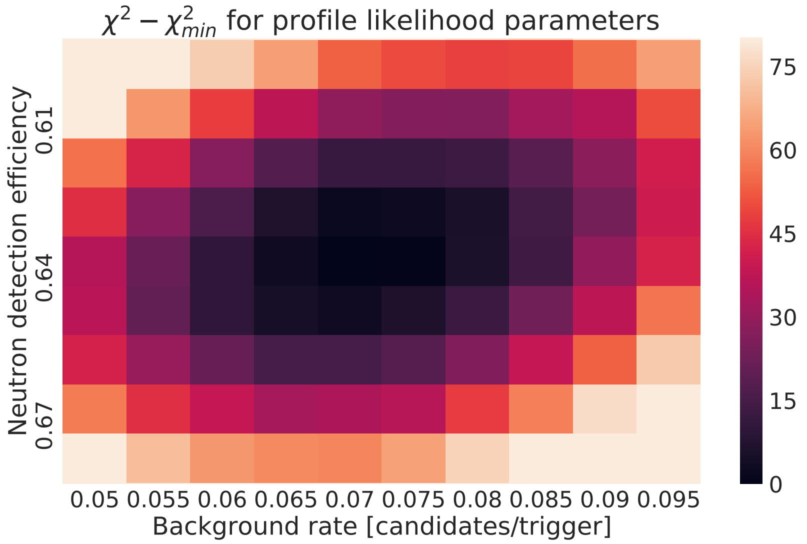

Figure 8.22. Two-dimensional goodness-of-fit profile for the multiplicity model assuming an uncorrelated background. The best fit neutron detection efficiency is $\epsilon_n = 0.64$, with a goodness-of-fit of $\chi^2/ndof = 11/5$.

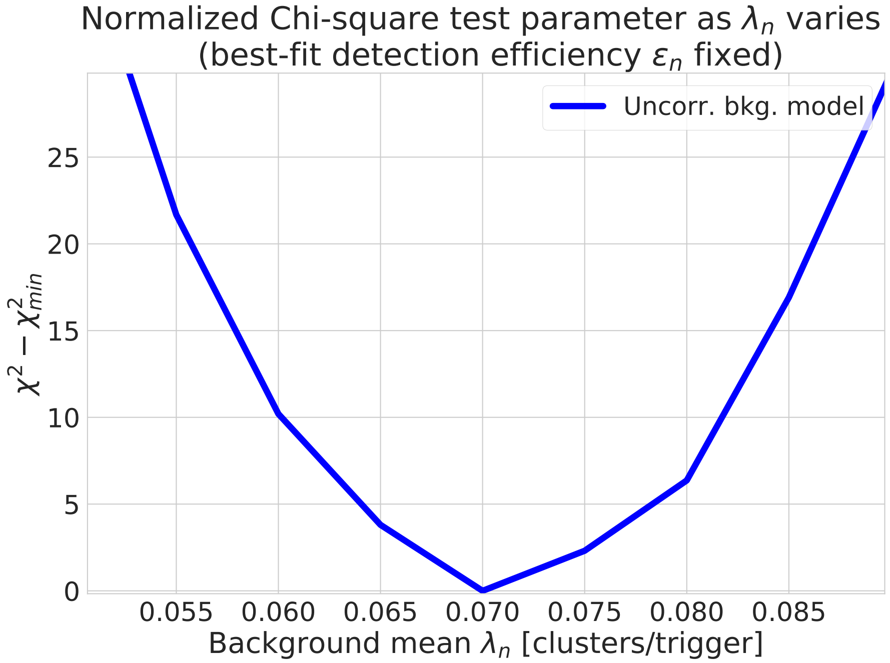

Figure 8.23. Goodness-of-fit profile for the uncorrelated background multiplicity model to AmBe source data for fixed best-fit detection efficiency $\epsilon_n$.

driven background fit also incorporates the background data's statistical uncertainties into the goodness-of-fit parameter. The uncertainties of the data-driven model fit should become comparable to the uncorrelated background model with the collection of more background data.

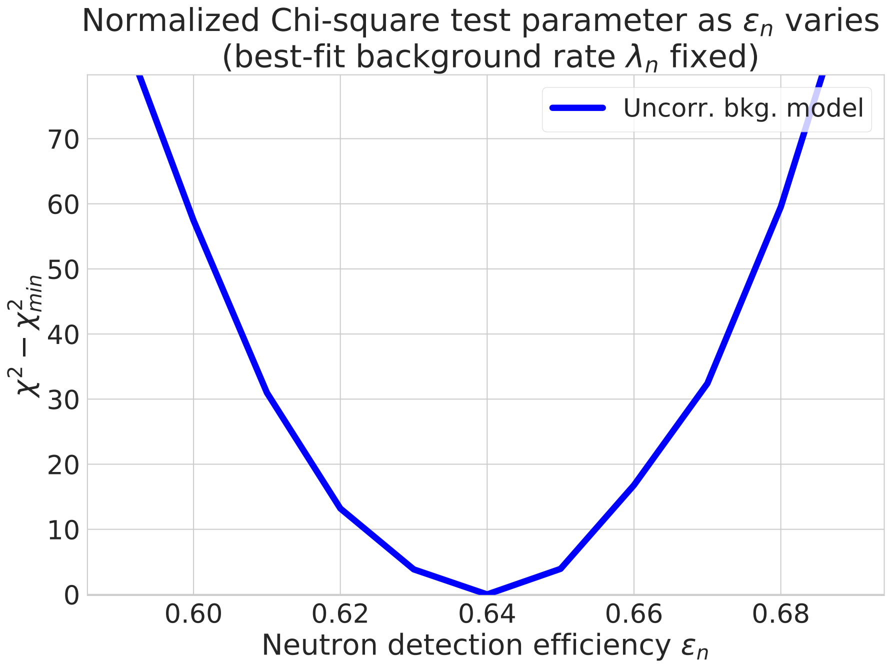

Figure 8.24. Goodness-of-fit profile for the uncorrelated background multiplicity model to AmBe source data for fixed best-fit background rate $\lambda_n$.

### 8.6.3 Neutron efficiency estimates for all AmBe source positions

The fit procedures described above are repeated for all source positions to quantify the neutron detection efficiency for each source position. A table containing the best fit neutron efficiencies as well as the $\chi^2/ndof$ is shown in table 8.4.

Given the overall more stable goodness-of-fit and higher uncertainties, the best fit detection efficiencies from the data-driven background model are conservatively taken as the final estimate. The difference in the estimates from the two models is taken as a systematic uncertainty.

As a cross-check for the uncorrelated background model, the best-fit background rate $\lambda_n$ was compared for all four source positions. Aside from any impacts due to shadowing or radioactivity contamination on the source housing, all positions should predict the same mean background rate within uncertainties. The background rate fits are in agreement for all source positions, as shown in table 8.5. It is interesting to note that position 0 shows a slight tension with the other positions; the potential source of this tension is currently unknown.

| Fit method | Position | Best fit $\epsilon_n$ | $\chi^2/ndof$ | $\sigma_{\epsilon_n}$ |
|---|---|---|---|---|
| Data-driven fit | Position 0 | 0.64 | 4/5 | +0.03, -0.02 |
| | Position 1 | 0.57 | 5/5 | +0.03, -0.02 |
| | Position 2 | 0.46 | 5/5 | +0.02, -0.03 |
| | Position 3 | 0.35 | 5/5 | +0.03,-0.02 |
| Uncorr. background fit | Position 0 | 0.64 | 11/5 | +0.01,-0.02 |
| | Position 1 | 0.57 | 9/5 | +0.01, -0.01 |
| | Position 2 | 0.45 | 16/5 | +0.01, -0.01 |
| | Position 3 | 0.36 | 1/5 | +0.01, -0.02 |

Table 8.4. Summary of neutron detection efficiency fits using both multiplicity models. Although the uncertainties are higher on the data-driven model, the efficiency predictions from both models are consistent with each other.

| Position | Best fit $\lambda_n$ [candidates/trigger] | $\sigma_{\lambda_n}$ |
|---|---|---|
| Position 0 | 0.073 | +0.004, -0.012 |
| Position 1 | 0.068 | +0.005, -0.006 |
| Position 2 | 0.067 | +0.004, -0.008 |
| Position 3 | 0.068 | +0.007,-0.007 |

Table 8.5. Summary of best-fit background rates in all AmBe source datasets. All positions are in agreement within the uncertainty on the fits.

## 8.7 Systematic uncertainties

Three main systematic uncertainties were considered when quoting the final efficiency results in the following section. The systematics taken into consideration include:

- Uncertainty in the background model
- Neutron captures on the AmBe source housing
- Contamination of AmBe data with acquisitions due to non-AmBe triggers (false starts)

### 8.7.1 Uncertainty in the background model

The uncertainty in the background model was taken as the difference between the best-fit neutron detection efficiency of each model (labeled $\delta_m$). Given the uncorrelated background multiplicity model underestimates the source data while the data-driven multiplicity model overestimates the data, the incorporation of this systematic should provide coverage over the true best-fit neutron multiplicity distribution.

### 8.7.2 Neutron captures on AmBe housing

Neutrons that capture on the AmBe housing produce a systematic error in the neutron detection efficiency which is not be present in beam data. Any neutrons that capture on the AmBe housing and produce a signal in the tank with less than five PMT hits would go undetected by the clustering algorithm; as such, neutrons captured on the housing result in a systematic error biased in lowering the neutron detection efficiency. The uncertainty associated with AmBe housing neutron captures is quantified using the AmBe RATPAC simulation.

Ten thousand AmBe neutrons were simulated in the AmBe housing in RATPAC, and the number of neutrons that capture on the source were counted. A total of 31 neutrons out of 10k neutrons generated captured on the AmBe housing, and never had the chance to capture on gadolinium in water. As such, the systematic correction due to the housing neutron captures $\delta_h$ would be

$$\delta_h = \frac{31}{1E5} \pm \frac{\sqrt{31}}{1E5} = 0.003 \pm 0.001 \; . \tag{8.8}$$

A positive systematic error of $0.4\%$ is propagated into the detection efficiency uncertainty to cover this effect.

### 8.7.3 Triggers caused by background activity (background false starts)

As seen in table 8.3, the background data indicates that after applying preliminary cuts, up to $0.005$ Hz of the trigger rate of the $1.15$ Hz rate seen in runs 1594-1596 can be contributed to non-AmBe activity. The ratio of these rates can be used to quantify an error in the neutron efficiency prediction due to background triggers.

The background trigger rate and source trigger rate in table 8.3 ($f_B = 0.005\,Hz$ and $f_S =$

$1.15\,Hz$) and their statistical uncertainties are used to estimate the background trigger contamination probability $\delta_{bt}$, written as

$$\begin{aligned} \delta_{bt} &= \tfrac{f_S}{f_B} \pm \left[ \tfrac{f_S}{f_B} \sqrt{\left(\tfrac{\delta_{f_S}}{f_S}\right)^2 + \left(\tfrac{\delta_{f_B}}{f_B}\right)^2} \right] \;, \\ &= 0.004 \pm 0.001 \;. \end{aligned} \tag{8.9}$$

The value in equation 8.9 estimates the fraction of background activity triggers, but not how much the background activity triggers impact the detection efficiency estimate. The uncertainty in the detection efficiency due to this contamination is reasoned as follows. In the most extreme error possible, any background activity trigger will have no neutron activity in the delayed window, negatively biasing the neutron efficiency estimate. The magnitude of this bias would be proportional to the fractional background trigger contamination probability itself ($\delta_{bt} = 0.4 + 0.1\%$). To conservatively cover the most extreme case, a positive systematic error of $0.5\%$ is propagated into the detection efficiency systematic uncertainty.

### 8.7.4 Neutron-induced triggers (false start neutrons)

Neutron-induced triggers, also referred to as “false start neutrons”, require a systematic correction to the neutron capture efficiency estimate. Consider a neutron produced in the AmBe source which either has no 4.4 MeV $\gamma$ or has a correlated 4.4 MeV $\gamma$ which does not trigger data acquisition. The neutron can capture on gadolinium near the source housing, producing de-excitation $\gamma$s which can scatter in the BGO crystal and initiate data acquisition (see figure 8.25). No correlated neutron will be observed in the delayed window for this trigger; as such, false start triggers result in a systematic underestimate of the neutron capture detection efficiency.

Most false start neutron triggers can be rejected using the tank activity cut. Figure 8.25 shows that most false start neutrons should have both AmBe source SiPM pulses (from the $\gamma$ that scatters in the BGO) and tank PMT pulses (from the $\gamma$s that Compton scatter on electrons in the tank volume). This coincident activity is a tag for false start neutrons, and can be used to reject most acquisitions caused by false start neutrons. However, some false start neutrons will not have any hits in the tank volume, and will pass the tank activity cut; the fraction of acquisitions triggered by these false start neutrons with no tank activity must be quantified.

To estimate the fraction of false starts with no tank activity, the PE distribution for all hits

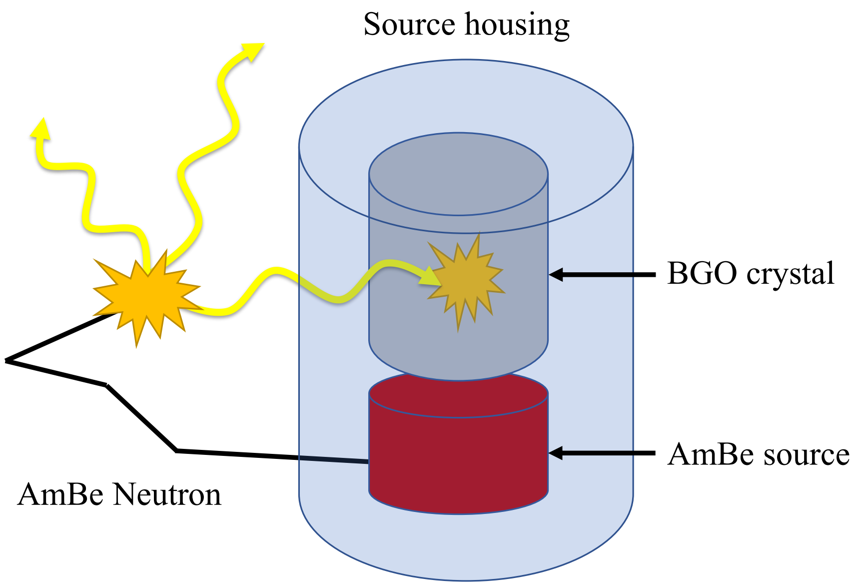

Figure 8.25. Diagram showing an example of a false start neutron. A de-excitation $\gamma$ from the neutron capture scatters in the BGO crystal, triggering data acquisition. The remaining de-excitation $\gamma$s can Compton scatter in the tank, producing PMT hits at the same time as the BGO scatter.

correlated with AmBe source SiPM pulses triggering data acquisition is used. For each trigger, the PE of all PMT hits within 300 nanoseconds of the acquisition's SiPM pulses are summed. This distribution is composed of acquisitions triggered by false start neutrons, cosmic muons passing preliminary cuts, and 4.4 MeV $\gamma$s that have secondary Compton scatters inside the tank volume. The SiPM-correlated tank PE distribution is shown in figure 8.26.

The distribution in figure 8.26 can then be simultaneously fit with the PE distributions from 4.4 MeV $\gamma$s, and false start neutrons. Note that at the $< 150$ PE regime, through-going cosmic muons can mostly be neglected in the fit because muons produce Cherenkov light on their way to AmBe housing at the center of the tank; this usually produces more than 150 PE in the tank PMTs. The total PE distribution for each component is estimated using RATPAC simulations of the 4.4 MeV $\gamma$ and neutrons produced in the AmBe source. 100k events were simulated for each component. Note that the distribution shape for each signal changes depending on what trigger threshold is set for the AmBe source SiPMs. The PE distribution shape for different BGO energy deposition thresholds is shown in figures 8.27 and 8.28.

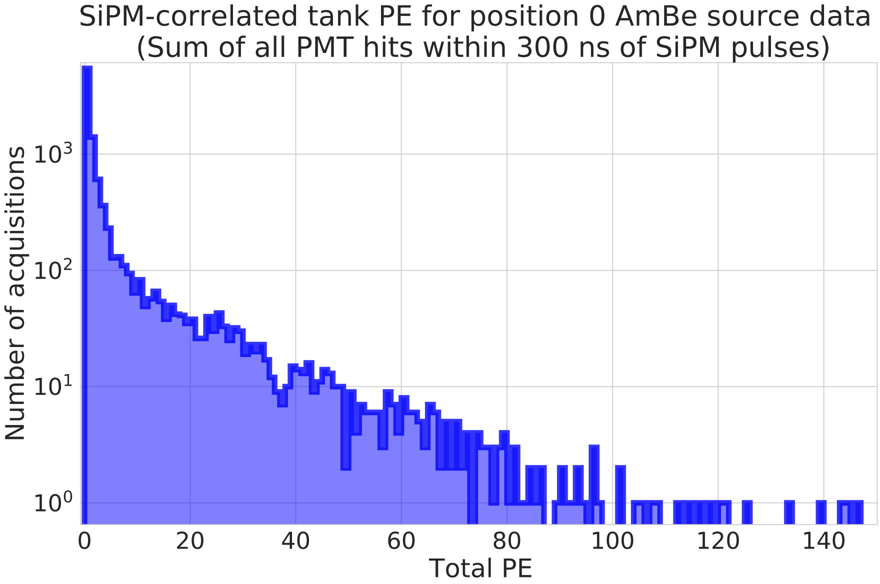

Figure 8.26. Histogram of total PE measured within 300 nanoseconds of each pair of AmBe source SiPM pulses triggering data acquisition. SiPM-correlated tank activity is due to a combination of cosmic muon-induced triggers, false start neutrons, true 4.4 MeV $\gamma$s, and uncorrelated backgrounds (such as radioactivity and background neutrons).

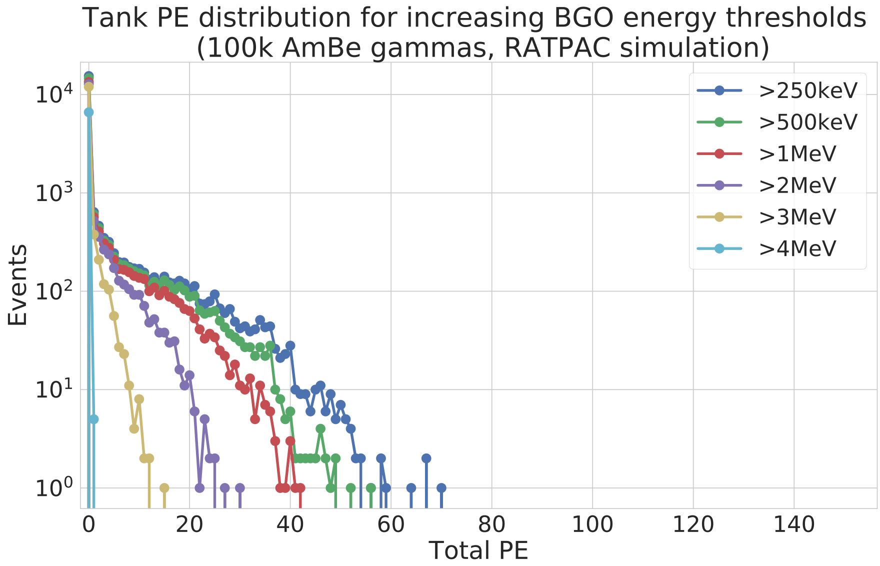

Figure 8.27. RATPAC-based tank PE predictions for 4.4 MeV $\gamma$s from the AmBe source which also deposit some energy in the BGO crystal. The PE distributions for several BGO energy deposition thresholds are shown. The lines connecting each point are for visual aid only.

The false start systematic correction could not be completed for inclusion in this thesis. An energy calibration of the AmBe housing BGO and SiPM setup is needed to choose the correct distributions from figures 8.27 and 8.28. These calibrations will be conducted during the next

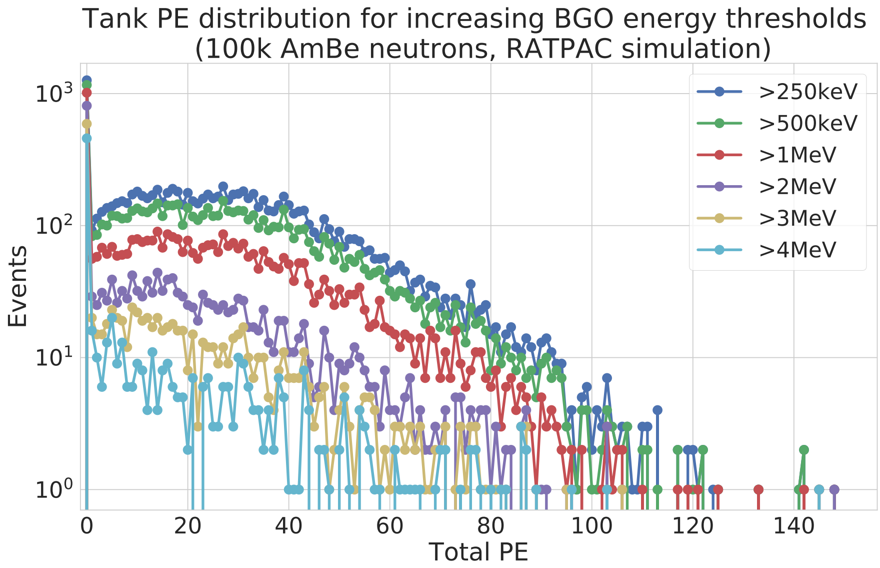

Figure 8.28. RATPAC-based tank PE predictions for neutrons from the AmBe source which also deposit some energy in the BGO crystal. The PE distributions for several BGO energy deposition thresholds are shown. The lines connecting each point are for visual aid only.

AmBe calibration campaign. A Cs-137 source, the 4.4 MeV $\gamma$ peak, and through-going muons will be used to energy calibrate the BGO crystal and AmBe source SiPMs. Following this calibration, the false start neutron fraction will be estimated and applied as a systematic correction.

## 8.8 Summary of systematic corrections

A summary of the systematic uncertainties for each position is given in table 8.6. These values compose the total systematic uncertainties quoted in the final efficiency values presented in section 8.9. The total uncertainty is taken as all systematic uncertainties added in quadrature.

## 8.9 Final neutron detection efficiency estimates

The final neutron efficiency estimates, along with the total uncertainties associated with the goodness-of-fit (stat) and the systematic uncertainties (sys) are quoted in table 8.7. The neutron efficiencies are valid for neutron searches that utilize the [2,67] microsecond time window to collect neutron data relative to the prompt event. Any other time window requires repeating the analysis described above in the time window of interest.

The results from table 8.7 are summarized in graphical form in figure 8.29.

| AmBe Position | $\delta_m$ | $\delta_h$ | $\delta_{bt}$ | Total |
|---|---|---|---|---|
| Position 0 | +0.00 | +0.004 | +0.006 | $^{+0.01}_{-0.00}$ |
| Position 1 | +0.00 | +0.004 | +0.006 | $^{+0.01}_{-0.00}$ |
| Position 2 | -0.01 | +0.004 | +0.006 | $^{+0.01}_{-0.01}$ |
| Position 3 | +0.01 | +0.004 | +0.006 | $^{+0.01}_{-0.00}$ |

Table 8.6. Summary of systematic error uncertainties incorporated into the final neutron detection efficiency estimate. The total systematic uncertainty for each direction is taken as all systematic uncertainties added in quadrature. Estimation of the false start neutron systematic correction and associated uncertainties are not present.

| Position label | AmBe Position (x,y,z) [cm] | Neutron detection efficiency $\epsilon_n$ |
|---|---|---|
| Position 0 | (0,0,0) | $0.64^{+0.03(stat)\ +0.01(sys)}_{-0.02(stat)\ -0.00(sys)}$ |
| Position 1 | (0,0,75) | $0.57^{+0.03(stat)\ +0.01(sys)}_{-0.02(stat)\ -0.00(sys)}$ |
| Position 2 | (0,0,102) | $0.46^{+0.02(stat)\ +0.01(sys)}_{-0.03(stat)\ -0.01(sys)}$ |
| Position 3 | (0,100,102) | $0.35^{+0.03(stat)\ +0.01(sys)}_{-0.02(stat)\ -0.00(sys)}$ |

Table 8.7. Neutron detection efficiency estimate for all four AmBe source positions analyzed, along with quoted total uncertainties.

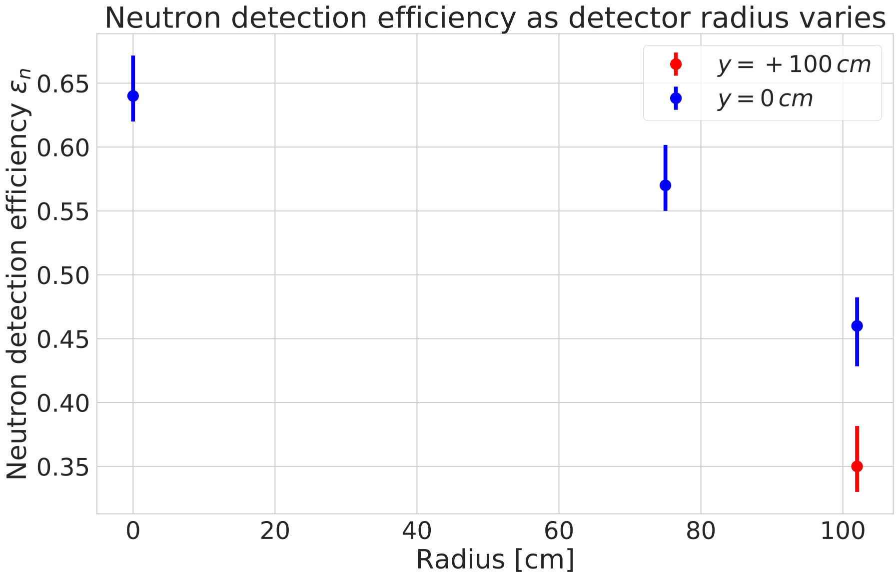

Figure 8.29. Summary of the estimated neutron detection efficiency in the ANNIE tank volume as a function of radius and vertical position. The estimated efficiency is valid for neutrons in the [2,67] microsecond acquisition window relative to the prompt event.

# Chapter 9

# ANNIE neutrino beam data

This thesis closes with a glimpse of ANNIE's first physics-quality neutrino beam data. The event selection used to select neutrino candidate events is described, and a comparison of the neutrino candidate's visible energy (defined in section 9.5) to simulation predictions is shown. The first neutron multiplicity distributions extracted from ANNIE beam data with statistical errors only are also presented. The primary systematic uncertainties are described to close the chapter; analyses used to quantify and apply these corrections to data are beyond the scope of this thesis.

## 9.1 Beam data run summary

The first beam data set collected following commissioning has just under four days of detector livetime in total. A summary of the run numbers, number of candidate triggers, and detector livetime are shown in table 9.1. Note that the first results are statistics-limited, as the BNB was shut down early for the 2019-2020 beam year.

## 9.2 Beam data triggering scheme

For every pulse from the Resistive Wall Monitor (RWM), two and four microseconds of data were taken for the tank PMTs and MRD PMTs, respectively. A single neutrino beam spill from the BNB has a $1.6\,\mu s$ spread; these window widths ensure both detector systems can capture the entire beam window. The acquisition time for the tank PMT and MRD DAQs were aligned relative to the RWM signal such that the entire beam was captured. An elevated rate of tank PMT hit clusters, referred to as "tank clusters", in the two microsecond acquisitions from the

| Run numbers | Number of triggers | Livetime [s] |
|---|---|---|
| 1623 | 299988 | 77797 |
| 1624 | 379991 | 94275 |
| 1625 | 329985 | 84980 |
| 1634 | 229994 | 56934 |
| Total | $1.24 \times 10^6$ | $3.1 \times 10^5$ |

Table 9.1. Summary of the beam runs used for the beam data shown below. The total livetime of the ANNIE detector was approximately 3.6 days.

beam dataset is present in the data, as seen in figure 9.2.

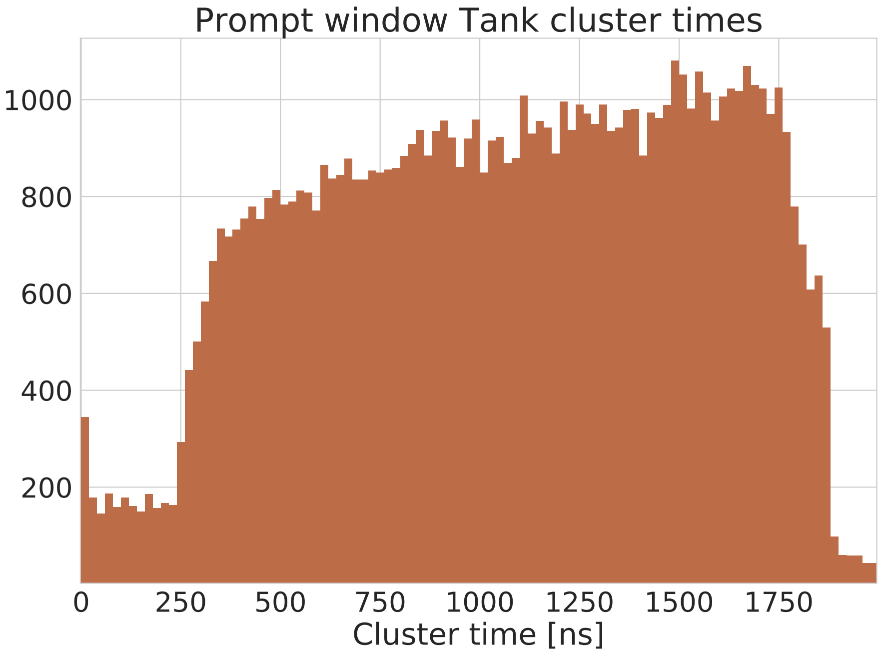

Figure 9.1. Number of hit clusters observed in the first two microseconds of data acquisition in beam data. The elevated number of hits between 300 ns and 1900 ns are due to beam-correlated activity in the ANNIE tank.

The MRD beam data also has an elevated rate of MRD paddle hit clusters, referred to as “MRD clusters”, consistent with the beam window. However, the MRD cluster distribution also has an additional peak near 1.7 microseconds; this peak is due to MRD data acquisitions triggered by the through-going cosmic trigger, which always had MRD hits register at this time in the acquisition window. The removal of cosmic triggers with uncorrelated beam activity will be seen after applying some data quality cuts (see section 9.3).

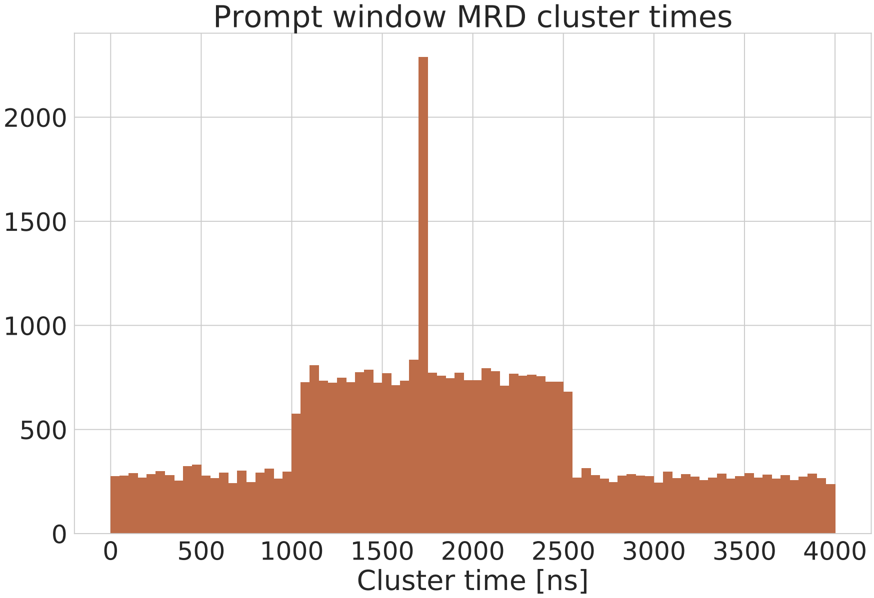

Figure 9.2. Number of MRD paddle clusters observed in beam data. The elevated number of hits between $[1, 2.6]$ microseconds are due to beam-correlated activity in the ANNIE tank. The peak at approximately 1.7 microseconds is due to through-going cosmics which triggered MRD acquisition.

If any single tank PMT ADC channel measures a voltage above baseline consistent with approximately 5 photoelectron counts, the two microsecond acquisition of the tank was extended to a 67 microsecond acquisition in all channels. This extended window could then be searched for tank clusters which were candidates for neutron capture events.

## 9.3 Preliminary beam data event selection

Several preliminary prompt window criteria were created to select coincident tank and MRD activity which could contain neutrino events. Further event selection based on MRD reconstruction and the total photoelectrons seen in the ANNIE tank was used to select neutrino candidate events, and is described in section 9.4.

### 9.3.1 Highest PE and paddle count clusters

When selecting candidate prompt events, the tank cluster with the largest PE and MRD cluster with the most paddle hits were selected. Lower PE events neighboring the largest PE event can be caused by secondary activity such as Michel electrons (electrons produced in a muon decay) or gammas from nuclear de-excitation) and are neglected. In the future, event selection could be made more sophisticated to collect these lower PE clusters for additional physics or calibration analyses.

### 9.3.2 Tank cluster charge balance

A charge balance cut was placed on the prompt clusters to primarily remove instrumental-based tank clusters. The tank PMT cluster charge balance as a function of cluster time is shown in figure 9.3. Notice that a large population of clusters with $CB \sim 1$ and a second subdmoinant population near $CB \sim 0.5$ are present in the 300 nanoseconds prior to the beam window. The cause of these is currently unknown; it is possible that baseline ringing from a previous beam spill or a cosmic muon prior to the acquisition causes these instrumentals. A prompt cluster charge balance cut of 0.9 was placed to ensure the removal of all high charge balance instrumentals.

### 9.3.3 Coincident tank and MRD activity

Any tank and MRD clusters which pass the highest PE/paddle count and charge balance cuts were rejected if their cluster times were not correlated in time. Since the PMT DAQ and MRD DAQ are completely separate systems, the two have different trigger times relative to the same RWM signal. Fortunately, by plotting the MRD cluster times and tank cluster times (see figure 9.4), a clear region of correlated activity is apparent. By taking the difference of the PMT and MRD cluster times, a time cut can be selected to only accept coincident tank and MRD activity. A time cut of $700 < \Delta t_c < 800$ ns was selected. The difference in MRD and tank time clusters, along with the selection window, for all highest PE and largest paddle count clusters are shown in figure 9.5.

### 9.3.4 Impact of preliminary cuts

The selection of the largest PE/paddle count clusters and coincident tank/MRD cluster activity reduces the total event rate, but virtually eliminates clusters outside the beam window. This

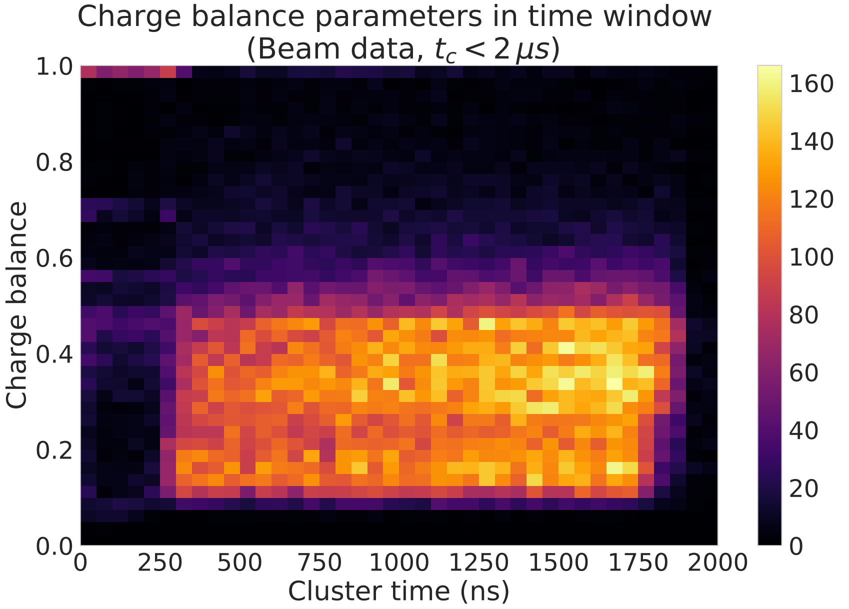

Figure 9.3. Charge balance distribution as a function of time for tank PMT hit clusters in the beam data prompt window. Charge balance populations of $CB \sim 1$ and $CB \sim 0.5$ are present in the first 300 nanoseconds, but are overwhelmed by beam window activity between 0.3-1.9 microseconds. Most clusters in the beam window have a charge balance $CB < 0.8$.

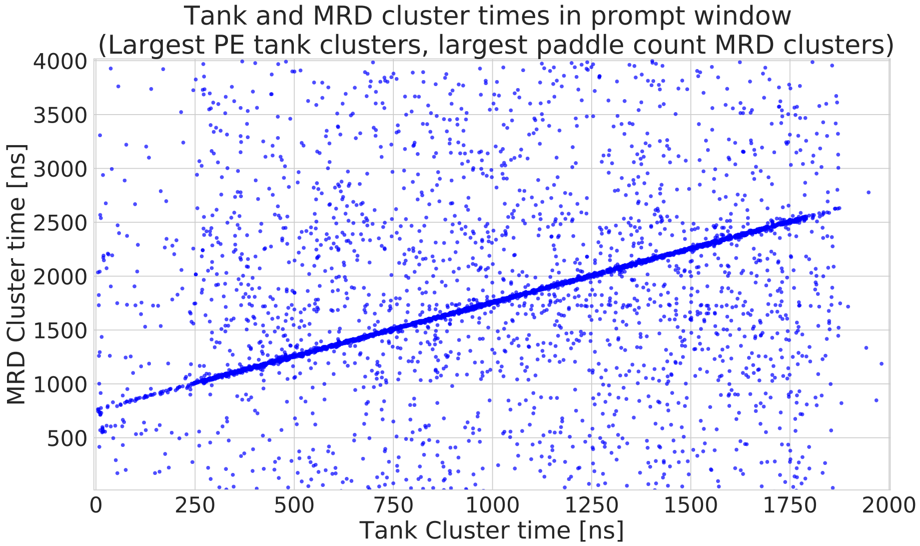

Figure 9.4. Scatter plot of the MRD and tank cluster times in ANNIE beam data. A clear line of correlated activity in the neutrino beam spill window is apparent.

removal of most events outside the beam window indicates the cuts are efficient at reducing non-beam related activity. The reductions in tank and MRD cluster counts due to the preliminary cuts are given in figures 9.6 and 9.7. A summary of the reductions in cluster counts with the

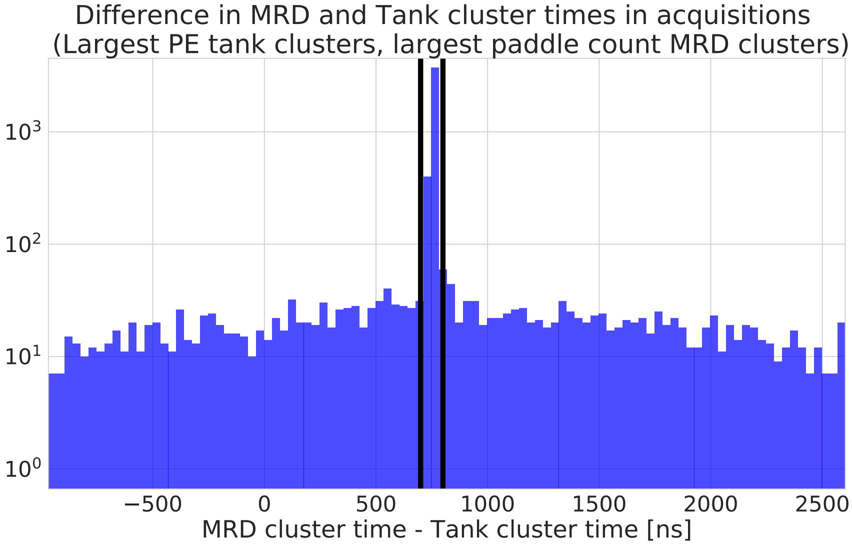

Figure 9.5. Difference in the tank and MRD cluster times. The accepted time window for correlated tank/MRD activity due to the beam is for $700 < \Delta t_c < 800$ ns (marked with black lines in the figure).

| Prompt selection criteria | Tank clusters | MRD clusters |
|---|---|---|
| No cuts | 73846 | 68821 |
| $CB < 0.9$ | 70836 | - |
| Highest PE/most paddles | 40200 | 66741 |
| $700 < \Delta t_c < 800$ ns | 4219 | 4219 |
| Spills/prompt candidate | | $293 \pm 5$ |

Table 9.2. Summary of the prompt candidate event selection impact. An event with coincident tank and MRD activity occurs approximately once every 293 beam spills.

application of preliminary cuts is shown in table 9.3. A prompt event candidate is seen approximately every 293 beam spills; given that the BNB has approximately $5 \times 10^{12}$ protons-on-target (POT) per spill [152], a prompt candidate occurs once every $1.5 \times 10^{15}$ POT.

## 9.4 Neutrino CCQE candidate event selection

Additional event selection is applied to select candidate CCQE events from the prompt event candidate dataset. Current CCQE candidate event selection relies primarily on MRD reconstruction information and front veto hit information. Reconstruction of the interaction vertex

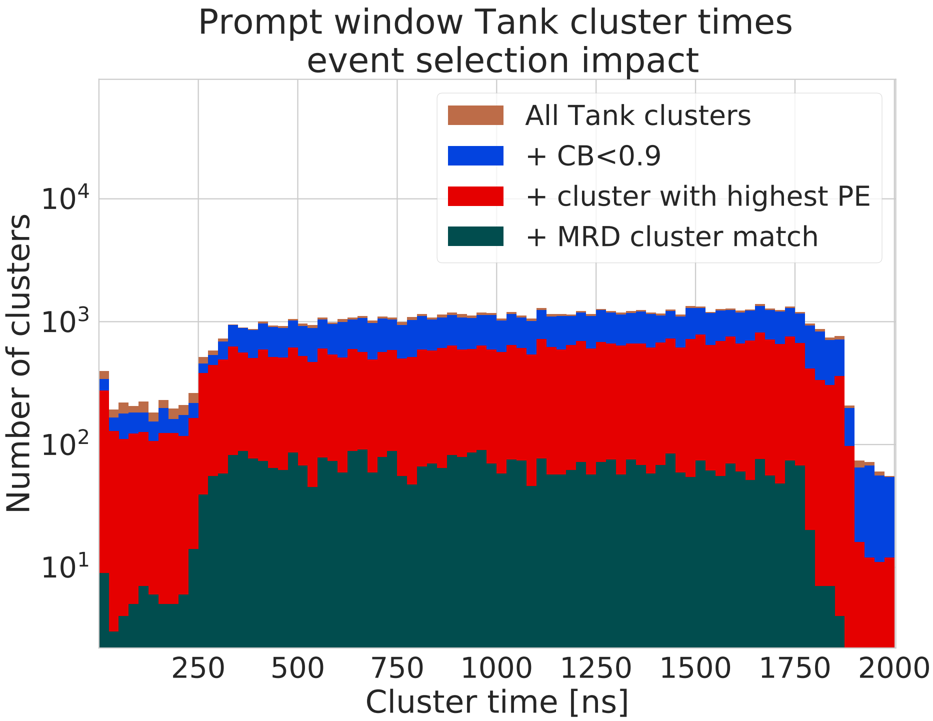

Figure 9.6. Tank clusters in the prompt acquisition window with preliminary event selection applied. The event selection requirements remove most events outside the beam window, indicating a reduction in background events. The tank/MRD time correlation has the greatest impact on selecting events in the beam window.

using tank PMT information will improve selection criteria in future analyses. These event selection criteria, and the analysis of the associated systematic uncertainties, will be modified as the ANNIE tank's calibration and offline analyses evolve.

### 9.4.1 MRD track reconstruction

For a first analysis, only prompt candidates with a single reconstructed track were selected as a neutrino CCQE candidate event. Multi-track events are primarily associated with resonant or deep-inelastic scattering neutrino interactions or contamination from coincident through-going cosmic activity. As such, selecting single-track events helps ensure the visible energy estimate is associated with the muon from a neutrino interaction alone.

### 9.4.2 No muon veto hit

Any event that has one or more paddle hits in the front veto is rejected from the neutrino candidate pool. Muons produced from neutrino interactions in the dirt upstream from the ANNIE tank

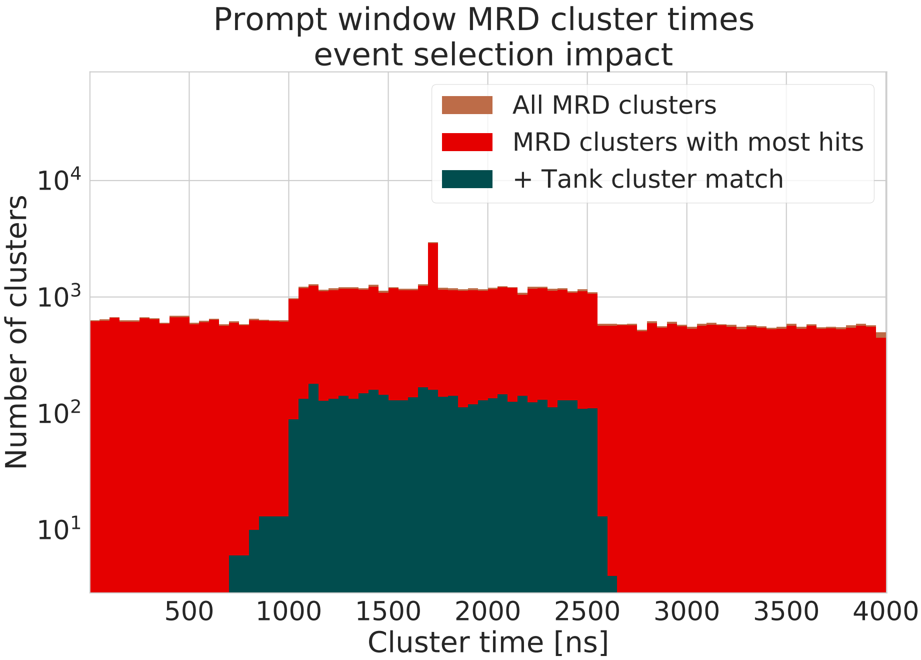

Figure 9.7. MRD clusters in the prompt acquisition window with preliminary event selection applied. The cosmic MRD triggers uncorrelated with beam activity have been removed from the dataset, and virtually all MRD clusters outside the beam window have been removed.

(known as “dirt muons”) constitute a background to neutrino interactions in the tank volume; the front veto helps tag this background when they pass through the front veto’s scintillation paddles. An estimate of the front muon veto efficiencies is currently ongoing. Paired with the tagged through-going muon rate, a contamination estimate of through-going muons could be made in future analyses of beam data.

### 9.4.3 Tank vertex reconstruction

Vertex reconstruction algorithms have been developed for reconstructing neutrino interactions via the muon produced in charged-current neutrino interactions. These algorithms use tank PMT time and charge information caused by the muon’s Cherenkov light to estimate the neutrino interaction point and muon track direction [206, 175]. Eventually, this information will be utilized alongside the reconstructed MRD track to improve neutrino interaction event selection.

Vertex reconstruction information is not included in the event selection for the data shown below. The current timing uncertainties of the PMTs make vertex reconstruction on the scale of the ANNIE tank size too uncertain for use. Tank vertex reconstruction information will be

| Selection criteria | Prompt event candidates |
|---|---|
| No cuts | 4219 |
| Single MRD track | 2574 |
| No veto hit | 3335 |
| Total neutrino candidates | 2001 |
| Spills/neutrino candidate | $620 \pm 13$ |

Table 9.3. Summary of the neutrino event selection impact on rates. An event with coincident tank and MRD activity passing neutrino candidate selection occurs approximately once every 620 beam spills.

incorporated into the neutrino candidate event selection criteria following a laser ball timing calibration deployment and reprocessing of data with the corrected PMT signal time delays.

### 9.4.4 Summary of neutrino candidate selection impact

The fraction of prompt events rejected with the addition of CCQE event selection is detailed in table 9.3. The data indicate that a large fraction of coincident tank/MRD activity are associated with a single veto hit. The high rate of veto hits indicates a contamination estimate using the calculated efficiencies of the veto paddles will be important in upcoming analyses.

## 9.5 Characterizing neutrino candidate visible energy

The visible energy of the neutrino candidate is needed to characterize the neutron multiplicity as a function of neutrino interaction energy. The visible energy for a candidate neutrino event is defined as

$$E_{vis} = E_{Tank} + E_{MRD} \ . \tag{9.1}$$

$E_{Tank}$ is estimated by summing the total PMT charge observed in the tank and converting to energy with the calibration described in 9.5.1. The energy deposition in the MRD $E_{MRD}$ is estimated using a simulation-driven approach as described in section 9.5.3. Note that energy losses in the air gap between the tank and MRD are neglected for the visible energy estimation, as the energy deposition is negligible compared to the energy loss in the tank water and MRD steel layers.

### 9.5.1 Visible tank energy scale determination

The Cherenkov light observed for a charged particle of known type and path length in the ANNIE tank can be related to the particle's total energy deposition in the tank. This relation is critical for estimating the energy deposited in the ANNIE tank given an observed PMT charge signal from Cherenkov radiation alone.

As seen in the Frank-Tamm formula in 1.31, a particle's Cherenkov emission spectrum is constant per unit length so long as the charged particle has $\beta \approx 1$. As discussed in section 6.1.2, the energy deposition per unit length of minimum ionizing particles is also relatively constant. In this case, the following relation then holds for minimum ionizing particles:

$$\frac{dN_{Cherenkov}}{dx} = \alpha_T \frac{dE}{dx} \rightarrow \alpha_T = \frac{dN_{Cherenkov}}{dE} \tag{9.2}$$

and a relation between deposited energy and total observed Cherenkov light can be made.

Muons (either cosmic or dirt) which traverse the entire PMT tank volume and have a visible track in the MRD are approximately minimum-ionizing in the tank volume, and can be utilized to estimate the relation in equation 9.2 for muons. Based on measurements made during construction, the volume of water subtended by the tank photomultiplier tubes is a cylinder with radius 100 cm and height 290 cm. As such, through-going muons traversing directly down the middle of the PMT volume will travel approximately $x_L = 200$ cm; given the current uncertainty of positions within the tank is $\pm 5$ cm, the uncertainty on this distance is taken conservatively to be $\delta_L = 10$ cm. Given that the $dE/dx = 1.992$ MeV/cm for minimum-ionizing muons in water (from table 6.2) and the diameter of the ANNIE tank $x_L$, the energy deposited by through-going muons is estimated to be

$$\Delta E_{MIP,\mu} = \frac{dE}{dx} x_L = 1.992 \, \frac{MeV}{cm} * (200 \pm 10 \, cm) = 400 \pm 20 \, MeV \ . \tag{9.3}$$

This energy estimate can be compared to the total number of photoelectrons seen for through-going muons to estimate the $\alpha_T$ parameter in equation 9.2.

### 9.5.2 Through-going event selection

Through-going muons were selected by finding prompt candidate events as described in section 8.3, and then selecting single-track events with a paddle hit in the front veto. Additional cuts on the reconstructed MRD track parameters were applied to select through-going muons with a tank traversal length near the tank diameter $x_L = 200\,cm$. The total photoelectrons observed for through-going muons with varying MRD track entry point and angle relative to the beam axis are shown in figures 9.8 and 9.9. A population of lower photoelectron tank clusters are seen for through-going muon candidates with an entry point far from the MRD center and a large track angle relative to the beam axis. This trend indicates that muons entering far from the MRD surface's center or with track directions off-beam axis clip the tank and do not deposit Cherenkov for the full $x_L$ length.

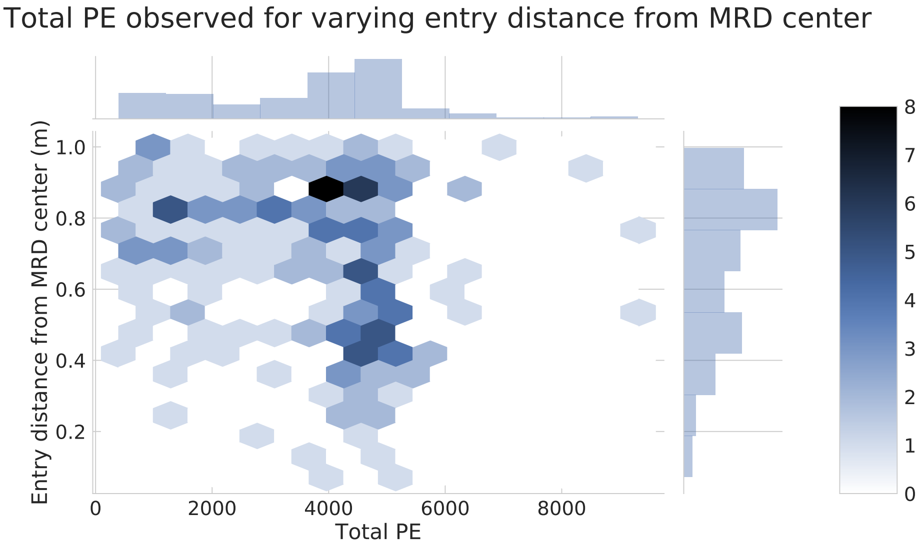

Figure 9.8. Total photoelectrons plotted against the reconstructed entry distance from the MRD center. A population of low-PE events is present for tracks with an entry point farther from the MRD center. Particles that enter far from the MRD center cannot traverse the entire PMT volume's diameter, and produce less visible Cherenkov light in the tank than directly through-going muons.

Based on the angle/radius distributions and some additional cuts designed to remove lower PE and non minimum-ionizing backgrounds, the through-going muon event selection was chosen as:

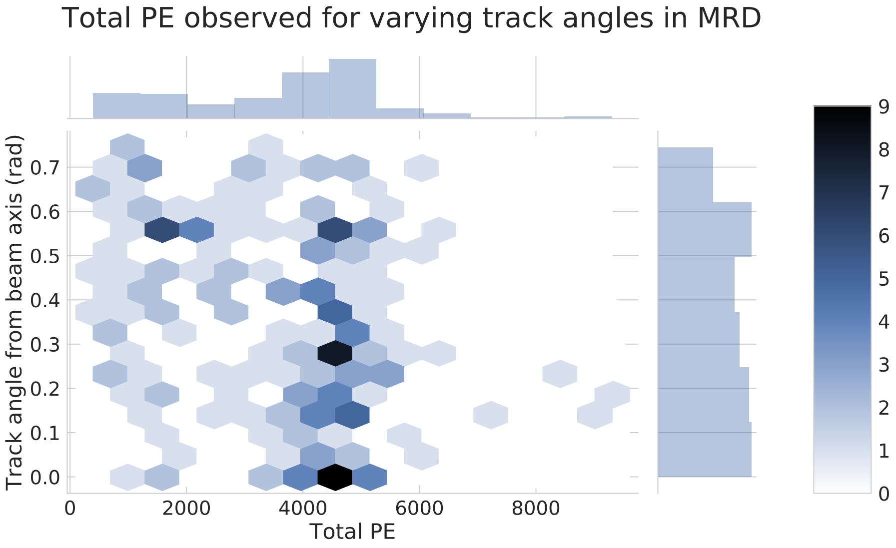

Figure 9.9. Total photoelectrons plotted against the reconstructed track angle relative to the beam axis. A population of low-PE events is present for tracks with a larger MRD angle, but some low PE events are also present at smaller angles. Particles with extreme track angles relative to the beam axis can not traverse the as much of the PMT inner volume, and produce less visible Cherenkov light in the tank than through-going muons on the beam axis.

- Greater than 70 PMTs hit within the beam acquisition window
- At least one paddle hit in the front muon veto
- One single reconstructed track in the MRD
- Reconstructed MRD track entry point is within $60$ cm of the center of the MRD's surface
- Reconstructed MRD track angle less than $20^o$ from the BNB beam axis

The total observed photoelectrons in the ANNIE tank for through-going muons with the above event selection is shown in 9.10. A clear peak lies in the distribution at $\sim 4500$ PE.

The total photoelectron distribution was fit with a Gaussian to extract the mean photoelectrons observed per tank traversal. Using this fit, the mean number of Cherenkov photoelectrons observed per MeV of minimum-ionizing muon energy deposition was estimated as

$$\alpha_T = \frac{4558 \pm 398\, PE}{400 \pm 20\, MeV} = 12 \pm 1 \frac{PE}{MeV} \; . \tag{9.4}$$

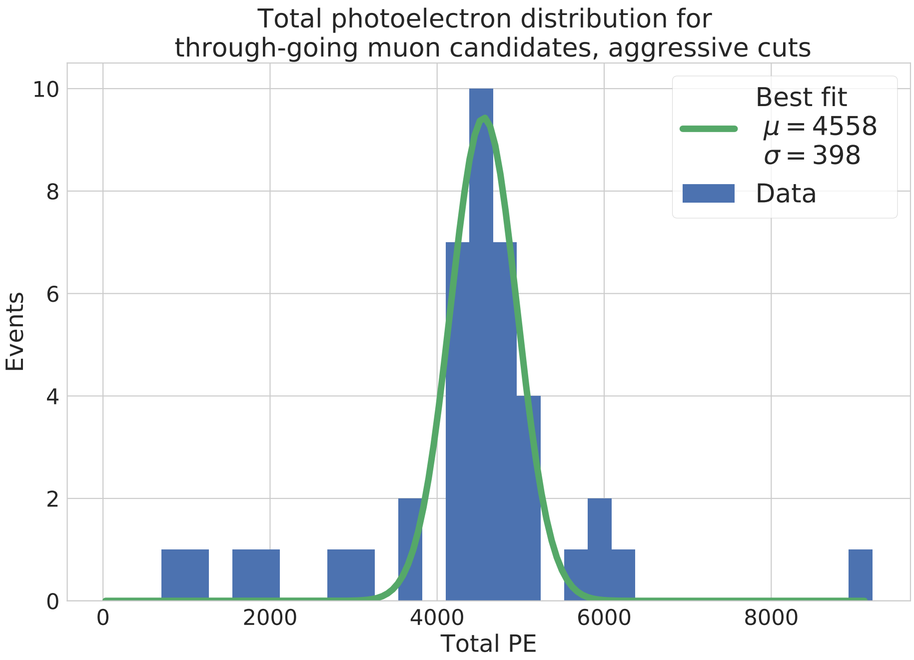

Figure 9.10. Distribution of total photoelectrons observed in through-going muon candidate events with more aggressive cuts on MRD track angle and entry point. A peak of $\sim 4500$ PE shows for the through-going muon candidates.

No systematic uncertainties have been taken into account for the above estimate, such as corrections associated with cosmic muon contamination or afterpulsing.

Finally, the visible energy in the tank for a prompt event is estimated as

$$E_{Tank} = \alpha_T \sum_i PE_i \ , \tag{9.5}$$

where $PE_i$ is the total photoelectron count observed for each PMT hit $i$ in a tank cluster.

### 9.5.3 Visible MRD energy reconstruction

The energy deposition in the MRD for through-going muons (labeled $E_{MRD}$) is predicted using lookup tables produced from detector simulations. Simulated muons with energies resulting from BNB-based neutrino interactions were produced and fired into the MRD at varying angles. GENIE was used to simulate neutrino interactions and WCSim (GEANT4 physics libraries) was used to simulate energy loss in the MRD. The total energy loss per unit length for a muon's track angle, along with the error on the energy loss for a given angle, was determined using the simulation's truth information and used to form lookup tables. These tables were then used to estimate the energy loss $E_{MRD}$ given a reconstructed track's angle and penetration depth. The lookup tables developed for the MRD are shown in figures 9.11 and 9.12.

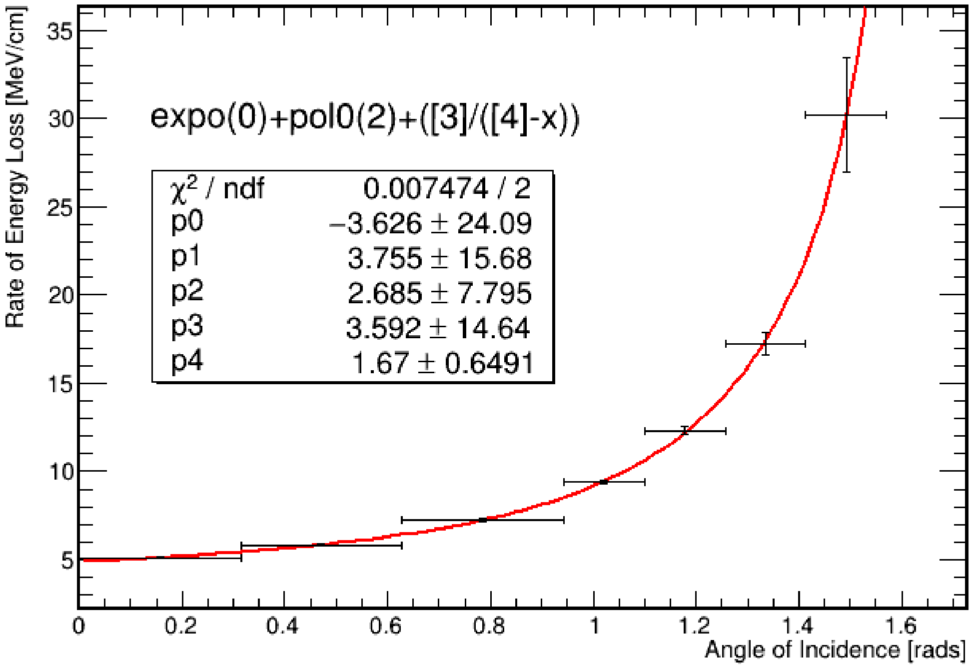

Figure 9.11. Average energy loss per unit centimeter for muons passing through the ANNIE MRD. The energy loss per centimeter varies as a function of angle due to the varying depth of steel that the muon passes through. Figure credit: Marcus O'Flaherty.

In general, a higher angle of MRD incidence results in a larger rate of energy loss, as the mean fraction of steel traversed by the muon becomes larger for more extreme angles.

## 9.6 Comparison of neutrino candidate visible energy to simulation

To validate the developed neutrino event selection and visible energy reconstruction, the reconstructed visible energy distribution for neutrino candidates in ANNIE beam data was compared to simulation. Charged-current neutrino interactions on oxygen were simulated using the GENIE simulation package, and the produced muon was propagated through the simulated ANNIE geometry in WCSim. The truth information of neutrino interactions which occur in the ANNIE tank, have no pion produced, and stop in the MRD were selected in simulation and used to form a probability distribution of the expected visible energy for single-track neutrino events

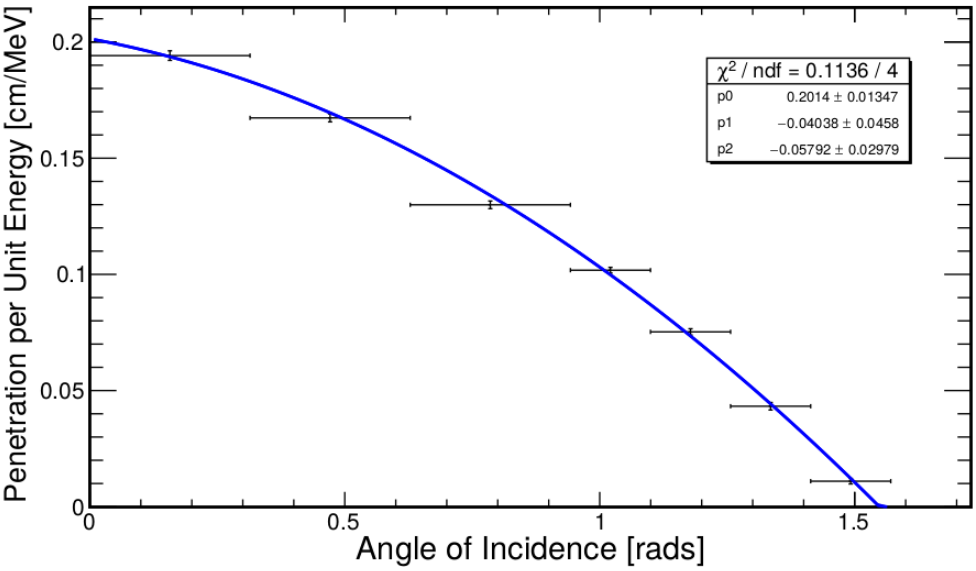

Figure 9.12. Beam-axis penetration per unit energy loss for muons passing through the ANNIE MRD. The penetration depth decreases as the angle increases due to an increase in the average length of steel traversed at large incidence angles. Figure credit: Marcus O'Flaherty.

in ANNIE. A comparison of the ANNIE beam data's visible energy distribution and the GENIE/WCSim simulation truth information is shown in figure 9.13.

The data's distribution peak occurs at $\sim 700$ MeV, in agreement with the MC truth and the expected peak neutrino energy for the BNB (recall figure 5.5). The reconstructed data demonstrate a larger fraction of low-energy interactions; this may be due to errors introduced in the data's energy reconstruction, and should be compared with the post-reconstructed simulation in future studies to see if the difference is resolved. A high-energy constant background also appears in the data at $E_{vis} > 1.5\,GeV$; this background could be due to contamination from through-going muons coincident with neutrino events or non-CCQE events which have only one reconstructed MRD track.

## 9.7 Neutron candidate multiplicity

The neutron candidate multiplicity of the neutrino candidate set was also analyzed. Although the statistics for neutron candidates in beam data are low, the data are useful to determine the amount of beam data necessary for a future neutron multiplicity publication. The total delayed tank PMT hit clusters for the entire dataset, plus the reduction in statistics due to delayed cluster

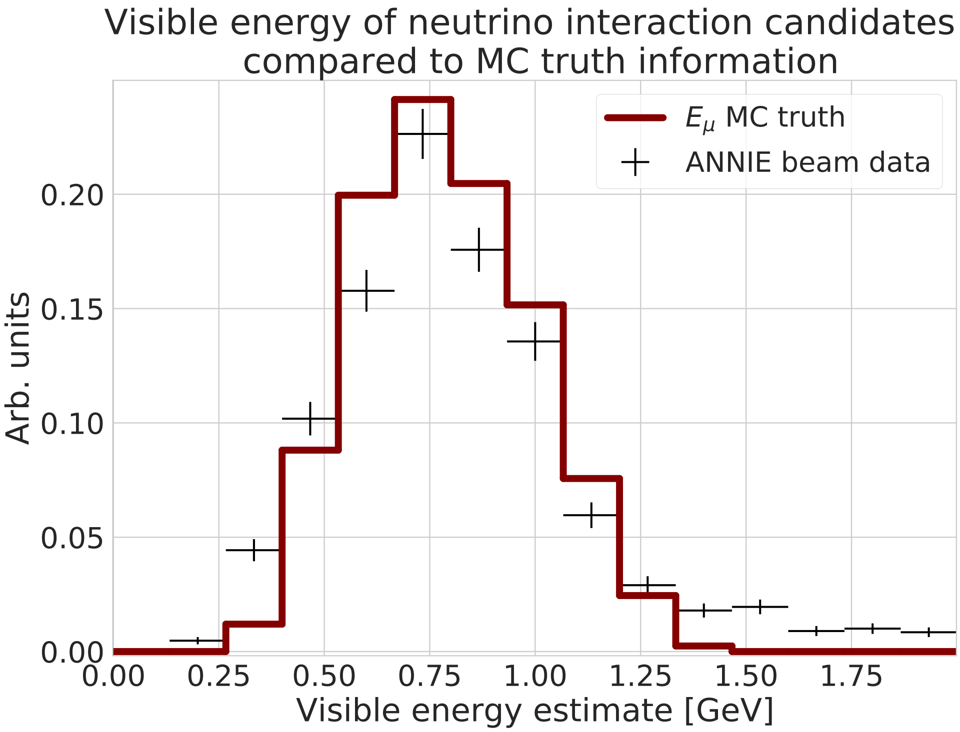

Figure 9.13. Distribution of visible energy for single-track neutrino candidate events in ANNIE beam data as compared to CC0$\pi$ MC truth. The data demonstrate a flat background at $E_{vis} > 1.5$ GeV and a larger fraction of events in the range $E_{vis} < 700$ MeV than seen in the simulation. The general shapes are in agreement, but further comparison will require the incorporation of backgrounds and reconstruction systematics into the simulation. Errors shown are statistical only.

event selection, are shown in figure 9.14. The requirement that delayed clusters follow a neutrino candidate event in the prompt window produces the largest reduction in neutron candidate statistics.

The neutron candidate multiplicity distribution for acquisitions with a neutrino candidate are shown in figure 9.15. The majority of interactions contain no delayed cluster in the $[12, 67]$ $\mu s$ acquisition window. No correction has been made for the neutron detection efficiency.

The mean number of neutron candidates observed per neutrino candidate as a function of visible energy is shown in figure 9.16. The data have a very high statistical uncertainty, due to the small sample of neutrino candidates and delayed neutron candidates. Errors are statistical only, and no correction has been applied for neutron detection efficiency.

The same neutron candidate multiplicity data for neutrino candidate events are shown as a function of photoelectrons seen in the ANNIE tank in figure 9.17. The lower observed neutron

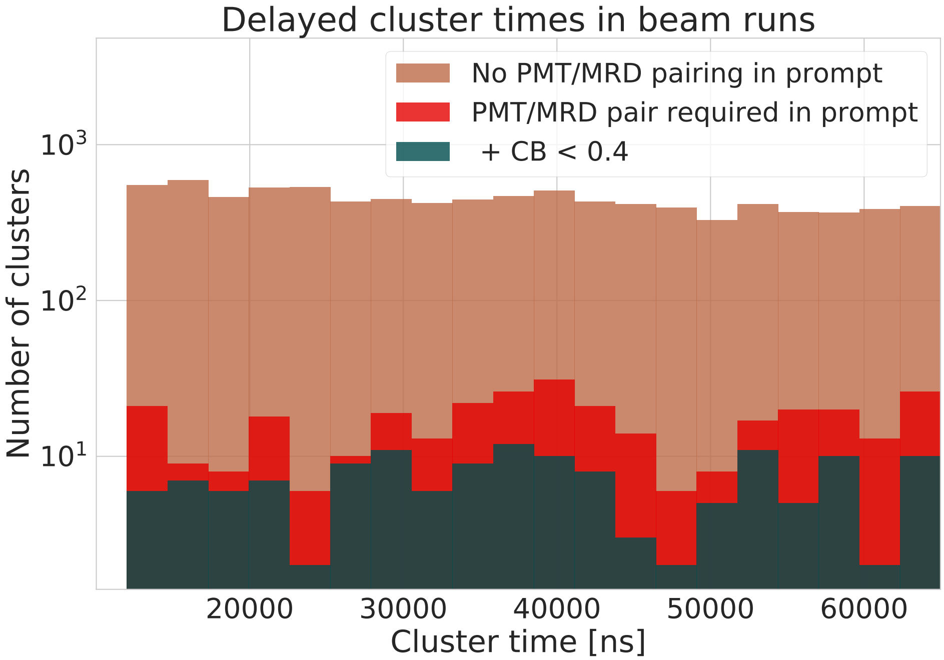

Figure 9.14. Delayed tank PMT hit cluster distribution for all beam data, with increasing levels of event selection required. The majority of delayed tank clusters are in data acquisitions with no neutrino candidate in the prompt window.

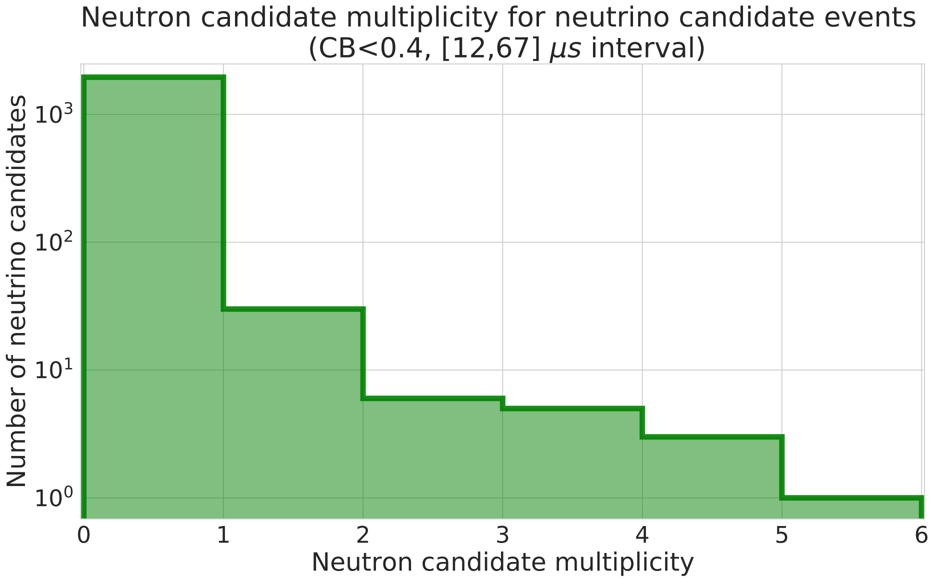

Figure 9.15. Neutron candidate multiplicity for acquisitions with a neutrino candidate event in the prompt acquisition window. The majority of acquisitions have no neutron candidate. No corrections have been made for neutron detection efficiency.

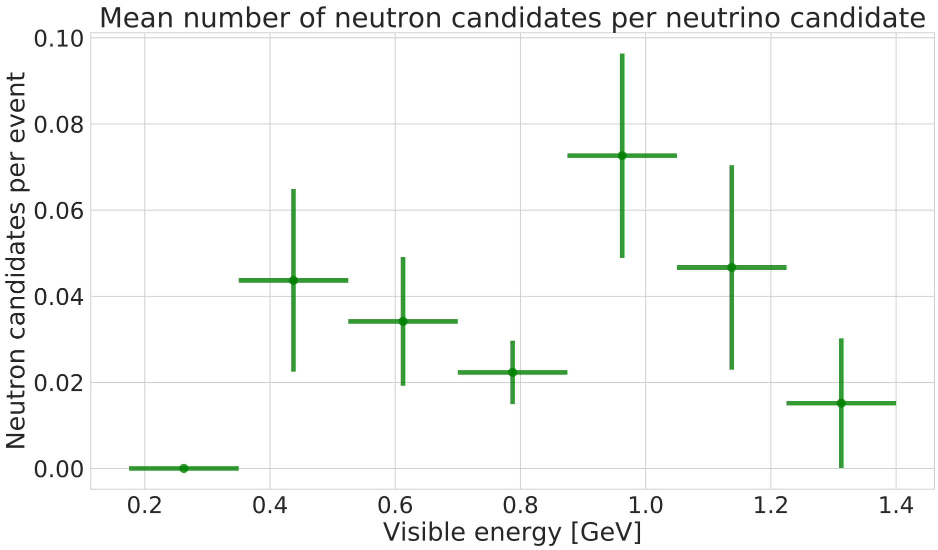

Figure 9.16. Mean neutron candidate multiplicity per event for acquisitions with a neutrino candidate event in the prompt acquisition window as a function of visible energy $E_{vis}$. The majority of acquisitions have no neutron candidate. No systematic corrections have been applied to the data. Errors are statistical only.

rate for lower PE neutrino candidates may be due to neutron containment losses; lower PE counts in the tank should be correlated to neutrino interactions that occur closer to the MRD and tank walls in general, where neutrons have a higher probability of escaping the PMT volume (see section 9.8.2).

An interesting feature in the visible tank energy distribution of figure 9.17 is the dip in neutron multiplicity near $\sim 4000\,PE$. One possible cause of this dip is through-going dirt muon contamination. Notice that prompt candidates with a veto hit, shown in figure 9.18, have a peaked distribution near $\sim 4000$ PE (consistent with through-going muons). Since through-going dirt muons are expected to produce fewer neutrons in the tank volume than neutrino interactions, through-going dirt muons contaminating the neutrino dataset's $\sim\ 4000$ PE range could systematically reduce the neutron multiplicity estimation. This hypothesis could be tested once the front veto efficiency is quantified, which provides the information to make an estimate of through-going muon contamination. Fiducialization using the reconstructed neutrino interaction vertex in future analyses should help to reduce this contamination considerably (see section 9.8.3).

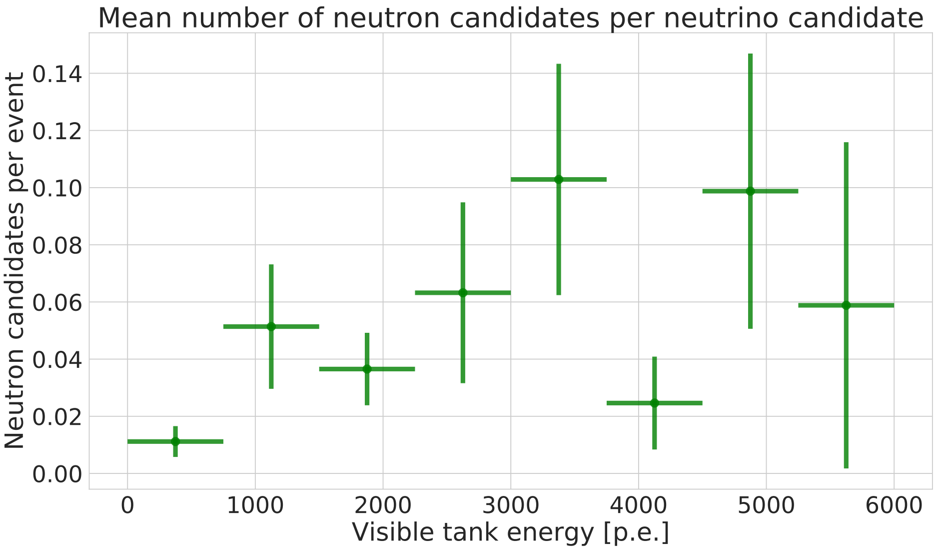

Figure 9.17. Mean neutron candidate multiplicity per event for acquisitions with a neutrino candidate event in the prompt acquisition window as a function of tank photoelectron counts. A dip is seen near $4000\,PE$, which may hint at contamination of through-going muons. No systematic corrections have been applied to the data. Errors are statistical only.

## 9.8 Beam-related systematic uncertainties

Systematic corrections to the observed neutron multiplicity rates in ANNIE are necessary to extract the true neutron multiplicity of neutrino interactions. After collecting more neutrino beam data to reduce statistical uncertainties to negligible levels, the uncertainties of these systematic corrections will dominate the neutron multiplicity measurement uncertainties and must be minimized wherever possible. Analyses to derive systematic corrections to data are still in development, but the primary corrections that will be needed are discussed below.

### 9.8.1 Neutron detection efficiency in tank

The neutron detection efficiency quantified from the analysis in chapter 8 must be applied to neutron detection rates observed in beam data. Since the ANNIE tank does not successfully observe all neutron captures that occur within the tank volume, a correction must be applied to determine the total neutron production rate as measured in the tank data.

The detection efficiency will be a function of neutron capture position, as seen in figure 8.29. Techniques for determining the neutron capture position based on PMT time/charge data are in development. The reconstructed neutron position can be combined with the reconstructed

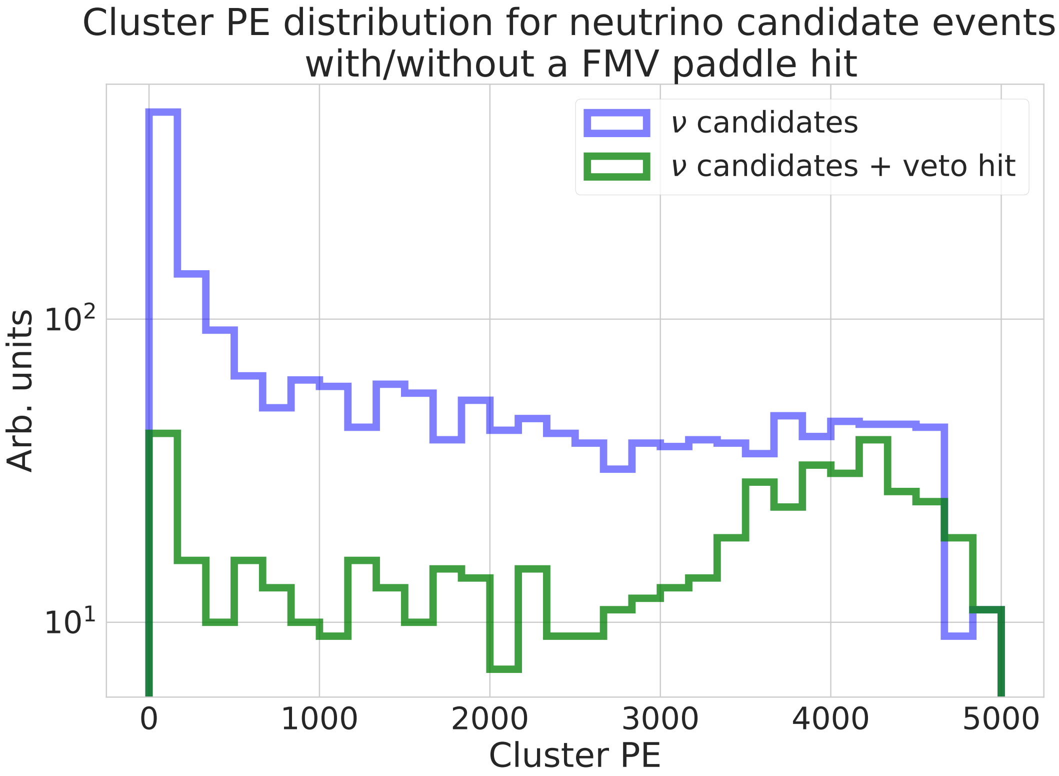

Figure 9.18. Cluster PE distribution for neutrino candidates that pass and fail the front veto cut. Neutrino candidate clusters which fail the veto cut (have at least one coincident veto hit) demonstrate a peak near $\sim 4000$ PE, similar to that observed in the through-going event selection analysis results in figure 9.10.

neutrino interaction vertex to apply neutron detection efficiency corrections on a per-event basis.

### 9.8.2 Neutron containment in the ANNIE tank

Corrections must be applied to the neutron detection rate for the population of neutrons produced in neutrino interactions that escape the tank. Any neutrons produced which exit the tank cannot be detected with the ANNIE PMTs, resulting in a systematic reduction of neutrons detected from neutrino interactions. Neutron containment corrections will be correlated with the pure neutron detection efficiency correction, as both corrections vary with the interaction position in the tank.

Neutrino interactions that occur closer to the downstream PMT wall have a higher probability of neutrons exiting the tank volume. Neutrons produced in neutrino interactions and the following final state interactions can have energies up to tens of MeV, providing enough momentum to easily leave the tank volume [152]. Preliminary simulations of neutron containment following neutrino interactions indicate corrections on the level of 30-70% depending on the neutrino interaction position in the ANNIE tank (see figure 9.19).

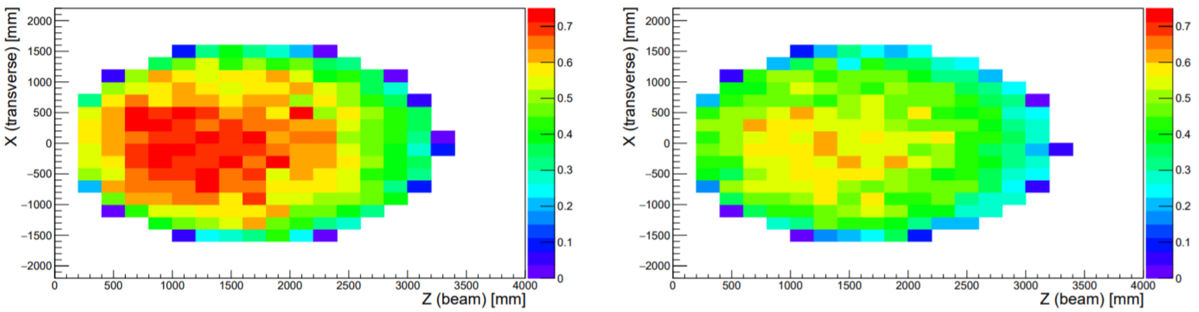

Figure 9.19. Simulations of the neutron detection efficiency in ANNIE as a function of *neutrino* interaction position in the tank. The detection efficiency with a 5 PE threshold (left) and 10 PE threshold (right) are shown. The neutron detection efficiency is lower for interactions closer to the downstream wall due to neutrons exiting the PMT volume. Figure from [152].

### 9.8.3 Dirt muon contamination

Contamination of through-going muons generated upstream of the ANNIE tank must be quantified and corrected for. Through-going muons misidentified as neutrino events will systematically reduce the estimated neutron production for neutrino events, as no neutrons from nuclear effects will be present. It is possible the effects of this contamination are already visible in the reduced mean multiplicity seen near 4000 PE in figure 9.17. Through-going muons can still produce some delayed tank clusters if the muon interacts directly with oxygen in the tank, producing cosmogenics or neutrons from nuclear break-up. Beyond using the front veto, tagging and rejection of through-going muons will primarily be achieved through fiducialization and rejection of events with an entry point on the tank wall.

Fiducialization, or the rejection of neutrino candidate events that do not occur within some defined volume in the ANNIE tank, can help remove through-going muon contamination. Some fiducialization is achievable by rejecting neutrino candidate events which have either too high or too low of a PE count in the ANNIE tank. For example, cutting events with PE counts consistent with through-going muons can increase the neutrino candidate dateset purity. However, following the calibration of PMT timing using a laserball, the PMT time uncertainties will be low enough to reconstruct the neutrino interaction point in the ANNIE tank with PMT hit time information. At this point, fiducialization can be performed with much higher precision. For through-going muons, the interaction point will reconstruct at the back tank wall and can be removed with the combination of a positional cut and PE cut.

An entry point cut could also be used to reject a portion of through-going muon contamination in beam data. If a through-going muon passes through a PMT as it enters the tank, a single tube will have a higher charge than the rest of the back wall (see figure 9.20). Cuts could be placed on the max PMT charge observed in the back half of the tank to reduce the contamination of through-going candidates.

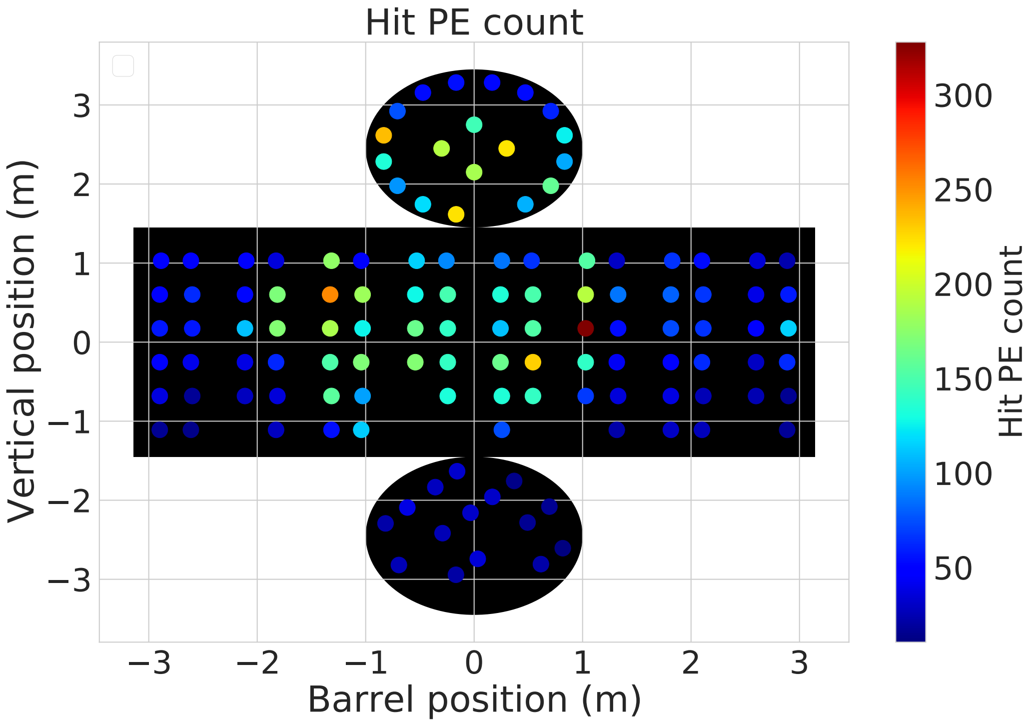

Figure 9.20. Single acquisition of a prompt interaction in neutrino beam data. A single PMT with an elevated PE count in the back-half of the ANNIE tank is visible, and could be used to reject through-going muon contamination.

### 9.8.4 Neutron backgrounds

Background signals that mimic true neutrino-interaction neutrons can contaminate beam data, and must be measured. Neutron backgrounds can be broadly classified into two categories: beam-uncorrelated and beam-correlated backgrounds. Beam-uncorrelated signals will form a constant-in-time, flat background in beam acquisitions; they can come from several sources such as artificial events produced by electronics activity, radioactivity in the detector components, or neutrons produced in the hall from muon spallation. Although the background rate should be roughly constant on short timescales (hours to days), the rates can fluctuate over the course of a beam-year and should be quantified at regular intervals. Beam-correlated signals are produced by activity coincident with the neutrino beam. The main contributors to beam-correlated backgrounds are expected to be neutrons produced in the BNB target hall that scatter into the atmosphere and back into the ANNIE hall (skyshine neutrons) and neutrons produced from neutrino interactions in the dirt upstream of ANNIE (dirt neutrons) [165].

Correlated neutron backgrounds were characterized in an engineering run known as ANNIE Phase I [165]. In Phase I, a 1-ton Gd-doped scintillation volume was moved throughout the ANNIE tank to characterize the neutron capture rate following beam spills (see figure 9.21). Any data acquisition with activity due to neutrino interactions or through-going muons were rejected to ensure only the neutron background was measured. 58 upward-facing PMTs were installed at the bottom of the ANNIE tank to tag through-going muons, while the front veto and first two layers of the MRD were used to tag beam-related activity.

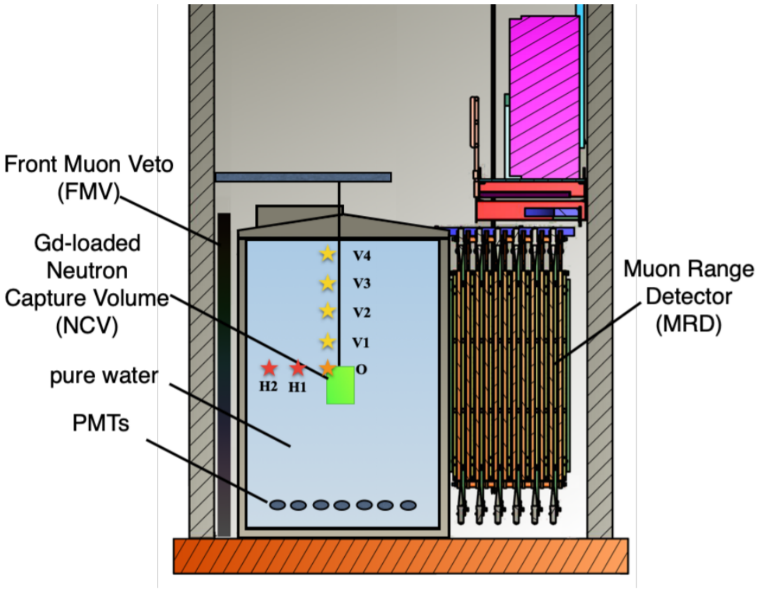

Figure 9.21. Diagram of the experimental setup from ANNIE Phase I. The scintillation volume was moved to all starred positions in the tank to quantify the beam-correlated neutron background. Figure from [165].

ANNIE Phase I measured that beam-correlated neutron rates in the PMT volume are minimal. The estimated neutron events in the ANNIE tank volume from Phase I results are shown in figure 9.22. Averaged across the entire active PMT volume, Phase I data found that the ANNIE PMT volume should see no more than one beam-correlated neutron event per 150 BNB beam spills [165]. This upper bound will be applied when modeling ANNIE's neutron candidate event rate and quantifying uncertainties in the neutrino-induced neutron multiplicity measurement.

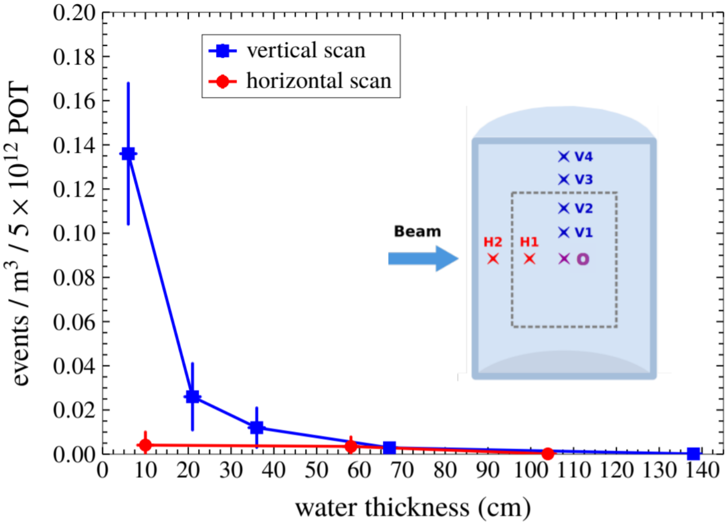

Figure 9.22. Final results from measuring beam-correlated neutron rates in ANNIE Phase I. The inset shows all positions of the scintillation volume measured, as well as the active PMT volume (dotted lines) used in the current ANNIE configuration. Figure from [165].

# Chapter 10

# Discussion and conclusions

A first analysis of both AmBe calibration data and neutrino beam data has demonstrated that the ANNIE detector is operational and taking high quality data. The AmBe source data contain physics events consistent with neutron captures on gadolinium, and were successfuly used to estimate an initial neutron capture detection efficiency of $0.64^{+0.03(stat)\,+0.01(sys)}_{-0.02(stat)\,-0.00(sys)}$ at the center of the ANNIE tank. Techniques for reconstructing the visible energy of neutrino interactions in the tank and MRD were also developed, and the reconstructed beam data show decent agreement with the true muon energy distribution predicted in simulations. The first neutron multiplicity distributions ANNIE beam data were also shown, along with an outline of the systematic corrections needed to complete a neutron multiplicity analysis.

## 10.1 Roadmap for future plans

Although the 2019-2020 BNB beam year was cut short due to the Coronavirus pandemic, the ANNIE detector is ready to continue data-taking when the beam is turned on again. During the beam's summer shutdown, AmBe calibrations will continue when normal operations resume. When the beam does return, ANNIE will continue to take physics-quality beam data for a neutron multiplicity analysis, deploy the LAPPDs in the ANNIE tank, and develop analyses necessary to apply and quantify systematic corrections along with their uncertainties. Progress towards testing even more future technologies in ANNIE Phase III is also expected.

### 10.1.1 Completion of Phase II

Given the BNB beam will likely not turn on again until fall 2020, a laser ball deployment and an AmBe calibration campaign with more neutron source positions will take priority in the upcoming summer. The laser ball deployment will greatly reduce the timing uncertainties of PMT pulses, allowing analyses to utilize a smaller tank PMT hit cluster time window and reduce contamination from dark noise and background pile-up. Using more AmBe calibration data, a full mapping of the ANNIE tank's neutron detection efficiency can also be completed using the neutron detection efficiency analysis presented in this thesis.

The deployment of ANNIE's LAPPDs is also anticipated this year. The LAPPD waterproof housings and cabling have been developed at UC Davis, and the firmware programming of LAPPD control boards will be completed in the coming months. The LAPPD deployment will be essential in the upcoming beam year, paired with the laserball-calibrated tank PMTs, for reconstructing neutrino interaction vertices in the tank. The neutrino interaction's reconstructed position will inform what neutron detection efficiency corrections to apply given where produced neutrons are expected to capture within the tank.

In short, the 2020-2021 beam year will only be more exciting and rich with neutrino interaction physics than what has been previewed in the commissioning phase and first collection of beam data.

### 10.1.2 ANNIE Phase III

Following the neutrino-neutron multiplicity analysis using a gadolinium-doped ANNIE, the ANNIE detector stands to continue operating as a testbed for more upcoming detector technologies. A particularly interesting potential upgrade for ANNIE is the addition of Water-based Liquid Scintillator (WbLS). The utility of WbLS lies in the production of both scintillation and Cherenkov light following a neutrino interaction. Cherenkov light from charged particles provides directionality for any particles with energies above their Cherenkov threshold, while the scintillation light provides more photons than the Cherenkov signal alone, improving energy resolution. Successful utilization of both the Cherenkov and scintillation light for these two purposes hinges on the ability to separate the two components using timing; the ability to do so has already been done in the CHESS experiment, with the Cherenkov-Scintillation separation shown in figure 10.1.

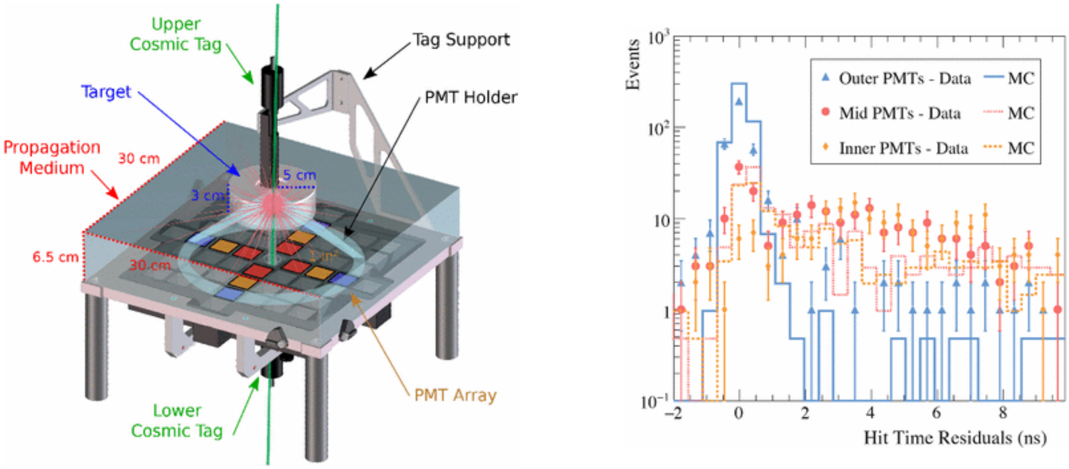

Figure 10.1. Experimental setup for the CHESS measurement (left) and the data from candidate cosmic events in an LAB target (right). The outer PMTs that receive Cherenkov light are peaked near a hit residual of zero due to Cherenkov's near-instantaneous emission. The inner PMTs see primarily scintillation light, which has a longer hit residual tail due to the LAB's scintillation de-excitation time profile. The mid PMTs see a fraction of both light sources. Taken from [207].

The ANNIE detector would be an excellent testbed for quantifying the performance and benefits of WbLS in neutrino detection. The LAPPDs in the ANNIE tank would allow for the separation of Cherenkov and scintillation light, preserving neutrino vertex reconstruction resolution while improving the energy resolution with a larger $PE/MeV$ ratio. Additionally, the scintillator component of WbLS would allow for detection of hadrons produced in the neutrino interaction below their Cherenkov threshold energy. Detection of the hadronic energy component would reduce the uncertainties in neutrino interaction energy reconstruction.

An immediate path to testing WbLS in ANNIE is to deploy a ton-scale WbLS-filled volume inside the tank. A WbLS deployment contained in a ton-scale acrylic volume would have little impact on the gadolinium-doped detector data while simultaneously demonstrating an exciting new detector technology. The containment of WbLS in a vessel would ensure the current ANNIE detector state is not changed by the WbLS deployment. Just a few weeks of WbLS-deployment data would be enough to study the potential physics impact of upgrading ANNIE to a full WbLS-doped detector volume with little impact to the total livetime of gadolinium-doped detector data acquisition.

# Appendix A

# Neutrino oscillation theory

## A.1 Three-flavor neutrino oscillation probability in vacuum

Consider the probability for an electron neutrino to oscillate into a muon flavor neutrino. The probability of an $e \rightarrow \mu$ transition is calculated with:

$$P(\nu_e \rightarrow \nu_{mu}, t) = |\langle\nu_\mu| \, |\nu_e(t)\rangle|^2$$

The time evolution of the electron neutrino is given by the solution to the Schrodinger equation:

$$i\frac{d}{dt}|\nu_e(t)\rangle = \mathcal{H}|\nu_e(t)\rangle \tag{A.1}$$

Which, in the mass eigenbasis, has a solution of the form:

$$|\nu_e(t)\rangle = \sum_{i=1}^{3} U_{ei}e^{-iE_i t}|\nu_i\rangle \tag{A.2}$$

Where $E_i = \sqrt{m_i^2 + |\vec{p_i}|^2}$. Returning this solution to the oscillation probability equation,

$$P(\nu_e \rightarrow \nu_{mu}, t) = \left|\langle\nu_\mu| \sum_{i=1}^{3} U_{ei}e^{-iE_i t}|\nu_i\rangle\right|^2 \tag{A.3}$$

$$P(\nu_e \rightarrow \nu_{mu}, t) = \left|\sum_{j=1}^{3}\sum_{i=1}^{3} \langle\nu_j| U_{\mu j}^* U_{ei}e^{-iE_i t}|\nu_i\rangle\right|^2 \tag{A.4}$$

And since $\langle \nu_j | \, | \nu_i \rangle = \delta_{ij}$,

$$P(\nu_e \rightarrow \nu_{mu}, t) = \left| \sum_{j=1}^{3} U^*_{\mu j} U_{ej} e^{-iE_j t} \right|^2 \tag{A.5}$$

And since $|a|^2 = a * a$,

$$P(\nu_e \rightarrow \nu_{mu}, t) = \sum_{k=1}^{3} \sum_{j=1}^{3} U_{\mu k} U^*_{ek} U^*_{\mu j} U_{ej} e^{-i((E_j - E_k)t} \tag{A.6}$$

For highly relativistic neutrinos, where $|\vec{p_j}| >> m_j$, the following approximations can safely be made:

$$E_j = |\vec{p_j}| \sqrt{1 + \frac{m_j^2}{|\vec{p_j}|^2}} \approx |\vec{p_j}|(1 + \frac{1}{2} \frac{m_j^2}{|\vec{p_j}|^2}) = |\vec{p_j}| + \frac{m_j^2}{2|\vec{p_j}|} \tag{A.7}$$

$$L \approx t \tag{A.8}$$

Under these approximations, the energy difference in equation A.6 is:

$$E_j - E_k \approx \frac{\Delta m^2_{jk}}{2E} \ , \ E = |\vec{p_j}| \approx |\vec{p_k}| \ , \ \Delta m^2_{jk} = m_j^2 - m_k^2 \tag{A.9}$$

Which leads to the general oscillation probability expression:

$$P(\nu_e \rightarrow \nu_{mu}, t) = \sum_{k=1}^{3} \sum_{j=1}^{3} U_{\mu k} U^*_{ek} U^*_{\mu j} U_{ej} e^{-i \frac{\Delta m^2_{jk} L}{2E}} \tag{A.10}$$

## A.2 Neutrino oscillations in matter

Neutrino oscillation models must be modified for neutrino propagation in matter. Neutrinos that propagate through matter will undergo coherent elastic scattering with both nucleons and electrons; these interactions will modify the neutrino wave's propagation and oscillation in the medium. These matter effects ultimate lead to modified mixing angles that vary with the medium's density and neutrino's momentum.

To account for matter effects in neutrino oscillations, the time propagator (i.e. the Hamiltonian) must be modified. The neutrino's coherent scattering effects can be modeled by incorporating an effective potential, given by [6]:

$$V_\alpha = V_{CC}\delta_{\alpha e} + V_{NC} = \sqrt{2}G_F(N_e\delta_{\alpha e} - \frac{1}{2}N_n) \tag{A.11}$$

where $N_e, N_n$ are the electron and neutron densities in the medium and $\alpha$ is the flavor of the neutrino. There are no proton and electron density contributions to the $V_{NC}$ term as the two potentials cancel each other (assuming the medium is neutral in charge). This effective contribution to the neutrino propagation Hamiltonian must be calculated by averaging over the scattering amplitudes yielded from neutrino charged-current and neutral-current interactions in a medium.

### A.2.1 Derivation of the oscillation probability in matter

How does this effective potential impact neutrino oscillation probabilities? Recall that the time evolution of a neutrino wavestate is determined via the Schrodinger equation:

$$i\frac{d}{dt}\left|\nu_\alpha(t)\right\rangle = \mathcal{H}\left|\nu_\alpha(t)\right\rangle \tag{A.12}$$

Where $\mathcal{H}$ is a combination of the vacuum Hamiltonian and the effective matter Hamiltonian:

$$\mathcal{H} = \mathcal{H}_{vac} + \mathcal{H}_{eff} \tag{A.13}$$

To calculate the probability of an oscillation from flavor $\alpha$ to $\beta$ after a time $t$, a projection onto the flavor state $\beta$ is made:

$$\left\langle\beta\right| i\frac{d}{dt}\left|\nu_\alpha(t)\right\rangle = \left\langle\beta\right| \mathcal{H}\left|\nu_\alpha(t)\right\rangle \tag{A.14}$$

While the vacuum term operates on mass eigenstates, the matter term operates on flavor eigenstates. To operate both the $\mathcal{H}_{vac}$ and $\mathcal{H}_{eff}$ on neutrino states, the identity operator in the flavor eigenbasis (labeled $I = \left|\eta\right\rangle\left\langle\eta\right|$) as well as an identity operator in the *mass* eigenbasis (labeled $I = \left|k\right\rangle\left\langle k\right|$) is placed conveniently. The result is:

$$\begin{aligned} i\tfrac{d}{dt}\psi_{\alpha\beta}(t) &= \textstyle\sum_\eta \sum_k \left\langle\beta\right| \mathcal{H}_{vac}\left|k\right\rangle \left\langle k|\eta\right\rangle \left\langle\eta|\nu_\alpha(t)\right\rangle + \sum_\eta \left\langle\beta\right| \mathcal{H}_{eff}\left|\eta\right\rangle \left\langle\eta|\nu_\alpha(t)\right\rangle \\ &= \textstyle\sum_\eta \sum_k \left\langle\beta\right| E_k \left|k\right\rangle \left\langle k|\eta\right\rangle \left\langle\eta|\nu_\alpha(t)\right\rangle + \sum_\eta \left\langle\beta\right| V_\eta \left|\eta\right\rangle \left\langle\eta|\nu_\alpha(t)\right\rangle \\ &= \textstyle\sum_\eta \left(\sum_k U_{\beta k}U^*_{k\eta}E_k + \delta_{\beta\eta}V_\eta\right)\psi_{\alpha\eta}(t) \end{aligned} \tag{A.15}$$

Considering neutrinos at highly relativistic speeds with $c = 1$, recall:

$$E_j \approx E + \frac{m_j^2}{2E}\ ,\ E \approx |\vec{p_j}|\ ,\ t \approx x \tag{A.16}$$

And then equation A.15 can be rewritten as:

$$i\frac{d}{dx}\nu_{\alpha\beta}(x) = \sum_{\eta}\left(\sum_{k} U_{\beta k}U^*_{k\eta}\left[E + \frac{m_k^2}{2E}\right] + \delta_{\beta\eta}\left[V_{CC}\delta_{\beta e} + V_{NC}\right]\right)\psi_{\alpha\eta}(t) \tag{A.17}$$

By adding in the term ($\left[E + \frac{m_1^2}{2E}\right] - \left[E + \frac{m_1^2}{2E}\right]$) into the first term, the expression can be massaged to become:

$$i\frac{d}{dx}\nu_{\alpha\beta}(x) = \left[p + \frac{m_1^2}{2E} + V_{NC}\right]\nu_{\alpha\beta}(x) + \sum_{\eta}\left(\sum_{k} U_{\beta k}U^*_{k\eta}\frac{\Delta m^2_{k1}}{2E} + \delta_{\beta\eta}\delta_{\eta e}V_{CC}\right)\psi_{\alpha\eta}(x) \tag{A.18}$$

The first term in equation A.18 can be removed with an overall phase shift of $\psi_{\alpha\beta}(t)$, which has no effect on the oscillation probability $P_{alpha\to\beta}(t) = |\psi_{\alpha\beta}(t)|^2$ [6]. Doing so gives the evolution of the neutrino as it propagates a distance $x$:

$$i\frac{d}{dx}\nu_{\alpha\beta}(x) = \sum_{\eta}\left(\sum_{k} U_{\beta k}U^*_{k\eta}\frac{\Delta m^2_{k1}}{2E} + \delta_{\beta\eta}\delta_{\eta e}V_{CC}\right)\psi_{\alpha\eta}(x) \tag{A.19}$$

It's interesting to note that the matter effects on oscillations are no longer dependent on any neutral current effects. Additionally, a unique dependence on the electron flavor of neutrinos has manifested in the $V_{CC}$ term.

### A.2.2 The MSW effect

The Mikheyev-Smirnov-Wolfenstein (MSW) effect is a neutrino oscillation phenomena unique to neutrinos propagating in matter. The MSW mechanism is well-known for successfully modeling the oscillation of solar neutrinos as they leave the Sun's core and helping resolve the solar neutrino problem. Only the two-flavor flux will be considered for example, as the three-flavor case proceeds in a similar fashion but is more complicated and cumbersome to derive.

To discuss the MSW effect, the oscillation probability $P_{e\to\mu}(x)$ for an electron neutrino passing through constant density matter must be found. Beginning from equation A.19 and assuming the initial neutrino flavor is an electron (as expected for production from fusion and decays in the Sun), the total differential equation for the transition and survival of the electron flavor neutrino is [6]:

$$i\frac{d}{dx}\begin{pmatrix}\psi_{ee}(x)\\ \psi_{e\mu}(x)\end{pmatrix} = \begin{pmatrix}-\Delta m^2_{12}\cos 2\theta_{12} + 2EV_{CC} & \Delta m^2_{12}\sin 2\theta_{12}\\ \Delta m^2_{12}\sin 2\theta_{12} & \Delta m^2_{12}\cos 2\theta_{12} - 2EV_{CC}\end{pmatrix} \tag{A.20}$$

Where the two-flavor mass mixing matrix is parameterized by:

$$U = \begin{pmatrix}\cos\theta_{12} & +\sin\theta_{12}\\ -\sin\theta_{12} & \cos\theta_{12}\end{pmatrix} \tag{A.21}$$

The differential equation in A.20 must be solved to determine the oscillation probability expression in terms of the mixing parameters. From here on, the $12$ subscripts will be dropped for convenience. To clean up notation, a definition of $A_{CC} \equiv 2EV_{CC}$ is also made.

Notice that the above expression in A.20 still looks like the Schrodinger equation, where the mixing matrix is the Hamiltonian. It's convenient to represent the above expression in a "matter basis" by diagonalizing the Hamiltonian. Doing so yields:

$$\mathcal{H}_M = \frac{1}{4E}\begin{pmatrix}-\Delta m^2_M & 0\\ 0 & \Delta m^2_M\end{pmatrix} \tag{A.22}$$

where:

$$\Delta m^2_M = \sqrt{(\Delta^2_m \cos 2\theta - A_{CC}) + (\Delta^2_m \sin 2\theta)^2} \tag{A.23}$$

The unitary matrix for this transformation has the same form in equation A.21 but letting $\theta_{12} \to \theta_M$. The $\theta_M$ parameter is defined relative to $\Delta^2_m$ and $\theta$ with the relations:

$$\cos 2\theta_M = \frac{\Delta m^2 \cos 2\theta - A_{CC}}{\Delta m^2_M}\ ,\ \sin 2\theta_M = \frac{\Delta m^2 \sin 2\theta}{\Delta m^2_M} \tag{A.24}$$

To simplify solving the differential equation A.20, variables are changed into the matter basis variables and the matter eigenbasis vectors (defined as $\psi(x) = U_M\Psi(x)$) and becomes:

$$i\frac{d}{dx}U_M \begin{pmatrix}\Psi_{e1}\\ \Psi_{e2}\end{pmatrix} = \frac{Deltam^2_M}{4E} \begin{pmatrix} -\cos 2\theta_M & \sin 2\theta_M \\ \sin 2\theta_M & \cos 2\theta_M \end{pmatrix} \begin{pmatrix}\psi_{ee}\\ \psi_{e\mu}\end{pmatrix} \tag{A.25}$$

Pushing the derivative through the left-hand side, and also operating on both sides of the expression in A.25 with $U^*_M$, the equation can be re-written as:

$$i\frac{d\Phi}{dx} = \frac{1}{4E} \begin{pmatrix} -\Delta m^2_M & -4Ei\frac{d\theta_M}{dx} \\ 4Ei\frac{d\theta_M}{dx} & \Delta m^2_M \end{pmatrix} \Phi \tag{A.26}$$

For the special case where the matter density is constant, $d\theta_M/dx = 0$. In this case, equation A.2.2.1 becomes a relatively straightforward differential equation to solve. The solution in terms of the initial conditions (position/density where the neutrino flavor was created), the neutrino wave function in the matter eigenbasis is:

$$\begin{pmatrix}\Phi_{e1}\\ \Phi_{e2}\end{pmatrix} = \begin{pmatrix} \cos\theta^{(i)}_M e^{i\frac{\Delta m^2_M}{4E}x} \\ \sin\theta^{(i)}_M e^{i\frac{\Delta m^2_M}{4E}x} \end{pmatrix} \tag{A.27}$$

Rotating back into the flavor basis using $U^*_M$ and taking only the $\psi_{e\mu}$ component, the $e\mu$ wavestate component is given by:

$$\psi_{e\mu}(x) = \sin\theta_M \cos\theta_M \left[ e^{i\frac{\Delta m^2_M}{4E}x} + e^{-i\frac{\Delta m^2_M}{4E}x} \right] \tag{A.28}$$

From this, the probability for oscillating from a flavor $e$ to flavor $\mu$ neutrino is given by:

$$P_{e\to\mu}(x) = |\psi_{e\mu}(x)^2| = \sin^2 2\theta_M \sin^2 \frac{\Delta m^2_M}{4E}x \tag{A.29}$$

One interesting limiting case in this expression is where the term $\theta_M = \pi/4$. Notice that the probability of $e \to \mu$ transitions becomes $1$ for particular values of propagation distance $x$. To relate this value of $\theta_M$ to the matter density and neutrino kinematics, the equations in A.24 can be divided and give the expression:

$$\tan 2\theta_M = \frac{\tan 2\theta}{1 - \frac{A_{CC}}{\Delta m^2 \cos 2\theta}} \tag{A.30}$$

The effective potential where $\theta_M = \pi/4$ occurs is for the special resonant $A^R_{CC}$ value where:

$$A_{CC}^R = \Delta m^2 \cos 2\theta \tag{A.31}$$

Which corresponds to an electron density/neutrino energy value of:

$$EN_e^R = \frac{\Delta m^2 \cos 2\theta}{2\sqrt{2}EG_F} \tag{A.32}$$

#### A.2.2.1 A note on non-constant matter density solutions

When attempting to predict the transition probability of neutrinos in objects with non-constant density (such as Earth or the Sun), the case is more complicated. In general, the differential equation must be solved given the matter's electron density as a function of position.

The special case of the Sun is worth a closer look, the probability of neutrinos produced above the resonant electron density $N_e^R$ (i.e. near the core), passing through resonance while propagating through a medium of decreasing density, and propagating to a detector essentially in vacuum is modeled by the Parke formula, given by [6, 208, 209]:

$$\bar{P}_{e\to e} = \frac{1}{2} + \left(\frac{1}{2} - P_c\right) \cos 2\theta_M^i \cos 2\theta \tag{A.33}$$

Where $P_c$ is the crossing probability at resonance, defined by:

$$P_c = \frac{e^{-\frac{\pi}{2}\gamma_R F} - e^{-\frac{\pi}{2}\gamma_R \frac{F}{\sin^2\theta}}}{1 - e^{-\frac{\pi}{2}\gamma_R \frac{F}{\sin^2\theta}}} \tag{A.34}$$

Where $\gamma_R$ is the adiabacity parameter at resonance, and $F$ is a calculable parameter based on the electron density profile. For example, if $N_e \propto x$, then $F = 1$.

# Appendix B

# Neutrino Interactions in the Standard Model

This appendix provides a brief review of how to develop particle interaction models using quantum electrodynamics as an example. The foundations of model development are followed with a presentation of the standard model's electroweak theory, and how observable cross sections are derived within the standard model. Finally, a discussion on modifying neutrino-quark cross sections to model nucleon effects is presented with an emphasis on deriving the charged current quasielastic cross section.

## B.1 Forming an interaction theory: an example through QED

Developing an accurate model that describes a physical system is fundamental to understanding data from physics experiments and making predictions for measurements in future measurements. Given that the full $U(3) \times SU(2)_L \times U(1)_Y$ Standard Model Lagrangian is a large and complicated beast, the theory of quantum electrodynamics (QED) , composed of a Lagrangian symmetric under a $U(1)$ transformation alone, is a good starting point for presenting the model-building process.

The formation of QED begins with a Lagrangian that yields the correct equations of motion for a spin-1/2 fermion in free space. The Lagrangian that describes the mass and kinetics terms for a spin-1/2 fermion can be written in natural units ($\hbar = c = 1$) as [6]:

$$\mathcal{L} = \overline{\psi}\,(x) \left( i\partial\!\!\!/ - m \right) \psi\,(x) \tag{B.1}$$

Where $\psi$ is a 4-component Dirac spinor describing the fermion and its antiparticle, $\overline{\psi}\,(x) \equiv \psi^{\dagger}(x)\gamma^{0}$ is the adjoint field, $\gamma_{\mu}$ are the Dirac gamma matrices, and $\partial\!\!\!/ \equiv \partial^{\mu}\gamma_{\mu}$. Notice that this Lagrangian is composed primarily of the Dirac equation, which can be derived from the Lagrangian using the Euler-Lagrange equations. All fundamental spin-1/2 particle fields must form a solution to this equation.

One property of note for this Lagrangian is it is already invariant under a global $U\,(1)$ symmetry. This invariance can be confirmed by applying a $U(1)$ global transformation to the fermion field as follows:

$$\begin{gathered}
\psi(x) \rightarrow \psi'(x) = e^{i\theta}\psi(x) \\
\mathcal{L} \rightarrow \mathcal{L}' = \left(e^{-i\theta}\overline{\psi}(x)\right) \left( i\partial\!\!\!/ - m \right) \left(e^{i\theta}\psi\,(x)\right) \\
= \mathcal{L}
\end{gathered}$$

The next step in developing the QED theory is to enforce a *local* gauge theory, wherein the Lagrangian becomes invariant under some locally defined transformation. Before doing this step, it's worth asking the question: why locally gauge a theory in the first place? Ultimately, the promotion of the theory to a local gauge theory is what results in the acquisition of interaction terms, as well as conserved quantities consistent with those observed in experiment.

The promotion of the current theory to a gauge theory is achieved by requiring the Lagrangian is invariant under a *local* gauge symmetry, where the transformation parameter $\theta$ is now a function of spacetime $\theta(x)$. Applying a local gauge transformation to the current Lagrangian to check for local gauge invariance gives:

$$\begin{gathered}
\psi(x) \rightarrow \psi'(x) = e^{i\theta(x)}\psi(x) \\
\mathcal{L} \rightarrow \mathcal{L}' = \left(e^{-i\theta(x)}\overline{\psi}(x)\right) \left( i\partial\!\!\!/ - m \right) \left(e^{i\theta(x)}\psi\,(x)\right) \\
= \left(e^{-i\theta(x)}\overline{\psi}(x)\right) i\partial\!\!\!/ \left(e^{i\theta(x)}\psi(x)\right) - m \left(e^{-i\theta(x)}\overline{\psi}(x)\right) \left(e^{i\theta(x)}\psi(x)\right) \\
\neq \mathcal{L}
\end{gathered}$$

The Lagrangian needs modification to become a local gauge theory. The offending term that prevents the Lagrangian from staying constant under the $U(1)$ local transformation is the derivative acting on $e^{i\theta(x)}$; the necessary modification is an addition of a gauge field $A_\mu$(x) to the derivative in the Lagrangian. The addition of this field is achieved by promoting the Lagrangian's derivative $\partial_\mu$ to:

$$\mathcal{D}_\mu = \partial_\mu + iqA_\mu(x)$$

Note that $A_\mu$ must transform under the local gauge transformation as follows:

$$A_\mu(x) \rightarrow A_\mu(x') = A_\mu(x) - \partial_\mu\theta(x)$$

Ultimately, the replacement of $\not\partial$ with $\not\mathcal{D}$ will lead to a Lagrangian of the form:

$$\begin{aligned}\mathcal{L} &= \overline{\psi}(x)\left(i\not\mathcal{D} - m\right)\psi\left(x\right) \\ &= \overline{\psi}(x)\left(i\not\partial - m\right)\psi\left(x\right) - q\overline{\psi}(x)\gamma_\mu\psi(x)A_\mu(x) \qquad \text{(B.2)}\end{aligned}$$

The addition of the gauge field $A_\mu$ to provide the Lagrangian's local gauge invariance has introduced a new term to the Lagrangian in equation B.2. This term can be interpreted as an interaction between the theory's spin-1/2 particle and the introduced gauge field. This exercise demonstrates how enforcing local gauge symmetries with the introduction of gauge fields can build up to a theoretical framework that can describe the particle interactions observed in experiments.

Before moving on from this QED example, there are several loose ends to tie up. First, note that with how the gauge field's transformation is defined, a mass term of the form $m_A A^\mu A_\mu$ cannot be placed into this Lagrangian without breaking the local gauge symmetry. As such, $A_\mu$ must be a massless gauge field. However, a term interpretable as the gauge boson's field strength in spacetime can be added, which takes the form:

$$-\frac{1}{\mu_0}F_{\mu\nu}F^{\mu\nu}$$

where

$$F_{\mu\nu} = [\mathcal{D}_\mu, \mathcal{D}_\nu] = \partial_\mu A_\nu - \partial \nu A_\mu$$

Additionally, Noether's theorem proves that every continuous symmetry associated with a Lagrangian will lead to a quantity that is conserved in time [210, 211]. In the case of QED, this conserved quantity is the charge of the spin-1/2 fermion. As more symmetries are introduced into a theory, more conserved quantities will arise and should be tracked.

### B.1.1 Left and right chiral components of fermionic fields

Before moving to electroweak theory and writing the electroweak Lagrangian under the $SU\left(2\right)_L XU(1)_Y$ symmetry in its common form, a change in representation of the fermionic fields in the Lagrangian must be made.

The $\gamma^5$ matrix is related to the Gamma matrices found in the QED Lagrangian by:

$$i\gamma^0\gamma^1\gamma^2\gamma^3 = \gamma^5$$

fermion fields that are eigenfunctions of the $\gamma^5$ matrix can then be defined as follows:

$$\gamma^5\psi_R = +\psi_R$$
$$\gamma^5\psi_L = -\psi_L$$

These fields above are known as the "right-chiral" and "left-chiral" fields. As defined, any fermionic field can be split into its right-chiral and left-chiral components:

$$\psi = \psi^R + \psi^L \tag{B.3}$$

Where

$$\psi^R = \frac{1+\gamma^5}{2}\psi$$
$$\psi^L = \frac{1-\gamma^5}{2}\psi$$

Substituting in the right-chiral and left-chiral component representation of the fermion field, the Lagrangian from the QED example performed in the previous section becomes:

$$\mathcal{L} = \left(\overline{\psi^R} + \overline{\psi^L}\right)(x)\left(i\partial\!\!\!/ - m\right)\left(\psi^R + \psi^L\right)(x) \tag{B.4}$$

$$\mathcal{L} = \overline{\psi^R} i\partial\!\!\!/ \psi^R + \overline{\psi^L} i\partial\!\!\!/ \psi^L - m(\overline{\psi^R}\psi^L + \overline{\psi^R}\psi^L) \tag{B.5}$$

Nothing has fundamentally changed in the theory; however, the change in representation shows that the right-chiral and left-chiral components of the fermion field have their own kinetic terms, and are related to one another through the mass term. Note that the presence of both the left-chiral and right-chiral components of a fermion is necessary to form the fermion's mass term. In the case of a massless particle (Weyl spinors), chirality and helicity coincide with each other; for massless neutrinos in the standard model, the exclusion of the neutrino's right-handed component results in the nonexistence of the neutrino mass.

## B.2 Electroweak theory

Using the same approach as in the QED example (and with the addition of more symmetries of different properties), the standard model of particle interactions was developed. Since all neutrino interactions proceed through weak interactions only, an overview of only the standard model's electroweak theory is presented. Nearly all of the electric and weak interactions observed to date can be represented using a Lagrangian that is invariant under a $SU\left(2\right)_L XU(1)_Y$ local symmetry group. There are still outstanding exceptions to this, the most prominent being the mass of the neutrino and neutrino oscillations.

### B.2.1 The $SU\left(2\right)_L XU(1)_Y$ symmetry

Recall that the introduction of local symmetries are what lead to boson fields, conserved quantities, and interaction terms that ultimately characterize the theory. The same procedure is followed here, only now enforcing the more complex $SU\left(2\right)_L XU(1)_Y$ symmetry.

As in the QED case, enforcing the symmetry will require modifying the covariant derivative with additional terms that will leave the Lagrangian invariant under the symmetry transformation. The necessary covariant derivative modification for the $SU\left(2\right)_L XU(1)_Y$ symmetry is [6]:

$$\mathcal{D}_\mu = \partial_\mu + ig\underline{A_\mu} \cdot \underline{I} + ig' B_\mu(x)\frac{Y}{2} \tag{B.6}$$

where

$$\underline{A_\mu} \equiv (A_1^\mu, A_2^\mu, A_3^\mu), \underline{I} \equiv (I_1, I_2, I_3)$$

A discussion of each term separately is warranted. The first term is associated directly with the enforcement of the $SU(2)_L$ symmetry, and is known as "weak isospin". The three matrices $I_1, I_2, I_3$ are known as the generators of the symmetry group and satisfy the angular momentum commutation relations. Additionally, the elements of the symmetry group only act on the left-handed components of the fermion fields in the Lagrangian.

The second term in the covariant derivative is associated with the enforcement of the $U(1)_Y$ symmetry and is known as "hypercharge". The operator $Y$ which acts on the fermionic fields is related to the charge operator $Q$ and the third component of the weak isospin group generators $I_3$ through the Gell-Mann-Nishijima relation

$$Q = I_3 + \frac{Y}{2} \tag{B.7}$$

To form a theory under this symmetry group that is ultimately consistent with experimentally observed interactions, the left-handed components of fermionic fields must be grouped into left-handed doublets while the right-handed components stay as singlets. For the first generation of leptons and quarks, the left-handed terms can be written as:

$$L_L = \begin{pmatrix} \nu_{eL} \\ e_L \end{pmatrix}, Q_L = \begin{pmatrix} u_L \\ d_L \end{pmatrix} \tag{B.8}$$

and the right-handed terms are singlets written as:

$$f_R = e_R, u_R, d_R \tag{B.9}$$

where no right-handed neutrino term is included in the theory to match experimental data that there is no right-handed neutrino (or left-handed antineutrino).

However, the presence of the fermion and boson fields alone is not enough to write the complete electroweak Lagrangian. There are two main issues. First, the fermion mass terms will not be invariant under the enforced local symmetries. Second, all gauge bosons in the Lagrangian would be massless as in the QED case; this is inconsistent with the massive $Z$ and $W$ bosons observed in experiment.

The complete electroweak Lagrangian can be realized through the *Higgs mechanism*, wherein another scalar field doublet is introduced to the theory [27]. With the Higgs doublet introduced, the electroweak Lagrangian for the first generation of leptons and quarks is given by [6]:

$$\begin{aligned}\mathcal{L} = i\overline{L_L}\not{D}L_L + i\overline{Q_L}\not{D}Q_L + \sum\nolimits_{f=e,u,d} i\overline{f_R}\not{D}f_R - \frac{1}{4}\underline{A_{\mu\nu}A^{\mu\nu}} + \frac{1}{4}B_{\mu\nu}B^{\mu\nu} + \\ (\mathcal{D}_\mu\Phi)^\dagger(\mathcal{D}^\mu)\Phi) - \mu^2\Phi^\dagger\Phi - \lambda(\Phi^\dagger\Phi)^2 - y^e(\overline{L_L}\Phi e_R + \overline{e_R}\Phi^\dagger L_L) - \\ y^d(\overline{Q_L}\Phi d_R + \overline{d_R}\Phi^\dagger Q_L) - y^u(\overline{Q_L}\widetilde{\Phi}u_R + \overline{u_R}\widetilde{\Phi}^\dagger Q_L)\end{aligned} \tag{B.10}$$

Note that a change of variables and an additional rotation by the weak mixing angle must be made in the Lagrangian given above to represent the vector bosons in terms of their mass eigenbasis (the $W^+$, $W^-$, and $Z$ bosons).

## B.3 Forming an interaction cross section

Up to this point, the procedures for forming a theory that yields terms interpretable as particle masses, kinetic energies, and interactions have been discussed. However, the formulation of an interaction's cross section or a particle's decay rate (both of which can be observed directly in experiment) within a theory's context is needed. Successfully doing so will bridge the gap between a theory's foundation and experimental measurables that can support or refute the theory.

Consider a process where two particles *a* and *b* interact, and there are $N_f$ particles in the final state following the interaction. The differential cross section of the process is given by [212]:

$$\sigma = S\overline{\sum}_{spin} \frac{(2\pi)^4\delta^4(P_i - P_j)\|\mathcal{A}\|^2}{4\sqrt{(p_a\dot{p}_b)^2 - m_a^2 m_b^2}} \prod_{f=1}^{N_f} \frac{d^3p_f}{(2\pi^3 2E_f)} \tag{B.11}$$

Where $p_a$ and $p_b$ are the 4-momenta of the initial state particles, $P_i$ and $P_f$ are the sum of all 4-momenta of the initial and final states, respectively, $m_a$ and $m_b$ are the masses of the initial and final state particles, $S$ is a statistical factor which is the product of $1/n!$ for each set of $n$ identical particles, and $\mathcal{A}$ is the total amplitude of the process in consideration. Note that the $\overline{\sum}_{spin}$ is an average over the initial particles' unobserved spin states and a sum over the possible unobserved spin states of the final particles.

Aside from the $\mathcal{A}$ term, the differential cross section's dynamics are related only to the initial and final particle's kinematics and masses. Thus, the $\mathcal{A}$ term is responsible for representing the nature of how different particles (and their possible interaction mediators) change the cross sections. In fact, $\mathcal{A}$ is a sum over all of the interaction terms formed with the possible Feynman diagrams that represent the interaction in consideration. In other words, $\mathcal{A}$ is the link between the particle interaction theory represented by a Lagrangian and the differential cross section of an interaction.

Feynman diagrams are an invaluable tool for quickly determining what interactions within a theory's framework contribute to the scattering amplitude of a given process. A good review of Feynman diagram usage at the tree level, along with an example of calculating the scattering cross section of $e^+e^- \to \mu^+\mu^-$, can be found [213]. Additionally, a summary of all the propagators and vertex terms associated with electroweak Feynman diagrams can also be found in the appendices of [6].

Using the tools described above, the process of calculating an interaction's cross section can be summarized into the following steps:

- Write down the differential cross section from Fermi's golden rule
- Sum all terms in the theory's Lagrangian that contribute to the interaction's total amplitude
    - Using Feynman diagrams will greatly simplify this process
- Calculate the scattering amplitude by performing the necessary integrals over all internal lines
- Return the scattering amplitude to the differential cross section

## B.4 Modeling the CCQE cross section

The following discussion of the CCQE interaction will focus on the $\nu_l + n \to l^- + p$ case, with the antineutrino alternative ultimately differing up to a sign. Using the Feynman diagrams at the tree level as shown in figure B.1, the CCQE scattering amplitude needed to calculate the CCQE cross section without any interquark interactions would be:

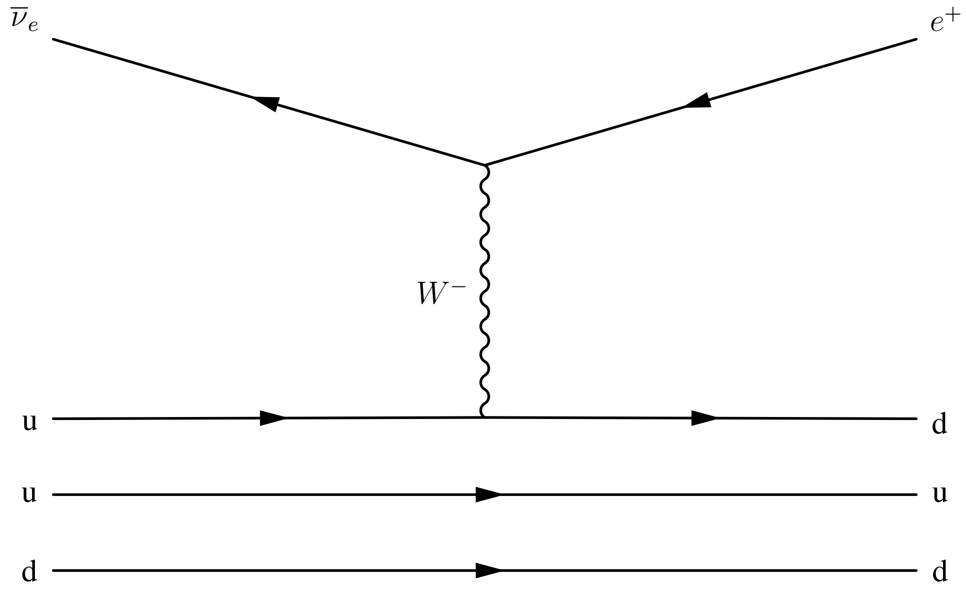

Figure B.1. Feynman diagram representing a charged-current quasielastic scatter at tree level

$$\mathcal{A}_{u\to d+e+\overline{\nu_e}} = -i\frac{G_F}{\sqrt{2}}V_{ud}\overline{u_u}(p_u)\gamma^\rho(1-\gamma^5)u_d(p_d)\overline{u_e}(p_e)\gamma_\rho(1-\gamma^5)v_{\nu_e}(p_{\nu_e}) \tag{B.12}$$

However, equation B.12 does not account for any effects resulting from strong interactions between quarks within the nucleon. To represent these interquark effects, the quark current term must be modified to become a nuclear matrix element as follows:

$$\overline{u_u}(p_u)\gamma^\rho(1-\gamma^5)u_d(p_d) \to \langle p(p_p)|\,\overline{u}(x)\gamma^\rho(1-\gamma^5)d(x)\,|n(p_n)\rangle \tag{B.13}$$

The nucleon corrections manifest within the matrix element as *weak charged-current form factors*. The form factors are dependent on the kinematics of the neutron pre-interaction and the proton post-interaction. Note that these form factors are not directly calculable and must be measured experimentally. It is convenient to produce the generalized forms of the vector and axial terms separately. The common general form of the vector component is given by [6]:

$$\langle p(p_p)|\,\overline{u}(x)\gamma^\rho d(x)\,|n(p_n)\rangle = \overline{u_p}(p_p)\left(\gamma^\rho F_1(Q^2) + \frac{i\sigma^{\rho\eta}q_\eta}{2m_N}F_2(Q^2) + \frac{q^\rho}{m_N}F_3(Q^2)\right)u_n(p_n) \tag{B.14}$$

while the axial component can be written as:

$$\langle p(p_p)|\, \overline{u}(x)\gamma^\rho\gamma^5 d(x)\, |n(p_n)\rangle = \overline{u_p}(p_p)\left(\gamma^\rho\gamma^5 G_A(Q^2) + \frac{q^\rho}{m_N}\gamma^5 G_P(Q^2) + \frac{p_p^\rho + p_n^{rho}}{m_N}\gamma^5 G_3(Q^2)\right) u_n(p_n) \tag{B.15}$$

Where $Q^2 = -q^2 = -(p_{\nu_l} - p_l)^2$, $m_N \approx m_p \approx m_n$, and $F_a, G_a$ for $a = [1, 2, 3, A, P]$ are the weak charged-current form factors. $F_1, F_2$ are known as the Dirac and Pauli weak charged-current form factors, while $G_A, G_P$ are the axial and pseudoscalar weak charged-current form factors. By performing an isospin rotation on the vector and axial terms and enforcing the isospin symmetry, it can be shown that:

$$\begin{aligned} F_3(Q^2) &= 0 \\ G_3(Q^2) &= 0 \end{aligned} \tag{B.16}$$

The Dirac and Pauli form weak form factors are also directly related to the electromagnetic form factors. This isn't so surprising given the inherent connection between the mass eigenstates of the $W, Z$ bosons and the photon. The weak charged-current form factors in terms of the electromagnetic form factors are:

$$F_j(Q^2) = F_j^p(Q^2) - F_j^n(Q^2)\ ,\ j = 1, 2 \tag{B.17}$$

Note that, under the assumption that the produced lepton is an electron and that $Q^2 \to 0$, the same scattering amplitude can be used for the theoretical description of neutron decay rate.

With the scattering amplitude at hand, the differential cross section can be written using Fermi's golden rule for cross sections (appendix B.3). The differential cross section for the $\nu_l$ and $\overline{\nu_l}$ processes in the lab frame, as written by Llewlyn-Smith, is given by [6, 126]:

$$\frac{d\sigma_{CC}^{\nu_l,\overline{\nu_l}}}{dQ^2} = \frac{G_F^2|V_{ud}|^2 m_N^4}{8_\pi(p_\nu \cdot p_{N_i})^2}\left[A(Q^2) \pm B(Q^2)\frac{s-u}{m_N^2} + C(Q^2)\frac{(s-u)^2}{m_N^4}\right] \tag{B.18}$$

where $s = (p_{nu} + p_N)^2$, $u = (p_l + p_N)^2$, and $-Q^2 = t$ are the Mandelstam variables, the $+/-$ signs refer to the neutrino/antineutrino scattering cases, and $A(Q^2)$, $B(Q^2)$, and $C(Q^2)$ are:

$$A = \frac{m_l^2 + Q^2}{m_N^2} \Bigg\{ \left(1 + \frac{Q^2}{4m_N^2}\right) G_A^2(Q^2) - \left(1 - \frac{Q^2}{4m_N^2}\right) \left(F_1^2(Q^2) - \frac{Q^2}{4m_N^2} F_2^2(Q^2)\right) + \frac{Q^2}{m_N^2} F_1(Q^2) F_2(Q^2) - \frac{m_l^2}{4m_N^2} \Big[ (F_1(Q^2) + F_2(Q^2))^2 + (G_A(Q^2) + 2G_P(Q^2))^2 - \frac{1}{4}\left(1 + \frac{Q^2}{4m_N^2}\right) G_P(Q^2)^2 \Big] \Bigg\} \tag{B.19}$$

$$B = \frac{Q^2}{m_N^2} G_A(Q^2) \left(F_1^2 + F_2^2\right) \tag{B.20}$$

$$C = \frac{1}{4} \left( G_A(Q^2)^2 + F_1(Q^2)^2 + \frac{Q^2}{4m_N^2} F_2(Q^2)^2 \right) \tag{B.21}$$

Notice that the term in square brackets within $A(Q^2)$ is proportional to $m_l^2/m_N^2$. For electron or muon scattering, this term is small enough to be neglected due to the small electron/neutrino masses relative to nucleons (for the muon, $(m_\mu/m_N)^2 \approx 1.3E - 2$ [15]).

# Appendix C

# Neutrino production at the Fermilab Booster Neutrino Beam

## C.1 8.89 GeV proton production

To produce the proton beam at Fermilab, negative hydrogen atoms are first formed and collected. At Fermilab, this process is completed using a surface-plasma source (SPS). In the SPS, a molybdenum cathode and anode, heated to about $500^oC$ and $250^oC$ respectively, are exposed to an $H_2$ gas and a plasma is formed near the cathode and anode [214]. A bias voltage of 100-200 V is applied to the anode-cathode pair; paired with the transverse magnetic field applied, the plasma drifts along the $\vec{E} \times \vec{B}$ trajectory. Near the cathode and anode surfaces, there is a possibility of forming $H^-$ ions through surface interactions of the molybdenum and plasma. cesium is flowed into the gas region to lower the surface work-function, which increases the probability of stripping electrons from the molybdenum. $H^-$ ions formed are accelerated towards an extractor, which accelerates the electrons to approximately 35 keV and shapes the beam via magnetic focusing. [215]. Currents leaving the extractor are typically on the order of $30\,mA$ with cesium present. The commonly utilized SPS geometries are the Penning and the Magnetron. A diagram of the Magnetron geometry (utilized at Fermilab) is shown in Figure C.1.

The beam of $H^-$ ions from the extractor is then passed to a radio frequency quadrupole (RFQ) for further acceleration, bunching, and shaping. The most common RFQ geometries are the 4-rod and 4-vane geometry; the current RFQ in the Fermilab beam line is a 4-rod geometry, but will be upgraded to a 4-vane geometry for the PIP-II upgrade. Focusing on the 4-rod

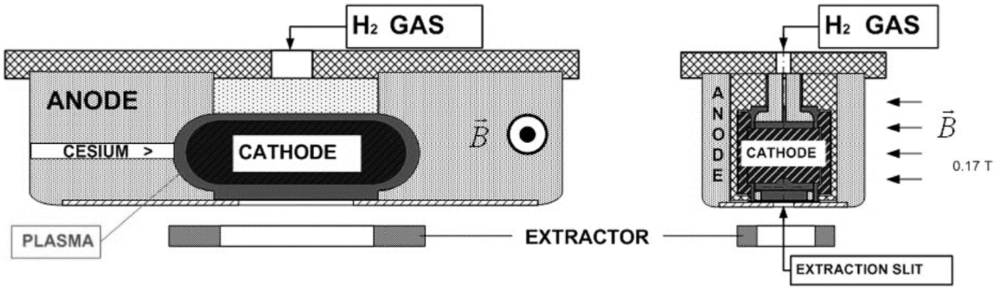

Figure C.1. Views of the surface-plasma source in the Magnetron geometry. Shown are the geometry parallel (left) and perpendicular (right) to the magnetic field applied to the plasma region. Taken from [215].

geometry, ions that pass through the RFQ are focused in the transverse direction by applying a potential of the form

$$V(t) = V_o \sin(\omega t) \tag{C.1}$$

to each rod. The Fermilab RFQ has a typical frequency of about 200 $MHz$. Simultaneously, ions passing through the RFQ are also accelerated by a ridge-like structure machined into each rod. The ridge width can be designed to match the operational RF frequency and input ion energy to accelerate the ions down the RFQ [216]. Fermilab's RFQ outputs $H^-$ ions with an energy of 750 keV.

The RFQ output ion bunches are then further accelerated to 805 $MeV$ of energy using two linear accelerators. The first linear accelerator is composed of five RF cavities that each contain a series of drift-tube cells, a design originally built by Luis Alvarez. To accelerate $H^-$ ions, the RF cavity's electric field is oscillated by varying the cavity's potential such that the ions are accelerated when outside the drift tubes, and "drift" in the shielded regions where the field would decelerate the ions [217]. The RF cavity field oscillation frequency is also about $200 MHz$, similar to the RFQ. Ions leaving the drift-tube linac have an energy of approximately 115 $MeV$.

At the end of the drift-tube cells, the $H^-$ beam passes through a "buncher" and "vernier", which match the beam bunch spacing to one usable with the 800 $MHz$ RF frequency utilized in the side-coupled linac [218].

The second linear accelerator still relies on RF cavities for beam acceleration, but utilizes a different cavity design to achieve a higher beam energy of 400 $MeV$. First, each cavity's drift field is oscillated at a higher frequency (800 $MHz$) to expose beam bunches to accelerating fields more frequently. Second, a single cavity section no longer has drift tubes; instead, it is composed of alternating accelerating cells and coupling cells. Rather than shield the ions with drift tubes, the cells are shaped such that standing or traveling electric field waves resonant in the cavity can accelerate the ion bunch through the section. The accelerating cells have a distinct oblong shape, known as a nose cone, that helps achieve this field resonance. Fermilab's side-coupled linac contains a total of seven modules, where each module contains four sections that each are composed of 16 accelerating cells and 15 coupling cells. A diagram of a single side-coupled module section and a picture of a single module are shown in figure C.2.

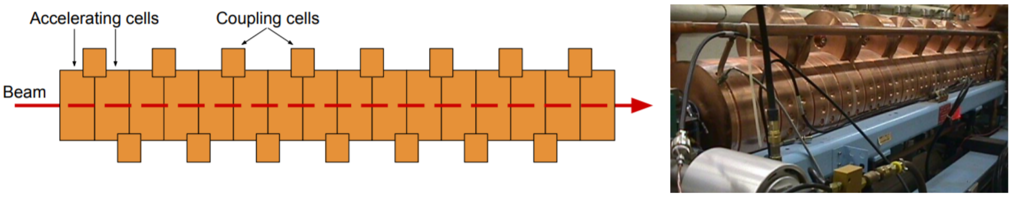

Figure C.2. Diagram of a single side-coupled module section (left) and a photo of one side-coupled module section (right). Figure taken from [218].

Before sending the beam into the booster ring, electrons are stripped from the $H^-$ ion using a carbon foil, producing protons.

The resulting proton beam is injected into the Booster ring. The Booster is a synchrotron composed of a combination of magnets and RF cavities, which work together to steer and accelerate the proton beam. Upon initial injection, the proton beam's bunch structure does not match that needed with the Booster's initial RF frequency. At the BNB hall, protons are delivered in 84 bunches over a 1.6 microsecond window to the target and horn [165].

## C.2 The proton target and horn

To produce a primarily neutrino or antineutrino beam, the BNB uses a beryllium target to produce the mesons which decay to neutrinos. A diagram of the target's main components is shown in C.3.

The bellows keeps the base block in electrical contact with the beryllium mount to prevent arcing (the target rises to a potential of several thousand volts during a single beam pulse). To

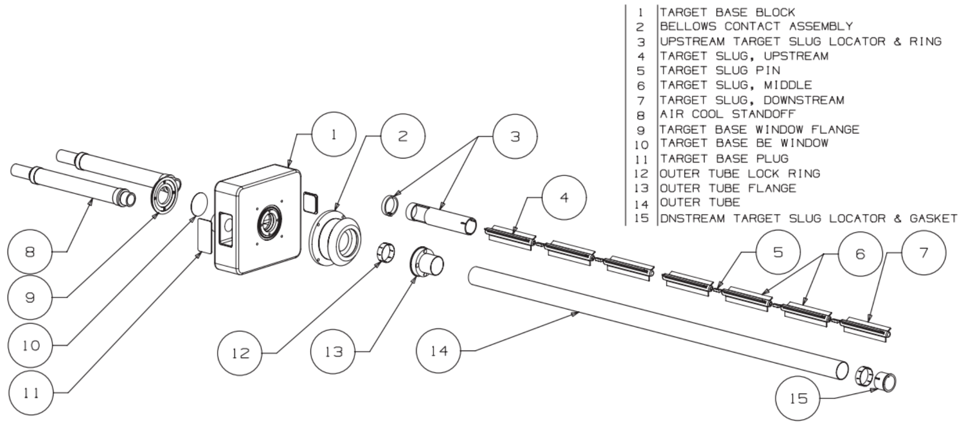

Figure C.3. Exploded view of the BNB's beryllium target. Figure taken from [166].

give a scale reference, each beryllium slug is 4 inches in length and 1 cm in diameter.

Beryllium was chosen as the target material to limit the build-in of radioactive isotopes during operation, the most radiologically important produced being $^{7}Be$ and tritium. Beryllium also has satisfactory structural properties so as not to degrade or break from beam exposure. A single injection raises the beryllium by about $6^{o}K$, resulting in compressive pressures of about $20\,MPa$; fatigue data on beryllium would put the limits of the target well above this, at about $300\,MPa$ [219].

The beryllium target mount is encased in a magnetic horn used to focus the pions produced in the proton-Be interactions. A diagram of the magnetic horn is shown in figure C.4. The horn is composed of an aluminum alloy, and is a pulsed toroidal magnetic field.

The magnetic field is generated by two coaxial conductors; the inner conductor flows current in the opposite direction of the outer conductor to create a magnetic field dependence with a $\frac{1}{r}$ dependence [166]. Currents of $174\,kA$ are typical for the horn, with current supplied in $143\,\mu s$-long pulses. Fields of $1.5T$ are obtained where the inner conductor is most narrow. The geometry of the horn and operation current were selected using a GEANT simulation of the horn to maximize the $\nu_{\mu}$ flux between $0.5 - 1\,GeV$ and minimize the flux above $1\,GeV$ [219].

## C.3 Collimator, decay region, and absorbers

A concrete collimator is used downstream of the horn. The collimator absorbs particles that would not contribute to the neutrino flux, and also helps to select the strongly forward-going

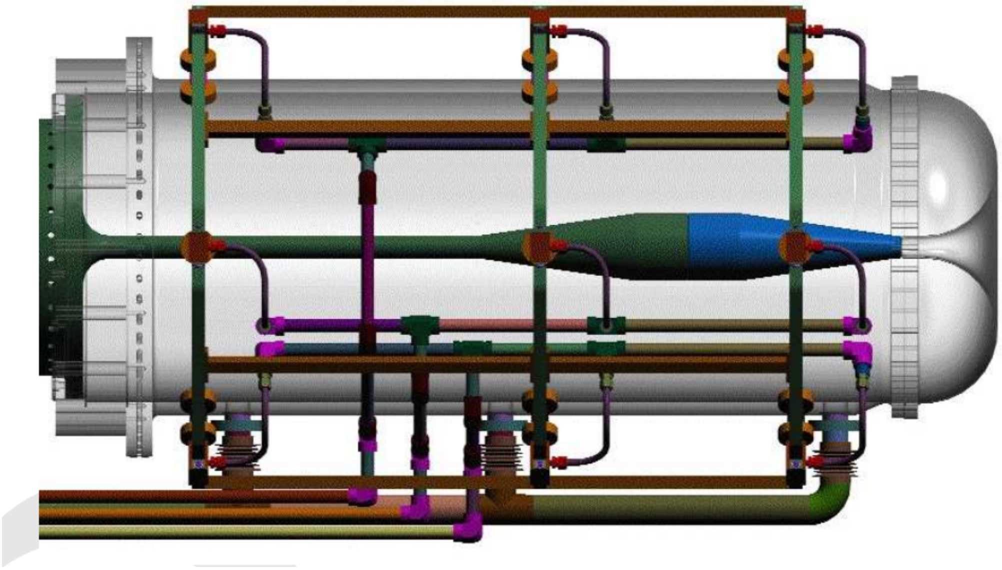

Figure C.4. Side view of the BNB magnetic horn. The outer conductor is transparent here to make the inner conductor visible. Pipes along the bottom provide cooling to the conductors. Figure taken from [219].

mesons. The collimator is 214 cm long, with an initial aperture radius of 30 cm that linearly increases to a final radius of 35.5 cm. The upstream end of the collimator is 259 cm from the upstream end of the beryllium target [167].

A decay region is placed beyond the collimator to provide space for the mesons to decay to muons and muon (anti)neutrinos. The decay region is approximately 50 meters long with a radius of 3 feet, and ends downstream with a beam stop. A deployable absorber hangs in the decay region at 25 meters from the upstream entrance, and allows for systematic studies of the beam if desired. The absorbers consist of “blue blocks”, which are composed of recycled waste steel produced by Energy Solutions, LLC in Oak Ridge, Tennessee [166, 220].

## C.4 BNB monitoring

The initial proton beam delivered to the BNB is monitored using four different systems. Two beam current toroids are used to measure the absolute intensity of the beam via the beam’s induced current in the toroids. Beam position monitors (BPMs) are split-plate devices, which measure the beam position based on the difference in charge induced on the plates by the beam. The BPMs are found to be accurate to within 0.1 mm. A multiwire chamber is used to determine the incident beam's profile, and is composed of $48 \times 48$ horizontal and vertical wires with 0.5 mm pitch. Finally, a resistive wall monitor (RWM) monitors both the time and intensity of beam spills. The proton flux measured with the toroids agree to within 2% [166].

The production of muons via meson decays is monitored using the Little Muon Counter (LMC) spectrometer. The LMC is contained at the end of a 40-foot drift pipe starting 9 meters upstream from the decay region's final absorber. The drift pipe is oriented at an angle of $7^o$ off-beam axis; at $7^o$ off-axis, kaon and pion two-body decays produce distinctly higher and lower energy muons respectively, allowing for an estimate of the kaon/ pion fraction in-beam. At the end of the drift pipe, the LMC first utilizes a dipole magnet and planes of scintillating fiber trackers to measure the momentum of incoming particles. Following the spectrometer, the particle then passes through alternating layers of scintillator and tungsten; the range through this stack, paired with the particle's momentum, identifies particles as muons, pions, kaons, etc. [166, 219].

# References

[1] W. Pauli. Dear radioactive ladies and gentlemen. *Physics Today*, 31N9(27), 1978.

[2] Frank N. Magill. *Great Lives from History: British and Commonwealth Series*. Salem Press, 1 edition, 1987.

[3] C.L Cowan Jr., F. Reines, F. B. Harrison, H. W. Kruse, and A. D. McGuire. Detection of the free neutrino: a confirmation. *Science*, 124(3212):103–4, 1956.

[4] F.L. Wilson. Fermi's Theory of Beta Decay. *American Journal of Physics*, 36(12):1150–1160, 1968.

[5] Standard model. `en.wikipedia.org/wiki/Standard_Model`, Accessed: 2019-09-17.

[6] C. Giunti and C.W. Kim. *Fundamentals of Neutrino Physics and Astrophysics*. Oxford University Press, 2007.

[7] J. Brau. Electroweak interactions and the standard model, 2018. U. of Oregon, Physics 662 lecture.

[8] H. Chang. The standard model. UC Davis, Electroweak theory lecture (245B).

[9] M. Baldoncini, I. Callegari, G. Fiorentini, F. Mantovani, B. Ricci, V. Strati, and G. Xhixha. Reference worldwide model for antineutrinos from reactors. *Physical Review D*, 91(6):1–17, 2015.

[10] C. S. Wu, E. Ambler, R. W. Hayward, D. D. Hoppes, and R. P. Hudson. Experimental test of parity conservation in beta decay . *Physical Review*, 105(4):1413–1415, 1957.

[11] M. Goldhaber, L. Grodzins, and A.W. Sunyar. Helicity of neutrinos . *Physical Review*, 109(3):1015–1017, 1958.

[12] G. Danby, J. M. Gaillard, K. Goulianos, L. M. Lederman, N. Mistry, M. Schwartz, and J. Steinberger. Observation of high-energy neutrino reactions and the existence of two kinds of neutrinos. *Physical Review Letters*, 9(1):36–44, 1962.

[13] N. Ushida et al (DONUT Collaboration) K. Kodama. Observation of tau neutrino interactions. *Physics Letters B*, 504:218–224, 2001.

[14] Alain Blondel. The number of neutrinos and the Z line shape. *The Standard Theory of PARTICLE Physics: Essays to Celebrate CERN's 60th Anniversary*, 26:145–160, 2016.

[15] M. Tanabashi et al. (PARTICLE Data Group). *Physical Review D*, 98, 2018.

[16] M. Gerbino and M. Lattanzi. Status of neutrino properties and future prospects-cosmological and astrophysical constraints. *Frontiers in Physics*, 5(FEB), 2018.

[17] B. Pontecorvo. Mesonium and antimesonium. *Journal of Experimental Theoretical Physics (U.S.S.R)*, 33:549 – 551, 1957.

[18] B. Pontecorvo. Neutrino Experiments and the Problem of Conservation of Leptonic Charge. *Soviet Journal of Experimental and Theoretical Physics*, 26(5):984, 1968.

[19] B. T. Cleveland, T. Daily, R. Davis, J. Distel, K. Lande, C. K. Lee, P. Wildenhain, and J. Ullman. Update on the measurement of the solar neutrino flux with the Homestake chlorine detector. *Nuclear Physics B (Proceedings Supplements)*, 38(1-3):47–53, 1995.

[20] S. Fukuda et al. (Super-Kamiokande Collaboration). Solar $^8B$ and hep Neutrino Measurements from 1258 Days of Super-Kamiokande Data. *Physical Review Letters*, 86(5651), 2001.

[21] S. Fukuda et al. (Super-Kamiokande Collaboration). Evidence for Oscillation of Atmospheric Neutrinos. *Physical Review Letters*, 81(8), 1998.

[22] Q.R. Ahmad et al. (The SNO Collaboration). Measurement of the rate of $\nu_e + d \to p + p + e^-$ interactions produced by 8B solar neutrinos at the Sudbury Neutrino Observatory. *Physical Review Letters*, 87(07), 2001.

[23] C. Giganti, S. Lavignac, and M. Zito. Neutrino oscillations: The rise of the PMNS paradigm. *Progress in PARTICLE and Nuclear Physics*, 98(Umr 3681):1–54, 2018.

[24] M. Apollonio et al. (CHOOZ Collaboration). Limits on neutrino oscillations from the chooz experiment. *Physics Letters B*, 466(415), 1999.

[25] K. Eguchi et al. (KamLAND Collaboration). First Results from KamLAND: Evidence for Reactor Antineutrino Disappearance. *Physical Review Letters*, 90(2), 2003.

[26] S. Abe and T. Ebihara et al. (KamLAND Collaboration). Precision measurement of neutrino oscillation parameters with KamLAND. *Physical Review Letters*, 100(22):4–7, 2008.

[27] M. Tanabashi et al. (Particle Data Group). Status of higgs boson physics. *Physics Review D*, 98(030001), 2019.

[28] J.A. Formaggio and G.P. Zeller. From eV to EeV: Neutrino cross sections across energy scales. *Reviews of Modern Physics*, 84(1307), 2012.

[29] Y. Huang, V. Chubakov, F. Mantovani, R.L. Rudnick, and W.F. McDonough. A reference Earth model for the heat-producing elements and associated geoneutrino flux. *Geochemistry, Geophysics, Geosystems*, 14(6):2003–2029, 2013.

[30] S.T. Dye. Geoneutrinos and the radioactive power of the earth. *Review of Geophysics*, 50(RG3007), 2012.

[31] I. Shimizu. KamLAND: Geo-neutrino measurement in Japan. *Annals of Geophysics*, 60(1), 2017.

[32] M. Agostini and S. Appel et al. (Borexino Collaboration). Spectroscopy of geoneutrinos from 2056 days of Borexino data. *Physical Review D*, 92(3), 2015.

[33] N. S. Bowden, A. Bernstein, S. Dazeley, R. Svoboda, A. Misner, and T. Palmer. Observation of the isotopic evolution of pressurized water reactor fuel using an antineutrino detector. *Journal of Applied Physics*, 105(6), 2009.

[34] D. A. Dwyer. Antineutrinos from nuclear reactors: Recent oscillation measurements. *New Journal of Physics*, 17:0–12, 2015.

[35] Z. Djurcic, J. A. Detwiler, A. Piepke, V. R. Foster, L. Miller, and G. Gratta. Uncertainties in the anti-neutrino production at nuclear reactors. *Journal of Physics G: Nuclear and PARTICLE Physics*, 36(4):1–20, 2009.

[36] A. A. Hahn, K. Schreckenbach, W. Gelletly, F. von Feilitzsch, G. Colvin, and B. Krusche. Antineutrino spectra from 241Pu and 239Pu thermal neutron fission products. *Physics Letters B*, 218(3):365–368, 1989.

[37] F. von Feilitzsch, A. A. Hahn, and K. Schreckenbach. Experimental beta-spectra from 239Pu and 235U thermal neutron fission products and their correlated antineutrino spectra. *Physics Letters B*, 118(1-3):162–166, 1982.

[38] Iaea power reactor information system. `pris.iaea.org/pris/`.

[39] et al. PARTICLE Data Group C. Patrignani. Introduction to the neutrino properties listings. *Chin. Phys. C*, 40(100001):1, 2016. `http://pdg.lbl.gov/2016/listings/rpp2016-list-neutrino-prop.pdf`.

[40] A. Serenelli. Alive and well: a short review about standard solar models. 2016.

[41] O. Smirnov et al. (Borexino Collaboration). Solar neutrino with Borexino: Results and perspectives. *Physics of Particles and Nuclei*, 46(2):166–173, 2015.

[42] A. Gando et al. (KamLAND Collaboration). Be 7 solar neutrino measurement with KamLAND. *Physical Review C - Nuclear Physics*, 92(5):1–8, 2015.

[43] M. Anderson and S. Andringa et al. (SNO+ collaboration). Measurement of the B 8 solar neutrino flux in SNO+ with very low backgrounds. *Physical Review D*, 99(1), 2019.

[44] A.M. Serenelli, W.C. Haxton, and C. Páž·a-Garay. Solar models with accretion. I. Application to the solar abundance problem. *Astrophysical Journal*, 743(1), 2011.

[45] S. E. Woosley and M. M. Phillips. Supernova 1987A. *Science*, 240(4853):750–759, 1988.

[46] K. Leach. Lecture 22: nuclear fusion and nuclear astrophysics, 2019. PHGN 422: Nuclear Physics, Colorado School of Mines.

[47] A.C. Phillips. *The Physics of Stars*. Wiley, 2 edition, 1999.

[48] S. Woosley and H.T. Janka. The Physics of Core-Collapse Supernovae. *Nature Physics*, 1:147–154, 2006.

[49] H.T. Janka. *Neutrino Emission from Supernovae*. Springer, 1966.

[50] I. Tamborra, G. Raffelt, F. Hanke, H.T. Janka, and B. Müller. Neutrino emission characteristics and detection opportunities based on three-dimensional supernova simulations. *Physical Review D*, 90(4):1–18, 2014.

[51] S. Kate. Supernova Neutrino Detection. *Annual Review of Nuclear PARTICLE Science*, 62:81–103, 2014.

[52] R.M. Bionta and G. Blewitt et al. (IMB Collaboration). Observation of a neutrino burst in coincidence with supernova 1987A in the large magellanic cloud. *Physical Review Letters*, 58(14):1494–1496, 1987.

[53] K. Hirata and T. Kajita et al. (Kamiokande Collaboration. Observation of a Neutrino Burst from the Supernova SN1987A. *Physical Review Letters*, 58(14):1490–1493, 1987.

[54] E.N.Alexeyev, L.N. Alexeyeva, I.V.Krivosheina, and V.I.Volchenko. Detection of the Neutrino Signal from SN 1987A Using the INR Baksan Underground Scintillation Telescope. *ESO Workshop on the SN 1987A Proceedings (A88-35301 14-90)*, pages 237–247, 1987.

[55] G.A. Tammann, W. Loffler, and A. Schroder. The Galactic Supernova Rate. *The Astrophysical Jounral Supplement Series*, 94:487–493, 1994.

[56] J.F. Beacom. The Diffuse Supernova Neutrino Background. *Annual Review of Nuclear and PARTICLE Science*, 60(1):439–462, 2010.

[57] A. Gandl et al. (KamLAND Collaboration). A study of extraterrestrial antineutrino sources with the kamland detector. *Astrophys. J*, 745:193, 2012.

[58] M.G. Aartsen and M. Ackermann et al. (IceCube Collaboration). Measurement of atmospheric tau neutrino appearance with IceCube DeepCore. *Physical Review D*, 99(3):1–33, 2019.

[59] M. Honda, M. S. Athar, T. Kajita, K. Kasahara, and S. Midorikawa. Atmospheric neutrino flux calculation using the NRLMSISE-00 atmospheric model. *Physical Review D*, 92(2):3–4, 2015.

[60] J. Seguinot and T. Ypsilantis. Photo-Ionization and Cherenkov Ring Imaging. *Nuclear Instruments and Methods*, 142:377–391, 1977.

[61] M. R. Vagins. Gadzooks! the future of super-kamiokande? *Nuclear Physics B*, 168:128 – 130, 2007.

[62] V. Fischer. Theia: A multi-purpose water-based liquid scintillator detector. *CIPANP2018 Proceedings*, 2018.

[63] translated by Vincent Sheean Eve Curie. *Madame Curie*. William Heinman Ltd., 1938.

[64] J. V. Jelley. Cerenkov radiation and its applications. *British Journal of Applied Physics*, 6(227):377–391, 1955.

[65] A. A. Watson. The discovery of Cherenkov radiation and its use in the detection of extensive air showers. *CRIS2010: Cosmic Ray International Seminar Proceedings*, 2010.

[66] P.A. Cherenkov. Visible radiation produced by electrons moving in a medium with velocities exceeding that of light. *Physical Review*, 52(4):378–379, 1937.

[67] J.D. Jackson. *Classical Electrodynamics*. New York :Wiley, 1925–2016.

[68] K. Nakamura et al. (PDG). Passage of particles through matter. *JP G*, 37(075021), 2010.

[69] Rat (is an analysis tool) user's guide. rat-pac.readthedocs.io/en/latest/.

[70] D. Segelstein. *The Complex Refractive Index of Water*. PhD thesis, University of Missouri, Kansas City, 9 1981. Data summarized at `www.philiphaven.com/Segelstein.txt`.

[71] Refractive index database. `refractiveindex.info/?shelf=main&book=H2O@page=Hale`, Accessed: 2019-08-14.

[72] S. J.M. Peeters and J. R. Wilson. Sudbury neutrino observatory. *Neutrino Oscillations: Present Status and Future Plans*, pages 45–69, 2008.

[73] M. Tanabashi et al. (Particle Data Group). Neutrino properties. *Physics Review D*, 98(030001), 2019.

[74] F.P. An and J.Z. Bai et al (Daya Bay Collaboration). Observation of electron-antineutrino disappearance at daya bay. *Physical Review Letters*, 108(171803), 2012.

[75] Y. Abe and C. Aberle et al. (Double Chooz Collaboration). Indication of reactor $\bar{\nu_e}$ disappearance in the double chooz experiment. *Physical Review Letters*, 108(131801), 2012.

[76] K. Abe et al. (The Super-Kamiokande Collaboration). Solar neutrino measurements in super-kamiokande-iv. *Physical Review D*, 94(052010), 2016.

[77] S. Andringa et al. (SNO+ Collaboration). Current status and future prospects of the sno+ experiment. *Advances in High Energy Physics*, 2016.

[78] K. Abe et al. (Super-Kamiokande Collaboration). Atmospheric neutrino oscillation analysis with external constraints in super-kamiokande i-iv. *Physical Review D*, 97(072001), 2018.

[79] E. Aliu et al. (K2K Collaboration). Evidence for muon neutrino oscillation in an accelerator-based experiment. *Physics Review Letters*, 94(8), 2005.

[80] H. Nunokawa, S. Parke, and R.Z. Funchal. Another possible way to determine the neutrino mass hierarchy. *Physical Review D*, 72(013009), 2005.

[81] P. Adamson and I. Anghel et al. (MINOS Collaboration). Combined analysis of $\nu_\mu$ disappearance and $\nu_\mu \to \nu_e$ appearance in minos using accelerator and atmospheric neutrinos. *Physical Review Letter*, 112(191801), 2014.

[82] A. Cerva, A. Donini, and M.B. Gavela et al. Golden measurements at a neutrino factory. *Nuclear Physics B*, 579:17 – 55, 2000.

[83] L. H. Whitehead. Neutrino oscillations with minos and minos+. 2016.

[84] M. A. Acero and P. Adamson et al. (NO$\nu$A Collaboration). First measurement of neutrino oscillation parameters using neutrinos and antineutrinos by no$\nu$a. *Physics Review Letters*, 123(151803), 2019.

[85] D. M. Webber on behalf of the Daya Bay Collaboration. An improved measurement of electron antineutrino disappearance at daya bay. *Nuclear Physics B Proceedings Supplements*, 233:96 – 101, 2012.

[86] S.B. Kim et al. (RENO Collaboration). Measurement of neutrino mixing angle $\theta_{13}$ and mass difference $\delta m^2_{ee}$ from reactor antineutrino disappearance in the reno experiment. *Nuclear Physics B*, 908:94 – 115, 2016.

[87] M. Chen. Tasi 2006 lectures on leptogenesis. 2007.

[88] K. Abe et al. (T2K Collaboration). Search for cp violation in neutrino and antineutrino oscillations by the t2k experiment with $2.2 \times 10^{21}$ protons on target. *Physics Review Letters*, 121(17), 2018.

[89] K. Abe and J. Amey et al. (T2K Collaboration). Measurement of neutrino and antineutrino oscillations by the t2k experiment including a new additional sample of $\nu_e$ interactions at the far detector. *Physical Review D*, 96(092006), 2017.

[90] Pip-ii conceptual design report. `pxie.fnal.gov/PIP-II_CDR/default.html`, Accessed: 2019-10-21.

[91] R. Acciarri et al. (The DUNE Collaboration). Long-baseline neutrino facility (lbnf) and deep underground neutrino experiment (dune) conceptual design report volume 1, 2016.

[92] R. Acciarri et al. (The DUNE Collaboration). Long-baseline neutrino facility (lbnf) and deep underground neutrino experiment (dune) conceptual design report volume 2, 2016.

[93] G. Yang. Neutrino mass hierarchy determination at reactor antineutrino experiments. In *Proceedings, 12th Conference on the Intersections of Particle and Nuclear Physics (CIPANP 2015): Vail, Colorado, USA*, 2015.

[94] R. N. Cahn and D. A. Dwyer et al. White paper: Measuring the neutrino mass hierarchy. In *Proceedings, 2013 Connumity Summer Study on the Future of U.S. Particle Physics: Snowmass on the Mississippi (CSS2013)*, 2013.

[95] H. Abramowicz and F. Dydak et al. Limit on right handed weak coupling parameters from inelastic neutrino interactions. *Particles and Fields*, 12:225 – 227, 1982.

[96] H. Murayama. The origin of neutrino mass. *Physics World*, pages 35 – 39, 2002.

[97] S. Boyd. Neutrino mass and direct measurements. `warwick.ac.uk/fac/sci/physics/staff/academic/boyd/warwick_week/neutrino_physics/lec_neutrinomass_writeup.pdf`, Lecture notes, Accessed: 2019-08-11.

[98] P.B. Pal. Dirac, majorana and weyl fermions, 2010.

[99] S. Dell'Oro, S. Marcocci, M. Viel, and F. Vissani. Neutrinoless double beta decay: 2015 review. *Advances in High Energy Physics*, 2016, 2016.

[100] S. R. Elliot. Experiments for neutrinoless double-beta decay. *International Journal of Modern Physics A*, 18(22):4097 – 4111.

[101] G.B. Franklin for the KATRIN Collaboration. The katrin neutrino mass measurement: Experiment, status, and outlook, 2018.

[102] M. Aker et al. (KATRIN Collaboration). An improved upper limit on the neutrino mass from a direct kinematic method by katrin, 2019.

[103] C. Weinheimer. The neutrino mass direct measurements, 2003.

[104] V.M. Lobashev. Proc. of the europh. conf. nucl. phys. in astrophysics npdc17, 2002. Debrecen, Hungary.

[105] J.E. Bautista et al. Measurement of baryon acoustic oscillation correlations at $z = 2.3$ with sdss dr12 ly $\alpha$-forests. *Astron. Astrophys.*, 603(A12), 2017.

[106] M. Gerbino and M. Lattanzi. Status of neutrino properties and future prospects - cosmological and astrophysical constraints, 2017.

[107] R. Adhikari and M. Agnosti et al. A white paper on keV sterile neutrino dark matter. *Journal of Cosmology and Astroparticle Physics*, 2017(01), 2017.

[108] K. N. Abazajian et al. Light sterile neutrinos: A white paper. 2012.

[109] M. D. Campos and W. Rodejohann. Testing kev sterile neutrino dark matter in future direct detection experiments. *Physical Review D*, 94(9), 2016.

[110] F. Kaether, W. Hampel, G. Heusser, J. Kiko, and T. Kirsten. Reanalysis of the gallex solar neutrino flux and source experiments. *Physics Letters B*, 685(1):47 – 54, 2010.

[111] J. N. Abdurashitov et al. Measurements of the solar neutrino capture rate with gallium metal. iii: Results for the 2002–2007 data-taking period. *Physical Review C*, 80, 2009.

[112] C. Giunti and M. Laveder. Statistical significance of the gallium anomaly. *Physical Review C*, 83, 2011.

[113] M. Dentler et al. Updated global analysis of neutrino oscillations in the presence of ev-scale sterile neutrinos. 2018.

[114] I. Alekseev and V. Belov et al. Search for sterile neutrinos at the danss experiment. *Physics Letters B*, 787:56 – 63, 2018.

[115] Y. J. Ko and B. R. Kim et al (NEOS Collaboration). Sterile neutrino search at neos experiment. *Physical review letters*, 118(121802), 2017.

[116] J. Ashenfelter and A.B. Blantekin et al. (PROSPECT collaboration). The prospect reactor antineutrino experiment. *Nucl. Inst. Meth. A*, 922:287 – 309, 2019.

[117] G. Mention and M. Fechner et al. Reactor antineutrino anomaly. *Physical Review D*, 83(073006), 2011.

[118] J. Kopp, P. Machado, M. Maltoni, and T. Schwetz. Sterile neutrino oscillations: The global picture. *JHEP*, 05, 2013.

[119] A. Aguilar and L.B. Auerbach et al. (LSND Collaboration). Evidence for neutrino oscillations from the observation of $\bar{\nu_e}$ appearance in a $\bar{\nu_\mu}$ beam. *Physical Review D*, 64(112007), 2001.

[120] A.A. Aguilar-Arevalo and B.C. Brown et al. (MiniBooNE Collaboration). Significant excess of electronlike events in the miniboone short-baseline neutrino experiment. *Physical Review Letters*, 121(221801), 2018.

[121] N. Agafonova and A. Alexandrov et al. (OPERA Collaboration). Final results on neutrino oscillation parameters from the opera experiment in the cngs beam. 2019.

[122] B. Armbruster and I.M. Blair et al. (KARMEN Collaboration). Upper limits for neutrino oscillations $\bar{\nu_\mu} \to \bar{\nu_e}$ fom muon decay at rest. *Physical Review D*, 65, 2002.

[123] M. Haraczyk. The icarus detector. past, present and future. *J. Phys.: Conf. Ser.*, 798(012162), 2017.

[124] N. McConkey and SBND collaboration. Sbnd: Status of the fermilab short-baseline near detector. *J. Phys.: Conf. Ser.*, 888(012148), 2017.

[125] J. A. Formaggio and G. P. Zeller. From ev to eev: Neutrino cross sections across energy scales. *Review of Modern Physics*, 84:1307 – 1341, 2012.

[126] C.H. Llewlyn Smith. Neutrino reactions at accelerator energies. *Physics. Rept.*, 3:261 – 379, 1972.

[127] D. Rein and L. M. Sehgal. Neutrino-excitation of baryon resonances and single pion production. *Annals of Physics*, 133:79 – 153, 1981.

[128] R. P. Feynman, M. Kislinger, and F.Ravndal. Current matrix elements from a relativistic quark model. *Physical Review D*, 3(11):2706 – 2732, 1971.

[129] S. J. Barish and M. Derrick et al. Study of neutrino interactions in hydrogen and deuterium. *Physical Review D*, 19(9), 1979.

[130] J. Bell and J. P. Berge et al. Study of the reactions $\nu p \to \mu^- \delta^{++}$ at high energies and comparisons with theory. *Physical Review Letters*, 41(15), 1978.

[131] P. Allen and J. Blietschau et al. Single $\pi^+$ production in charged current neutrino-hydrogen interactions. *Nuclear Physics B*, 176:269–284, 1980.

[132] J. M. Conrad, M. H. Shaevits, and T. Bolton. Precision measurements with high-energy neutrino beams. *Review of Modern Physics*, 70:1341–1392, 1998.

[133] D. Grover, K. Saraswat, P. Shukla, and V. Singh. Charged-current inelastic scattering of muon neutrinos ($\nu_\mu$) off $^{56}fe$. *Physical Review C*, 98, 2018.

[134] M. O. Wospakrik. *Measurement of Neutrino Absolute Deep Inelastic Scattering Cross Section in Iron, Lead, Carbon, and Plastic Using MINERvA Detector at* $E_\mu = 6$ *GeV*. PhD thesis, Florida U., 2018. FERMILAB-THESIS-2018-22.

[135] D. Casper. The nuance neutrino physics simulation, and the future. *Nuclear Physics B (Proc. Suppl)*, 112:161 – 170, 2002.

[136] S. Dytman. Genie v3.0.0 major physics release, 2018. Fermilab Neutrino Seminar Series.

[137] Genie physics and user manual, 2003 – 2018. version 3.0.0b1.

[138] T. Golan, J.T. Sobczyk, and J. Zmuda. Nuwro: the wroclaw monte carlo generator of neutrino interactions. *Nucl. Phys. Proc. Suppl.*, page 499, 2012.

[139] Y. Hayato (Kamioka Observatory). A neutrino interaction simulation program library neut. *Acta Phys. Polon. B*, 40:2477–2489, 2019.

[140] O. Benhar and N. Farina et al. Electron- and neutrino-nucleus scattering in the impulse approximation regime. *Physical Review D*, 72, 2005.

[141] R. A. Smith and E. J. Moniz. Neutrino reactons on nuclear targets. *Nuclear Physics B*, 43:605 – 622, 1972.

[142] K.S. Kuzmin, V.V. Lyubushkin, and V.A. Naumov. Quasielastic axial-vector mass from experiments on neutrino-nucleus scattering. *European Physics Journal C*, 54:517 – 538, 2008.

[143] K. Saraswat, P. Shukla, and V. Kumar. Charged current quasi elastic scattering of muon neutrino with nuclei. *Indian Journal of Physics*, 92(2):249 – 257, 2018.

[144] A. A. Aguilar-Arevalo et al. (MiniBooNE Collaboration). Measurement of muon neutrino quasi-elastic scattering on carbon. *Physical Review Letters*, 100, 2008.

[145] J. Nieves, J. E. Amaro, and M. Valverde. Inclusive quasi-elastic neutrino reactions. *Physical Review C*, 70, 2004.

[146] J. Nieves, M. Valverde, and M. J. V. Vacas. Inclusive nucleon emission induced by quasielastic neutrino-nucleus interactions. *Physical Review C*, 73, 2006.

[147] D. Zongker. Chicken chicken chicken: Chicken chicken, 2006. University of Washington.

[148] M. Martini, M. Ericson, G. Chanfray, and J. Marteau. Neutrino and antineutrino quasielastic interactions with nuclei. *Physical Review C*, 81, 2010.

[149] M. Martini, M. Ericson, G. Chanfray, and J. Marteau. A unified approach for nucleon knock-out, coherent and incoherent pion production in neutrino interactions with nuclei. *Physical review C*, 80, 2009.

[150] M. Martini, M. Ericson, and G. Chanfray. Neutrino energy reconstruction problems and neutrino oscillations. *Physical Review D*, 85:093012, 2012.

[151] C. Andreopoulos et al. The genie neutrino monte carlo generator. *Nuclear Instrumentation Methods A*, 614:87 – 104, 2010.

[152] A. R. Back et al. (ANNIE Collaboration). Accelerator neutrino neutron interaction experiment (annie): Preliminary results and physics phase proposal, 2017.

[153] K. Abe et al. (T2K Collaboration). First measurement of the $\nu_\mu$ charged-current cross section on a water target without pions in the final state. *Physical Review D*, 97:012001, 2018.

[154] W. de Boer. Grand unified theories and supersymmetry in particle physics and cosmology. *Progress in Particle and Nuclear Physics*, 33:201 – 302, 1994.

[155] M. Anderson et al. (The SNO+ Collaboration). Search for invisible modes of nucleon decay in water with the sno+ detector. *Physical Review D*, 99:032008, 2019.

[156] H. Ejiri. Nuclear deexcitations of nucleon holes associated with nucleon decays in nuclei. *Physical Review C*, 48:1442, 1993.

[157] F. Ajzenberg-selove. *Nucl. Physics A*, 523(1), 1991.

[158] K. Abe et al. (The Super-Kamiokande Collaboration). Search for proton decay via $p \rightarrow e^+\pi^0$ and $p \rightarrow \mu^+\pi^0$ in 0.31 megaton-years exposure of the super-kamiokande water cherenkov detector. *Physical Review D*, 95:012004, 2017.

[159] S. Horiuchi, J. F. Beacom, and E. Dwek. Diffuse supernova neutrino background is detectable in super-kamiokande. *Physical Review D*, 79:083013, 2009.

[160] K. J. Kelly and P. AN. Machado et al. Sub-gev atmospheric neutrinos and cp-violation in dune. *Physical Review Letters*, 123:081801, 2019.

[161] R. Acciarri et al. (The ArgoNeuT Collaboration). Demonstration of mev-scale physics in liquid argon time projection chambers using argoneut. *Physical Review D*, 99:012002, 2019.

[162] M. Elkins et al. (The MINERvA Collaboration). Neutron measurements from antineutrino hydrocarbon reactions. *Physical Review D*, 100:052002, 2019.

[163] S. E. Kopp. The numi neutrino beam at fermilab. *AIP Conf. Proc.*, 773(1):276–278, 2005.

[164] S.J. Brice and R.L. Cooper et al. A new method for measuring coherent elastic neutrino nucleus scattering at an off-axis high-energy neutrino beam target. 2013.

[165] A. R. Back et al. (ANNIE Collaboration). Measurement of beam-correlated background neutrons from the fermilab booster neutrino beam in annie phase-i, 2019.

[166] A.A. Gauilar-Arevalo and C.E. Anderson et al. (MiniBooNE Collaboration). Neutrino flux prediction at miniboone. *Physical Review D*, 79:072002, 2009.

[167] MicroBooNE Collaboration. Booster neutrino flux prediction at microboone. Collaboration note (MICROBOONE-NOTE-1031-PUB).

[168] W. Coleman, A. Bernstein, S. Dazeley, and R. Svoboda. Transparency of 0.2% gdcl3 doped water in a stainless steel test environment. *Nucl. Inst. Meth. A*, 595:339, 2008.

[169] E. Tiras. Detector r&d for annie and future neutrino experiments. In *Proceedings: 2019 Meeting of the Division of Particles and Fields of the American Physical Society (DPF2019)*, 2019.

[170] D.S. Akerib et al. (LUX Collaboration). The large underground xenon (lux) experiment. *Nucl. Instrum. Meth. A*, 704:111 – 126, 2012.

[171] S. Dazeley and M. Askins et al. A search for cosmogenic production of $\beta$-emitting radionuclides in water. *Nucl. Instrum. Meth. A*, 821:151 – 159, 2016.

[172] M. Askins and M. Bergevin et al. The physics and nuclear nonproliferation goals of watchman: A water cherenkov monitor for antineutrinos. 2015.

[173] Hamamatsu. Photomultiplier Tubes: Basics and Applications, 2007.

[174] A.V. Lyashenko and B.W. Adams et al. Performance of large area picosecond photodetectors ($lappd^{TM}$). *Nucl. Instrum. Meth. A*, 162834, 2019.

[175] T. Pershing. Annie in 10 minutes: multiplicities, cross sections, and models (oh my!), 2018. Fermilab New Perspectives 2019.

[176] K. Hagiwara et al. Gamma ray spectrum from thermal neutron capture on gadolinium-157. *Prog. Theor. Exp. Phys.*, 2019(2):023D01, 2019.

[177] W. Beriguete et al. Production of a gadolinium-loaded liquid scintillator for the daya bay reactor neutrino experiment. *Nucl. Instrum. Meth. A*, 763:82 – 88, 2014.

[178] G. Leinweber and D.P. Barry et al. Neutron capture and total cross-section measurements and resonance parameters of gadolinium. *Nuclear Science and Engineering*, 154:261 – 279, 2006.

[179] B. Hamermesh, G.R. Ringo, and S. Wexler. The thermal neutron capture cross section of hydrogen. *Physics Review*, 90:603, 1953.

[180] H. de Kerret et al. (Double Chooz Collaboration). First double chooz $\theta_{13}$ measurement via total neutron capture detection.

[181] A. Renshaw et al. (Super-Kamiokande Collaboration). Research and development for a gadolinium doped water cherenkov detector. In *Proceedings, 2nd International Conference on Technology and Instrumentation in Particle Physics 2011 (TIPP 2011)*, 2011.

[182] V. Fischer, J. He, M. Irving, and R. Svoboda. Development of an ion exchange resion for gadolinium-loaded water. 2020.

[183] V. Fischer. Annie gadolinium loading - status. Internal note.

[184] F. Abe and D. Amidei et al. The cdf detector: an overview. *Nucl. Inst. Meth. A*, 271(3):387 – 403, 1988.

[185] J. Eisch. Annie daq electronics overview, 2020. Internal collaboration meeting note.

[186] V. Fischer. Annie: Neutron multiplicity in neutrino interactions and technologies. *Journal of Physics: Conference Series (TAUP 2019)*, 1468(012226), 2020.

[187] HVSys company. Light emitting diode sources of calibrated short light flashes. Manual (2013).

[188] P. Shukla and S. Sankrith. Energy and angular distributions of atmospheric muons at the earth. *Int. J. Mod. Phys.*, A33(30):1850175, 2018.

[189] D. Groom, N. Mokhov, and S. Striganov. Muon stopping power and range tables 10 mev - 100 tev. *Atomic Data and Nuclear Data Tables*, 78(2):183 – 356, 2001.

[190] J. Scherzinger and J.R.M. Annand et al. Tagging fast neutrons from an $^{241}am/^{9}be$ source. *Applied Radiation and Isotopes*, 98:74 – 79, 2015.

[191] R. Koohi-Fayegh A. A. Mowlavi. Determination of 4.438 mev $\gamma$-ray to neutron emission ratio from a $^{241}am$- $^{9}be$ neutron source. *Applied Radiation and Isotopes*, 60(6):959 – 962, 2004.

[192] Z. Liu, J. Chen, P. Zhu, Y. Li, and G. Zhang. The 4.438 mev gamma to neutron raio for the am-be neutron source. *Applied Radiation and Isotopes*, 65(12):1318 – 1321, 2007.

[193] L. Pickard. Neutron capture calibration using ambe source, 2019. Internal note, ANNIE Collaboration meeting.

[194] L. Pickard. Annie calibration status, 2019. Internal collaboration meeting note.

[195] ON Semiconductors. J-series sipm sensors, 2018. Rev. 6.

[196] P. Amaudruz et al. In-situ characterization of the hamamatsu r5912-hqe photomultiplier tubes used in the deap-3600 experiment. *Nucl. Instrum. Meth. A*, 922:373 – 384, 2019.

[197] Shimadzu Corporation. Operation guide: Uv-1800 shimadzu spectrophotometer. 2008.

[198] S. J. Gardiner. *Nuclear Effects in Neutrino Detection*. PhD thesis, U.C. Davis, 2018.

[199] S. Dazeley, A. Bernstein, and N. Bowden. The watchboy radionuclide detector deployment and analysis, 2014. LLNL-TR-661658.

[200] K. Nitta et al. (K2K Collaboration). The k2k scibar detector. *Nucl. Instrum. Meth. A*, 535:147 – 151, 2004.

[201] H. Maesaka. *Evidence for Muon Neutrino Oscillation in an Accelerator Based Experiment*. PhD thesis, Kyoto U., 2005. `http://neutrino.kek.jp/publications/theses/maesaka_dt.pdf`.

[202] T. Kikawa. *Measurement of Neutrino Interactions and Three Flavor Neutrino Oscillations in the T2K Experiment*. PhD thesis, Kyoto U. (main), 9 2014.

[203] M. O'flaherty. Truth mrd acceptance and mrd track reconstruction update, 2017. Internal note.

[204] The annie software repository (anniesoft). `https://github.com/ANNIEsoft`.

[205] K. A. Olive et al. (PDG). Review of particle physics. *Chinese Phys. C*, 38(9), 2014.

[206] T. Pershing. The accelerator neutrino neutron interaction experiment (annie): measuring the neutron multiplicity from neutrino-nucleus interactions, 2018. NorCal HEP-EXchange 2018.

[207] J. Caravaca, F.B. Descamps, B.J. Land, M. Yeh, and G. D. Orebi Gann. Cherenkov and scintillation light separation in organic liquid scintillators. *Eur. Phys. J. C*, 77, 2017.

[208] S. J. Parke. *Phys. Rev. Lett.*, 57:1275 – 1278, 1986.

[209] P.J.E. Peebles and J. T. Yu. *Astrophys J.*, 162:815–836, 1970.

[210] E. Noether. Invariant variation problems. *Gott. Nachr.*, 1918:235 – 257, 1918.

[211] M. Banados and I. Reyes. A short review on noether's theorems, gauge symmetries and boundary terms, 2017.

[212] V.B. Berestetskii, E.M. Lifshitz, and L.P. Pitaevskii. *Course of Theoretical Physics Vol. 4*. Pergamon Press, 1971.

[213] K. Kumericki. Feynman diagrams for beginners, 2016.

[214] V. Dudnikov and R.P. Johnson. Cesiation in highly efficient surface plasma sources. *Phys. Rev. Spec. Topics - Acc. and Beams*, 14(054801), 2011.

[215] D. P. Moehs, J. Peters, and J. Sherman. Negative hydrogen ion sources for accelerators. *IEEE Transactions on Plasma Science*, 33(6), 2005.

[216] M. Weiss. Introduction to rf linear accelerators, 1994. CERN Document Server.

[217] D. Alesini. Linear accelerators, 2016. The CERN Accelerator School - Introduction to Accelerator Physics.

[218] D. Barak, B. Harrison, and A. Watts. Fermilab concepts rookie book, 2013. Fermilab Accelerator Division – Operations Department.

[219] I. Stancu and S. Koutsoliotas et al. Technical design report for the miniboone neutrino beam, 2001.

[220] A. Heavey. Going green with blue blocks, 2018. Online article. Accessed 08/18/2019.